



FACULTY OF PHARMACEUTICAL SCIENCES

Improving FRAP and SPT for mobility and interaction measurements of molecules and nanoparticles in biomaterials

Hendrik Deschout

Master of Physics and Engineering Physics

Thesis submitted to obtain the degree of Doctor in Pharmaceutical Sciences

2013

Promoter

prof. dr. Kevin Braeckmans

Co-promoters

prof. dr. ir. Kristiaan Neyts
prof. dr. apr. Jo Demeester

The author and the promotor give the authorization to consult and to copy parts of this thesis for personal use only. Any other use is limited by the laws of copyright, especially the obligation to refer to the source whenever results from this thesis are cited.

De auteur en de promotor geven de toestemming om enkel voor persoonlijk gebruik stukken van deze thesis te raadplegen en te kopiëren. Elk ander gebruik valt onder de beperkingen van het auteursrecht, in het bijzonder de verplichting om te verwijzen naar de bron wanneer resultaten uit deze thesis worden aangehaald.

Ghent, May 27th 2013,

Promoter

prof. dr. Kevin Braeckmans

Author

Hendrik Deschout

TABLE OF CONTENTS

Introduction		7
PART I	FLUORESCENCE RECOVERY AFTER PHOTOBLEACHING	15
Chapter 1	FRAP in pharmaceutical research: from drug delivery to diagnostics	17
Chapter 2	Straightforward FRAP for quantitative diffusion measurements with a laser scanning microscope	51
PART II	SINGLE PARTICLE TRACKING	81
Chapter 3	An introduction to single particle tracking with selected applications in pharmaceutical research	83
Chapter 4	Precisely and accurately localizing single molecules in fluorescence microscopy: state-of-the-art and best practice	95
Chapter 5	The influence of movement on the localization precision of sub-resolution particles in fluorescence microscopy	123
Chapter 6	Correlation of dual colour single particle trajectories for improved detection and analysis of interactions in living cells	153
Chapter 7	On-chip light sheet illumination enables diagnostic size and concentration measurements of submicron membrane vesicles in biofluids	183
Summary		207
Samenvatting		215
Acknowledgements		223
Appendix A	Supplementary information of Chapter 5	227
Appendix B	Supplementary information of Chapter 7	239
Appendix C	Scientific curriculum vitae	249

Introduction

CONTEXT

An increasing amount of pharmaceutical and biomedical technologies are being developed in which nanoparticles play a crucial role. For instance, in the field of gene therapy, intelligent nanomedicines based on polymers or lipids are being designed that are capable of delivering nucleic acids to specific cell types. Among other properties, these nanoparticles should protect their therapeutic payload while manoeuvring through tissues, while having the capability of releasing the nucleic acids inside the target cells. Detailed knowledge is required on the behaviour of these nanomedicines in biological materials in order to optimize their efficiency and safety. In the field of diagnostics, biological vesicles that diffuse inside body fluids such as blood or saliva are being investigated for their potential as diagnostic markers. Properties of these nanoparticles, like size or concentration, could be linked to the progression of certain diseases such as cancer or Alzheimer's disease.

Techniques capable of measuring nanoparticle characteristics like mobility or interaction play a crucial role in this development. However, such measurements are challenging, considering that the nanoparticles are located inside complex biomaterials such as cells, tissues, or blood. Fluorescence microscopy is an interesting technique in this regard, as it allows to selectively visualize nanoparticles that are labelled with a certain fluorescent dye, enabling highly specific and non-invasive measurements. Unfortunately, optical microscopy is limited by its spatial resolution of about 250 nm, which means that nanoparticles cannot be well characterized by mere imaging. Advanced methods based on fluorescence microscopy have, therefore, been developed that extract mobility information from time sequences of images, which in turn reveals information on the physicochemical properties of the nanoparticles and their interaction with their local environment.

One of the first fluorescence microscopy based methods to measure the mobility of molecules and nanoparticles in (bio)materials, developed in the 1970s, is fluorescence recovery after photobleaching (FRAP). In a FRAP experiment, a region in the sample is exposed to a high intensity light beam for a short period of time, causing the fluorescently labelled species in that area to be photobleached. Subsequently, the recovery of the fluorescence inside the photobleached region caused by diffusion of the labelled species is monitored. Fitting the observed recovery to a suitable mathematical model yields quantitative information on the diffusion rate and interactions of the labelled compounds in the biomaterial. Since these experiments can be performed on a standard confocal laser scanning microscope, FRAP has become a frequently used

Introduction

technique in pharmaceutical research. However, accuracy in FRAP data analysis is often hampered by using analysis models that rely on too crude approximations. In particular, the effect of the scanning laser beam and the photochemistry on the shape of the photobleached region is usually either ignored or incorrectly accounted for. Also, FRAP methods are needed that allow for straightforward data analysis while making use of the full tempo-spatial information available in fluorescence recovery images.

FRAP has the fundamental limitation that it only provides information on the ensemble average over all molecules or nanoparticles that participate in the fluorescence recovery. A fluorescence microscopy based method that does not suffer from this drawback is single particle tracking (SPT), first reported one decade after FRAP. An SPT experiment consists of recording a time sequence of images with a detector that is sufficiently sensitive to visualize individual fluorescently labelled nanoparticles (or molecules). By applying image processing, all nanoparticles in the images are identified and their motion trajectories are calculated based on their positions. From these trajectories detailed information on the mobility and interactions of the nanoparticles can be derived. However, just like for FRAP, SPT data analysis can be inaccurate because of certain experimental factors that are incorrectly accounted for. This is especially the case for the experimental uncertainty with which the nanoparticle positions are determined, which is either ignored or at best assumed to be equal to the case of immobile nanoparticles. An even more fundamental issue that degrades the accuracy in SPT is the contrast with which the nanoparticles are visible. In case of conventional widefield illumination, this contrast can become very low due to background fluorescence coming from free dye or nanoparticles that are located out of focus. An interesting recent solution to this problem is light sheet illumination, with which only the nanoparticles in the focal plane area are illuminated, while the nanoparticles outside out of focus remain dark, leading to a much higher contrast. However, current light sheet microscope set-ups typically produce the light sheet by an extra objective lens, thus requiring a special sample holder that allows to position the illumination and imaging objective lens perpendicularly in close proximity with the sample in between. Such a sample holder is not suitable for high-throughput SPT measurements in biofluids, for which inexpensive disposable sample holders are preferred to avoid extensive cleaning procedures and sample contamination.

In this PhD thesis, a number of these problems are addressed to enable improved FRAP and SPT measurements of nanoparticles in biomaterials for pharmaceutical and diagnostic applications.

AIM

The general aim of this PhD thesis is to improve the accuracy of mobility measurements by fluorescence microscopy for the characterization of nanoparticles and molecules in biomaterials. In particular, the fluorescence microscopy based methods FRAP and SPT are considered. FRAP modelling of the fluorescence recovery is revisited in order to incorporate the effect of the scanning laser beam on the shape of the photobleached region in a full tempo-spatial framework. Since FRAP is easily performed with a confocal laser scanning microscope, this new FRAP model should lead to more straightforward and accurate FRAP measurements.

The second and largest part of the PhD thesis deals with SPT, starting with a theoretical and experimental investigation of how motion during image acquisition affects the experimental uncertainty with which the nanoparticle positions are determined. This knowledge is used to develop a method that is able to identify interactions between nanoparticles more reliably and in more detail than classic colocalization measurements, by scanning the nanoparticle trajectories for correlated positions. This method should provide information that can be helpful in the optimization of nanomedicines that are targeted to cells, by measuring the interactions of the nanomedicines with intracellular constituents, such as endosomes. Besides SPT data analysis, it is also explored how light sheet illumination, which allows to strongly reduce the out of focus fluorescence that degrades the contrast in SPT experiments, can be generated by a planar waveguide that is incorporated on a disposable chip. This should make accurate SPT measurements in biofluids available, without the need for extensive cleaning procedures and pre-processing steps in order to remove unbound fluorescent dye. Especially of interest are on-chip SPT size and concentration measurements on cell-derived membrane vesicles, that are currently emerging as non-invasive biomarkers for diseases such as cancer.

OUTLINE

This PhD thesis is divided in two separate parts, each one devoted to an advanced fluorescence microscopy based method for mobility measurements of molecules and nanoparticles. FRAP is the topic of **PART I** that includes **Chapters 1 and 2**. The principle of FRAP and its many applications in pharmaceutical and biomedical research are

Introduction

reviewed in **Chapter 1**. This chapter has the purpose of illustrating the importance and popularity of FRAP in pharmaceutical research, providing a justification for further efforts in improving this fluorescence microscopy based method. An account of this effort is given in **Chapter 2**, where a new theoretical model is developed for the fitting to the fluorescence recovery, observed in FRAP experiments performed with a standard confocal laser scanning microscope. Unlike most conventional models, the full spatial and temporal recovery of a photobleached rectangular area is described by the new model. This has the advantage that the shape of the scanning laser beam can be included in the fitting procedure, allowing for straightforward and accurate FRAP measurements without prior calibration. In collaboration with Dr. Niklas Lorén from the Swedish Institute for Food and Technology, the model is applied to measure the diffusion of macromolecules inside a biopolymer system that consist of two separate phases, which has applications in food as well as pharmaceutical technology.

PART II of this PhD thesis, which comprises **Chapters 3 to 7**, is devoted to SPT. Although SPT is not yet an established and routinely used method in pharmaceutical research, it has great potential, as is briefly discussed in **Chapter 3**. For instance, SPT has already been used to measure the aggregation of nanomedicines in the blood circulation and to investigate their intracellular trafficking. One of the key aspects in all these SPT experiments is the localization of the individual nanoparticles in the recorded microscopy images. The experimental uncertainty with which these locations can be determined is a topic that has recently received a great deal of interest, as it directly influences all subsequent data analysis. An overview of the different theories and experimental techniques to correctly determine this quantity is given in **Chapter 4**. This shows that the localization uncertainty primarily depends on the number of detected photons and the shape of the image of the nanoparticle. Surprisingly, the distortion of this shape because of motion during image acquisition, which is inherently present in all SPT experiments, is in most cases not accounted for. A new theoretical description of the increase in localization uncertainty because of diffusion during image acquisition is therefore introduced in **Chapter 5**, together with a unique approach to experimentally measure the localization precision for moving nanoparticles. This improved description of the localization precision in SPT is then applied to a new method to measure interaction between different nanoparticles with high spatial and temporal resolution, as detailed in **Chapter 6**. Such information is valuable in the field of drug delivery, as illustrated by applying the method to investigate the endosomal trafficking of polymeric gene complexes inside living cells. Besides the localization uncertainty, the quality of SPT experiments is also largely determined by the contrast with which the nanoparticles are visible. Usually, widefield illumination is used for SPT, resulting in limited contrast because out of focus fluorescence. Although this type of

background can be avoided by only illuminating the focal plane area with a light sheet, this generally requires an extra objective lens and a custom-built sample holder. This complicates high-throughput SPT measurements in biofluids, demanding extensive cleaning procedures and running the risk of sample contamination. An alternative and more simple solution is presented in **Chapter 7**, where the development of a disposable microfluidics chip with an integrated planar waveguide for light sheet illumination is discussed. To illustrate its potential as a diagnostics tool, the chip is used for improved SPT size and concentration measurements of cell derived vesicles in interstitial fluid of a human breast tumour.

PART I

FLUORESCENCE RECOVERY AFTER PHOTOBLEACHING

Chapter 1

FRAP in pharmaceutical research: from drug delivery to diagnostics

This chapter is submitted for publication:

Hendrik Deschout^{1,2}, Koen Raemdonck¹, Jo Demeester¹, Stefaan C. De Smedt¹, Kevin Braeckmans^{1,2}

¹Laboratory of General Biochemistry and Physical Pharmacy, Ghent University, Belgium

²Centre for Nano- and Biophotonics, Ghent University, Belgium

ABSTRACT

Fluorescence recovery after photobleaching (FRAP) is a fluorescence microscopy technique that has attracted a lot of interest in pharmaceutical research during the last decades. The main purpose of FRAP is to measure diffusion on a micrometer scale in a non-invasive and highly specific way, making it capable of measurements in biomaterials, even *in vivo*. This has proven to be very useful in the investigation of drug diffusion inside different tissues of the body and in materials for controlled drug delivery. FRAP has even found applications for the improvement of several medical therapies as well as for diagnostics. In **Chapter 1**, an overview is given of the different applications of FRAP in pharmaceutical research, together with essential guidelines on how to perform and analyse FRAP experiments.

1.1 INTRODUCTION AND HISTORICAL OVERVIEW

Being able to measure the diffusion of molecules and nanoparticles inside biological or artificial materials has always been of great interest in pharmaceutically oriented research, and more generally in the life sciences. Fluorescence recovery after photobleaching (FRAP) is an interesting technique for this purpose, as it is fast, non-invasive, highly specific, and relatively easy to perform. FRAP is a fluorescence microscopy method, requiring that the species of interest, which can be molecules or nanoparticles, are labelled with fluorophores. As illustrated in **Fig. 1.1**, a FRAP experiment starts by applying a high intensity light beam for a short period of time to a microscopic region inside the sample. This destroys the fluorescent property of the fluorophores in that region, a phenomenon called photobleaching. Immediately afterwards, the fluorescence in the photobleached region will start to recover, because diffusion causes some of the photobleached molecules to leave and other fluorescent molecules to enter. This recovery is monitored by means of a fluorescence microscope and afterwards a suitable mathematical model is used for analysis, generally yielding the fraction of molecules that are mobile and their diffusion coefficient.

FRAP was developed in the 1970s, using specialized microscope set-ups featuring a stationary (i.e. non-scanning) focused light beam for bleaching and a photo multiplying tube (PMT) or avalanche photodiode (APD) for the fluorescence recovery detection [1]. As illustrated in **Fig. 1.2**, for bleaching, the full intensity of the light source was used, while for imaging the light intensity was strongly attenuated. The shape of the photobleached region was restricted to a circular spot with a Gaussian- or uniform-like intensity distribution. Due to the stationary light beam, no spatial information was available of the recovery process and only the total fluorescence in the bleached spot was measured as a function of time. The first applications of FRAP were mainly situated in the field of cell biology, in particular for measuring the diffusion of proteins in the cell membrane [2,3].

A couple of years later, FRAP was also reported to be used for protein diffusion measurements inside the cell [4,5]. At this time, some groups started to replace the PMT or APD by a camera that was able to capture two-dimensional images of the fluorescence recovery. The additional spatial information could be exploited to analyze the recovery in terms of anisotropic diffusion as well, rather than being limited to isotropic diffusion only [6]. At the end of the 1980s, it was shown that FRAP could be applied for diffusion measurements *in vivo* [7]. The first pharmaceutical applications of FRAP were reported in the early 1990s, when it was applied for measuring the diffusion

rate of proteins inside artificial and biological hydrogels, which is of interest for the development of drug delivery systems [8,9]. Some groups were adapting the mathematical FRAP models for measuring binding instead of diffusion in the cell membrane [10], thus allowing to assess the binding affinity of drug delivery systems for target cell receptors on the plasma membrane.

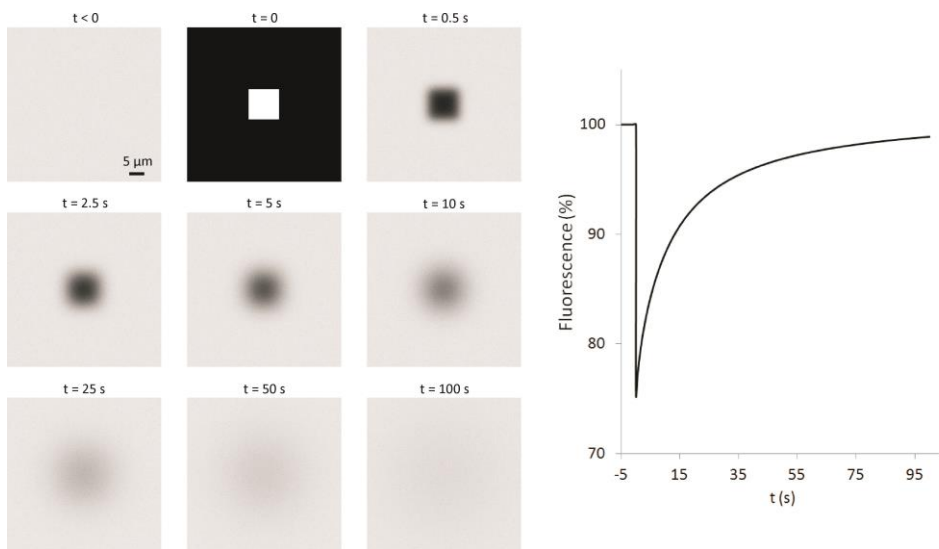


Figure 1.1 | An illustration of a FRAP experiment. On the left, fluorescence microscopy images at different time points t are shown. At $t < 0$, before the photobleaching, the initial fluorescence intensity is registered. At $t = 0$, a square region of $10 \mu\text{m}$ by $10 \mu\text{m}$ is photobleached in the centre of the image by a high intensity laser beam. In the images at the different time points $t > 0$ the recovery of the fluorescence inside the photobleached area is visible. On the right, the total fluorescence in the photobleached square normalized to the initial fluorescence is shown in function of time.

In the 1990s, user-friendly confocal laser scanning microscopes (CLSMs) became more widespread. This type of microscope can be equipped with an acousto optic modulator (AOM) or an acousto optic tunable filter (AOTF), which allows to change the intensity of the scanning laser beam on a pixel by pixel basis in the image. Thus, as illustrated in **Fig. 1.2**, arbitrary patterns could easily be photobleached using standard CLSM equipment [11,12]. Another instrumental development that had important consequences for FRAP in pharmaceutical research was multi-photon fluorescence microscopy. Combining this technique with FRAP allows for diffusion measurements much deeper in tissue than possible with conventional single-photon FRAP [13,14]. At the same time, it became

Chapter 1

clear that the use of the fluorescent protein had important advantages for FRAP measurements inside cells. Until then, the fluorescently labelled proteins had to be microinjected into the cells, a cumbersome manipulation that can disturb the cell's normal working mechanism. Letting the cell express fluorescent proteins, it became possible to perform completely non-invasive FRAP measurements inside cells [15-17]. The combination of all these developments resulted in a steep increase in the use of FRAP in the life sciences [18,19]. However, despite the CLSM being able to photobleach complex shapes and to record two-dimensional recovery images, the analysis was usually limited to the total fluorescence of a circular bleached spot. It was only in the 1990s, with enough computer memory and processing power becoming available in standard computers, that FRAP models were developed that started to exploit more of the available spatial information [20,21]. As discussed in **Chapter 2**, this development is on-going and allows to extract increasingly more information with better accuracy from the observed fluorescence recovery [22-24].

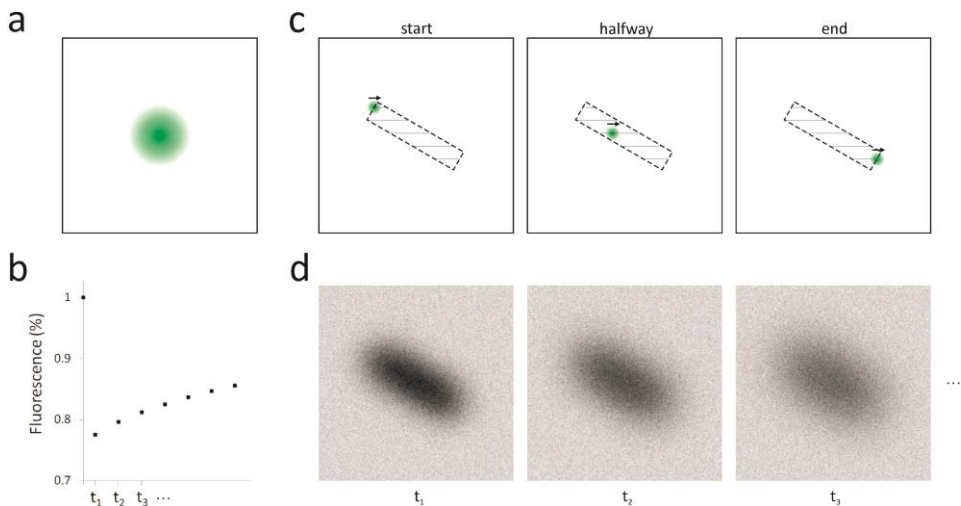


Figure 1.2 | Illustration of a FRAP experiment using a stationary light source and the scanning beam of a CLSM. (a) A stationary light source can only be used to photobleach a circular region. (b) Detection of the fluorescence recovery with a stationary light source is limited to recording the total intensity in the photobleached spot at different time points t_1, t_2, t_3, \dots after photobleaching. (c) In case of a CLSM, arbitrary patterns can be photobleached by scanning the laser beam over the image and applying full laser intensity (green spot) inside the pattern and zero intensity outside. (d) Detection of the fluorescence recovery with a CLSM happens by scanning the laser beam with a constant intensity that is attenuated with respect to the photobleaching intensity. This results in 2D images at different time points t_1, t_2, t_3, \dots after photobleaching. Thus, not only temporal but also spatial information is obtained.

In **Chapter 1**, the most important practical aspects of FRAP experiments and data analysis will be summarized, followed by a discussion of the different applications of FRAP in pharmaceutically oriented research. Not only pharmaceutically relevant applications will be addressed, like the design and optimization of drug delivery systems, also research will be discussed that is situated more on the interface between pharmacy and medicine, such as the improvement of medical therapies and the development of diagnostic tests.

1.2 THEORETICAL FRAP MODELS

Although FRAP is a conceptually simple technique, the analysis of the observed fluorescence recovery can be quite involved. Different types of theoretical models have been developed that describe the recovery process in a number of different circumstances. Here, these FRAP models are briefly discussed.

1.2.1 Diffusion

The original goal of FRAP was to obtain information on the diffusion coefficient of molecules or other nanoparticles, and this is still the most frequent application today. A simple type of analysis is to determine the time it takes until a certain percentage of the fluorescence in the photobleached spot has recovered after photobleaching [25]. However, this approach only allows for qualitative comparison of the diffusion coefficient, and requires identical experimental circumstances. A more quantitative type of analysis requires a theoretical model of the recovery process. There are a number of approaches, all starting from the second law of Fick which describes diffusion in the presence of a concentration gradient [26].

Conventional models

The first type of FRAP models consisted of a mathematical description of the total fluorescence inside the photobleached spot as a function of the time after photobleaching (see **Fig. 1.1**). This was an obvious choice, since that was the only signal that could be measured with early instruments where a stationary light beam was used for photobleaching and imaging [1]. Fitting the model to the experimental recovery

Chapter 1

curve yields the diffusion coefficient and the mobile fraction. Nowadays, even with the CLSM as the standard FRAP instrument, this is still common practice. An expression of the total fluorescence recovery inside the photobleached spot can be obtained by solving the second law of Fick with appropriate boundary and initial conditions. For the boundary condition, it is usually assumed that the sample volume is 'infinitely large'. The initial condition is the concentration profile of the fluorophores immediately after photobleaching, which requires a good description of the photobleaching intensity. Considering a stationary focused laser beam for photobleaching (see **Fig. 1.2a**), the first conventional FRAP models approximated the photobleaching intensity by a circular beam with Gaussian or uniform intensity distribution [1,27]. Similar models have been reported for CLSMs, additionally accounting for the imaging point spread function (PSF) [28]. However, the description of the photobleaching intensity is complicated for a CLSM, i.e. the convolution of the scanning motion with the photobleaching PSF (see **Fig. 1.2c**). Models have been developed that describe the total fluorescence recovery inside a photobleached disk, assuming a Gaussian distributed photobleaching PSF that is identical to the imaging PSF [29]. This approach has been extended for multi-photon FRAP as well [14].

Spatially resolved models

A lot of information is lost by integrating all fluorescence in the photobleached spot, rather than using the full spatial information that is available in the fluorescence recovery images. This limits the analysis in practice to the identification of a diffusion coefficient and a mobile fraction. More complicated situations, like multiple diffusing species, anisotropic diffusion, or flow can be more accurately detected by using the spatial information as well. This can be done by fitting a spatially resolved model to the observed 2D fluorescence recovery. One of the first reports considered the photobleaching of a uniform disk with a CLSM [30]. Similar methods were developed for a line and point source [31] or a Gaussian distribution [28] as initial profiles of the fluorophore concentration after photobleaching. As discussed in **Chapter 2**, we recently developed a flexible and accurate spatially resolved model making use of a photobleached rectangle that can have any size or aspect ratio [22].

Numerical models

The analytical models described above are quite convenient, as they only require to perform a best fit of a mathematical formula to the experimental recovery data. In

order for these models to be valid, it is important to realize that they are derived for particular conditions to which the experiment should comply. In practice, however, this is sometimes difficult, if not impossible, to achieve. For instance, the sample might not be 'infinitely large' but quite limited, such as when performing FRAP experiments in cells. Problems might also arise when diffusion occurs during the photobleaching phase, which is typically not accounted for in the theoretical models. Also, non-linear effects during the high intensity photobleaching phase, may cause substantial deviation of the photobleached area from the theoretically assumed geometry [32]. In these situations that are mathematically complex, only numerical solutions of the second law of Fick might provide a solution, an approach that started to draw attention as soon as standard computers became equipped with sufficient processing power and memory. In a first attempt, the recovery of the average fluorescence of a photobleached line obtained by a CLSM was numerically modelled, incorporating the photobleaching PSF as a Gaussian distribution [33]. However, this method still assumes a specific photobleached shape. This limitation was circumvented by using the first image after photobleaching as the initial condition in order to numerically solve the second law of Fick [34]. In that way, several diffusion coefficients could be included in the analysis. In similar work, a radially symmetric and non-decreasing initial photobleached profile was assumed, which could be estimated from the first image after photobleaching [23]. The drawback of this type of approach is that it requires specific programming expertise that might be too involved for the non-expert user.

Transform models

Besides the numerical models (see above), making use of the Fourier transform of the recovery images is another approach that does not require an analytical description of the initial fluorophore concentration directly after photobleaching [8,21]. This framework has been extended to incorporate anisotropic diffusion [21]. The disadvantage is that a constant fluorophore concentration at the edges of the images is assumed, restricting the size of the photobleached region. In a related effort, the properties of the Hankel transform have been used to distinguish multiple components of diffusion coefficients [24].

1.2.2 Binding

Besides diffusion (see **Section 1.2.1**), also information on the binding kinetics can be derived from the fluorescence recovery in FRAP experiments. Usually, a reversible first

Chapter 1

order reaction is assumed, described by two partial differential equations, one for the concentration of the diffusing fluorophores and one for the concentration of the bound fluorophores [10,35]. Just like the conventional FRAP models for diffusion (see **Section 1.2.1**), these equations are solved for the total fluorescence recovery over the photobleached spot, considering initial and boundary conditions. Besides the concentration of the diffusing fluorophores directly after photobleaching as initial condition, it is also assumed that the system is in equilibrium before photobleaching. Three different regimes can be distinguished from each other [35]. If free diffusion is dominant, the binding can be ignored and the problem reduces to the case of diffusion. When the binding events happen much faster than the diffusion, the recovery can still be described by free diffusion, but with a lower effective diffusion coefficient. A third regime can be considered if the diffusion is very fast compared to the binding reaction and to the timescale of the FRAP measurement. In this case, diffusion is not detected, and the fluorescence recovery is completely determined by the values of the binding rate. The reader is referred elsewhere for more information on this topic [35,36].

1.3 GUIDELINES FOR FRAP EXPERIMENTS

Most FRAP models are specific solutions of the second law of Fick (see **Section 1.2**). The way a FRAP experiment is performed thus has important consequences for the validity of the chosen model. Here, some general guidelines for FRAP experiments are given.

1.3.1 Fluorescent labelling

Since FRAP is a fluorescence microscopy technique, the molecules or nanoparticles of interest should be labelled with fluorophores. It is important that the type of fluorophore is small enough, so that it does not significantly influence the diffusion of the labelled molecule or nanoparticle. Additionally, the dye has to have the property that it photobleaches relatively easily. One of the most commonly used dyes for FRAP is fluorescein or its derivative fluorescein isothiocyanate (FITC). In the case that protein mobility inside a living cell is investigated, the use of the green fluorescent protein (GFP) or a variant is mostly used nowadays. Fluorophores that do not photobleach, but instead switch from a dark state to a bright one (photoactivation) or convert from emission in one spectral band to a different one (photoconversion) can also be used for FRAP [37].

One of the basic assumptions in most FRAP models concerning the fluorescent labelling is that the observed fluorescence scales linearly with the concentration of fluorophores. In a FRAP experiment, this generally means that the fluorophore concentration should be low enough, so that fluorescent light emitted by one fluorophore is not likely to be absorbed by neighbouring fluorophores [38]. If at all possible it is strongly advised to check linearity of the fluorescence signal by making an appropriate dilution series of the fluorescent probe and determine the maximum concentration that is allowed to be used.

1.3.2 Photobleaching

The essential part of a FRAP experiment is the photobleaching of a region in the fluorescent sample. The validity of conventional and spatially resolved FRAP models (see **Section 1.2.1**) is crucially dependent on the way this is done, since the photobleached spot determines the initial condition for solving the second law of Fick.

Light source

A high intensity light source with a wavelength suitable for absorption by the fluorophores is required for photobleaching. Although originally the focused light from a xenon or mercury light bulb was used, nowadays preference is given to lasers which offer a high intensity collimated beam at a specific wavelength. The argon ion gas laser is popular, because it exhibits high intensity laser lines around 488 nm and 514 nm. However, these lasers are being replaced by smaller and more convenient solid state alternatives that are becoming available with increasing power. High intensity pico- or femtosecond pulsed laser sources are capable of two-photon photobleaching, in which case the wavelength should be twice the fluorophore absorption wavelength [39]. The titanium-sapphire laser that has a tunable wavelength in the range of 700 - 1000 nm is often used in combination with green fluorescent dyes. Although the light source should be intense enough to induce photobleaching, care should be taken to avoid non-linear effects that are not considered by most FRAP models [32].

Spot shape and size

Most conventional and spatially resolved FRAP models require a specific shape of the photobleached spot. When a stationary focused light source is used, the models that assume a Gaussian shape can be used, although in practice it is often very difficult to determine the exact width of the spot as it depends on many variables, including the laser intensity, type of fluorophore and the chemical nature of the sample [32]. Yet, accurate knowledge of the spot size is of crucial importance as the calculated diffusion coefficient depends on the square of the spot size. Also, care should be taken when the photobleaching is done by a CLSM. The initial condition is then described by the convolution of the photobleaching PSF with the pattern that is scanned by the CLSM. Many FRAP models ignore the influence of the photobleaching PSF, but this is only permissible if the photobleached spot is sufficiently large (i.e. five times larger than the standard deviation of the photobleaching PSF) [29].

The actual shape of the photobleached spot can deviate from the intended shape because of a significant amount of recovery already taking place during photobleaching, which is not accounted for by most conventional FRAP models [40]. When the model does not correct for this effect, the time it takes for photobleaching should be minimized as much as possible. Photobleaching by long exposure or by repeating the photobleaching step several times should thus be avoided. As a rule of thumb, the photobleaching time is usually taken to be at least 15 times smaller than the characteristic recovery time, that is defined as the average time it takes for a molecule or nanoparticle to diffuse from the centre to the edge of the spot [18]. The effect of recovery during photobleaching can thus also be limited by increasing the size of the photobleached spot.

Objective lens

In case of a high numerical aperture (NA) objective lens (e.g. $NA = 1.2$), the photobleached volume in the direction of the optical axis is not uniform, but has a distinct conical shape and concentration gradient, meaning that recovery along this direction cannot be ignored, see **Fig. 1.3**. The only exception is the specific case of molecules or nanoparticles that diffuse in a 2D plane (e.g. in the cell membrane). That is the reason why low NA objective lenses (e.g. $NA = 0.2$) are often used in FRAP, since these have a low axial resolution that distributes the photobleaching light intensity over an extended cylindrical profile along the optical axis (see **Fig. 1.3**). The drawback of low NA objective lenses for photobleaching is of course the low resolution, which results in

less detailed recovery images. Regardless of the objective lens NA, the effect of recovery in the direction of the optical axis is even stronger in multi-photon than in single-photon FRAP, requiring specialized models [14].

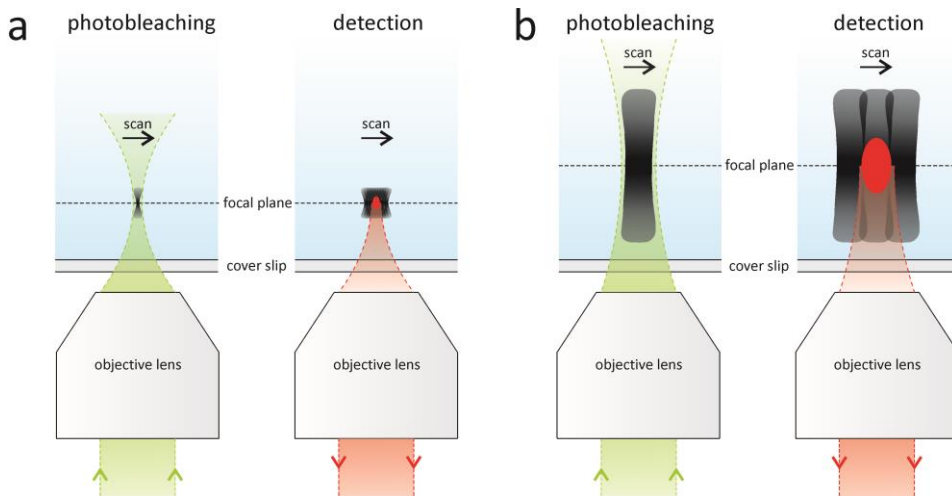


Figure 1.3 | The effect of the numerical aperture of the objective lens on the shape of the photobleached volume when using a CLSM. (a) For high numerical apertures, the extension of the photobleached volume in the direction of the optical axis is limited, meaning that fluorescence recovery in that direction cannot be ignored. **(b)** In case of a low numerical aperture, the photobleached volume is much more extended in the direction of the optical axis, which allows to ignore the fluorescence recovery in that direction.

1.3.3 Fluorescence recovery

After photobleaching, the fluorescence recovery is monitored in a FRAP experiment. The way this is done and the nature of the recovery both affect the validity of the selected FRAP model.

Detection of the recovery

The recovery of the fluorescence is usually monitored at several time points fast enough after photobleaching so that the beginning of the recovery is captured in detail. As a rule of thumb, the time interval between these different time points is taken to be three times smaller than the characteristic recovery time (see **Section 1.3.2**). If there is

Chapter 1

an immobile fraction present, enough time points should be included so that recovery in a later stage is also monitored.

However, photobleaching during detection of the fluorescence recovery can alter the apparent recovery kinetics, as illustrated in **Fig. 1.4**. A balance is, therefore, needed between the number of time points (i.e. the amount of recorded images) and the photobleaching during imaging. This effect can be corrected for, either by including it explicitly in the FRAP model [41], or by monitoring the fluorescence of a suitable background region in the recovery images. The second option is of course only possible with instruments such as a CLSM that acquire images that cover a significantly larger field of view than the photobleached spot. This solution has the advantage that it also corrects for possible intensity fluctuations during imaging.

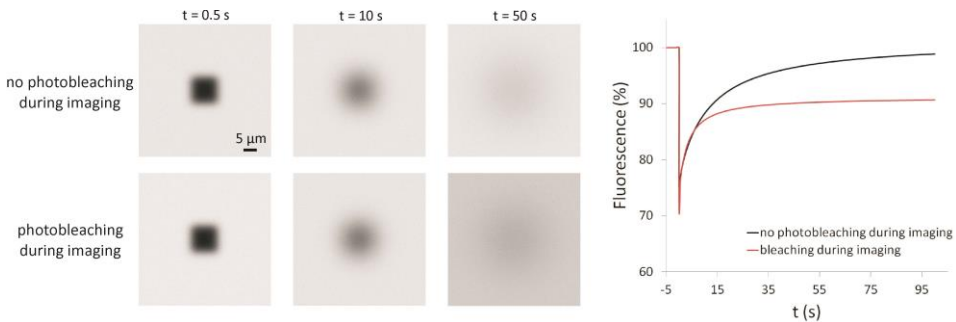


Figure 1.4 | The effect of photobleaching during imaging on a FRAP experiment. On the left, fluorescence microscopy images at three different time points t after photobleaching are shown, for both the situation of photobleaching and no photobleaching during imaging. At $t = 0$, a square region of $10\ \mu\text{m}$ by $10\ \mu\text{m}$ is photobleached in the centre of the image. On the right, the total fluorescence in the photobleached square as normalized to the fluorescence before photobleaching is shown for both situations in function of time. When the photobleaching during imaging is not corrected for, the observed fluorescence recovery is distorted.

Deviations from ideal recovery

Many FRAP models consider only one diffusing species, sometimes in combination with an immobile fraction. If flow is present, the recovery will occur faster than would be expected based on diffusion alone, leading to an overestimation of the real diffusion rate [1]. Care should therefore be taken to avoid flow in the sample. Related to this, the sample should be in thermodynamic equilibrium so that no net mass transport is occurring that would distort the FRAP measurement. In case of deviations from simple

one-component diffusion, e.g. anomalous diffusion or multiple diffusing species, a specialized FRAP model should be applied.

Almost all FRAP models assume that the sample has an infinite volume as boundary condition. In practice, this means that the diffusing molecules or nanoparticles should not be hindered during the monitoring of the fluorescence recovery. Deviations from this boundary condition should be avoided as much as possible, which is especially a concern inside cells.

1.4 APPLICATIONS OF FRAP IN PHARMACEUTICAL RESEARCH

1.4.1 Designing drug delivery systems

Drug delivery systems are being developed to achieve time-controlled delivery of encapsulated drugs. FRAP has been used to characterize diffusion in such materials in order to understand the macroscopic release profiles. This kind of information is needed to guide the optimization of these systems.

Diffusion inside hydrogels

Hydrogels comprise an important class of matrix materials for time-controlled drug delivery. A hydrogel consists of a physically or chemically cross-linked 3D network of hydrophilic polymers that has absorbed a large amount of water [42]. Drug molecules can be trapped in the hydrogel by chemical bonds and hydrophobic or electrostatic interactions. Dependent on the mesh size of the polymeric network, some therapeutic molecules (e.g. pharmaceutical proteins) can be physically trapped in the hydrogel pores. This not only shields the molecules from the environment, but also allows to tailor drug release from the hydrogel matrix. The drug release is often mediated by a gradual degradation and/or swelling of the hydrogel network [43]. FRAP has proven to be a valuable technique for characterization of the diffusion process underlying the overall release profile.

A variety of techniques and polymers have been used to fabricate hydrogels for drug delivery. One example is the use of peptide sequences that fold and self-assemble into hydrogels [44]. Using fluorescently labelled dextrans as model drug molecule, FRAP measurements showed that their mobility and release could be modulated by varying

Chapter 1

the mesh size. Another self-assembling hydrogel was based on biodegradable dextran microspheres [45]. The hydrogel was obtained by hydration of mixtures of oppositely charged dextran microspheres with a protein solution. FRAP was used to study the mobility of proteins in these gels, showing a continuous release of entrapped proteins with preservation of their activity.

Other preparation methods exist besides self-assembly, such as step-growth polymerization of poly(ethylene glycol) (PEG) [46]. FRAP measurements of dextrans inside these gels corresponded well with results from NMR spectroscopy and release experiments. Another PEG-based hydrogel was formed by the radically cross-linkable oligo(poly(ethylene glycol)fumarate) together with two cross-linking agents [47]. FRAP experiments were performed to measure the diffusion coefficient of dextrans inside this hydrogel. Hydrogels have also been fabricated from chitosan by chemical cross-linking with dialdehydes [48]. FRAP was used to measure the diffusion of dextrans with different molecular weight in these hydrogels and in aqueous solution. Above a molecular weight of 100 kDa, the dextrans were found to diffuse slower in the hydrogel, indicating hindered diffusion.

Composite hydrogel systems have also been of interest, such as agarose-dextran composite gels [49]. FRAP was used to measure diffusion of proteins and polysaccharides in these hydrogels and in aqueous solution, indicating an increase in hindered diffusion with hydrodynamic diameter. Additionally, the diffusion was more hindered in hydrogels with higher dextran concentrations. Another example are gelatin hydrogels in which chondroitin sulfate (ChS) was incorporated to retard the release of cationic proteins because of electrostatic interactions [50]. FRAP showed that diffusion of lysozymes inside the hydrogel increases with increasing ChS content.

More complicated fabrication processes allow for greater flexibility in hydrogel properties. Hydrogels consisting out of ABA triblock copolymers were fabricated, in which the A-block is a thermosensitive polymer and the B-block is a PEG [51]. The gels were prepared by thermogelling combined with photopolymerization, which is a fast and simple cross-linking method that improves stability and mechanical properties. FRAP showed that the release rate of bovine serum albumin (BSA) depended on the protein size and the hydrogel molecular weight between the cross-links. In related work, FRAP was used to measure the diffusion of dextrans in the same type of hydrogel for different temperatures used during thermogelling [52]. The diffusion and mobile fractions were found to decrease upon elevating the temperature above 25° C, and the mobility could be adjusted by changing the PEG block length.

Complicated hydrogel fabrication can lead to interesting hydrogel structures. For instance, hydrogels with nanostructured porosity were produced by synthesizing and cross-linking ABA triblock copolymers, with ϵ -caprolactone (PCL) A-blocks and a poly(ethylene oxide) (PEO) B-block [53]. By subsequently degrading the gels by hydrolysis to remove the PCL domains, pores are formed which allow fast transport of molecules through the hydrogel. By using FRAP, it was shown that diffusion of proteins and polystyrene beads inside the hydrogel is higher than in comparable homogeneous hydrogels.

Intelligent stimuli-sensitive hydrogels that change behaviour in response to varying environmental conditions have also been developed. A hydrogel for colon drug delivery was fabricated, using an enzymatic procedure to modify a galactomannan hydrogel and guar oligomer in order to entrap the guar oligomer [54]. The hydrogel retains the guar oligomer until it reaches the colonic environment where bacteria-secreted enzymes degrade the hydrogel. FRAP was used to quantify the diffusion of guar oligomer inside the hydrogel, showing that diffusion was decreased significantly compared to non-interacting probes and remained constant over a couple of hours, resulting in a gradual release. Another system intended for colonic drug delivery is a hydrogel based on konjac glucomannan, which is a polysaccharide that is not degradable in the small intestine but is degradable by anaerobic human intestinal bacteria [55]. FRAP was performed to measure the diffusion and mobile fraction of dextrans in the system and it was found that the diffusion behaviour cannot only be explained by macroscopic properties of the medium. Also the molecular size and a sieving mechanism have to be taken into account.

Permeability of polyelectrolyte capsules

Layer-by-Layer (LbL) polyelectrolyte capsules are microparticles that are being evaluated for controlled drug delivery [56]. The polyelectrolyte shells of the capsules are semi-permeable, so that large molecules cannot diffuse through the polymer wall, resulting in their protection from environmental degradation. In this context, FRAP has been used to assess the permeability of the capsule walls by monitoring the fluorescence recovery after completely photobleaching the fluorescence inside the capsule.

Different methods have been investigated to load molecules inside LbL polyelectrolyte capsules. For instance, in the case of capsules that consist of eight layers of poly(diallyldimethylammonium chloride) and poly(styrene sulfonate), this could be done by temperature induced rearrangements within the shells [57]. FRAP was used to demonstrate that the permeability for dextrans decreases after heat incubation.

Chapter 1

Another example are composite systems composed of poly-L-lysine and trisodium citrate LbL polyelectrolyte capsules that contain magnetic particles [58]. Using FRAP, it was found that the permeability for dextrans could be controlled by altering the extent of glutaraldehyde cross-linking. It has been argued that polysaccharides offer an attractive biocompatible alternative over synthetic polyelectrolytes. For instance, the anionic alginate sodium and cationic chitosan were used as wall components for multilayer LbL capsules [59]. The shells displayed high stability in poly(styrenesulfonate sodium) and FRAP was used to study the permeability of the shells.

1.4.2 Overcoming drug delivery barriers

When soluble drugs or drug-loaded nanoparticles (i.e. nanomedicines) are administered to the human body, they need to manoeuvre inside extracellular matrices (ECMs) before they reach their target cells. A variety of ECMs exist, which have in common that they are rather complex materials that consist of networks of biomacromolecules that can hinder the transport of drugs, and thus act as a barrier for drug delivery. FRAP has been used to measure the mobility in these ECMs, information that is useful in the design of carriers for drugs that could assist them to reach their destination.

Solutions and gels as model ECM

Different types of gels and solutions have been used as a model to study mobility in ECMs. One example is agarose gel and simulated tissue consisting of cells embedded in agarose gel [8]. FRAP was used to study the diffusion of dextrans and proteins in these gels. In another study, the diffusion of proteins, polystyrene microspheres, dextrans, and dendrimers in PEO and guar galactomannan solutions was measured with FRAP [60]. The purpose was to investigate the effect on diffusion of different probe sizes and shapes relative to the PEO and guar galactomannan mesh. It was found that diffusion of nanospheres was more hindered than dextrans with the same hydrodynamic diameter. At equal mesh size, the diffusion through the more rigid guar galactomannan solution was hindered compared to the more flexible PEO solution. Mobility in ECMs was also modelled with cross-linked matrices consisting of the proteins fibrinogen, fibronectin, and concanavalin A [61]. The mobility of Texas red and dextrans inside these matrices and in solution was measured with FRAP. Diffusion was found to be 3 to 4 orders of magnitude slower than in solution, and hindered diffusion was observed as well, caused by specific molecular interactions of the probes with the matrix proteins.

Tumour interstitium

The tumour interstitium is an important barrier for drug delivery in cancer therapy [62]. This ECM consists of a collagen network embedded in a gel of the proteins glycosaminoglycan and proteoglycan. FRAP is a particularly interesting technique in this context, because diffusion is the most important transport mechanism for nanomedicines inside tumours [63].

To investigate the effect of collagen in the tumour interstitium, FRAP was used to measure the diffusion of immunoglobulin (IgG) in different human tumour xenografts in mice [64]. The diffusion of IgG was found to decrease with the amount of collagen in the tumour, while collagenase treatment significantly increased diffusion, identifying collagen as an important diffusion barrier for tumour interstitium penetration. A similar investigation was carried out on the effect of different tumour types and anatomical locations on the diffusion rate [63]. The diffusion of proteins, dextrans, and liposomes inside two different human tumour xenografts grown in cranial windows and dorsal chambers in mice was investigated with FRAP. Diffusion was faster in the cranial window than in the dorsal chamber tumours, which correlates with a lower density of host stromal cells that synthesize collagen in the cranial window tumours, confirming that collagen plays an important role in diffusion hindrance in the tumour interstitial fluid. To investigate the effect of collagen in more detail, FRAP measurements were carried out on diffusing proteins and dextrans inside collagen gels [65]. Good agreement was found with *in vivo* measurements in tumours with a comparable collagen concentration.

More recently, investigations have been undertaken to identify the role of other tumour interstitium properties on the mobility besides collagen content. For instance, the spatial orientation of the collagen network was studied by measuring the diffusion of dextrans inside collagen gels and human tumour xenografts using multi-photon FRAP [66]. It was shown that the network orientation leads to diffusion anisotropy, although it does not affect overall diffusion. This was confirmed in another investigation, where two-photon FRAP was used to measure the diffusion of dextrans in collagen gels that were aligned in a magnetic field [67]. In the same study, the effect of glycosaminoglycans (e.g. hyaluronan) and proteoglycans (e.g. decorin) was also investigated by adding decorin and hyaluronan to the collagen gels. The presence of decorin had no effect on the diffusion, while high concentrations of hyaluronan increased diffusion. In relation to these findings, the effect of collagen and hyaluronan degrading enzymes on the diffusion of dextrans in human tumor xenografts was investigated [68]. FRAP showed that the diffusion increased largely due to the collagen degrading enzymes. Investigation of the difference in diffusion hindrance caused by

Chapter 1

interstitial versus cellular constituent was also carried out [69]. Multi-photon FRAP measurements of the diffusion of IgG in tumours and gels consisting out of collagen and hyaluronan showed that decreasing the cell density increases diffusion.

Although it is possible to perform FRAP in human tumours *in vivo*, it is more convenient to conduct such experiments *ex vivo* on biopsies. To quantify the effect of excision and cooling, FRAP was used to measure the diffusion of BSA and IgM in human tumour xenografts in mice both *in vivo* and *ex vivo* [13]. The correction determined from these measurements was applied to calculate the diffusion of BSA and IgM in human tumours *in vivo* from the values obtained in biopsies. A higher diffusion was found in human tumour xenografts *in vivo*, probably because of a lower concentration of collagen in the accessible regions of human tumours. A solution to this problem is given by microfiberoptic epifluorescence photobleaching, in which a fiber with a micron sized tip is introduced deep inside tissue *in vivo* [70]. Inside subcutaneous tumours in mice, the diffusion of dextrans was indeed found to be slower deeper inside the tumour tissue. Other experimental complications such as the effect of flow in tumours have been investigated as well. A method based on multi-photon FRAP has been developed to account for such flow [71]. Both diffusion and flow of dextrans were measured in murine tumours implanted in dorsal chambers in mice *in vivo*.

Brain extracellular matrix

The brain ECM in which neurons, glial cells, and blood vessels are embedded, consists of ions, neurotransmitters, metabolites, peptides, and other molecules [72]. This ECM is an important barrier for drugs that treat diseases and disorders related to the brain function. To enable successful drug delivery to the brain, it is thus important to understand transport inside the brain ECM, for which FRAP can again be useful [73].

For instance, FRAP was applied to measure the diffusion of dextrans in mouse brain *in vivo*, showing that it is threefold slower than in solution [72]. In case of seizure activity or cytotoxic brain edema associated with head injury, the diffusion was found to decrease by more than a factor of 10. In a similar study, a drop in diffusion was also found in the presence of cytotoxic brain edema, while a slight increase in diffusion was measured in case of vasogenic brain edema associated with brain tumour [74]. However, a fourfold decrease in diffusion was found inside the brain tumour itself. The extent of diffusion hindrance in the brain ECM was investigated in detail by performing FRAP on dextran inside mouse brain ECM and inside solution [75].

To measure diffusion in the ECM in parts of the brain that are not accessible by light microscopes, microfiberoptic epifluorescence photobleaching (see above) was applied [76]. Dextran was found to diffuse more than 4 times slower in the cerebral cortex ECM compared in solution, independent of the depth inside the cerebral cortex. It was also shown that diffusion varied strongly in different parts of the brain, with faster diffusion in the thalamus and slower in the hippocampus compared to the cerebral cortex. Deep inside the brain, the diffusion compared to free solution was strongly dependent on the dextran size, indicating hindered diffusion, while this was not the case in the cerebral cortex.

Mucus

Several epithelial surfaces in mammalian organs in the respiratory, gastrointestinal, and reproductive tract are covered with a mucus layer. This layer limits the exposure of human tissues to external pathogens and as such also represents a significant barrier for drugs that have to reach or get across these epithelial linings [77]. Mucus is a viscoelastic gel with as main components water, mucin, inorganic salts, carbohydrates, and lipids. The thickness of the mucus layer ranges from a few micron to several hundred microns, depending on the organ. FRAP can be used to study the ability of drugs to diffuse within the mucosal network [78].

FRAP was used to measure the diffusion of immunoglobulin (IgA, IgG, and IgM) inside human cervical mucus [9]. It was found that immunoglobulin diffusion was relatively unhindered, suggesting pore sizes in the mucus of around 100 nm. In a similar investigation, FRAP was used to determine the diffusion of proteins, viruses, and polystyrene microspheres in human cervical mucus [79]. Most proteins and even the smaller viruses could diffuse as rapidly in mucus as in water. The larger microspheres and viruses did not diffuse, probably because of sticking to mucin strands. In line with these results, a FRAP study in expectorated cystic fibrosis lung sputum revealed that the mucus network did not hinder diffusion of dextrans with different molecular weights up to 2000 kDa (corresponding to a hydrodynamic diameter of approx. 65 nm) [29]. Taken together, these investigations suggest that mucus does not pose a sterical barrier to molecules or small nanoparticles, although adhesion to the biopolymers might be an issue.

In the context of gene therapy, FRAP was employed to measure diffusion of plasmid DNA in bovine cervical mucus [80]. Supercoiled DNA was found to diffuse faster than linear DNA, and complexation of the DNA with liposomes increased the diffusion two-fold.

Other drug delivery barriers

For the treatment of bone diseases such as osteoporosis or osteonecrosis, it is essential that drugs are able to traverse the bone tissue. Bone mainly consists out of osteocytes that form a cellular network embedded within a mineralized matrix that is largely impermeable. Instead of diffusion, it is hypothesized that load-induced flow within the bone lacunar-canalicular system serves as the main transport mechanism in bone [81]. FRAP is an interesting technique to gain better understanding of this flow, as it complements the classic perfusion measurements that lack temporal dynamics and that are prone to histologic artefacts [82]. The technique was applied to measure the diffusion and flow of sodium fluorescein in the lacunar-canalicular system of mouse bone, confirming the hypothesis of a load-induced flow [83].

In the treatment of retinal diseases, intravitreal injection is an attractive administration route for drugs, since systemic delivery is impeded by the blood-retina barrier. The vitreous humour is a hydrogel formed by a network of collagen fibrils that are cross-linked by proteoglycan filaments. Besides collagen and proteoglycan, the vitreous also contains other proteins such as hyaluronan. Contrary to the case of cystic fibrosis sputum (see above), FRAP measurements showed that dextrans in the vitreous experience a sterical hindrance that is proportional to their molecular weight, likely due to the dense network of hyaluronic acid polymers [29]. In the context of gene therapy, FRAP has been used to measure the diffusion of polystyrene nanospheres and complexes of plasmid DNA and liposomes in the vitreous of bovine eyes [84]. While nanospheres functionalized with PEG were found to be mobile, the DNA complexes were immobilized because of aggregation and binding to fibrillar structures in the vitreous. By adding a PEG coating to the DNA complexes, aggregation and binding could be prevented.

The stratum corneum is the top layer of the skin and consists of several layers of corneocytes. Since its purpose is to protect the underlying tissue, it constitutes the primary barrier for transdermal drug delivery. Mobility measurements inside the stratum corneum are, therefore, of interest in the development of drug formulations intended for topical administration. In this context, FRAP was used to measure the diffusion of several lipophilic probes of different molecular weight in model lipid bilayers and in a lipid bilayer consisting of human stratum corneum extracted lipids [85].

1.4.3 Drug delivery inside cells

An increasing number of nanomedicines are developed for drug delivery in the intracellular space of target cells, which means they need to find their way inside the cytoplasm, and sometimes even to the cell nucleus. A better understanding of mobility inside the cell is thus of great importance in this effort [19].

FRAP has been used to investigate the diffusion of a variety of macromolecules inside living cells. For instance, the technique was used to measure the diffusion of microinjected dextrans with different molecular weights inside the cytoplasm and nucleus of epithelial cells and fibroblasts [86]. The diffusion in both cytoplasm and nucleus was found to be approximately 4 times slower than in water. This factor was independent of the molecular weight up to 500 kDa, indicating that the diffusion is unhindered. This result was contradicted by other studies, where FRAP was used to measure the diffusion of dextrans [87] and proteins [88] with different molecular weights in the cytoplasm of muscle cells. The diffusion of the dextrans and especially the proteins was found to be hindered with increasing molecular weight, likely because of different compounds of the cytoskeleton. Recently, FRAP was used to show that the cytoplasm of cells behaves like a poroelastic material [89].

Besides these general investigations, FRAP has also been applied to measure the intracellular diffusion of nucleic acids, which is of relevance to gene therapy. The diffusion of double stranded DNA fragments with different numbers of base pairs was measured after microinjection into the cytoplasm and nucleus of HeLa cells [90]. In the cytoplasm, diffusion was found to be significantly lower than in water, and the diffusion was found to be increasingly hindered with an increasing number of base pairs. In the nucleus, the DNA fragments were immobile, in contrast to dextrans with similar molecular weight, indicating that DNA immobilization is caused by binding. FRAP was also used to investigate the diffusion of single stranded DNA. For instance, after introduction into the nucleus of rat myoblasts, the diffusion of oligodeoxynucleotides was found to be similar to its diffusion in solution [91].

Potential intracellular drug delivery carriers, such as Tat-derived peptides [92], have also been studied. FRAP was used to investigate the intracellular mobility of Tat-peptides with cargoes of different molecular weights below and above the threshold for diffusion through the nuclear pores [93]. This was done by photobleaching the fluorescence inside the nucleus and subsequently monitoring the recovery coming from the cytoplasm, and vice versa. Combined with FRAP diffusion measurements, it was found that the Tat-peptides with cargoes with a molecular weight below the threshold are able to cross the nuclear envelope by diffusion.

1.4.4 Improving therapy

FRAP can also be of interest for providing information that helps improving medical therapies. FRAP has found a number of different and sometimes surprising applications in this context.

Several neuro-degenerative diseases, such as Parkinson's and Alzheimer's disease, are related to protein or peptide aggregates inside the brain. FRAP has been reported for measuring the diffusion of α -synuclein [94] and amyloid- β [95] aggregates, providing information that is not only useful for a better understanding of the molecular mechanisms that cause these diseases, but also for assessing potential treatments that can reverse this aggregation. Besides these mobility measurements, FRAP has also been employed to assess cell membrane perturbations caused by amyloid- β aggregates [96]. This can be done by measuring the membrane fluidity, which basically means verifying whether lipids inside the membrane are undergoing free diffusion or not.

Stem cell therapy is a promising approach for the treatment of a variety of pathologies. In this context, it is important to assess the gap junctional intercellular communication (GJIC), as it is essential for maintaining homeostatic balance and normal differentiation of cells. FRAP was used to measure the presence of GJIC, not by measuring diffusion in the classical sense, but by monitoring the fluorescence recovery rate in one cell due to influx of fluorescence from another cell through the gap junction channels between both cells [97-99].

For cancer therapy, FRAP was used to monitor the change in mobility of tumour associated proteins inside living cells induced by candidate anti-cancer drugs such as dihydroartemisinin [100], apigenin [101], cytosine arabinoside [102], and multimeric RGD-peptides [103]. FRAP can also be used to determine binding kinetics, which is useful in the context of cancer therapy in order to assess the binding affinity of antibodies to their tumour-associated antigen [104,105]. FRAP has also been reported to measure the effect of an apoptosis inducing drug on the GJIC [106], and to measure the cell membrane fluidity in the context of electro-chemotherapy [107].

Injury treatment is also of interest in pharmaceutical research and FRAP has found some applications in this context. For instance, the diffusion of dextrans was measured *in vivo* inside blood vessels of injured muscle tissue of mice in order to assess the endothelial barrier function [108]. In the context of retinal injuries, the diffusion of dextrans in the retina ECM of mice was measured after damage was induced by elevated intraocular pressure [109]. Furthermore, FRAP has been used to study the effect of the antioxidant α -tocopherol on the membrane fluidity after arterial injury [110].

Some specific applications of FRAP have also been reported in the context of a variety of other medical treatments. Pulsed high intensity focused ultrasound is a technique that has potential to treat thrombolysis. FRAP was used to measure the diffusion of dextrans in blood clots after treatment, and it was found that the diffusion coefficient increased significantly [111]. In the context of cystic fibrosis, FRAP was used to measure the diffusion of dextrans in the fluid of submucosal glands [112]. A decrease in diffusion was found compared to the normal situation, providing evidence for defects in submucosal gland function caused by cystic fibrosis. In research on the human immunodeficiency virus type 1, FRAP was used to determine the effect of sphingomyelinase treatment on the diffusion of several receptor proteins in the cell membrane [113]. It was found that the diffusion of the HIV receptor CD4 decreased after treatment. FRAP measurements of diffusion of proteins inside cells were also undertaken in research aimed at improving the treatment of diarrheal diseases [114], neuropsychiatric disorders [115], and obesity [116].

1.4.5 Diagnostics

A less obvious application of FRAP is situated in the field of diagnostics. Medical conditions are sometimes preceded by a change in the structure of the affected cells or the surrounding ECM. This, in turn, can result in a change of mobility inside these cells or the ECM. In this context, some efforts have been undertaken to use FRAP as a diagnostic assay by measuring such changes in mobility. In one case, FRAP was used to measure the diffusion of dextrans in the ECM of mouse brain *in vivo*, since diffusion inside the brain ECM is related to neural activity [72]. It was found that slowed diffusion preceded seizure activity, indicating that FRAP measurements can be used as a predictor of impending brain seizure. In another study, FRAP was used to investigate the diffusion of dextrans inside a tissue-engineered skeletal muscle model in compressed and uncompressed state [117]. A significantly reduced diffusion coefficient was found in the compressed state, which could be considered in the development of a screening method for early detection of pressure-related deep tissue injuries.

1.5 CONCLUSION AND FUTURE OUTLOOK

Almost 40 years after its conception, FRAP has become a mature technique that is of great value to pharmaceutical research. The technique has been employed to tailor the

Chapter 1

properties of drug delivery systems, to test how drugs can overcome delivery barriers inside the body, to improve several medical therapies, and even to serve as a diagnostic tool.

The success of FRAP has several explanations. First of all, the technique is conceptually simple and in recent years widely available to everyone with access to a standard CLSM. Secondly, it is one of the few tools that is able to perform diffusion measurements inside living tissue and even inside living cells. This is an invaluable asset to pharmaceutical research and more generally to the life sciences. And last but not least, FRAP is a versatile technique, not being limited to measuring diffusion coefficients, but also allowing investigation of binding kinetics, membrane fluidity, gap junctional intracellular communication, and permeability of vesicles.

Despite the success of FRAP, some critical remarks are in place. Most theoretical FRAP models make assumptions that are not always correct in reality, even when applied in simple drug delivery systems like hydrogels. In particular, when using a CLSM, the effect of the scanning laser beam is often ignored or incorrectly accounted for. A model that accounts for this issue is developed in **Chapter 2**. Further problems can still arise in more complicated biological systems. For instance, inside living cells, deviations in the fluorescence recovery caused by the cell boundaries cannot easily be corrected for. Apart from these theoretical issues, another important but underreported problem when performing FRAP in living systems is the amount of damage caused by photobleaching and the possible related increase in temperature [118]. These effects should be minimized as much as possible since they can distort the measurements.

Besides FRAP, other fluorescence techniques exist that are capable of diffusion measurements. In particular, fluorescence correlation spectroscopy (FCS) and single particle tracking (SPT), which is the topic of **PART II**, are interesting techniques that do not suffer from some of the drawbacks listed above, simply because they do not rely on deliberate photobleaching [119,120]. For some applications, FRAP might become replaced by FCS and SPT, but the technique will continue to be of use to pharmaceutical research because of its obvious advantages.

REFERENCES

1. D. Axelrod, D. E. Koppel, J. Schlessinger, E. Elson, and W. W. Webb, "Mobility Measurement by Analysis of Fluorescence Photobleaching Recovery Kinetics," *Biophysical Journal* **16**, 1055-1069 (1976).
2. J. Schlessinger, D. E. Koppel, D. Axelrod, K. Jacobson, W. W. Webb, and E. L. Elson, "Lateral Transport on Cell-Membranes - Mobility of Concanavalin A Receptors on Myoblasts," *Proceedings of the National Academy of Sciences of the United States of America* **73**, 2409-2413 (1976).
3. M. Edidin, Y. Zagayansky, and T. J. Lardner, "Measurement of Membrane Protein Lateral Diffusion in Single Cells," *Science* **191**, 466-468 (1976).
4. Y. Wang, F. Lanni, P. L. Mcneil, B. R. Ware, and D. L. Taylor, "Mobility of Cytoplasmic and Membrane-Associated Actin in Living Cells," *Proceedings of the National Academy of Sciences of the United States of America-Biological Sciences* **79**, 4660-4664 (1982).
5. J. W. Wojcieszyn, R. A. Schlegel, E. S. Wu, and K. A. Jacobson, "Diffusion of Injected Macromolecules Within the Cytoplasm of Living Cells," *Proceedings of the National Academy of Sciences of the United States of America-Biological Sciences* **78**, 4407-4410 (1981).
6. H. G. Kapitza, G. McGregor, and K. A. Jacobson, "Direct Measurement of Lateral Transport in Membranes by Using Time-Resolved Spatial Photometry," *Proceedings of the National Academy of Sciences of the United States of America* **82**, 4122-4126 (1985).
7. S. R. Chary and R. K. Jain, "Direct Measurement of Interstitial Convection and Diffusion of Albumin in Normal and Neoplastic Tissues by Fluorescence Photobleaching," *Proceedings of the National Academy of Sciences of the United States of America* **86**, 5385-5389 (1989).
8. D. A. Berk, F. Yuan, M. Leunig, and R. K. Jain, "Fluorescence Photobleaching with Spatial Fourier-Analysis - Measurement of Diffusion in Light-Scattering Media," *Biophysical Journal* **65**, 2428-2436 (1993).
9. W. M. Saltzman, M. L. Radomsky, K. J. Whaley, and R. A. Cone, "Antibody Diffusion in Human Cervical-Mucus," *Biophysical Journal* **66**, 508-515 (1994).
10. E. N. Kaufman and R. K. Jain, "Quantification of Transport and Binding Parameters Using Fluorescence Recovery After Photobleaching - Potential for In Vivo Applications," *Biophysical Journal* **58**, 873-885 (1990).
11. K. Braeckmans, S. C. De Smedt, M. Leblans, R. Pauwels, and J. Demeester, "Encoding microcarriers: Present and future technologies," *Nature Reviews Drug Discovery* **1**, 447-456 (2002).
12. K. Braeckmans, S. C. De Smedt, C. Roelant, M. Leblans, R. Pauwels, and J. Demeester, "Encoding microcarriers by spatial selective photobleaching," *Nature Materials* **2**, 169-173 (2003).
13. E. B. Brown, E. S. Wu, W. Zipfel, and W. W. Webb, "Measurement of molecular diffusion in solution by multiphoton fluorescence photobleaching recovery," *Biophysical Journal* **77**, 2837-2849 (1999).
14. D. Mazza, K. Braeckmans, F. Cella, I. Testa, D. Vercauteren, J. Demeester, S. S. De Smedt, and A. Diaspro, "A new FRAP/FRAPa method for three-dimensional diffusion measurements based on multiphoton excitation microscopy," *Biophysical Journal* **95**, 3457-3469 (2008).

Chapter 1

15. J. G. McNally, W. G. Muller, D. Walker, R. Wolford, and G. L. Hager, "The glucocorticoid receptor: Rapid exchange with regulatory sites in living cells," *Science* **287**, 1262-1265 (2000).
16. R. Swaminathan, C. P. Hoang, and A. S. Verkman, "Photobleaching recovery and anisotropy decay of green fluorescent protein GFP-S65T in solution and cells: Cytoplasmic viscosity probed by green fluorescent protein translational and rotational diffusion," *Biophysical Journal* **72**, 1900-1907 (1997).
17. J. White and E. Stelzer, "Photobleaching GFP reveals protein dynamics inside live cells," *Trends in Cell Biology* **9**, 61-65 (1999).
18. T. K. L. Meyvis, S. C. De Smedt, P. Van Oostveldt, and J. Demeester, "Fluorescence recovery after photobleaching: A versatile tool for mobility and interaction measurements in pharmaceutical research," *Pharmaceutical Research* **16**, 1153-1162 (1999).
19. A. S. Verkman, "Solute and macromolecule diffusion in cellular aqueous compartments," *Trends in Biochemical Sciences* **27**, 27-33 (2002).
20. U. Kubitscheck, P. Wedekind, and R. Peters, "Three-dimensional diffusion measurements by scanning microphotolysis," *Journal of Microscopy-Oxford* **192**, 126-138 (1998).
21. T. T. Tsay and K. A. Jacobson, "Spatial Fourier-Analysis of Video Photobleaching Measurements - Principles and Optimization," *Biophysical Journal* **60**, 360-368 (1991).
22. H. Deschout, J. Hagman, S. Fransson, J. Jonasson, M. Rudemo, N. Loren, and K. Braeckmans, "Straightforward FRAP for quantitative diffusion measurements with a laser scanning microscope," *Optics Express* **18**, 22886-22905 (2010).
23. J. K. Jonasson, J. Hagman, N. Loren, D. Bernin, M. Nyden, and M. Rudemo, "Pixel-based analysis of FRAP data with a general initial bleaching profile," *Journal of Microscopy* **239**, 142-153 (2010).
24. P. Jonsson, M. P. Jonsson, J. O. Tegenfeldt, and F. Hook, "A Method Improving the Accuracy of Fluorescence Recovery after Photobleaching Analysis," *Biophysical Journal* **95**, 5334-5348 (2008).
25. H. G. Kapitza, G. McGregor, and K. A. Jacobson, "Direct Measurement of Lateral Transport in Membranes by Using Time-Resolved Spatial Photometry," *Proceedings of the National Academy of Sciences of the United States of America* **82**, 4122-4126 (1985).
26. J. Crank, *The Mathematics of Diffusion*, (Oxford University Press, Oxford, 1975).
27. D. M. Soumpasis, "Theoretical-Analysis of Fluorescence Photobleaching Recovery Experiments," *Biophysical Journal* **41**, 95-97 (1983).
28. J. K. Jonasson, N. Loren, P. Olofsson, M. Nyden, and M. Rudemo, "A pixel-based likelihood framework for analysis of fluorescence recovery after photobleaching data," *Journal of Microscopy* **232**, 260-269 (2008).
29. K. Braeckmans, L. Peeters, N. N. Sanders, S. C. De Smedt, and J. Demeester, "Three-dimensional fluorescence recovery after photobleaching with the confocal scanning laser microscope," *Biophysical Journal* **85**, 2240-2252 (2003).
30. U. Kubitscheck, P. Wedekind, and R. Peters, "Lateral Diffusion Measurement at High-Spatial-Resolution by Scanning Microphotolysis in A Confocal Microscope," *Biophysical Journal* **67**, 948-956 (1994).
31. S. Seiffert and W. Oppermann, "Systematic evaluation of FRAP experiments performed in a confocal laser scanning microscope," *Journal of Microscopy-Oxford* **220**, 20-30 (2005).
32. K. Braeckmans, B. G. Stubbe, K. Remaut, J. Demeester, and S. C. De Smedt, "Anomalous photobleaching in fluorescence recovery after photobleaching measurements due to excitation saturation- a case study for fluorescein," *Journal of Biomedical Optics* **11**, (2006).

33. P. Wedekind, U. Kubitscheck, O. Heinrich, and R. Peters, "Line-scanning microphotolysis for diffraction-limited measurements of lateral diffusion," *Biophysical Journal* **71**, 1621-1632 (1996).
34. A. Tannert, S. Tannert, S. Burgold, and M. Schaefer, "Convolution-based one and two component FRAP analysis: theory and application," *European Biophysics Journal with Biophysics Letters* **38**, 649-661 (2009).
35. B. L. Sprague, R. L. Pego, D. A. Stavreva, and J. G. McNally, "Analysis of binding reactions by fluorescence recovery after photobleaching," *Biophysical Journal* **86**, 3473-3495 (2004).
36. F. Mueller, D. Mazza, T. J. Stasevich, and J. G. McNally, "FRAP and kinetic modeling in the analysis of nuclear protein dynamics: what do we really know?," *Current Opinion in Cell Biology* **22**, 403-411 (2010).
37. J. Lippincott-Schwartz, N. tan-Bonnet, and G. H. Patterson, "Photobleaching and photoactivation: following protein dynamics in living cells," *Nature Cell Biology* **S7-S14** (2003).
38. P. Van Oostveldt and S. Bauwens, "Quantitative Fluorescence in Confocal Microscopy - the Effect of the Detection Pinhole Aperture on the Reabsorption and Inner Filter Phenomena," *Journal of Microscopy-Oxford* **158**, 121-132 (1990).
39. F. Cella and A. Diaspro, "Two-Photon Excitation Microscopy: A Superb Wizard for Fluorescence Imaging," in *Nanoscopy and Multidimensional Optical Fluorescence Microscopy*, A. Diaspro, ed., (Chapman & Hall, Boca Raton, 2010).
40. J. Braga, J. M. P. Desterro, and M. Carmo-Fonseca, "Intracellular macromolecular mobility measured by fluorescence recovery after photobleaching with confocal laser scanning microscopes," *Molecular Biology of the Cell* **15**, 4749-4760 (2004).
41. J. Wu, N. Shekhar, P. P. Lele, and T. P. Lele, "FRAP Analysis: Accounting for Bleaching during Image Capture," *Plos One* **7**, (2012).
42. W. E. Hennink and C. F. van Nostrum, "Novel crosslinking methods to design hydrogels," *Advanced Drug Delivery Reviews* **54**, 13-36 (2002).
43. T. Vermonden, R. Censi, and W. E. Hennink, "Hydrogels for Protein Delivery," *Chemical Reviews* **112**, 2853-2888 (2012).
44. M. C. Branco, D. J. Pochan, N. J. Wagner, and J. P. Schneider, "Macromolecular diffusion and release from self-assembled beta-hairpin peptide hydrogels," *Biomaterials* **30**, 1339-1347 (2009).
45. S. R. Van Tomme, B. G. De Geest, K. Braeckmans, S. C. De Smedt, F. Siepmann, J. Siepmann, C. F. van Nostrum, and W. E. Hennink, "Mobility of model proteins in hydrogels composed of oppositely charged dextran microspheres studied by protein release and fluorescence recovery after photobleaching," *Journal of Controlled Release* **110**, 67-78 (2005).
46. F. Brandl, F. Kastner, R. M. Gschwind, T. Blunk, J. Tessmar, and A. Gopferich, "Hydrogel-based drug delivery systems: Comparison of drug diffusivity and release kinetics," *Journal of Controlled Release* **142**, 221-228 (2010).
47. M. Henke, F. Brandl, A. M. Goepferich, and J. K. Tessmar, "Size-dependent release of fluorescent macromolecules and nanoparticles from radically cross-linked hydrogels," *European Journal of Pharmaceutics and Biopharmaceutics* **74**, 184-192 (2010).
48. L. Payet, A. Ponton, L. Leger, H. Hervet, J. L. Grossiord, and F. Agnely, "Self-Diffusion in Chitosan Networks: From a Gel-Gel Method to Fluorescence Recovery after Photobleaching by Fringe Pattern," *Macromolecules* **41**, 9376-9381 (2008).
49. K. B. Kosto and W. M. Deen, "Diffusivities of macromolecules in composite hydrogels," *Aiche Journal* **50**, 2648-2658 (2004).

Chapter 1

50. A. J. Kuijpers, G. H. M. Engbers, T. K. L. Meyvis, S. S. C. de Smedt, J. Demeester, J. Krijgsveld, S. A. J. Zaat, J. Dankert, and J. Feijen, "Combined gelatin-chondroitin sulfate hydrogels for controlled release of cationic antibacterial proteins," *Macromolecules* **33**, 3705-3713 (2000).
51. R. Censi, T. Vermonden, M. J. van Steenberghe, H. Deschout, K. Braeckmans, S. C. De Smedt, C. F. van Nostrum, P. di Martino, and W. E. Hennink, "Photopolymerized thermosensitive hydrogels for tailorable diffusion-controlled protein delivery," *Journal of Controlled Release* **140**, 230-236 (2009).
52. T. Vermonden, S. S. Jena, D. Barriet, R. Censi, J. van der Gucht, W. E. Hennink, and R. A. Siegel, "Macromolecular Diffusion in Self-Assembling Biodegradable Thermosensitive Hydrogels," *Macromolecules* **43**, 782-789 (2010).
53. J. Kang and K. J. Beers, "Macromolecular transport through nanostructured and porous hydrogels synthesized using the amphiphilic copolymer, PCL-b-PEO-b-PCL," *European Polymer Journal* **45**, 3004-3009 (2009).
54. M. D. Burke, J. O. Park, M. Srinivasarao, and S. A. Khan, "A novel enzymatic technique for limiting drug mobility in a hydrogel matrix," *Journal of Controlled Release* **104**, 141-153 (2005).
55. F. Alvarez-Mancenido, K. Braeckmans, S. C. De Smedt, J. Demeester, M. Landin, and R. Martinez-Pacheco, "Characterization of diffusion of macromolecules in konjac glucomannan solutions and gels by fluorescence recovery after photobleaching technique," *International Journal of Pharmaceutics* **316**, 37-46 (2006).
56. R. Xiong, S. Soenen, K. Braeckmans, and A. G. Skirtach, "Towards Theranostic Multicompartment Microcapsules: in-situ Diagnostics and Laser-induced Treatment," *Theranostics* **3**, 141-151 (2013).
57. K. Kohler and G. B. Sukhorukov, "Heat treatment of polyelectrolyte multilayer capsules: A versatile method for encapsulation," *Advanced Functional Materials* **17**, 2053-2061 (2007).
58. M. S. Toprak, B. J. McKenna, J. H. Waite, and G. D. Stucky, "Control of size and permeability of nanocomposite microspheres," *Chemistry of Materials* **19**, 4263-4269 (2007).
59. X. Tao, X. J. Sun, J. M. Su, J. F. Chen, and W. Roa, "Natural microshells of alginate-chitosan: Unexpected stability and permeability," *Polymer* **47**, 6167-6171 (2006).
60. Y. Cheng, R. K. Prud'homme, and J. L. Thomas, "Diffusion of mesoscopic probes in aqueous polymer solutions measured by fluorescence recovery after photobleaching," *Macromolecules* **35**, 8111-8121 (2002).
61. S. Basu and P. J. Campagnola, "Properties of crosslinked protein matrices for tissue engineering applications synthesized by multiphoton excitation," *Journal of Biomedical Materials Research Part A* **71A**, 359-368 (2004).
62. K. Remaut, N. N. Sanders, B. G. De Geest, K. Braeckmans, J. Demeester, and S. C. De Smedt, "Nucleic acid delivery: Where material sciences and bio-sciences meet," *Materials Science & Engineering R-Reports* **58**, 117-161 (2007).
63. A. Pluen, Y. Boucher, S. Ramanujan, T. D. Mckee, T. Gohongi, E. di Tomaso, E. B. Brown, Y. Izumi, R. B. Campbell, D. A. Berk, and R. K. Jain, "Role of tumor-host interactions in interstitial diffusion of macromolecules: Cranial vs. subcutaneous tumors," *Proceedings of the National Academy of Sciences of the United States of America* **98**, 4628-4633 (2001).
64. P. A. Netti, D. A. Berk, M. A. Swartz, A. J. Grodzinsky, and R. K. Jain, "Role of extracellular matrix assembly in interstitial transport in solid tumors," *Cancer Research* **60**, 2497-2503 (2000).

65. S. Ramanujan, A. Pluen, T. D. Mckee, E. B. Brown, Y. Boucher, and R. K. Jain, "Diffusion and convection in collagen gels: Implications for transport in the tumor interstitium," *Biophysical Journal* **83**, 1650-1660 (2002).
66. T. Stylianopoulos, B. op-Frimpong, L. L. Munn, and R. K. Jain, "Diffusion Anisotropy in Collagen Gels and Tumors: The Effect of Fiber Network Orientation," *Biophysical Journal* **99**, 3119-3128 (2010).
67. A. Erikson, H. N. Andersen, S. N. Naess, P. Sikorski, and C. D. Davies, "Physical and chemical modifications of collagen gels: Impact on diffusion," *Biopolymers* **89**, 135-143 (2008).
68. L. Eikenes, I. Tufto, E. A. Schnell, A. Bjorkoy, and C. D. Davies, "Effect of Collagenase and Hyaluronidase on Free and Anomalous Diffusion in Multicellular Spheroids and Xenografts," *Anticancer Research* **30**, 359-368 (2010).
69. V. P. Chauhan, R. M. Lanning, B. op-Frimpong, W. Mok, E. B. Brown, T. P. Padera, Y. Boucher, and R. K. Jain, "Multiscale Measurements Distinguish Cellular and Interstitial Hindrances to Diffusion In Vivo," *Biophysical Journal* **97**, 330-336 (2009).
70. M. Magzoub, S. Jin, and A. S. Verkman, "Enhanced macromolecule diffusion deep in tumors after enzymatic digestion of extracellular matrix collagen and its associated proteoglycan decorin," *Faseb Journal* **22**, 276-284 (2008).
71. K. D. Sullivan, W. H. Sipprell, E. B. Brown, and E. B. Brown, "Improved Model of Fluorescence Recovery Expands the Application of Multiphoton Fluorescence Recovery after Photobleaching in Vivo," *Biophysical Journal* **96**, 5082-5094 (2009).
72. D. K. Binder, M. C. Papadopoulos, P. M. Haggie, and A. S. Verkman, "In vivo measurement of brain extracellular space diffusion by cortical surface photobleaching," *Journal of Neuroscience* **24**, 8049-8056 (2004).
73. E. Sykova and C. Nicholson, "Diffusion in brain extracellular space," *Physiological Reviews* **88**, 1277-1340 (2008).
74. M. C. Papadopoulos, D. K. Binder, and A. S. Verkman, "Enhanced macromolecular diffusion in brain extracellular space in mouse models of vasogenic edema measured by cortical surface photobleaching," *Faseb Journal* **18**, 425-+ (2004).
75. M. C. Papadopoulos, J. K. Kim, and A. S. Verkman, "Extracellular space diffusion in central nervous system: Anisotropic diffusion measured by elliptical surface photobleaching," *Biophysical Journal* **89**, 3660-3668 (2005).
76. Z. Zador, M. Magzoub, S. Jin, G. T. Manley, M. C. Papadopoulos, and A. S. Verkman, "Microfiberoptic fluorescence photobleaching reveals size-dependent macromolecule diffusion in extracellular space deep in brain," *Faseb Journal* **22**, 870-879 (2008).
77. N. N. Sanders, S. C. De Smedt, and J. Demeester, "The physical properties of biogels and their permeability for macromolecular drugs and colloidal drug carriers," *Journal of Pharmaceutical Sciences* **89**, 835-849 (2000).
78. P. Occhipinti and P. C. Griffiths, "Quantifying diffusion in mucosal systems by pulsed-gradient spin-echo NMR," *Advanced Drug Delivery Reviews* **60**, 1570-1582 (2008).
79. S. S. Olmsted, J. L. Padgett, A. I. Yudin, K. J. Whaley, T. R. Moench, and R. A. Cone, "Diffusion of macromolecules and virus-like particles in human cervical mucus," *Biophysical Journal* **81**, 1930-1937 (2001).
80. H. Shen, Y. Y. Hu, and W. M. Saltzman, "DNA diffusion in mucus: Effect of size, topology of DNAs, and transfection reagents," *Biophysical Journal* **91**, 639-644 (2006).
81. E. H. Burger and J. Klein-Nulend, "Mechanotransduction in bone - role of the lacuno-canalicular network," *Faseb Journal* **13**, S101-S112 (1999).

Chapter 1

82. X. Z. Zhou, J. E. Novotny, and L. Y. Wang, "Modeling Fluorescence Recovery After Photobleaching in Loaded Bone: Potential Applications in Measuring Fluid and Solute Transport in the Osteocytic Lacunar-Canalicular System," *Annals of Biomedical Engineering* **36**, 1961-1977 (2008).
83. C. Price, X. Z. Zhou, W. Li, and L. Y. Wang, "Real-Time Measurement of Solute Transport Within the Lacunar-Canalicular System of Mechanically Loaded Bone: Direct Evidence for Load-Induced Fluid Flow," *Journal of Bone and Mineral Research* **26**, 277-285 (2011).
84. L. Peeters, N. N. Sanders, K. Braeckmans, K. Boussey, J. V. de Voorde, S. C. De Smedt, and J. Demeester, "Vitreous: A barrier to nonviral ocular gene therapy," *Investigative Ophthalmology & Visual Science* **46**, 3553-3561 (2005).
85. M. E. Johnson, D. A. Berk, D. Blankshtein, D. E. Golan, R. K. Jain, and R. S. Langer, "Lateral diffusion of small compounds in human stratum corneum and model lipid bilayer systems," *Biophysical Journal* **71**, 2656-2668 (1996).
86. O. Seksek, J. Biwersi, and A. S. Verkman, "Translational diffusion of macromolecule-sized solutes in cytoplasm and nucleus," *Journal of Cell Biology* **138**, 131-142 (1997).
87. M. ArrioDupont, S. Cribier, G. Foucault, P. F. Devaux, and A. d'Albis, "Diffusion of fluorescently labeled macromolecules in cultured muscle cells," *Biophysical Journal* **70**, 2327-2332 (1996).
88. M. ArrioDupont, G. Foucault, M. Vacher, P. F. Devaux, and S. Cribier, "Translational diffusion of globular proteins in the cytoplasm of cultured muscle cells," *Biophysical Journal* **78**, 901-907 (2000).
89. E. Moeendarbary, L. Valon, M. Fritzsche, A. R. Harris, D. A. Moulding, A. J. Thrasher, E. Stride, L. Mahadevan, and G. T. Charras, "The cytoplasm of living cells behaves as a poroelastic material," *Nature Materials* **12**, 253-261 (2013).
90. G. L. Lukacs, P. Haggie, O. Seksek, D. Lechardeur, N. Freedman, and A. S. Verkman, "Size-dependent DNA mobility in cytoplasm and nucleus," *Journal of Biological Chemistry* **275**, 1625-1629 (2000).
91. J. C. Politz, E. S. Browne, D. E. Wolf, and T. Pederson, "Intranuclear diffusion and hybridization state of oligonucleotides measured by fluorescence correlation spectroscopy in living cells," *Proceedings of the National Academy of Sciences of the United States of America* **95**, 6043-6048 (1998).
92. A. T. Jones and E. J. Sayers, "Cell entry of cell penetrating peptides: tales of tails wagging dogs," *Journal of Controlled Release* **161**, 582-591 (2012).
93. F. Cardarelli, M. Serresi, R. Bizzarri, M. Giacca, and F. Beltram, "In vivo study of HIV-1 Tat arginine-rich motif unveils its transport properties," *Molecular Therapy* **15**, 1313-1322 (2007).
94. M. J. Roberti, T. M. Jovin, and E. Jares-Erijman, "Confocal Fluorescence Anisotropy and FRAP Imaging of alpha-Synuclein Amyloid Aggregates in Living Cells," *Plos One* **6**, (2011).
95. N. J. Edwin, R. P. Hammer, R. L. McCarley, and P. S. Russo, "Reversibility of beta-Amyloid Self-Assembly: Effects of pH and Added Salts Assessed by Fluorescence Photobleaching Recovery," *Biomacromolecules* **11**, 341-347 (2010).
96. I. Sponne, A. Fife, A. Drouet, C. Klein, V. Koziel, M. Pingon-Raymond, J. L. Olivier, J. Chambaz, and T. Pilot, "Apoptotic neuronal cell death induced by the non-fibrillar amyloid-beta peptide proceeds through an early reactive oxygen species-dependent cytoskeleton perturbation," *Journal of Biological Chemistry* **278**, 3437-3445 (2003).

97. K. Guan, S. Wagner, B. Unsold, L. S. Maier, D. Kaiser, B. Hemmerlein, K. Nayernia, W. Engel, and G. Hasenfuss, "Generation of functional cardiomyocytes from adult mouse spermatogonial stem cells," *Circulation Research* **100**, 1615-1625 (2007).
98. B. J. Muller-Borer, W. E. Cascio, P. A. W. Anderson, J. N. Snowwaert, J. R. Frye, N. Desai, G. L. Esch, J. A. Brackham, C. R. Bagnell, W. B. Coleman, J. W. Grisham, and N. N. Malouf, "Adult-derived liver stem cells acquire a cardiomyocyte structural and functional phenotype ex vivo," *American Journal of Pathology* **165**, 135-145 (2004).
99. M. G. Todorova, B. Soria, and I. Quesada, "Gap junctional intercellular communication is required to maintain embryonic stem cells in a non-differentiated and proliferative state," *Journal of Cellular Physiology* **214**, 354-362 (2008).
100. Y. Y. Lu, T. S. Chen, X. P. Wang, and L. Li, "Single-cell analysis of dihydroartemisinin-induced apoptosis through reactive oxygen species-mediated caspase-8 activation and mitochondrial pathway in ASTC-a-1 cells using fluorescence imaging techniques," *Journal of Biomedical Optics* **15**, (2010).
101. X. H. Long, M. Y. Fan, R. M. Bigsby, and K. P. Nephew, "Apigenin inhibits antiestrogen-resistant breast cancer cell growth through estrogen receptor-alpha-dependent and estrogen receptor-alpha-independent mechanisms," *Molecular Cancer Therapeutics* **7**, 2096-2108 (2008).
102. M. S. Phadke, N. F. Krynetskaia, A. K. Mishra, and E. Krynetskiy, "Glyceraldehyde 3-Phosphate Dehydrogenase Depletion Induces Cell Cycle Arrest and Resistance to Antimetabolites in Human Carcinoma Cell Lines," *Journal of Pharmacology and Experimental Therapeutics* **331**, 77-86 (2009).
103. L. Sancey, E. Garanger, S. Foillard, G. Schoehn, A. Hurbin, C. biges-Rizo, D. Boturyn, C. Souchier, A. Grichine, P. Dumy, and J. L. Coll, "Clustering and Internalization of Integrin alpha(v)beta(3) With a Tetrameric RGD-synthetic Peptide," *Molecular Therapy* **17**, 837-843 (2009).
104. D. A. Berk, F. Yuan, M. Leunig, and R. K. Jain, "Direct in vivo measurement of targeted binding in a human tumor xenograft," *Proceedings of the National Academy of Sciences of the United States of America* **94**, 1785-1790 (1997).
105. E. N. Kaufman and R. K. Jain, "Effect of Bivalent Interaction Upon Apparent Antibody-Affinity - Experimental Confirmation of Theory Using Fluorescence Photobleaching and Implications for Antibody-Binding Assays," *Cancer Research* **52**, 4157-4167 (1992).
106. T. Ogawa, T. Hayashi, M. Tokunou, K. Nakachi, J. E. Trosko, C. C. Chang, and N. Yorioka, "Suberoylanilide hydroxamic acid enhances gap junctional intercellular communication via acetylation of histone containing Connexin 43 gene locus," *Cancer Research* **65**, 9771-9778 (2005).
107. H. Sauer, V. Putz, K. Fischer, J. Hescheler, and M. Wartenberg, "Increased doxorubicin uptake and toxicity in multicellular tumour spheroids treated with DC electrical fields," *British Journal of Cancer* **80**, 1204-1213 (1999).
108. M. J. C. Machado and C. A. Mitchell, "Temporal changes in microvessel leakiness during wound healing discriminated by in vivo fluorescence recovery after photobleaching," *Journal of Physiology-London* **589**, 4681-4696 (2011).
109. T. Da and A. S. Verkman, "Aquaporin-4 gene disruption in mice protects against impaired retinal function and cell death after ischemia," *Investigative Ophthalmology & Visual Science* **45**, 4477-4483 (2004).
110. J. A. van Aalst, W. Burmeister, P. L. Fox, and L. M. Graham, "alpha-Tocopherol preserves endothelial cell migration in the presence of cell-oxidized low-density lipoprotein by

Chapter 1

- inhibiting changes in cell membrane fluidity," *Journal of Vascular Surgery* **39**, 229-237 (2004).
111. G. Jones, F. Hunter, H. A. Hancock, A. Kapoor, M. J. Stone, B. J. Wood, J. W. Xie, M. R. Dreher, and V. Frenkel, "In Vitro Investigations Into Enhancement of tPA Bioavailability in Whole Blood Clots Using Pulsed-High Intensity Focused Ultrasound Exposures," *Ieee Transactions on Biomedical Engineering* **57**, 33-36 (2010).
 112. D. Salinas, P. M. Haggie, J. R. Thiagarajah, Y. L. Song, K. Rosbe, W. E. Finkbeiner, D. W. Nielson, and A. S. Verkman, "Submucosal gland dysfunction as a primary defect in cystic fibrosis," *Faseb Journal* **18**, 431-+ (2004).
 113. C. M. Finnegan, S. S. Rawat, E. H. Cho, D. L. Guiffre, S. Lockett, A. H. Merrill, and R. Blumenthal, "Sphingomyelinase restricts the lateral diffusion of CD4 and inhibits human immunodeficiency virus fusion," *Journal of Virology* **81**, 5294-5304 (2007).
 114. R. Lin, R. Murtazina, B. Y. Cha, M. Chakraborty, R. Sarker, T. E. Chen, Z. H. Lin, B. M. Hogema, H. R. de Jonge, U. Seidler, J. R. Turner, X. H. Li, O. Kovbasnjuk, and M. Donowitz, "D-Glucose Acts via Sodium/Glucose Cotransporter 1 to Increase NHE3 in Mouse Jejunal Brush Border by a Na plus/H plus Exchange Regulatory Factor 2-Dependent Process," *Gastroenterology* **140**, 560-571 (2011).
 115. R. Saxena and A. Chattopadhyay, "Membrane organization and dynamics of the serotonin(1A) receptor in live cells," *Journal of Neurochemistry* **116**, 726-733 (2011).
 116. E. Meimaridou, S. B. Gooljar, N. Ramnarace, L. Anthonypillai, A. J. L. Clark, and J. P. Chapple, "The Cytosolic Chaperone Hsc70 Promotes Traffic to the Cell Surface of Intracellular Retained Melanocortin-4 Receptor Mutants," *Molecular Endocrinology* **25**, 1650-1660 (2011).
 117. A. Gefen, L. H. Cornelissen, D. Gawlitta, D. L. Bader, and C. W. J. Oomens, "The free diffusion of macromolecules in tissue-engineered skeletal muscle subjected to large compression strains," *Journal of Biomechanics* **41**, 845-853 (2008).
 118. J. W. Dobrucki, D. Feret, and A. Noatynska, "Scattering of exciting light by live cells in fluorescence Confocal imaging: Phototoxic effects and relevance for FRAP studies," *Biophysical Journal* **93**, 1778-1786 (2007).
 119. S. T. Hess, S. H. Huang, A. A. Heikal, and W. W. Webb, "Biological and chemical applications of fluorescence correlation spectroscopy: A review," *Biochemistry* **41**, 697-705 (2002).
 120. M. J. Saxton and K. Jacobson, "Single-particle tracking: Applications to membrane dynamics," *Annual Review of Biophysics and Biomolecular Structure* **26**, 373-399 (1997).

Chapter 2

Straightforward FRAP for quantitative diffusion measurements with a laser scanning microscope

This chapter is published as:

Hendrik Deschout^{1,2}, Joel Hagman³, Sophia Fransson³, Jenny Jonasson⁴, Mats Rudemo⁴, Niklas Lorén³, and Kevin Braeckmans^{1,2}. *Optics Express*, Volume 18, Issue 22, Pages 22886-22905, 2010.

¹Laboratory for General Biochemistry and Physical Pharmacy, Ghent University, Belgium

²Centre for Nano- and Biophotonics, Ghent University, Belgium

³Structure and Material Design, The Swedish Institute for Food and Biotechnology, Sweden

⁴Mathematical Sciences, Chalmers University of Technology and Gothenburg University, Sweden

ABSTRACT

Confocal or multi-photon laser scanning microscopes are convenient tools to perform FRAP diffusion measurements, rendering it a popular technique in pharmaceutical research, as discussed in **Chapter 1**. Nonetheless, accurate FRAP remains often challenging since current methods are either limited to relatively large bleach regions or can be complicated for non-specialists. In order to bring reliable quantitative FRAP measurements to the broad community of laser scanning microscopy users, here we have revised FRAP theory and present a new pixel based FRAP method relying on the photo bleaching of rectangular regions of any size and aspect ratio. The method allows for fast and straightforward quantitative diffusion measurements due to a closed-form expression for the recovery process utilizing all available spatial and temporal data. After a detailed validation, its versatility is demonstrated by diffusion studies in heterogeneous biopolymer mixtures.

2.1 INTRODUCTION

Molecular transport is essential for the functionality of cells and for the properties of many industrial products such as pharmaceuticals, pharmaceutical devices, foods, cosmetics etc. Different methods based on fluorescence microscopy exist to characterize the local mobility of molecules in terms of a diffusion coefficient. One of them is fluorescence recovery after photobleaching (FRAP), which is most useful for studying diffusion in the range of 0.1 to 100 $\mu\text{m}^2/\text{s}$ on a micrometer scale. FRAP diffusion measurements are based on creating a concentration gradient through local photobleaching of the fluorescently labelled molecules, which is the photochemical process through which a fluorescent molecule loses its fluorescence properties after being excited by an incoming photon. By illuminating a certain area in the microscope sample with high-intensity excitation light, the fluorescent molecules within that area can photobleach, leading to a local reduction in fluorescence intensity. Exchange via diffusion of these photobleached molecules with intact fluorescent molecules outside the illuminated area leads to a gradual recovery of the fluorescence inside that area. The rate of fluorescence recovery is proportional to the rate of diffusion of the fluorescently labelled molecules. Using a suitable FRAP model, analysis of the fluorescence recovery can yield the physical quantities describing the local diffusion in the sample, such as the diffusion coefficient in case of free diffusion. FRAP has become a popular technique to study the diffusion of molecules in a variety of systems like cell membranes [1-3], polymer gel systems [4-9] and living cells [10-12].

The first FRAP methods were developed in the 1970s, using fluorescence microscopes with non-scanning lasers as light sources and photo-multiplier tubes as detectors [13]. The photobleached area was determined by the intensity distribution of the focused laser beam which had either a Gaussian or a uniform circular profile. As the fluorescence recovery was monitored by the same (attenuated) laser beam, only temporal information was available of the fluorescence recovery (i.e. spot photobleaching measurements). To include spatial information as well, video cameras were used during the 1980s, allowing visualisation of the fluorescence recovery inside and outside the photobleached region. During this period, also the confocal laser scanning microscope (CLSM) became available, opening up new possibilities for more flexible FRAP experiments.

By means of the scanning laser beam of a CLSM it is possible to define a photobleaching area of any size and shape, resulting in a large range of detectable diffusion coefficients. Since confocal microscopy is an imaging technique, both spatial and

temporal information are in principle available from the recovery images. However, due to the mathematical complexity of the problem, quantitative interpretation of FRAP data to date remains mostly limited to temporal analysis of the average fluorescence in the photobleached area. When spatial information is not taken into account, a prerequisite for accurate results is the exact knowledge of the initial concentration of bleached molecules after photobleaching. However, because of non-linear saturation effects during the highly intense photobleaching phase that depend on the photon flux, the type of fluorophore and the local chemical environment, it is very difficult to estimate or calibrate the initial bleaching profile exactly [14-16]. While these non-linear effects can be neglected when using large photobleaching areas [17], they have a substantial effect when using small areas close to the resolution of the microscope [15,16].

The necessity of *a priori* knowledge of the exact initial bleaching profile can be circumvented by taking into account the spatial information of the recovery images. Inventive FRAP models have been proposed along this line that make use of mathematical transformations, such as the Fourier transform or Hankel transform [18-20]. However, the methods published so far do not take the microscope's imaging point-spread function into account so that deviations could arise for very small regions. Moreover, these methods have not been extended to 3-D diffusion for e.g. 2-photon FRAP measurements [16]. A pixelbased maximum likelihood framework was reported, assuming that the initial bleaching profile can be approximated by a Gaussian distribution [21]. To alleviate the latter restriction, recently a numerical method has been introduced [22], where the maximum likelihood framework is extended to a general initial profile only assuming that the profile is a non-decreasing function of the distance to the bleaching centre. While this method is accurate for all types of initial profiles studied, similar to other numerical approaches [23-25], it generally requires special programming expertise, while data analysis can take hours on modern computers. Therefore, there remains the need for quantitative but straightforward and fast FRAP methods that take the full spatial and temporal information into account without posing any restrictions on the size of the bleaching area.

In order to bring highly reliable quantitative FRAP measurements to the broad community of laser scanning microscopy users, here we present a new and versatile FRAP model that describes the full temporal and spatial diffusion process after photobleaching by a scanning laser beam of an arbitrary rectangular area (rFRAP). A rectangular area was chosen instead of the more typical circular region because this enabled us to find a closed-form expression for the recovery process, thus allowing for fast and straightforward analysis of the recovery images. Moreover, by taking the microscope's effective photobleaching and imaging resolution into account, the

Chapter 2

rectangle can have any size and aspect ratio, thus providing for maximum flexibility. The new pixelbased FRAP model effectively utilises all information in the image set to estimate the diffusion rate. First we give an outline of the mathematical derivation leading to the general 3-D multi-photon FRAP expression, followed by a discussion on the practical 2-D limit for single photon CLSM experiments. We present a detailed experimental validation of the method where we demonstrate that the method is valid for any size and aspect ratio of the rectangle. Furthermore we compare two ways of analyzing the recovery images, either by a straightforward least squares analysis or by a robust maximum likelihood framework. Finally, in collaboration with Dr. Niklas Lorén from the Swedish Institute for Food and Technology, we demonstrate the usefulness and versatility of the method on a mixed biopolymer system of gelatin and maltodextrin which is of relevance to the food and pharmaceutical industry.

2.2 THEORY

2.2.1 Derivation of the general rFRAP expression

Consider a sample with a uniform concentration C_0 of fluorescent molecules. Let $I_b^n(x, y, z, t)$ be the n -photon illumination intensity distribution of the laser scanning microscope (LSM) with a temporal average intensity of the (pulsed) laser beam $\langle I_b^n(x, y, z, t) \rangle$. Assuming first order photobleaching kinetics and a short photobleaching time to avoid significant diffusion during bleaching, the fluorophore concentration C_b after n -photon photobleaching of a 2-D geometry $B(x, y)$ with a scanning beam can be calculated from [16]:

$$C_b(x, y, z) = C_0 e^{-\frac{\sigma_n q_n}{n v \Delta y} K(x, y, z)}, \quad (2.1)$$

where σ_n is the n -photon absorption cross-section and q_n the quantum efficiency for n -photon photobleaching. v is the scanning speed of the laser beam and Δy the distance between adjacent scanning lines. The effective bleaching intensity distribution $K(x, y, z)$ is calculated from the convolution product of the geometry $B(x, y)$ and the time-average bleaching intensity distribution:

$$K(x, y, z) = \int_{-\infty}^{+\infty} \int_{-\infty}^{+\infty} B(x', y') \langle I_b^n(x - x', y - y', z, t) \rangle dx' dy'. \quad (2.2)$$

Here we assume a rectangular photobleaching area as illustrated in **Fig. 2.1**:

$$B(x, y) = \begin{cases} 1, & -\frac{l_x}{2} \leq x \leq \frac{l_x}{2} \text{ and } -\frac{l_y}{2} \leq y \leq \frac{l_y}{2} \\ 0, & \text{elsewhere} \end{cases} \quad (2.3)$$

and a Gaussian photobleaching intensity distribution [16,26]:

$$\langle I_b^n(x, y, z, t) \rangle = \langle I_b^n(0, 0, 0, t) \rangle e^{-2n \left(\frac{x^2 + y^2}{r_{b,0}^2} + \frac{z^2}{z_{b,0}^2} \right)}, \quad (2.4)$$

where $r_{b,0}$ is the lateral and $z_{b,0}$ is the axial effective resolution for single photon photobleaching. $\langle I_b^n(0, 0, 0, t) \rangle$ is the temporal average intensity of the (pulsed) laser beam at the origin for n -photon photobleaching.

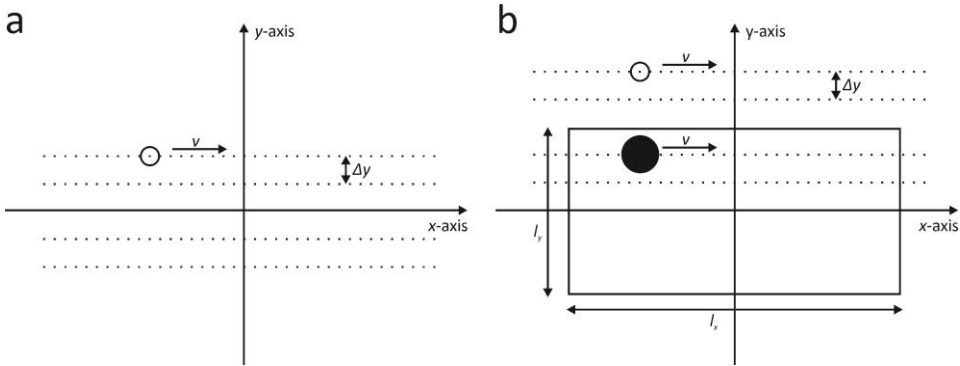


Figure 2.1 | The use of a confocal laser scanning microscope in a FRAP measurement. The scanning speed is v and the distance between the consecutive scanning lines is Δy . (a) Images are acquired by scanning the imaging point spread function (open circle) across the focal plane. (b) By increasing the laser intensity within the indicated rectangle, a rectangular area can be photobleached.

Inserting Eqs. (2.3) and (2.4) into Eq. (2.2) results in:

$$K(x, y, z) = \langle I_b^n(0, 0, 0, t) \rangle e^{-\frac{2n}{z_{b,0}^2} z^2} \int_{-\frac{l_x}{2}}^{\frac{l_x}{2}} e^{-\frac{2n}{r_{b,0}^2} (x-x')^2} dx' \int_{-\frac{l_y}{2}}^{\frac{l_y}{2}} e^{-\frac{2n}{r_{b,0}^2} (y-y')^2} dy'. \quad (2.5)$$

Since it is our aim to finally come to a closed-form expression, we further assume a limited amount of photobleaching such that the exponential photobleaching process

Chapter 2

from Eq. (2.1) can be approximated by a linear process (first order of the Taylor expansion):

$$C_b(x, y, z) = C_0 - C_0 \frac{\sigma_n q_n}{n v \Delta y} K(x, y, z). \quad (2.6)$$

We will show experimentally that this assumption in practice does not impose a big limitation. Furthermore, we will demonstrate that in practice diffusion during photobleaching in fact can be accounted for by the rectangle FRAP method, despite the fact that this is formally neglected at this point in the derivation. To model the fluorescence recovery after photobleaching of the rectangle, Fick's second law has to be solved for the initial condition in Eq. (2.6). Inserting Eq. (2.6) into the integral form of Fick's second law gives the concentration C of the fluorophores as a function of time and space after photobleaching [27]:

$$C(x, y, z, t) = \frac{1}{(4\pi Dt)^{\frac{3}{2}}} \times \int_{-\infty}^{+\infty} \int_{-\infty}^{+\infty} \int_{-\infty}^{+\infty} C_b(x - x', y - y', z - z') e^{-\frac{1}{4Dt}(x'^2 + y'^2 + z'^2)} dx' dy' dz'. \quad (2.7)$$

Eq. (2.7). can be rewritten using Eq. (2.5), finally leading to:

$$\begin{aligned} \frac{C(x, y, z, t)}{C_0} = 1 - \frac{\sigma_n q_n}{n v \Delta y} \langle I_b^n(0, 0, 0, t) \rangle_{z_{b,0} r_{b,0}^2} \sqrt{\frac{1}{z_{b,0}^2 + 8nDt}} \frac{1}{r_{b,0}^2 + 8nDt} \\ \times e^{-\frac{2n}{z_{b,0}^2 + 8nDt} z^2} \int_{-\frac{l_x}{2}}^{\frac{l_x}{2}} e^{-\frac{2n}{r_{b,0}^2 + 8nDt} (x-x')^2} dx' \int_{-\frac{l_y}{2}}^{\frac{l_y}{2}} e^{-\frac{2n}{r_{b,0}^2 + 8nDt} (y-y')^2} dy', \end{aligned} \quad (2.8)$$

where D is the isotropic diffusion coefficient of the diffusing species. If the fluorescence recovery is imaged by m -photon microscopy, the observed fluorescence can be calculated from the convolution product of the real concentration according to Eq. (2.8) and the overall microscope's imaging point spread function $\langle I_d^m(x, y, z, t) \rangle$:

$$F(x, y, z, t) = q \int_{-\infty}^{+\infty} \int_{-\infty}^{+\infty} \int_{-\infty}^{+\infty} \langle I_d^m(x, y, z, t) \rangle C(x - x', y - y', z - z', t) dx' dy' dz'. \quad (2.9)$$

The imaging point spread function $\langle I_d^m(x, y, z, t) \rangle$ can be modelled as a 3-D Gaussian function:

$$\langle I_d^m(x, y, z, t) \rangle = \langle I_d^m(0, 0, 0, t) \rangle e^{-2m \left(\frac{x^2 + y^2}{r_{d,0}^2} + \frac{z^2}{z_{d,0}^2} \right)} \quad (2.10)$$

where $r_{d,0}$ is the lateral and $z_{d,0}$ is the axial resolution for single photon imaging. Note that we allow the resolution (radial and axial) of the imaging point spread function to be different from the bleaching intensity distribution in Eq. (2.4) since it was previously shown that saturation effects can increase the effective resolution of the bleaching intensity distribution [14-16]. First, define the following parameters as:

$$r_{m,n}^2 = \frac{r_{d,0}^2}{m} + \frac{r_{b,0}^2}{n}, z_{m,n}^2 = \frac{z_{d,0}^2}{m} + \frac{z_{b,0}^2}{n}, K_0 = \frac{\pi \sigma_n q_n}{2 n v \Delta y} \langle I_b^n(0, 0, 0, t) \rangle \left(\frac{r_{b,0}}{n} \right)^2. \quad (2.11)$$

Substituting Eq. (2.10) in (2.9) subsequently leads to:

$$\frac{F(x, y, z, t)}{F_0} = 1 - \frac{K_0}{4} \frac{z_{b,0}}{\sqrt{2n}} \frac{1}{\sqrt{z_{m,n}^2 + 4Dt}} e^{-\frac{1}{z_{m,n}^2 + 4Dt} z^2} \times \left[\operatorname{erf} \left(\frac{x + \frac{l_x}{2}}{\sqrt{r_{m,n}^2 + 4Dt}} \right) - \operatorname{erf} \left(\frac{x - \frac{l_x}{2}}{\sqrt{r_{m,n}^2 + 4Dt}} \right) \right] \left[\operatorname{erf} \left(\frac{y + \frac{l_y}{2}}{\sqrt{r_{m,n}^2 + 4Dt}} \right) - \operatorname{erf} \left(\frac{y - \frac{l_y}{2}}{\sqrt{r_{m,n}^2 + 4Dt}} \right) \right], \quad (2.12)$$

which describes the three-dimensional fluorescence recovery at a time t after photobleaching. Excitation is assumed to be an m - and n -photon process for imaging and bleaching, respectively, and the bleached area is a rectangle centred in the origin with width l_x and height l_y (see **Fig. 2.1**). Equation (2.12) contains the error function, which is defined as $\operatorname{erf}(z) = \frac{2}{\sqrt{\pi}} \int_0^z e^{-x^2} dx$.

2.2.2 Single photon rFRAP

It is useful to consider the case $m = n = 1$ (we denote $r_{1,1}^2$ as r^2 in Eq. (2.11)) which corresponds to FRAP experiments performed on a regular (single photon) CLSM. However, in that case the above formula is incorrect as far as the axial diffusion is concerned (z -direction). This is because the single photon illumination profile has a conical shape which is not taken into account by Eq. (2.4) and this will lead to a discrepancy between the theory and the actual experiment. Therefore, when performing FRAP experiments on a regular (single photon) CLSM, diffusion along the

Chapter 2

optical axis should be avoided so that 2-D diffusion can be assumed. This is e.g. the case when the diffusion is restricted to a plane, such as for membrane transport. In a 3-D extended sample, a 2-D situation can be mimicked by using a low numerical aperture lens which produces a cylindrical illumination profile instead of a conical one [15,17,28]. In that case, there will be substantial photobleaching above and below the focal plane, thus avoiding net diffusion along the optical axis. The single photon 2-D rFRAP model can be derived from Eq. (2.12) by letting $z_{b,0}$ approach infinity, and setting $m = n = 1$ and $z = 0$ (observation in focal plane):

$$\frac{F(x, y, t)}{F_0} = 1 - \frac{K_0}{4} \left[\operatorname{erf} \left(\frac{x + \frac{l_x}{2}}{\sqrt{r^2 + 4Dt}} \right) - \operatorname{erf} \left(\frac{x - \frac{l_x}{2}}{\sqrt{r^2 + 4Dt}} \right) \right] \left[\operatorname{erf} \left(\frac{y + \frac{l_y}{2}}{\sqrt{r^2 + 4Dt}} \right) - \operatorname{erf} \left(\frac{y - \frac{l_y}{2}}{\sqrt{r^2 + 4Dt}} \right) \right]. \quad (2.13)$$

Note that the percentage of photobleaching P at the centre of the rectangle, follows immediately from $F(0,0,0)$:

$$P = 100 \left(1 - \frac{F(0,0,0)}{F_0} \right) = 100 \left(1 - K_0 \operatorname{erf} \left(\frac{l_x}{2r} \right) \operatorname{erf} \left(\frac{l_y}{2r} \right) \right). \quad (2.14)$$

One special case is when the combination of a mobile and immobile fraction is assumed. Let k be the fraction of mobile molecules, the fluorescence $F_k(x, y, t)$ is then given by [15]:

$$F_k(x, y, t) = F(x, y, 0) + k[F(x, y, t) - F(x, y, 0)], \quad (2.15)$$

where $F(x, y, t)$ is defined by Eq. (2.13). All experiments presented in this work were analyzed using Eqs. (2.13) and (2.15).

2.2.3 Parameter estimation by maximum likelihood and least squares fitting

As is illustrated in **Fig. 2.2a**, a CLSM FRAP experiment results in a time lapse movie consisting of one or more pre-bleach images, the photobleaching image (depending on the instrument) and the recovery images. After normalization to the initial fluorescence and optional correction for photobleaching during imaging, Eq. (2.13) or (2.15) can be fitted to the entire set of pixel values from the recovery images. Since all available data is used, this method achieves maximum precision and also allows to include the resolution parameter r^2 as a free fitting parameter. In this way calibration of the photobleaching resolution $r_{b,0}$ can be avoided [15]. We have evaluated two different

fitting procedures, one based on classic least squares analysis and another one on a maximum likelihood framework.

Maximum likelihood is an efficient statistical method for estimating parameters of a model [29]. To use it in this context, a probabilistic description of the noise is needed. Let $p(x, y, t)$ denote the pixel value at a pixel with coordinates (x, y) at time t . The pixel value or intensity is assumed to be linearly proportional to the number of photons $N(x, y, t)$ observed at that pixel, which we write as $p(x, y, t) = \beta N(x, y, t)$. The expectation of $p(x, y, t)$ is given by $F(x, y, t)$ from Eq. (2.13). Furthermore, we assume that $N(x, y, t)$ is Poisson distributed with expectation $F(x, y, t)/\beta$. The Poisson distribution is approximated by a normal distribution with expectation and variance $F(x, y, t)/\beta$, that is, $p(x, y, t)$ is approximately normal with expectation $F(x, y, t)$ and variance $\beta F(x, y, t)$. The approximation should be excellent since the expectation of the Poisson distribution, corresponding to pixel values, is at least 100 as estimated from our images.

The parameters β and F_0 can be estimated from the pre-bleach image(s) independent from the other model parameters. The expectation of a pixel value in the pre-bleach images is F_0 and its variance is βF_0 . F_0 is estimated by the average pixel value in the pre-bleach image(s), while β is estimated by the variance of the pre-bleach pixel values divided by the estimate of F_0 . The set of remaining model parameters $\theta = (D, k, K_0, r^2)$ is estimated by maximum likelihood. To indicate that $F(x, y, t)$ depends on the parameter vector θ , we will write $F(x, y, t; \theta)$ further on. The likelihood function for all pixels $(x, y) \in S$ for all times $t \in T$ can then be written as:

$$L(x, y, t; \theta) = \prod_{(x,y) \in S} \prod_{t \in T} \frac{1}{\sqrt{2\pi\beta F(x, y, t; \theta)}} \exp \left\{ -\frac{(p(x, y, t) - F(x, y, t; \theta))^2}{2\beta F(x, y, t; \theta)} \right\}. \quad (2.16)$$

The log-likelihood that is to be maximized, is given by:

$$l(\theta; x, y, t) = -\frac{|S||T|}{2} \log 2\pi\beta - \frac{1}{2} \sum_{(x,y) \in S} \sum_{t \in T} \log F(x, y, t; \theta) - \frac{1}{2\beta} \sum_{(x,y) \in S} \sum_{t \in T} \frac{(p(x, y, t) - F(x, y, t; \theta))^2}{F(x, y, t; \theta)}, \quad (2.17)$$

where $|S|$ and $|T|$ denote the number of elements in the sets S and T . Let $\hat{\theta}$ denote the θ -value maximizing the log-likelihood. From the large sample theory for likelihood

Chapter 2

estimators it is known that $\hat{\theta}$ is asymptotically normal with a covariance matrix V_{θ} which is the inverse of the observed Fisher information, $I(\hat{\theta})$ whose (i, j) th element is given by:

$$-\frac{\partial^2}{\partial \theta_i \partial \theta_j} l(\theta) \Big|_{\theta=\hat{\theta}}. \quad (2.18)$$

Hence the standard error of θ_i is given by the square root of the i th diagonal term of $I(\hat{\theta})^{-1}$. When analyzing the rFRAP data by least squares fitting, we minimize:

$$Q(\theta) = \sum_{(x,y) \in S} \sum_{t \in T} (p(x, y, t) - F(x, y, t; \theta))^2. \quad (2.19)$$

Note that, at the expense of additional programming and considerably extended computing time standard errors may also be obtained by use of bootstrap techniques [30].

2.3 MATERIALS AND METHODS

2.3.1 Confocal microscopy

Validation experiments were performed on a confocal laser scanning microscope (model MRC1024 UV, Bio-Rad, UK). A 488 nm line of a 4 W Ar-ion laser (model Stabilite 2017, Spectra-Physics, Germany) was used for (single photon) imaging and photobleaching in combination with a 10× Nikon CFI Plan Apochromat objective lens with a numerical aperture (NA) of 0.45 (Nikon, The Netherlands). On the Bio-Rad MRC1024 UV, this lens achieves an imaging resolution of $r_{d,0} = 1.0 \mu\text{m}$, as determined from images of 200 nm fluorescent nanospheres immobilized on a microscope slide.

The experiments on biopolymer mixtures were performed on a confocal laser scanning microscope (model TCP SP2, Leica, Germany) equipped with a heating and cooling stage (model TMS 92, Linkam, UK). The light source for imaging and bleaching was the 488 nm line from a built-in Ar-ion laser. An 63× HC PL APO water immersion objective lens with a NA of 0.90 was used. As the beam expander function was not used, the effective NA was lower than 0.90.

2.3.2 Test solutions

The validation measurements of the rFRAP method are performed on 150 kDalton FITC-dextran (Sigma-Aldrich, Belgium) solutions prepared in HEPES buffer at pH 7.4. The concentration range in which a linear relation exists between the observed fluorescence and the concentration of the fluorophore was determined to be below 4 mg/ml. It was decided to use a 3 mg/ml FITC-dextran stock solution for all validation experiments.

The solutions contained different amounts of sucrose in order to vary the dynamic viscosity η and to obtain diffusion coefficients in the range of $0.1 \mu\text{m}^2/\text{s}$ to $10 \mu\text{m}^2/\text{s}$. For rFRAP experiments, 5 μl of the FITC-dextran solution was dispensed on a microscope slide and sealed with a coverslip using a 120 μm thick double adhesive spacer (Secure-Seal Spacer, Molecular Probes, The Netherlands).

2.3.3 Biopolymer mixtures

Biopolymer mixtures were prepared from gelatin LH type with Bloom 240 (System Bio Industries, France) and Paselli SA2 maltodextrin (Avebe Group, Netherlands). The maltodextrin was covalently labeled with Rhodamine B isothiocyanate (RITC) to visually differentiate between gelatin and maltodextrin on the microscope images. Gelatin and RITC-maltodextrin were dissolved in a 150 ppm 10kDa FITC dextran solution under continuous slow agitation at 70 °C for 40 minutes and at 95 °C for 30 minutes, respectively. The gelatin and maltodextrin mixtures were subsequently mixed so that a final biopolymer concentration of 4% w/w gelatin and 6% w/w maltodextrin was obtained. The mixture was put in a water bath at 70 °C to avoid a loss of heat and was stirred for a few minutes. The sample was subsequently transferred to a sample cup that was preheated to 70 °C in a furnace. The furnace was finally set to cool the sample from 70 °C to room temperature at 21 °C at a cooling rate of approximately 0.2 °C/min.

2.3.4 Measurement protocol

The validation experiments on the FITC-dextran solutions were performed in the middle of the sample, at approximately 60 μm above the coverslip. A typical FRAP measurement consisted of a time series of 30 images of 512 by 512 pixels, as illustrated in Fig. 2.2a.

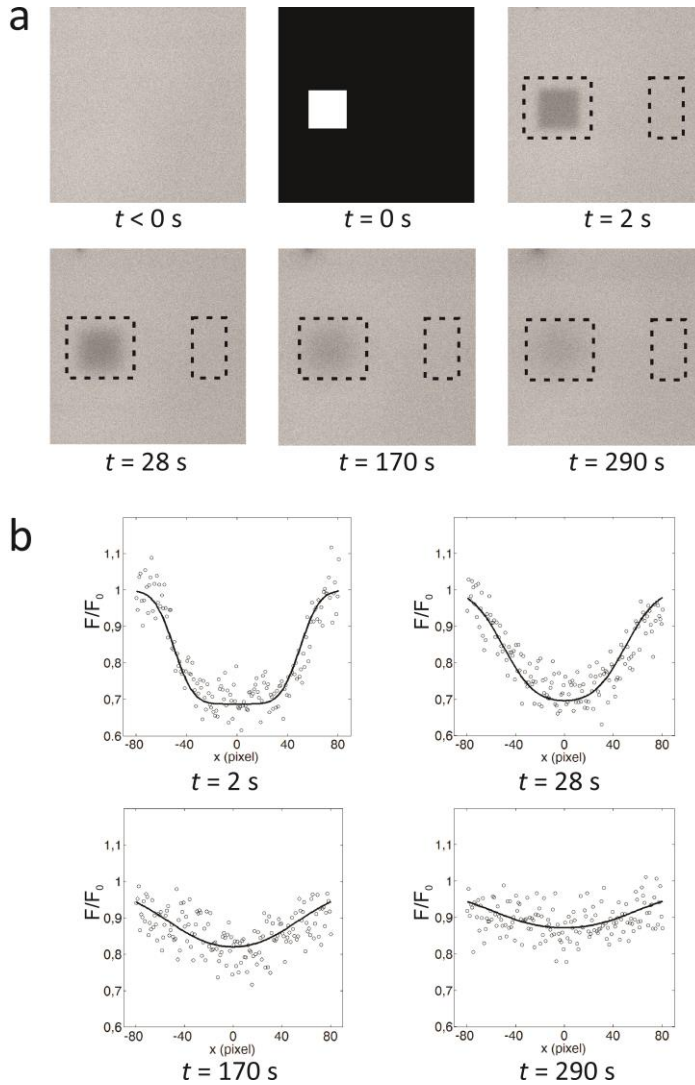


Figure 2.2 | Illustration of a rFRAP experiment. The sample is a 150 kD FITC-dextran solution in HEPES buffer with 60% sucrose. **(a)** Several frames (512 by 512 pixels) of the time lapse movie are shown. The first frame shows the pre-bleach image. At time $t = 0 \text{ s}$, a square region is bleached (30 by 30 μm) at the left side of the field of view, as is illustrated in the second frame. The following frames show the fluorescence recovery at four different times t after bleaching. The dashed square around the bleached area indicates the region that was taken into account in the analysis. The dashed rectangle to the right shows the region that was used for the background correction. **(b)** The intensity values with the result from the fitting procedure (solid line) are shown for a cross section along the x -direction of the square.

The first image shows the sample before bleaching, the second one shows the bleaching pattern at the time of bleaching, and the subsequent images show the recovery process after bleaching. The pattern is usually bleached at the left side of the image as this allows the user to define a background region at the right side of the image that is not affected by the diffusion front during the image acquisition. This background is used to correct for possible laser intensity fluctuations and bleaching during imaging. All validation experiments were performed at 22.5° C.

The FRAP protocol for the experiments performed in biopolymer mixtures was as follows. First, 20 pre-bleach images were recorded after which a rectangle was photobleached in a single step. The acousto optical tunable filter (AOTF) was set to 100% to obtain maximal bleaching. In addition, the zoom-in function was used to further increase the efficiency of the bleaching. Finally, 50 recovery images were recorded with an AOTF setting of 2%. The image format used, was 256 by 256 pixels with a scan rate of 800 Hz, leading to an image acquisition time of 0.5 s per image. The size of the bleaching region was between 5 by 5 μm and 10 by 10 μm . The sample was always examined in three dimensions before bleaching in order to avoid influence of the opposite phase along the z-direction. All experiments in biopolymer mixtures were performed at 21° C.

2.3.5 Data analysis

Before fitting of the data to the rFRAP model, the recovery data was normalized to the fluorescence before bleaching, and corrected for intensity fluctuations and photobleaching during imaging. Normalization to the pre-bleach intensity was performed by dividing every pixel in the recovery images by the corresponding pixel in the pre-bleach image. To limit the corresponding amplification of noise, the pre-bleach image was first smoothed by a 15 by 15 pixel median kernel. Correction for laser fluctuations and bleaching during imaging is performed by dividing the pixels of each recovery images by the average value from a reference background region in the same image. As indicated in **Fig 2.2a**, this reference region should be placed sufficiently far from the bleach region so as to remain unaffected by the diffusion front. Finally, the pixel values of the entire stack of images of the time lapse movie are simultaneously fitted (least squares fit or maximum likelihood analysis) to Eqs. (2.13) and (2.15) of the rFRAP model with custom written routines in the Matlab programming environment (The Mathworks, USA). As motivated in the **Section 2.2.2**, Eq. (2.13) is used because in this work we have made use of a low NA lens for single-photon FRAP experiments. A representative example is shown in **Fig. 2.2b**. Details on the maximum likelihood

estimation are discussed in the **Section 2.2**. To limit the computation time, the analysis is performed on a subregion as illustrated in **Fig 2.2a** usually consisting of the bleached area extended with 30 pixels in each direction. In our experience, including more pixels did not substantially improve the analysis precision.

2.4 RESULTS

2.4.1 Validation of the rFRAP method

To validate the new rFRAP method, experiments are performed on 150 kD FITC-dextran (FD150) solutions in HEPES buffer. Different amounts of sucrose were added to obtain a wide range of viscosities and hence diffusion coefficients. The influence of several model parameters was assessed on the calculated diffusion coefficient, as is below. In all cases, the free fitting parameters were the diffusion coefficient D , the bleaching parameter K_0 , the mobile fraction k and the average squared resolution r^2 . The mobile fraction was correctly found to be close to 1 throughout all the validation experiments independent of the other parameters and is therefore not discussed any further.

Time step

The first question that was addressed is if there is an influence of the frame rate on an rFRAP experiment. It is useful to consider this question in relation to a characteristic recovery time τ , which is defined as the average time it takes for a molecule with diffusion coefficient D to diffuse from the centre to the edge of the bleached region. In two dimensions this average time is given by:

$$\tau = \frac{(L/2)^2}{4D}, \quad (2.20)$$

where L is the length of the shortest side of the rectangle. rFRAP measurements were performed on an FD150 solution (containing 24% sucrose) for different times Δt between the subsequent recovery images ($\Delta t = \tau$, $\Delta t = \tau/2$, $\Delta t = \tau/3$, $\Delta t = \tau/4$, $\Delta t = \tau/5$) using a constant square bleach region of 50 by 50 μm . Uniform disk FRAP measurements were performed on the same sample to obtain an independent reference value for the diffusion coefficient [17]. In **Fig. 2.3a** the diffusion coefficient as obtained from the rFRAP experiments ($n = 5$, with n the number of performed rFRAP

experiments) is plotted as a function of the time step Δt , from which it is clear that the calculated diffusion coefficient is hardly influenced by the selected frame rate. The data suggest a slight increase ($\sim 5\%$) of the measured diffusion coefficient for smaller time steps. However, this could very well be due to some polydispersity of the FITC-dextran because of which the larger and more slowly moving molecules are contributing less to the recovery at short time intervals. From this result it was decided to use a time interval $\Delta t = \tau$ for all further experiments.

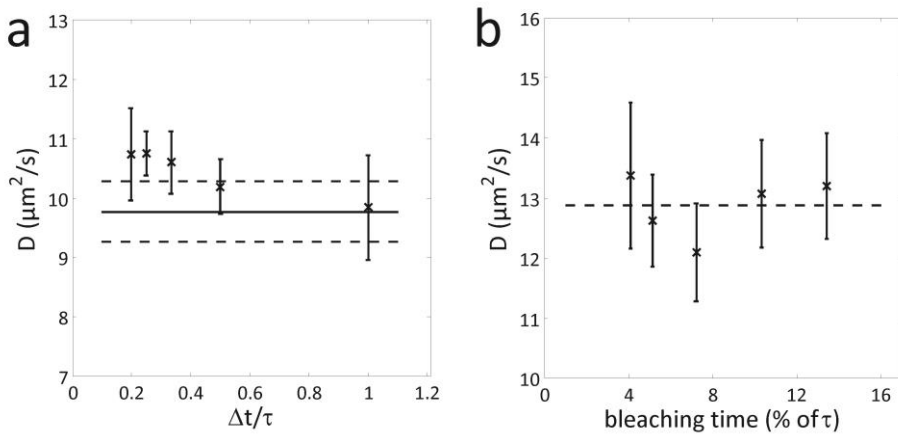


Figure 2.3 | The influence of the time step and diffusion during bleaching. (a) The average diffusion coefficient of 5 rFRAP measurements on a FD150 solution (24% sucrose) is plotted as a function of the time interval Δt (relative to the characteristic recovery time τ) between the images. In all cases a square region of 50 by 50 μm was bleached. The solid horizontal line indicates the diffusion coefficient of a uniform disk FRAP reference measurement ($D = 9.8 \pm 0.5 \mu\text{m}^2/\text{s}$). The dashed lines indicate the corresponding standard deviation of $0.5 \mu\text{m}^2/\text{s}$. (b) The average diffusion coefficient for rFRAP measurements on FD150 solutions with 16% sucrose in function of the bleaching time (expressed as the percentage of the characteristic recovery time τ) that was needed in order to bleach a square of 20 by 20 μm . The dashed line indicates the average value of the data points ($D = 12.88 \pm 1.0 \mu\text{m}^2/\text{s}$).

Eq. (2.20) is also useful to make sure that the acquisition time of a single image is small compared to the typical recovery time so that the image can be considered as a snapshot of the fluorophore concentration distribution at that time. In case of very slow scanning rates, the pixels at the beginning of the image would be recorded at a substantially different time than the last pixels in the same image, which could lead to erroneous results.

Diffusion during bleaching

In the theoretical derivation of the rectangle FRAP model we assumed that bleaching happens instantaneous so as to ignore diffusion during bleaching. However, on a laser scanning microscope the bleaching can never be entirely instantaneous. This is because of the scanning motion of the laser beam by which the last pixels of the bleach area are bleached at a later point in time than the first ones. The experimental bleach step therefore deviates from the theory by the fact that the rectangle (or any other shape) is not bleached at once and that diffusion inside the bleach area might already start during the bleaching step. This can result in a deviation of the effective initial profile of the bleached fluorophores from the theoretically expected one [10,31]. Therefore, we have explicitly tested the effect of diffusion during photobleaching on the measured diffusion coefficient for a number of bleach times. The experiment was carried out on an FD150 solution (16% sucrose) in which square regions of $20\ \mu\text{m} \times 20\ \mu\text{m}$ were bleached with different zoom settings so as to obtain different bleaching times. The amount of photobleaching was kept below 50% for all zoom settings, this will be shown to be valid below.

The results are shown in **Fig. 2.3b** ($n = 10$) where the measured diffusion coefficient is plotted versus the bleaching time which is expressed as a percentage of the recovery time τ (see Eq. (2.20)). Within the tested range of 4-14% (which was maximum for our CLSM), no significant difference could be found in the measured diffusion coefficient. This demonstrates the capability of the rectangle FRAP method to compensate for at least a limited amount of diffusion during bleaching. All further experiments reported here were conducted with bleaching times shorter than 14% of the recovery time τ .

Amount of photobleaching

An important assumption in the rFRAP model is the linearity of the photobleaching process (cfr. Eq. (2.6)). Since normally the photobleaching process is modeled as an exponential decay, in theory this could mean that only a small amount of bleaching is allowed ($< 30\%$). We tested this experimentally on a FD150 solution (52% sucrose) for different percentages of photobleaching of a $5\ \mu\text{m}$ by $5\ \mu\text{m}$ square bleach region. The percentage of photobleaching was calculated using Eq. (2.14). The amount of photobleaching was increased by increasing the zoom setting of the microscope.

As indicated in **Fig. 2.4a** ($n = 5$), the diffusion coefficient was found to be constant within the experimental precision for at least up to $\sim 50\%$ of photobleaching. Apparently the (possible) deviation from linearity is counter-acted by an increase of the

resolution parameter r^2 (see **Fig. 2.4b**). However, when increasing the amount of photobleaching further to 70-90%, the resolution parameter cannot fully compensate for the deviation from linearity leading to an over-estimation (~25%) of the diffusion coefficient. We conclude that the calculated diffusion coefficient by the rFRAP method in practice is independent of the amount of photobleaching for at least up to 50%.

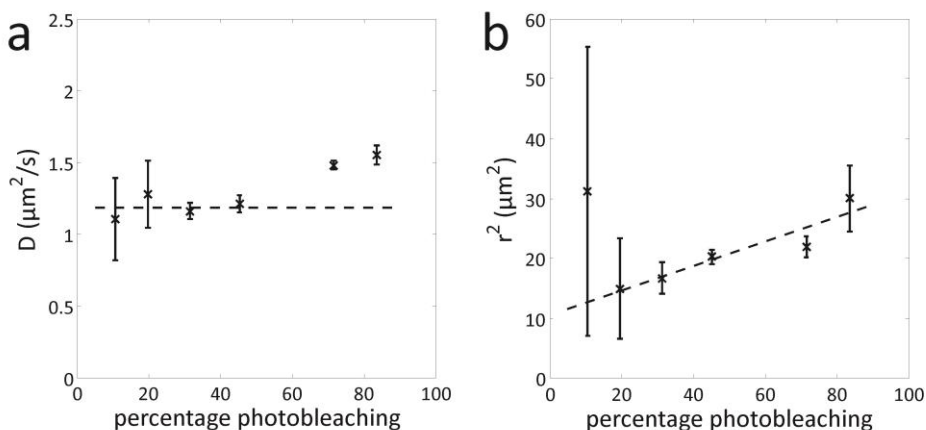


Figure 2.4 | The influence of the amount of photobleaching. rFRAP measurements were performed for different bleaching percentages on an FITC-dextran solution. **(a)** The average diffusion coefficient is plotted in function of percentage of bleaching. The straight dashed line represents the average value over the first 3 data points. **(b)** The resolution parameter is shown in function of the percentage of bleaching. The dashed line represents a linear fit to the measured average values (the data point at 10% was excluded).

Rectangle size

Since in the derivation of the rFRAP model we have included the effective photobleaching resolution as well as the imaging resolution, the method should be valid for all sizes of the bleaching rectangle. This was tested on an FD150 solution (60% sucrose) by photobleaching square regions of different sizes: 2.4 μm , 5 μm , 7.4 μm , 10 μm and 12.4 μm . The results are shown in **Fig. 2.5a** ($n = 10$), from which it is clear that the calculated diffusion coefficient is indeed independent of the size of the bleach region. The standard error on the average D values increases for smaller sizes of the bleach region since the available number of pixels in the data set decreases.

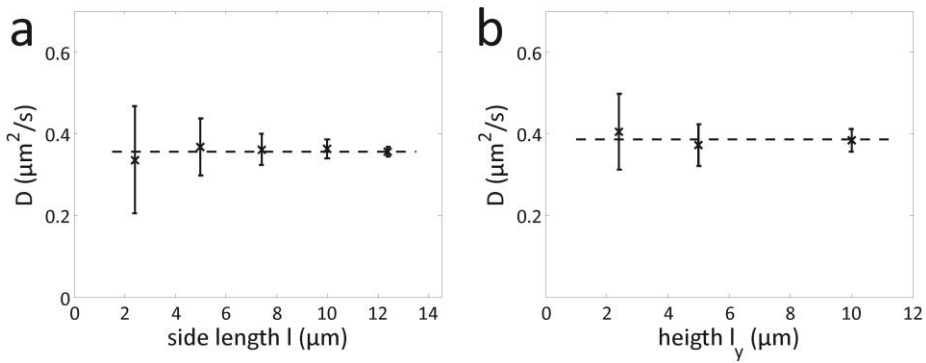


Figure 2.5 | The influence of the rectangle size and aspect ratio. (a) The average diffusion coefficient for rFRAP measurements on FITC-dextran solutions with 60% sucrose in function of the size of the bleached square with side length l . The dashed line indicates the average value of the data points. (b) The diffusion coefficient is calculated from rFRAP measurements on an FD150 solution (60% sucrose) using rectangles of length 10 μm but with a varying height l_y . The dashed line indicates the average value over all measurements.

Rectangle aspect ratio

In a next step we tested the validity of the rectangle FRAP method for different aspect ratios of the rectangle. rFRAP experiments were performed on an FD150 solution (60% sucrose) for bleach rectangles all having a width of 10 μm , but a variable height: 2.4 μm , 5 μm and 10 μm . The results in **Fig. 2.5b** ($n = 5$) confirm that the diffusion coefficient is independent of the aspect ratio. The larger the height of the rectangle, the more precise the diffusion coefficient could be determined because of more pixels being available in the bleached area.

Validation of the calculated diffusion coefficient

The diffusion coefficients predicted by the new rFRAP model are validated against measurements by the uniform disk model on FD150 solutions containing different amounts of sucrose : 0%, 5%, 10%, 16%, 24%, 32% and 44%. The uniform disk model is used as a reference since it is an independent FRAP method that has been extensively validated [17].

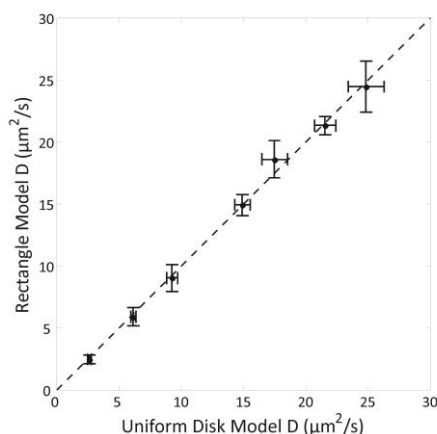


Figure 2.6 | Validation of the calculated diffusion coefficient. The average diffusion coefficient D as determined by the rFRAP method is plotted vs. the average diffusion coefficient D determined by the disk model for FD150 solutions with different amounts of sucrose. The dashed line represents the ideal case in which both methods predict exactly the same diffusion coefficient.

For all measurements a rectangle of 30 by 30 μm and a disk of 50 μm diameter was used. The effect of the size of the bleaching region on the estimated diffusion coefficient was discussed above. As can be seen from the data in **Fig. 2.6**, the rFRAP measurements are in excellent agreement with the disk FRAP measurements. A linear fit to the data yields a slope of 1.0065 and an offset of $-0.0987 \mu\text{m}^2/\text{s}$. An additional two-tailed t -test confirmed that the rFRAP measurements are not different from the disk FRAP measurements at the 5% significance level. Despite the extra free fitting parameter in case of the rectangle method (average squared resolution r^2), the precision of the individual diffusion coefficients is similar for both methods, ranging between between 5% and 15%. This can be attributed to the spatial information that is taken into account by the rFRAP method. We conclude that the rFRAP method is capable of accurately measuring diffusion for a wide range of diffusion coefficients with good precision.

Comparison of least squares estimation and maximum likelihood estimation

Maximum Likelihood (ML) was recently suggested as an alternative to the classic least-squares (LS) fit for analysis of FRAP data [21]. It is therefore interesting to compare both analysis methods side by side. A series of rFRAP experiments was performed on an

Chapter 2

FD150 solution (60% sucrose) using a constant bleach region but an increasing laser intensity so as to obtain a range of different K_0 and r^2 values. These data sets were analyzed by both LS and ML.

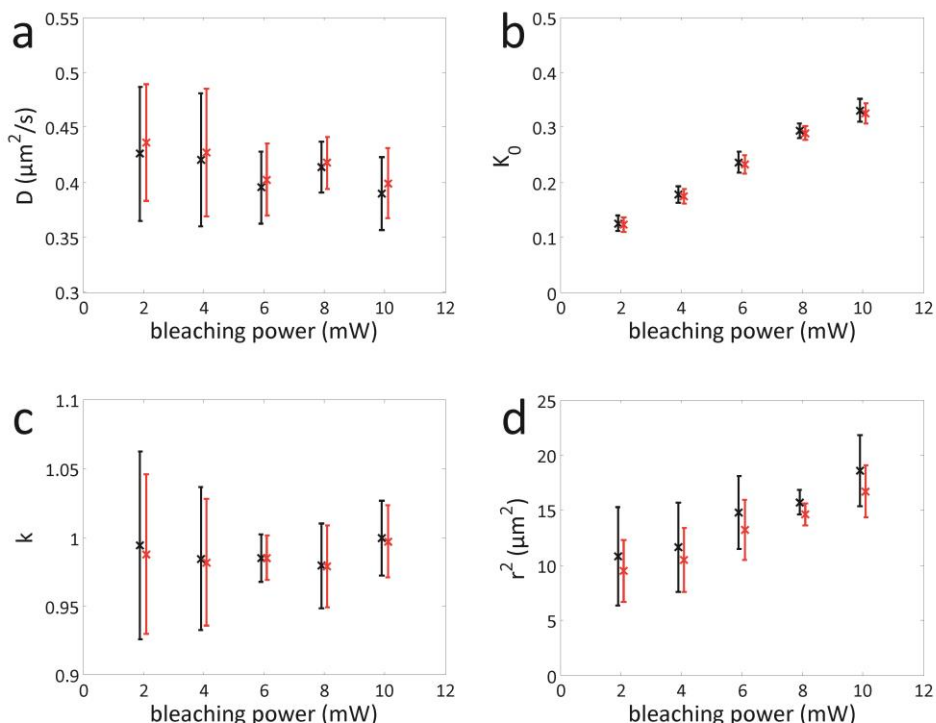


Figure 2.7 | Comparison of least squares estimation and maximum likelihood estimation. Least squares estimates (black) and maximum likelihood estimates (red) for rFRAP experiments performed on an FD150 solution (60% sucrose) using a constant bleach region but an increasing laser intensity between 2 mW and 10 mW are shown. The data points are the averages of 10 measurements with error bars corresponding to one standard deviation.

As can be seen in **Fig. 2.7**, the estimates of D , k and K_0 are essentially the same for both analysis methods, whereas r^2 is slightly lower for the ML estimation. The standard deviations of the estimates are also similar but generally a little smaller for the ML method. The computation time for the ML method was generally longer than for the LS method, particularly if the initial guesses of the unknown parameters were far from the optimal values. ML and LS can both produce standard errors for the estimated

parameters, which can be used both to get an idea of the precision of the estimates and to give prediction bounds in residual plots as a guideline for the quality of the model fit. This is especially useful in case of heterogeneous samples where it might be difficult to repeat FRAP experiments under identical conditions and thus to obtain the standard error from repeated measurements. We note that in some cases it was difficult to come to a good estimate of the resolution parameter r^2 by direct optimization of the likelihood. In this case, iteration with the profile likelihood [29] turned out to be useful.

2.4.2 rFRAP measurements on biopolymer mixtures

Mixed biopolymer systems are widely utilized in industries for foods, pharmaceuticals and personal care to control texture and mass transport in a product. Many mixed biopolymer systems are incompatible and will phase separate and gel under certain conditions. The protein-polysaccharide mixture of gelatin and maltodextrin is a thermodynamically instable system, having a segregative phase separation process generating regions enriched in either one of the polymers [32,33]. In addition, the system will gel when a temperature below the gelling temperature of gelatin is reached, which kinetically traps the system in a nonequilibrium state.

The final morphology of the mixed biopolymer system will be determined by the kinetics of phase separation and gelation together with the relative rate between the two processes [34]. By changing the biopolymer concentration, quench temperature, cooling rate, ionic conditions and confinement, it has been shown that the morphology of the gelatin-maltodextrin system can be designed to desired microstructures [35].

Kinetically trapped phase separated biopolymer mixtures, such as mixtures of gelatin and maltodextrin, often have a very heterogeneous microstructure. **Fig. 2.8a** shows an example of such a structure with 4 w/w% gelatin and 6 w/w% maltodextrin. The dark phase is the gelatin phase and the bright phase is the maltodextrin phase. It can be seen that the structure is very heterogeneous with a bicontinuous morphology that contains spherical inclusions of the opposite phase. The characteristic length scales of the phase separated domains in this system ranges from a few micrometers up to hundreds of micrometers. One of the main objectives with the rFRAP method is to measure the local diffusion rate in small regions of such heterogeneous materials.

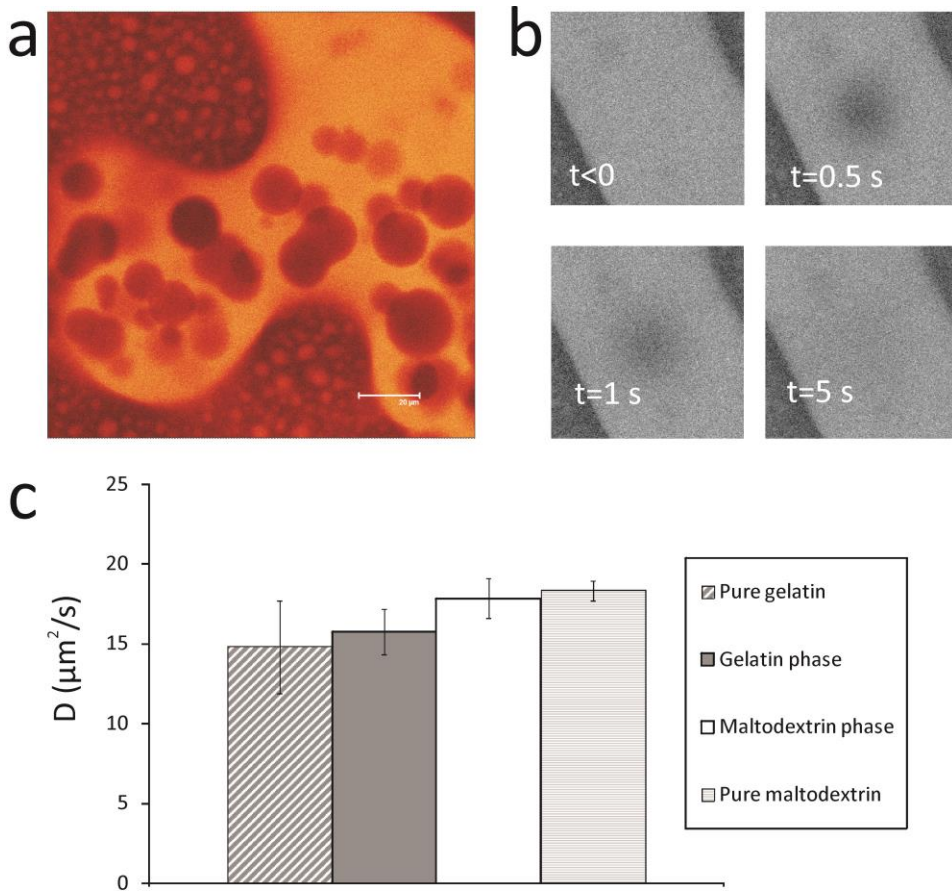


Figure 2.8 | rFRAP measurements on biopolymer mixtures. (a) CLSM image of a kinetically trapped and phase separated gelatin/maltodextrin mixture. The maltodextrin phase is bright and the gelatin phase is dark. The scale bar is 20 μm . (b) An rFRAP measurement in the maltodextrin phase of a phase separated gelatin/maltodextrin system. The bleached square is 7 by 7 μm and the field of view is 60 by 60 μm . (c) Diffusion coefficients determined using rFRAP in pure gelatine and maltodextrin, as well as in the phase-separated gelatin/maltodextrin mixture.

Fig. 2.8b shows an rFRAP experiment in the maltodextrin phase of a kinetically trapped and phase separated gelatin/maltodextrin mixture containing FITC-dextran molecules of 10 kDa. The first ($t < 0$) and second ($t = 0.5$ s) image in **Fig. 2.8b** show the structure before bleaching and after bleaching, respectively. Images 3 ($t = 1$ s) and 4 ($t = 5$ s) show the subsequent fluorescence recovery of the FITC-dextran molecules.

Fig. 2.8c shows the results from rectangle FRAP measurements in both the pure gelatin and maltodextrin gels, as well as in the gelatin and maltodextrin phases of the kinetically trapped phase separated mixture. The leftmost and the rightmost bar in **Fig. 2.8c** are the diffusion rates in pure gelatin and pure maltodextrin respectively. The diffusion coefficient of FITC-dextran 10 kDa in pure gelatin is $14.8 \pm 2.9 \mu\text{m}^2/\text{s}$ and $18.3 \pm 0.6 \mu\text{m}^2/\text{s}$ in pure maltodextrin. The diffusion coefficient obtained by rFRAP in the phase-separated mixture is $15.8 \pm 1.4 \mu\text{m}^2/\text{s}$ ($n = 14$) in the gelatin phase and $17.9 \pm 1.2 \mu\text{m}^2/\text{s}$ in the maltodextrin phase ($n = 13$). The diffusion coefficients in the phase separated system differ slightly from the values obtained in corresponding pure phases. This can be attributed to the fact that the maltodextrin phase will always contain a small amount of gelatin and vice versa due to entropic reasons. This means that the gelatin will contribute to the diffusion rate in maltodextrin and maltodextrin will contribute to the diffusion in gelatin. A *t*-test performed on the data from the polymer mixture showed that the diffusion coefficients in the different phases were significantly different with a *p*-value of 0.0004. It can therefore be concluded that rFRAP has the power to differentiate between the diffusion rate of FITC-dextran in the individual phases in a heterogeneous phase separated and gelled biopolymer mixture even when the difference is small.

2.5 DISCUSSION

Over the years, FRAP has become one of the most well-known methods to study local diffusion on the micrometer scale in biological media and biopharmaceutical materials. While several quantitative FRAP methods have been put forward in literature, it is a fact that most of the reported applied FRAP mobility studies remain qualitative or semi-quantitative at best because of the limited usefulness or complexity of published FRAP methods. In order to bring quantitative FRAP measurements to the larger community of biologists and material scientists, we feel there is a clear need for FRAP methods that are more versatile, are easily implemented on commercial microscopes and allow for straightforward and fast data analysis. Here we have addressed this need by developing a new pixelbased FRAP method with a closed-form expression that describes the full temporal and spatial information of the recovery process. A closed-form expression could be obtained by assuming a rectangular bleaching area and making the assumption of a linear photobleaching process. Note that a similar closed-formed expression is currently not available for the conventionally used circular bleaching area. By taking into account the relevant microscope resolution parameters (effective

photobleaching resolution and imaging resolution), the rectangle can have any size and aspect ratio, even down to the size of the point spread function. We have shown before that the effective photobleaching resolution can be substantially larger than the theoretical one because of triplet saturation of the fluorophores that might arise during the highly intense photobleaching phase [14,15]. The actual value of the effective photobleaching resolution depends on the excitation photon flux, the photochemical properties of the fluorophore and the local chemical environment. Hence it is important to include the photobleaching and imaging resolution as independent parameters. Nevertheless, in the final expression of the rFRAP model, both resolution parameters combine to a single one (the average square resolution r^2) that can be included as a free fitting parameter during the data analysis, thus eliminating the need for prior calibration. Including r^2 as a free fitting parameter is possible since not only temporal but also spatial information is taken into account.

Using well-characterized FITC-dextran solutions we have shown that the rFRAP method can reliably measure the diffusion coefficient in a wide range of conditions. It was demonstrated that the rectangle can be arbitrarily small or large with any aspect ratio. Furthermore it was shown that, despite the theoretical assumption of linear photobleaching, substantial photobleaching up to at least 50% is allowed thanks to including the resolution r^2 as a free fitting parameter, which was found to increase with increasing bleaching power, as expected [14,15]. Diffusion during bleaching was found to have a negligible effect on the predicted diffusion coefficient. This can be explained by the fact that the rectangle FRAP model is based on a rectangular bleach area that is convolved with a Gaussian function (cfr. Eq. (2.2)). Although the original reason was to incorporate an independent effective bleaching intensity distribution, it is not surprising that diffusion during bleaching can also be captured by this convolution since the progression of free diffusion follows from a Gaussian propagator as well (cfr. Eq. (2.7)). Finally, the rFRAP method was thoroughly validated against conventional large disk FRAP measurements on a series of FITC-dextran solutions with different viscosities.

In the data analysis of the rFRAP method, two fitting algorithms were evaluated, the least squares method and the maximum likelihood method. We found that the classic least squares fit gives acceptable results, while the maximum likelihood method can obtain slightly improved estimates at the expense of a longer calculation time. Both methods allow to calculate standard errors from a single experiment. This is an advantage in case of heterogeneous samples where it might be difficult to obtain repetitions of exactly the same measurement. As mentioned in **Section 2.2.3**, with additional programming and extended computing time standard errors may also be obtained for least squares fitting by use of bootstrap techniques.

In collaboration with Dr. Niklas Lorén from the Swedish Institute for Food and Technology, the rFRAP method was finally used to study the diffusion coefficient in a phase separated mixture of gelatin and maltodextrin having characteristic length scales between five and hundreds of micrometers. The diffusion coefficient in the separate phases could be accurately determined.

2.6 CONCLUSION

The rFRAP method proves to be a versatile approach for accurate and precise diffusion measurements by a (confocal) laser scanning microscope. Because the model can make use of a closed-form solution describing the full recovery in time and space, independent calibration of the effective microscope resolution parameters is no longer required. Combined with the possibility to photobleach rectangles of any size and aspect ratio, it opens up the field for performing diffusion measurements on both small and large samples with or without heterogeneous structures on the micrometer length scale.

REFERENCES

1. M. Edidin, "Translational diffusion of membrane proteins," in *The Structure of Biological Membranes*, P. Yeagle, ed., (CRC Press, Boca Raton, 1992), pp. 539-572.
2. A. Ishihara and K. Jacobson, "A Closer Look at How Membrane-Proteins Move," *Biophysical Journal* **65**, 1754-1755 (1993).
3. F. Umenishi, J. M. Verbavatz, and A. S. Verkman, "cAMP regulated membrane diffusion of a green fluorescent protein-aquaporin 2 chimera," *Biophysical Journal* **78**, 1024-1035 (2000).
4. F. Alvarez-Mancenido, K. Braeckmans, S. C. De Smedt, J. Demeester, M. Landin, and R. Martinez-Pacheco, "Characterization of diffusion of macromolecules in konjac glucomannan solutions and gels by fluorescence recovery after photobleaching technique," *International Journal of Pharmaceutics* **316**, 37-46 (2006).
5. M. D. Burke, J. O. Park, M. Srinivasarao, and S. A. Khan, "Diffusion of macromolecules in polymer solutions and gels: A laser scanning confocal microscopy study," *Macromolecules* **33**, 7500-7507 (2000).
6. Censi R., Vermonden T., van Steenberg M.J., Deschout H., Braeckmans K., De Smedt S.C., van Nostrum C.F., di Martino P., and Hennink W.E., "Photopolymerized thermosensitive hydrogels for tailorable diffusion-controlled protein delivery," *Journal of Controlled Release* **140**, 230-236 (2009).
7. S. C. DeSmedt, T. K. L. Meyvis, J. Demeester, P. VanOostveldt, J. C. G. Blonk, and W. E. Hennink, "Diffusion of macromolecules in dextran methacrylate solutions and gels as studied by confocal scanning laser microscopy," *Macromolecules* **30**, 4863-4870 (1997).
8. F. van de Manakker, K. Braeckmans, N. el Morabit, S. C. De Smedt, C. F. van Nostrum, and W. E. Hennink, "Protein-Release Behavior of Self-Assembled PEG-beta-Cyclodextrin/PEG-Cholesterol Hydrogels," *Advanced Functional Materials* **19**, 2992-3001 (2009).
9. S. R. Van Tomme, B. G. De Geest, K. Braeckmans, S. C. De Smedt, F. Siepmann, J. Siepmann, van Nostrum C.F., and W. E. Hennink, "Mobility of model proteins in hydrogels composed of oppositely charged dextran microspheres studied by protein release and fluorescence after photobleaching," *Journal of Controlled Release* **110**, 67-78 (2005).
10. J. Braga, J. M. P. Desterro, and M. Carmo-Fonseca, "Intracellular macromolecular mobility measured by fluorescence recovery after photobleaching with confocal laser scanning microscopes," *Molecular Biology of the Cell* **15**, 4749-4760 (2004).
11. O. Seksek, J. Biwersi, and A. S. Verkman, "Translational diffusion of macromolecule-sized solutes in cytoplasm and nucleus," *Journal of Cell Biology* **138**, 131-142 (1997).
12. A. S. Verkman, "Diffusion in cells measured by fluorescence recovery after photobleaching," *Biophotonics, Pt A* **360**, 635-648 (2003).
13. D. Axelrod, D. E. Koppel, J. Schlessinger, E. Elson, and W. W. Webb, "Mobility Measurement by Analysis of Fluorescence Photobleaching Recovery Kinetics," *Biophysical Journal* **16**, 1055-1069 (1976).
14. K. Braeckmans, B. G. Stubbe, K. Remaut, J. Demeester, and S. C. De Smedt, "Anomalous photobleaching in fluorescence recovery after photobleaching measurements due to excitation saturation- a case study for fluorescein," *Journal of Biomedical Optics* **11**, (2006).
15. K. Braeckmans, K. Remaut, R. E. Vandenbroucke, B. Lucas, S. C. De Smedt, and J. Demeester, "Line FRAP with the confocal laser scanning microscope for diffusion measurements in small regions of 3-D samples," *Biophysical Journal* **92**, 2172-2183 (2007).

16. D. Mazza, K. Braeckmans, F. Cella, I. Testa, D. Vercauteren, J. Demeester, S. S. De Smedt, and A. Diaspro, "A new FRAP/FRAPa method for three-dimensional diffusion measurements based on multiphoton excitation microscopy," *Biophysical Journal* **95**, 3457-3469 (2008).
17. K. Braeckmans, L. Peeters, N. N. Sanders, S. C. De Smedt, and J. Demeester, "Three-dimensional fluorescence recovery after photobleaching with the confocal scanning laser microscope," *Biophysical Journal* **85**, 2240-2252 (2003).
18. D. A. Berk, F. Yuan, M. Leunig, and R. K. Jain, "Fluorescence Photobleaching with Spatial Fourier-Analysis - Measurement of Diffusion in Light-Scattering Media," *Biophysical Journal* **65**, 2428-2436 (1993).
19. P. Jonsson, M. P. Jonsson, J. O. Tegenfeldt, and F. Hook, "A Method Improving the Accuracy of Fluorescence Recovery after Photobleaching Analysis," *Biophysical Journal* **95**, 5334-5348 (2008).
20. T. T. Tsay and K. A. Jacobson, "Spatial Fourier-Analysis of Video Photobleaching Measurements - Principles and Optimization," *Biophysical Journal* **60**, 360-368 (1991).
21. J. K. Jonasson, N. Loren, P. Olofsson, M. Nyden, and M. Rudemo, "A pixel-based likelihood framework for analysis of fluorescence recovery after photobleaching data," *Journal of Microscopy-Oxford* **232**, 260-269 (2008).
22. J. K. Jonasson, J. Hagman, N. Loren, D. Bernin, M. Nyden, and M. Rudemo, "Pixel-based analysis of FRAP data with a general initial bleaching profile," *Journal of Microscopy-Oxford* **239**, 142-153 (2010).
23. A. Tannert, S. Tannert, S. Burgold, and M. Schaefer, "Convolution-based one and two component FRAP analysis: theory and application," *European Biophysics Journal with Biophysics Letters* **38**, 649-661 (2009).
24. P. Wedekind, U. Kubitscheck, and R. Peters, "Scanning Microphotolysis - A New Photobleaching Technique Based on Fast Intensity Modulation of A Scanned Laser-Beam and Confocal Imaging," *Journal of Microscopy-Oxford* **176**, 23-33 (1994).
25. P. Wedekind, U. Kubitscheck, O. Heinrich, and R. Peters, "Line-scanning microphotolysis for diffraction-limited measurements of lateral diffusion," *Biophysical Journal* **71**, 1621-1632 (1996).
26. E. B. Brown, E. S. Wu, W. Zipfel, and W. W. Webb, "Measurement of molecular diffusion in solution by multiphoton fluorescence photobleaching recovery," *Biophysical Journal* **77**, 2837-2849 (1999).
27. J. Crank, *The Mathematics of Diffusion*, (Clarendon Press, Oxford, 1975).
28. J. C. G. Blonk, A. Don, H. Vanaalst, and J. J. Birmingham, "Fluorescence Photobleaching Recovery in the Confocal Scanning Light-Microscope," *Journal of Microscopy-Oxford* **169**, 363-374 (1993).
29. Y. Pawitan, *In All Likelihood*, (Clarendon Press, Oxford, 2001).
30. W. H. Press, S. A. Teukolsky, W. T. Vetterling, and B. P. Flannery, "Confidence Limits on Estimated Model Parameters," in *Numerical Recipes in C*, (Cambridge University Press, Cambridge, 1992).
31. M. Kang, C. A. Day, K. Drake, A. K. Kenworthy, and E. DiBenedetto, "A Generalization of Theory for Two-Dimensional Fluorescence Recovery after Photobleaching Applicable to Confocal Laser Scanning Microscopes," *Biophysical Journal* **97**, 1501-1511 (2009).
32. S. Fransson, N. Loren, A. Altskar, and A. M. Hermansson, "Effect of Confinement and Kinetics on the Morphology of Phase Separating Gelatin-Maltodextrin Droplets," *Biomacromolecules* **10**, 1446-1453 (2009).

Chapter 2

33. N. Loren, A. Altskar, and A. M. Hermansson, "Structure evolution during gelation at later stages of spinodal decomposition in gelatin/maltodextrin mixtures," *Macromolecules* **34**, 8117-8128 (2001).
34. N. Loren and A. M. Hermansson, "Phase separation and gel formation in kinetically trapped gelatin/maltodextrin gels," *International Journal of Biological Macromolecules* **27**, 249-262 (2000).
35. N. Loren and A. M. Hermansson, "Structure evolution during phase separation and gelation of biopolymer mixtures," in *Food Colloids - Biopolymers and Materials*, Dickinson E. and Van Vliet T., eds., (The Royal Society of Chemistry, Cambridge, 2003), pp. 298-308.

PART II

SINGLE PARTICLE TRACKING

Chapter 3

**An introduction to single particle tracking with
selected applications in pharmaceutical research**

ABSTRACT

Fluorescence microscopy based methods for measuring biophysical nanoparticle properties inside biomaterials are of interest in pharmaceutical research. As discussed in **PART I**, a well-known example of such a technique is fluorescence recovery after photobleaching (FRAP). Single particle tracking (SPT) is another emerging method that is arguably proving to be even more useful for this purpose. Just like FRAP, SPT can be of great help in the systematic optimization of nanoparticles that protect, transport and deliver therapeutic macromolecules in cells and tissues. Additionally, SPT shows potential for diagnostic assays as well. Here, the basic principles of SPT are discussed and a brief overview is given of its possible applications in pharmacology.

3.1 INTRODUCTION

In pharmaceutical research, a lot of effort goes to the development and optimization of nanomedicines, i.e. nanoparticles that function as drug delivery systems. For instance, in the field of gene therapy, nanomedicines are being designed with the purpose of delivering therapeutic nucleic acids to specific cells [1]. A common approach to fabricate these nanoparticles is by electrostatic complexation of the nucleic acids with a carrier material like cationic polymers or lipids. The carrier material, also called vector, should protect the nucleic acid payload from degradation after administration into the body. Moreover, the nanomedicines should remain stable and should not aggregate nor dissociate before reaching the target location. In case of an intracellular target, the carrier material should also facilitate efficient (endocytic) uptake in cells, and if necessary, release from endosomes into the cytosol. Engineering of such nanoparticles thus requires detailed knowledge of their behaviour in a variety of biomaterials, according to the delivery route.

Advanced fluorescence microscopy methods have already been reported to be useful for nanoparticle characterization in the context of drug delivery [1,5-7]. Especially SPT can be of great help, since the technique is capable of measuring properties of individual nanoparticles, such as the type of motion [8], size [9], interaction [10], and concentration [11] directly inside biomaterials. Interaction measurements with SPT are the topic of **Chapter 6**.

Besides drug delivery, characterization of nanoparticles is also of interest in diagnostics. For instance, it is being investigated in which way the properties of cell derived membrane vesicles in body fluids, such as blood or urine, could be predictive for different diseases, like cancer or thrombosis [2,3]. Another example is aggregation of amyloid β in cerebrospinal fluid, which is suggested to indicate the presence of neurodegenerative disorders like Parkinson's or Alzheimer's disease [4]. Accurate and precise characterization of biological nanoparticles in biomaterials, therefore, shows potential towards diagnosing medical conditions.

In **Chapter 3**, a brief overview is given of the different nanoparticle properties that can be studied with SPT, together with corresponding pharmaceutical applications. But first, the basic principles of SPT will be discussed in **Section 3.2**.

3.2 PRINCIPLES OF SPT

SPT is a fluorescence microscopy method capable of visualising the motion of individual fluorescently labelled nanoparticles that have a size below the microscope resolution (typically 250 nm).

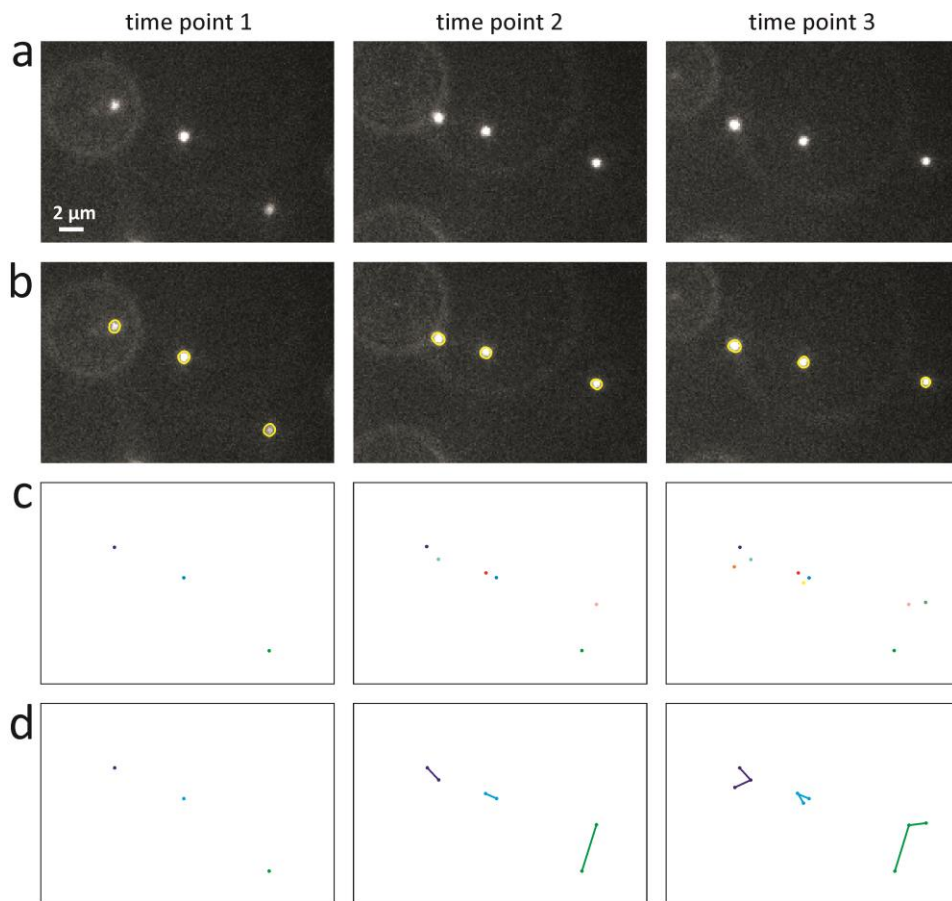


Figure 3.1 | The concept of single particle tracking. (a) A sequence of images is recorded at successive time points. (b) Using image processing software, the individual nanoparticles are identified in each image (yellow contours). (c) The position of each identified nanoparticle in each image is calculated (dots in different colours), e.g. by least-squares fitting of a Gaussian function. (d) The positions in the different images belonging to the same nanoparticle are connected to each other to form the nanoparticle trajectory, for instance with a nearest neighbour algorithm.

Chapter 3

When a sufficient number of fluorescent photons (e.g. more than 100) coming from a single nanoparticle are detected, they will form a distinct spot in the image that has a width in the same order as the resolution. Usually, this spot has a Gaussian shape, which means that the location of the nanoparticle can be estimated from the centre of the spot, with a precision much better than the resolution of the microscope, e.g. up to 10 nm using least-squares fitting of a Gaussian function (see **Chapter 4** for a discussion on this topic). Recording a time sequence of images thus allows to precisely determine the trajectory of the individual nanoparticle. These experiments require excitation, usually by laser light, of the fluorescently labelled nanoparticle over the entire field of view. Furthermore, a fast and sensitive detector like an electron multiplying charge coupled (EMCCD) device is necessary to detect as much photons as possible. For an exemplary experimental SPT set-up, the reader is referred to **Section 5.3.2** of **Chapter 5**.

Although usually more than one nanoparticle is present in the field of view, SPT can still be performed without much complications if the nanoparticle concentration is sufficiently low so that each spot in the image is corresponding to an individual nanoparticle (i.e. all nanoparticles are at least 500 nm removed from each other). As illustrated in **Fig. 3.1**, after recording the time sequence of images, the individual nanoparticles are identified by image processing (see **Section 5.3.4** in **Chapter 5** for more details on how it is done in our group). Subsequently the position of each identified nanoparticle in each image is calculated, and then the trajectories of the different nanoparticles can be obtained, e.g. by using a nearest neighbour algorithm. These trajectories form the basis of further analysis that yields information on a variety of properties of the nanoparticles, as explained in **Section 3.3**.

3.3 TRAJECTORY ANALYSIS

3.3.1 Type of motion

Often one is interested in determining the type of motion of the nanoparticles [12]. This is usually done by investigation of the mean square displacements in the nanoparticle trajectory. For instance, when the nanoparticle is undergoing free diffusion, its mean square displacement is linearly related to time, with a proportionality constant that is defined by the diffusion coefficient (see Eq. (5.13) in **Chapter 5**). Other types of motion, such as directed transport or anomalous diffusion, result in a different behaviour of the mean square displacements [8,13,14].

In this way, SPT can reveal the modes of transport of a nanoparticle in different biomaterials, which is indicative of its interaction with the biomaterial constituents. In the case of extracellular matrices, SPT has for instance been applied to determine which surface functionalization of polystyrene nanospheres ensures the highest mobility in mucus [15-17], and vitreous [18,19]. Similarly, SPT has been used to study the different types of motion of polymeric gene complexes that are taken up by cells [20-22]. Such information is of great interest in designing efficient nanoparticles for drug delivery.

3.3.2 Size

Besides the type of motion, analysis of the mean square displacements in the trajectory can also yield information on the size of the nanoparticle. When the nanoparticle is undergoing Brownian motion, its diffusion coefficient is inversely related to the size through the Stokes-Einstein equation (see Eq. (7.2) in **Chapter 7**). Measuring the trajectories of many nanoparticles with SPT and calculating their diffusion coefficients thus allows to determine the nanoparticle size distribution [9]. The main advantage over techniques like dynamic light scattering is that these are only able to measure size distributions inside transparent media that contain little or no other scattering components, while SPT can be performed in any biomaterial if the nanoparticle is fluorescently labelled.

One important pharmaceutical application of SPT size measurements is investigating whether or not nanoparticles aggregate in blood upon intravenous administration. For instance, SPT was used to measure the size distribution inside blood of liposomes that contain different amounts of polyethylene glycol (PEG) [9]. Liposomes with small amounts of PEG were found to aggregate strongly over time, while larger amounts of PEG significantly inhibited this behaviour. Similarly it was shown that SPT sizing allows to study potential aggregation of therapeutic proteins upon intravenous administration [23,24]. SPT size measurements are also potentially useful in the field of diagnostics, since the size distribution of cell-derived membrane vesicles present in biological fluids are believed to be related to different stadia of medical conditions such as cancer [2].

3.3.3 Interaction

In the context of fluorescence microscopy, interactions between nanoparticles and biological structures are often investigated by labelling them with different types of

fluorophores and recording multi-colour images. The colocalization of colours is then taken as a measure for this interaction. Quantification can either be done by comparing the pixel values between the images, or by first identifying the relevant objects in each image and subsequently determining the distance between their centre positions. However, these approaches only use the information of one time point, which means that coincidental colocalization is indistinguishable from interaction. New methods have therefore been developed that take both spatial and temporal information into account, i.e. by performing SPT instead of recording a single image in the different colours. In this approach, interaction between nanoparticles is defined as colocalization or correlation between trajectories in the corresponding colours [10,25,26]. This allows a more accurate identification of interaction, since colocalized or correlated trajectories are not likely to arise by coincidence.

This SPT method has been used in the field of gene therapy to investigate the interaction of polymeric gene complexes with certain types of endosomes inside cells [26]. If a complex is transported by a certain endosome, their corresponding trajectories exhibit correlation. Another possible application in drug delivery research is the investigation of the stability of nanoparticles in biomaterials, by labelling the carrier material and the therapeutic payload with different fluorophores and looking for interaction between the corresponding trajectories.

3.3.4 Concentration

Although the number of observed nanoparticles is immediately available from an SPT experiment as the number of trajectories, it is also necessary to know the volume in which these nanoparticles have been detected to determine the number concentration. This volume, however, is not straightforward to calculate, since the thickness of the focal volume in which the nanoparticles are detected does not only depend on the objective lens, but also on the brightness of the nanoparticles and the image processing settings for identification of the nanoparticles. To avoid a separate calibration of the detection volume for each experiment, a method has been proposed to estimate the detection volume directly from the trajectory information, assuming that the nanoparticles are undergoing Brownian motion [11]. The concentration of nanoparticles inside biomaterials can thus be calculated directly from the SPT data without any calibration.

This method has been applied in the field of drug delivery to characterize the behaviour of nucleic acid containing nanogels in blood [27]. Measuring the concentration of nanogels in both plasma and blood allowed to estimate the fraction of nanogels that

are not bound to cells. The method has potential applications in diagnostics too, since not only the size distribution, but also the concentration of certain types of cell-derived membrane vesicles is believed to be a biomarker for specific diseases.

3.4 CONCLUSION

SPT allows to investigate the properties of nanoparticles directly inside biomaterials by determining their trajectories. Unlike FRAP, which is an ensemble average technique, the mobility of each individual nanoparticle is analyzed in SPT, yielding highly precise and accurate results. SPT is also versatile in the sense that not only the type of motion, but also properties like concentration, size, and interaction can be derived from the trajectories. In the field of drug delivery, this information can strongly aid the systematic optimization of nanoparticles that should be able to protect, transport and deliver therapeutic macromolecules to target cells. Detection of the size and concentration of nanoparticles inside biomaterials is also of great interest for diagnostic assays based on nanoparticulate biomarkers. SPT is thus a powerful fluorescence microscopy technique with many potential applications in pharmaceutical research.

In order to realize this potential, several aspects of SPT experiments and data analysis still need optimization. One important issue is the experimental uncertainty with which the nanoparticle positions are determined, this is discussed in **Chapter 4 and 5**. An even more fundamental issue that limits the accuracy of SPT data analysis is the contrast with which the nanoparticles are visible, this is the topic of **Chapter 7**.

REFERENCES

1. K. Remaut, N. N. Sanders, B. G. De Geest, K. Braeckmans, J. Demeester, and S. C. De Smedt, "Nucleic acid delivery: Where material sciences and bio-sciences meet," *Materials Science & Engineering R-Reports* **58**, 117-161 (2007).
2. C. D'Souza-Schorey and J. W. Clancy, "Tumor-derived microvesicles: shedding light on novel microenvironment modulators and prospective cancer biomarkers," *Genes & Development* **26**, 1287-1299 (2012).
3. E. van der Pol, A. N. Boing, P. Harrison, A. Sturk, and R. Nieuwland, "Classification, Functions, and Clinical Relevance of Extracellular Vesicles," *Pharmacological Reviews* **64**, 676-705 (2012).
4. C. A. Ross and M. A. Poirier, "Protein aggregation and neurodegenerative disease," *Nature Medicine* **10**, S10-S17 (2004).
5. K. Braeckmans, K. Buyens, B. Naeye, D. Vercauteren, H. Deschout, K. Raemdonck, K. Remaut, N. N. Sanders, J. Demeester, and S. C. De Smedt, "Advanced fluorescence microscopy methods illuminate the transfection pathway of nucleic acid nanoparticles," *Journal of Controlled Release* **148**, 69-74 (2010).
6. S. C. De Smedt, K. Remaut, B. Lucas, K. Braeckmans, N. N. Sanders, and J. Demeester, "Studying biophysical barriers to DNA delivery by advanced light microscopy," *Advanced Drug Delivery Reviews* **57**, 191-210 (2005).
7. L. M. Ensign, C. Schneider, J. S. Suk, R. Cone, and J. Hanes, "Mucus Penetrating Nanoparticles: Biophysical Tool and Method of Drug and Gene Delivery," *Advanced Materials* **24**, 3887-3894 (2012).
8. M. J. Saxton and K. Jacobson, "Single-particle tracking: Applications to membrane dynamics," *Annual Review of Biophysics and Biomolecular Structure* **26**, 373-399 (1997).
9. K. Braeckmans, K. Buyens, W. Bouquet, C. Vervaet, P. Joye, F. De Vos, L. Plawinski, L. Doeuve, E. ngles-Cano, N. N. Sanders, J. Demeester, and S. C. De Smedt, "Sizing Nanomatter in Biological Fluids by Fluorescence Single Particle Tracking," *Nano Letters* **10**, 4435-4442 (2010).
10. I. Koyama-Honda, K. Ritchie, T. Fujiwara, R. Iino, H. Murakoshi, R. S. Kasai, and A. Kusumi, "Fluorescence imaging for monitoring the colocalization of two single molecules in living cells," *Biophysical Journal* **88**, 2126-2136 (2005).
11. M. Roding, H. Deschout, K. Braeckmans, and M. Rudemo, "Measuring absolute number concentrations of nanoparticles using single-particle tracking," *Physical Review e* **84**, (2011).
12. M. J. Saxton and K. Jacobson, "Single-particle tracking: Applications to membrane dynamics," *Annual Review of Biophysics and Biomolecular Structure* **26**, 373-399 (1997).
13. V. Levi and E. Gratton, "Exploring dynamics in living cells by tracking single particles," *Cell Biochemistry and Biophysics* **48**, 1-15 (2007).
14. J. Suh, M. Dawson, and J. Hanes, "Real-time multiple-particle tracking: applications to drug and gene delivery," *Advanced Drug Delivery Reviews* **57**, 63-78 (2005).
15. K. Forier, Messiaen A.S., Raemdonck K., Deschout H., Rejman J., De Baets F., Nelis H., De Smedt S.C., Demeester J., Coenye T., and Braeckmans K., "Transport of nanoparticles in cystic fibrosis sputum and bacterial biofilms by single-particle tracking microscopy," *Nanomedicine* (2012).

16. J. S. Suk, S. K. Lai, Y. Y. Wang, L. M. Ensign, P. L. Zeitlin, M. P. Boyle, and J. Hanes, "The penetration of fresh undiluted sputum expectorated by cystic fibrosis patients by non-adhesive polymer nanoparticles," *Biomaterials* **30**, 2591-2597 (2009).
17. Y. Y. Wang, S. K. Lai, J. S. Suk, A. Pace, R. Cone, and J. Hanes, "Addressing the PEG Mucoadhesivity Paradox to Engineer Nanoparticles that "Slip" through the Human Mucus Barrier," *Angewandte Chemie-International Edition* **47**, 9726-9729 (2008).
18. T. F. Martens, D. Vercauteren, K. Forier, H. Deschout, K. Remaut, R. Paesen, M. Ameloot, J. F. Engbersen, J. Demeester, S. C. De Smedt, and K. Braeckmans, "Measuring the intravitreal mobility of nanomedicines with single-particle tracking microscopy," *Nanomedicine* (2013).
19. Q. Xu, N. Boylan, J. S. Suk, Y. Wang, E. Nance, J. Yang, P. McDonnell, R. Cone, E. J. Duh, and J. Hanes, "Nanoparticle diffusion in, and microrheology of, the bovine vitreous ex vivo," *Journal of Controlled Release* (2013).
20. R. Bausinger, K. von Gersdorff, K. Braeckmans, M. Ogris, E. Wagner, C. Brauchle, and A. Zumbusch, "The transport of nanosized gene carriers unraveled by live-cell imaging," *Angewandte Chemie-International Edition* **45**, 1568-1572 (2006).
21. K. de Bruin, N. Ruthardt, K. von Gersdorff, R. Bausinger, E. Wagner, M. Ogris, and C. Brauchle, "Cellular dynamics of EGF receptor-targeted synthetic viruses," *Molecular Therapy* **15**, 1297-1305 (2007).
22. A. M. Sauer, K. G. de Bruin, N. Ruthardt, O. Mykhaylyk, C. Plank, and C. Brauchle, "Dynamics of magnetic lipoplexes studied by single particle tracking in living cells," *Journal of Controlled Release* **137**, 136-145 (2009).
23. V. Filipe, R. Poole, M. Kutscher, K. Forier, K. Braeckmans, and W. Jiskoot, "Fluorescence Single Particle Tracking for the Characterization of Submicron Protein Aggregates in Biological Fluids and Complex Formulations," *Pharmaceutical Research* **28**, 1112-1120 (2011).
24. V. Filipe, R. Poole, O. Oladunjoye, K. Braeckmans, and W. Jiskoot, "Detection and Characterization of Subvisible Aggregates of Monoclonal IgG in Serum," *Pharmaceutical Research* **29**, 2202-2212 (2012).
25. P. D. Dunne, R. A. Fernandes, J. McColl, J. W. Yoon, J. R. James, S. J. Davis, and D. Klenerman, "DySCo: Quantitating Associations of Membrane Proteins Using Two-Color Single-Molecule Tracking," *Biophysical Journal* **97**, L5-L7 (2009).
26. D. Vercauteren, H. Deschout, K. Remaut, J. F. J. Engbersen, A. T. Jones, J. Demeester, S. C. De Smedt, and K. Braeckmans, "Dynamic Colocalization Microscopy To Characterize Intracellular Trafficking of Nanomedicines," *Acs Nano* **5**, 7874-7884 (2011).
27. B. Naeye, H. Deschout, M. Roding, M. Rudemo, J. Delanghe, K. Devreese, J. Demeester, K. Braeckmans, S. C. De Smedt, and K. Raemdonck, "Hemocompatibility of siRNA loaded dextran nanogels," *Biomaterials* **32**, 9120-9127 (2011).

Chapter 4

Precisely and accurately localizing single molecules in fluorescence microscopy: state-of-the-art and best practice

This chapter is in preparation for publication:

Hendrik Deschout^{1,2}, Francesca Cella Zanacchi^{3,4}, Alberto Diaspro^{3,4}, Joerg Bewersdorf⁵, Samuel T. Hess⁶, Kevin Braeckmans^{1,2}.

¹Laboratory for General Biochemistry and Physical Pharmacy, Ghent University, Belgium

²Centre for Nano- and Biophotonics, Ghent University, Belgium

³Department of Nanophysics, Istituto Italiano di Tecnologia, Italy

⁴Department of Physics, Università degli Studi di Genova, Italy

⁵Department of Cell Biology and Department of Biomedical Engineering, Yale University School of Medicine, USA

⁶Department of Physics and Astronomy, University of Maine, USA

ABSTRACT

For decades, scientists have yearned for better resolution in light microscopy. Recently, methods based on single molecule localization and photophysics have brought into reach nanoscale imaging with visible light. On the one hand this has enabled single particle tracking applications for studying the dynamics of molecules and nanoparticles, as discussed in **Chapter 3**. On the other hand it has led to the recent revolution in super-resolution localization microscopy techniques. Crucial to the optimization of such methods are the precision and accuracy with which single fluorophores and nanoparticles can be localized. While previous reports address aspects of determining and optimizing the localization precision and accuracy, the aim of **Chapter 4** is to present a lucid synthesis of these developments and their practical implications, in order to guide the increasing number of researchers using single particle tracking and super-resolution localization microscopy.

4.1 INTRODUCTION

One of the major quests in fluorescence microscopy is to image specimens with the highest detail possible. The amount of detail that can be resolved by a conventional light microscope is, however, fundamentally limited by the diffraction of light. Even an infinitely small point source of light is still imaged as a spot of finite volume, known as the point spread function (PSF). Consequently, the PSFs of two point sources that are closer together than the PSF width will show significant overlap, making it difficult or impossible to distinguish them from one another. Based on the pioneering work by Abbe [1] and Rayleigh [2], the resolution in the focal plane is often approximated as $0.5 \lambda / \text{NA}$, with λ being the wavelength of light and NA the numerical aperture of the microscope objective lens. The attainable resolution is thus fundamentally limited to around 200 nm for visible light ($\lambda = 550$ nm) using a high-NA objective lens ($\text{NA} = 1.4$). However, when it comes to determining the location of a single, isolated sub-resolution particle, such as a single fluorophore, this limit is less important as the isolated spot of light coming from this particle does not need to be distinguished from any other structure in the vicinity. While the spot shape is related to the PSF, the particle's location can be determined with a precision and accuracy (cfr. **Section 4.2**) usually much smaller than the PSF width, even down to the nanometer scale, as illustrated in **Fig. 4.1**.

Although this intuitive concept has been known for a long time [3,4], it was not before the 1980s that sub-resolution localization of fluorescent particles was put into practice, when light detectors became sensitive enough. It was first applied in a technique called single particle tracking (SPT) or single molecule tracking. SPT was initially mostly used to investigate the motion of fluorescently labeled proteins on the cell membrane [5], but was later on extended to many other applications, such as rheology [6], imaging of intracellular dynamics [7] and particle sizing [8], to name just a few. Not before long it was realized that knowledge of the precision with which the position of a single fluorescent particle can be estimated, is of vital importance for correct analysis of the particle trajectories, e.g. for the determination of the diffusion coefficient from Brownian motion trajectories [9]. By now, SPT has become a mature and widely used technique [10,11], so that correctly assessing the localization precision and accuracy is an important topical issue.

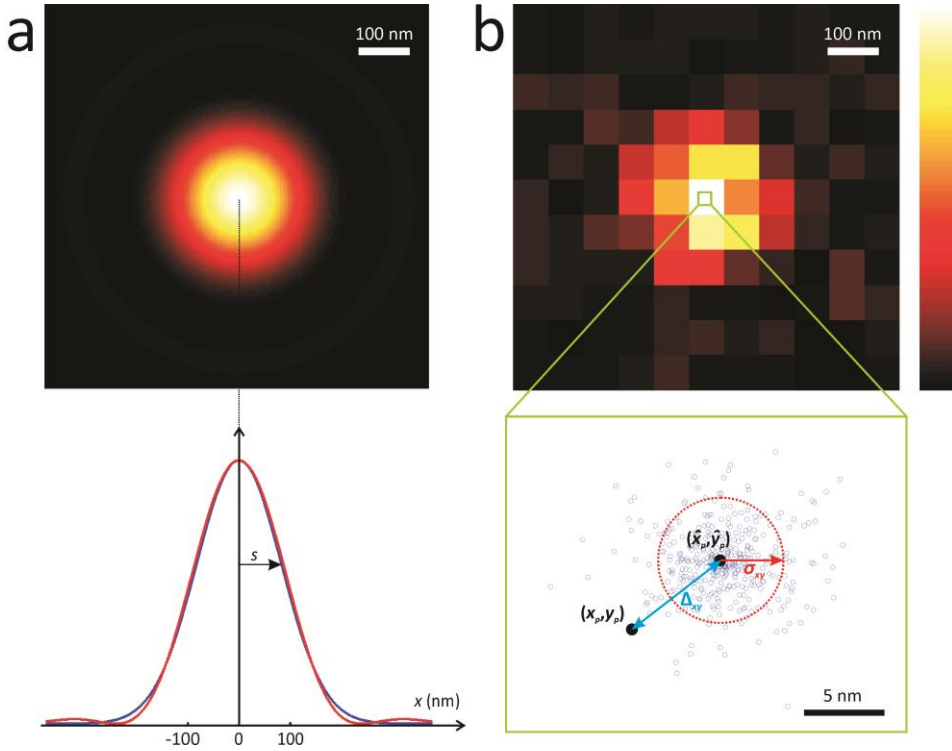


Figure 4.1 | The concept of localization precision and accuracy. (a) The particle position is encoded in the image shape. In case of an isotropic emitter in the focal plane, the image can be described by the Airy pattern (red curve). The Airy pattern can be approximated by a two-dimensional Gaussian function (blue curve) with standard deviation s . (b) An example of an experimentally recorded image of an isotropic emitter in the focal plane. The real particle position (x_p, y_p) can be estimated from such an image with a lateral localization precision $\sigma_{xy} = \sqrt{\sigma_x^2 + \sigma_y^2}$ and a lateral localization accuracy $\Delta_{xy} = \sqrt{\Delta_x^2 + \Delta_y^2}$. The blue circles denote experimentally determined position estimates from different images, and (\hat{x}_p, \hat{y}_p) is the average of these individual values.

The interest in localization precision and accuracy has recently increased considerably due to the development of super-resolution localization microscopy (LM) techniques, such as photo-activated localization microscopy (PALM) [12], fluorescence photoactivation localization microscopy (FPALM) [13] and stochastic optical reconstruction microscopy (STORM) [14]. Key to LM is the consecutive on- and off-switching of fluorophores within a spectral detection window [15]. The imaging procedure starts with the fluorophores in an off (dark) state, either by using fluorescent proteins which are natively expressed in a dark state [12,13], or by using fluorophores which are converted into a dark state by a suitable illumination procedure [14]. Next, a

random but sparse subset of fluorophores is activated by illuminating the sample with suitable wavelength and intensity. This subset is then imaged by either a different read-out wavelength or, in special cases, by the same wavelength resulting in a fluorescence image with spatially separated images of each fluorophore (i.e. diffraction limited spots of light). This allows the position of the activated fluorophores to be determined with a precision and accuracy smaller than the resolution. By repeating the off/on cycle many times, the position of many or all fluorophores in the sample can be determined and a super-resolution image can be constructed from their estimated positions. The effective achievable resolution is therefore closely related to the localization precision and accuracy, making it indispensable to have a clear understanding of how these parameters can be quantified and optimized (cfr. **Section 4.6.1**). The desire to improve resolution is a motivation for the LM field, and consideration of the issues detailed in this review will help users get the best resolution possible for their experiments.

4.2 LOCALIZATION PRECISION AND ACCURACY

The position coordinates (x_p, y_p, z_p) of an isolated fluorescent particle can be estimated from a microscopy image with a limited certainty that comprises both a precision and an accuracy, as illustrated in **Fig. 4.1b**. The localization precision σ_x on the coordinate x_p can be determined from the standard deviation of a sufficiently large amount of estimated positions $x_{p,i}$:

$$\sigma_x = \sqrt{\frac{1}{n-1} \sum_{i=1}^n (x_{p,i} - \hat{x}_p)^2}, \quad (4.1)$$

where n is the number of estimates, and \hat{x}_p the mean of the estimated positions:

$$\hat{x}_p = \frac{1}{n} \sum_{i=1}^n x_{p,i}. \quad (4.2)$$

Similar expressions for the localization precision σ_y and σ_z hold for the position coordinates y_p and z_p , respectively. The localization precision is essentially determined by the photons that make up the image. On the one hand, the number of photons arriving in a certain time interval follows a Poisson distribution, the standard deviation of which is known as shot noise. On the other hand, the photon positions have a spatial

distribution that is dictated by the emission profile of the particle in combination with light diffraction in the microscope (cfr. **Section 4.3**). Experimental factors, such as detector and sample properties, further influence the localization precision (cfr. **Section 4.4**). The best localization precision theoretically achievable is given by the square root of the Cramér-Rao lower bound (CRLB), which is defined as the smallest possible variance any unbiased estimation algorithm can have [16,17]. For an isotropic emitter in or close to the focal plane, the particle image is often approximated by a two-dimensional Gaussian function [18], see **Fig. 4.1a**. Considering only shot noise, the limit on the lateral localization precision in this simple case is given by [19,20]:

$$\sigma_x \geq \frac{s}{\sqrt{N}} \text{ and } \sigma_y \geq \frac{s}{\sqrt{N}} \quad (4.3)$$

with N being the total number of detected photons and s the standard deviation of the Gaussian function. Besides shot noise, detector properties such as pixelation and read-out noise can be included in the CRLB [19]. The limit on the axial and lateral localization precision outside the focal plane cannot be described by a simple analytical expression, since 3-D models of the particle image are significantly more complex (cfr. **Section 4.3.2**).

If the algorithm that is used for the estimation of x_p is unbiased, the mean of its estimates approaches the true particle position with an increasing number of estimates n , i.e. $\hat{x}_p = x_p$. However, when the algorithm is biased, the mean \hat{x}_p predicts the wrong position. Such an algorithm is called inaccurate, with a non-zero localization accuracy Δ_x on the x -coordinate given by:

$$\Delta_x = \hat{x}_p - x_p. \quad (4.4)$$

Similar expressions of the localization accuracy Δ_y and Δ_z hold for the position coordinates y_p and z_p , respectively. Since the localization accuracy does not involve individual measurements $x_{p,i}$, it is not sensitive to shot noise. However, the other factors that influence the localization precision, i.e. the spatial distribution of the photons in the image and the properties of the detector and sample, can in principle also affect the localization accuracy. However, unlike the case of the localization precision, there is no fundamental limit on the achievable localization accuracy.

4.3. EMITTER PROPERTIES INFLUENCING PRECISION AND ACCURACY

The location of single emitters can be determined from microscopy images using a specific algorithm, referred to as the position estimator. Examples of such estimators are fitting of a Gaussian function to the observed particle image or calculating its centre-of-mass [21]. Perfect localization accuracy can be achieved if the position estimator is unbiased (cfr. **Section 4.2**). The localization precision, on the other hand, can never be perfect as it is fundamentally limited by the Cramér-Rao lower bound (CRLB) (cfr. **Section 4.2**). The localization precision and accuracy theories of commonly used position estimators for the different situations that can be encountered in SPT or LM are summarized in **Table 4.1**.

4.3.1 Isotropic emitters in focus

Arguably the most frequently used position estimator, especially in the context of LM, is Gaussian fitting, either by least-squares or maximum likelihood procedures. The underlying assumption is that the particle image can be regarded as a two-dimensional Gaussian function, which is reasonable for an isotropic emitter in or close to the focal plane [18]. If these conditions are fulfilled, this position estimator is unbiased.

In terms of precision, the maximum likelihood procedure has been shown to be the best choice, since it approaches the CRLB [22]. Despite this fact, weighted least-squares fitting has historically been more popular [20,21,23,24]. Although this procedure theoretically can attain the same precision as maximum likelihood, it suffers from practical problems with the weights approaching zero at the edge of the particle image [22]. The unweighted least-squares fitting, also known as the Gaussian mask, does not have this problem, at the expense of a lower precision. For example, it has been shown that in the absence of background fluorescence the precision is 33% worse than in the case of maximum likelihood [20,22].

Besides fitting procedures there also exist a variety of algebraic estimators. The centre-of-mass algorithm is a well-known algebraic estimator, whose localization precision [25] and accuracy [26] has already been studied extensively in other contexts than SPT and LM. The centre-of-mass algorithm is computationally faster than Gaussian fitting [27], but has a reduced precision [21]. Note that other algebraic estimators have been developed with better precision than the centre-of-mass, e.g. an estimator based on the radial symmetry of the particle image [28]. Localization inaccuracy, typically arising

from detector pixelation or sample background, can also be a problem for the centre-of-mass (cfr. **Section 4.4**), although unbiased adaptations have been reported [26,29]. On the other hand, significant efforts have been undertaken to speed up the maximum likelihood estimation of the Gaussian function while retaining its precision [30].

4.3.2 3-D localization of isotropic emitters

If an isotropic emitter is located at a distance of a few hundred nanometers from the focal plane, the Gaussian approximation still holds, but with a standard deviation that increases with the axial position. On one hand this means that the lateral localization precision decreases with increasing out of focus distance (see Eq. (4.3)). On the other hand this has the advantage that the axial position can be estimated by fitting a Gaussian function with variable standard deviation, although with a significantly lower precision than for the lateral position [31,32]. For an isotropic emitter further out of focus, the image can exhibit a distinct pattern of diffraction rings that are unique to each axial position, as illustrated in **Fig. 4.2a**. Avoiding axial localization inaccuracies in this case requires more elaborate 3-D scalar [33,34] or vectorial [35-37] PSF models. Maximum likelihood estimation of a scalar PSF model [34] has been used to determine the axial position, with a precision close to the CRLB [38]. As apparent from **Table 4.1**, estimator-specific precision theories are challenging to derive in the case of complicated image models, and instead the performance is usually compared to the CRLB.

A common aspect in any of these approaches is that the axial position is indirectly determined from the lateral shape of the particle image. This leads to especially poor axial localization precision for particles far out of focus or close to the focal plane, where the signal is distributed over a large area or the change in shape is minimal, respectively. Additionally, for axially symmetric PSFs, it cannot be inferred from the lateral shape if the emitter is below or above the focal plane. A recently developed technique, called multifocal plane or biplane microscopy, overcomes these problems by simultaneously imaging different focal planes in the sample [39-41]. Comparing images simultaneously acquired in multiple focal planes allows to determine the axial position unambiguously over several microns and results in a fairly constant localization precision in all three directions [42,43], close to the CRLB [44]. Other recently reported techniques that achieve an almost isotropic 3-D nanometer precision make use of a side view in addition to the normal front image [45,46].

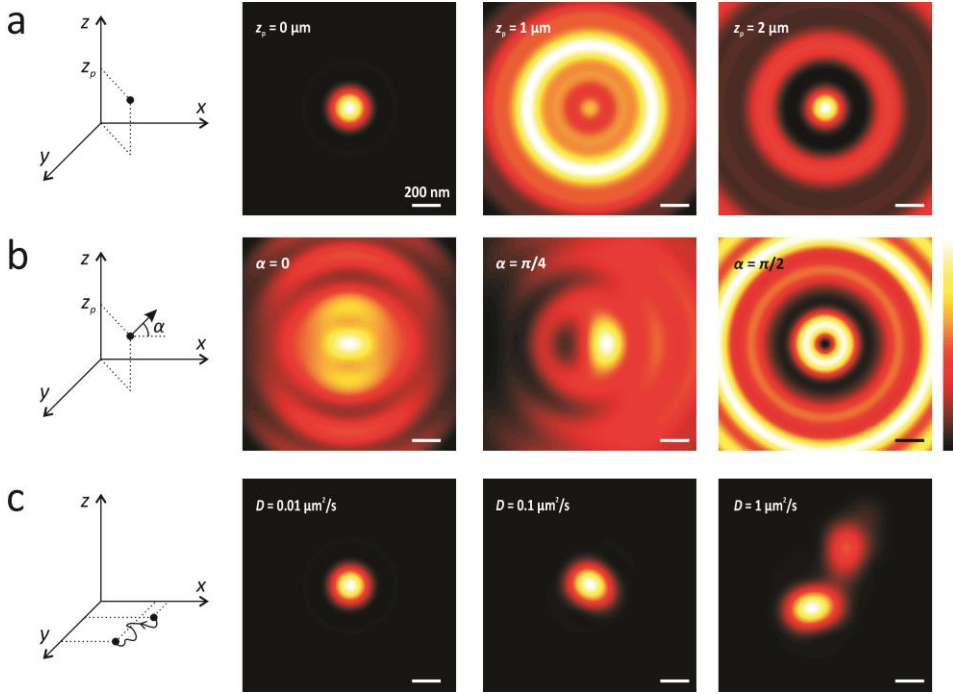


Figure 4.2 | Emitter properties that influence the localization precision and accuracy. Visible light ($\lambda = 550 \text{ nm}$) and a high-NA objective lens ($\text{NA} = 1.4$) are assumed. **(a)** The image of an isotropic emitter at different axial positions z_p . Outside the focal plane $z = 0$, the image features distinct diffraction rings. **(b)** The image of a dipole emitter at $z_p = 1 \mu\text{m}$. Different dipole angles α with the x -axis result in different types of asymmetric images. **(c)** Particle movement in the focal plane $z = 0$, e.g. Brownian motion with diffusion coefficient D over an image acquisition time of 100 ms, distorts the image. All images are normalized to their maximum values.

In an alternative approach, optical elements added to the microscope induce an axially dependent deformation of the PSF so that the shape of a single lateral image unambiguously encodes the axial position of the emitter. In one embodiment a cylindrical lens is introduced, leading to an astigmatic elliptical particle image with changing ellipticity and orientation depending on the axial position [47,48]. This has been shown to result in a precision similar to the multifocal plane approach, although less isotropic in 3-D [42,49]. In another embodiment, a PSF consisting of two lobes whose relative distance depends on the axial position of the emitter is engineered by adding a prism over half the emission path, resulting in comparable precision to the astigmatic case [50,51]. In a similar technique, called parallax, this is done by two closely spaced parallel mirrors [52]. Alternatively, a spatial light modulator has been used to engineer a single-helix PSF [53] or double-helix PSF [54,55], resulting in a 3-D

localization precision that is largely independent of the axial position over a range of several microns [49,56,57] and generally outperforms the astigmatism or multifocal plane methods [49,58]. A recently developed technique that provides superior axial precision, even down to nanometers, is based on the self-interference of the light emitted by a particle and collected by two opposing objectives [43,59,60].

4.3.3 Localization of dipole emitters

A single fluorophore does not emit light in an isotropic fashion, but rather behaves as an electric dipole [61]. This means that the assumption of an isotropic emitter in focus does not necessarily hold for a single fluorophore image, as illustrated in **Fig. 4.2b**. This has important repercussions for the localization precision and accuracy, a fact that is increasingly being appreciated in the field of LM [62].

For a stationary fluorophore, e.g. by being linked to a stationary structure, the dipole can have a fixed orientation. Depending on the orientation, the fluorophore image usually exhibits a significant amount of asymmetry, with a shift in the intensity peak with respect to its actual position. This asymmetry becomes more pronounced further out of focus, in case of $NA = 1.4$ even leading to a lateral bias up to 100 nm for the centre-of-mass algorithm [63]. This bias is significantly reduced for lower values of the NA [62,64]. Although fitting of a Gaussian function can still achieve a good precision close to the CRLB [22], a lateral bias of tens of nanometers can be introduced [62,64]. This can only be avoided by fitting of an image model that takes the dipole orientation into account [22,65]. However, this approach is only valid if the amount of defocus is known, since different combinations of dipole orientation and defocus can result in similar images. Methods that do not suffer from this drawback have recently been reported, making use of polarization optics to measure the dipole orientation [66]. This approach can be combined with the double-helix PSF (cfr. **Section 4.3.2**) which allows to determine the 3-D position of the dipole emitter [67].

If the dipole emitter exhibits sufficiently fast rotation relative to the image acquisition time, the resulting image can be described as coming from a superposition of randomly oriented fixed dipoles, giving rise to a symmetric image [64]. It has been shown that maximum likelihood estimation of the exact superposition vectorial model results in unbiased estimation with a precision approaching the CRLB [22]. Interestingly, a similar precision was obtained with maximum likelihood estimation using the simpler Gaussian function [22,64].

Emitter	Sample	Detector	Position estimator	Localization theory	References
Isotropic emitter in focus	Homogeneous background fluorescence	Pixelation & excess noise	MLE of 2-D Gauss	σ_{xy}	Eq. (5) in [22]
			WLS of 2-D Gauss	σ_{xy}	Eq. (5)in [22]
			ULS of 2-D Gauss	σ_{xy}	Eq. (6) in [22]
		Pixelation & read-out noise	CM	σ_{xy}	Eq. (17) in [25]
			CM	Δ_{xy}	Eq. (6) in [29]
			Unspecified	CRLB on σ_{xy}	[19]
	Not accounted for	Pixelation & excess + read-out noise	Unspecified	CRLB on σ_{xy}	[72]
		Pixelation	CM	Δ_{xy}	Eq. (12) in [26]
Isotropic emitter in 3-D	Homogeneous background fluorescence	Pixelation & read-out noise	WLS of 2-D Gauss	σ_z	Eq. (5) in [31]
			MLE of vector model	CRLB on σ_{xy} and σ_z (AS, BP, IF)	[43]
			ULS of scalar model	CRLB on σ_{xy} and σ_z (BP)	[44]
		Pixelation	Unspecified	CRLB on σ_{xy} and σ_z (DH, AS, BP)	[49]
	Not accounted for	Pixelation	MLE of scalar model	CRLB on σ_z	[38]
			Unspecified	CRLB on σ_{xy} and σ_z (DH, AS, BP)	[58]
			CM based estimation	CRLB on σ_{xy} and σ_z (DH)	[54]
	Dipole emitter	Homogeneous background fluorescence	Pixelation & excess noise	MLE of vector model	CRLB on σ_{xy}
Pixelation			ULS of vector model	CRLB on σ_{xy}	[65]
			MLE of scalar model	CRLB on σ_{xy} (PL)	[66]
			ULS based estimation	CRLB on σ_{xy} and σ_z (DH and PL)	[67]
Motion during image acquisition	Homogeneous background fluorescence	Pixelation & excess noise	CM	σ_{xy} (diffusion)	Eq. (12) in [71]
		Pixelation & read-out noise	Unspecified	CRLB on σ_{xy} (linear and circular motion)	[70]

Table 4.1 | Localization precision and accuracy theories. A non-exhaustive list of theoretical investigations of the lateral or axial localization precision (σ_{xy} or σ_z), and the lateral localization accuracy (Δ_{xy}). Each theory makes assumptions on the emitter, sample, and detector, and is applicable for a certain position estimator, such as the centre-of-mass (CM), unweighted or weighted least-squares (ULS or WLS), or maximum likelihood estimation (MLE). While expressions for the localization precision of simple estimators have been derived, for complicated estimators the performance is usually compared to the Cramér-Rao lower bound (CRLB). Some theories assume a non-conventional microscope set-up: double-helix PSF (DH), astigmatic imaging (AS), biplane microscopy (BP), self-interference (IF), or polarization imaging (PL).

In SPT often the mobility of a nanoparticle or macromolecule having several fluorophores attached to it is studied. If such an emitter is stationary, the ensemble of fluorophores can be considered as a superposition of fixed but randomly oriented dipoles. Using widefield illumination, the image is symmetric and fitting of the Gaussian function remains an unbiased estimator. However, care should be taken when using total internal reflection (TIRF) illumination in which case the electric field does not have a random orientation, thus resulting in an asymmetric image and making the Gaussian estimator inaccurate. However, the bias will be identical for all fluorescent particles in the field of view [22], so the position estimates are unbiased relative to each other and trajectory analysis remains possible. The determination of molecular trajectories is also gaining interest in LM [68]. In this case, bias due to molecular dipole orientation can be important if the fluorophore is unable to freely rotate within the acquisition time per camera frame.

4.3.4 Motion during image acquisition

Translational particle movement during image acquisition is common in SPT experiments and can cause a significant deformation of the observed particle image, as illustrated in **Fig. 4.2c** for Brownian motion. This in turn influences the localization precision and accuracy. The effect of linear and circular motion on the CRLB has been investigated [69,70], which is of relevance for sample drift (cfr. **Section 4.4.2**). However, particle motion at the microscopic scale more commonly exhibits a stochastic component. In **Chapter 5**, it will be shown that numerical fitting of a Gaussian function becomes inaccurate and imprecise in the case of significant diffusion during the image acquisition time. Instead, the centre-of-mass algorithm is affected to a much lesser extent as it does not depend on a particular shape of the particle image [71].

4.4. EXPERIMENTAL FACTORS INFLUENCING PRECISION AND ACCURACY

In any SPT or LM experiment, an emitter is located inside a sample and a detector is used to record the image. Besides the shape of the image (cfr. **Section 4.3**), many properties of the detector and the sample can also affect the precision and accuracy with which the emitter is localized. **Table 4.1** summarizes the localization precision and accuracy theories for different sample and detector properties typically encountered in SPT or LM.

4.4.1 Detector

Detector pixelation

Detector pixelation limits the achievable localization precision since the location at which the individual photons arrive within the pixel area is unknown. Larger pixel sizes thus result in a reduced localization precision, as accounted for in most localization theories listed in **Table 4.1**. However, smaller pixel sizes might cause several detector noise sources to overwhelm the reduced amount of detected photons per pixel (see below). Usually, the pixel size is selected so that the width of the PSF is 2-3× larger, according to the Nyquist criterion. Besides generally affecting the localization precision, detector pixelation also adds a lateral bias to position estimates obtained with the centre-of-mass algorithm [26,29].

Detector noise

The classic detector in LM and SPT is the charge coupled device (CCD) in which thermally induced dark current introduces a Poisson distributed background that increases with the image acquisition time [73]. Also the electron multiplying charge coupled device (EMCCD) and scientific complementary metal oxide semiconductor (sCMOS) detector suffer from dark current. However, modern detectors are cooled in order to reduce the amount of dark current, rendering it effectively insignificant during the short exposure times that are typical for SPT and LM applications.

The CCD detector features read-out noise, originating from the conversion of the electrons in each pixel to a digital signal. As this noise follows a Gaussian distribution independent of the pixel intensity, it degrades the localization precision [19,69], especially for low light levels. Read-out noise is usually not included in precision theories, arguably because the EMCCD has replaced the CCD in recent years. The on-chip electron-multiplication process renders the read-out noise effectively negligible and thus is not an issue for EMCCD detectors. The increasingly popular sCMOS also features low read-out noise. Its localization precision performance was found to be competitive with EMCCD for relatively high light levels, but performs worse for low light levels [74,75].

However, the electron-multiplication process in EMCCDs is a stochastic process that adds so-called excess noise to the pixel intensities. It has been shown that in case of

high multiplication levels (e.g. 10^3) the pixel electrons remain Poisson distributed after multiplication, but with twice the variance [76,77]. This, in turn, decreases the localization precision by a factor of $\sqrt{2}$ [22,72,76], although it was argued recently that low light levels or low electron multiplication values require a more complex treatment [72].

Detector background

Non-uniform sensitivity of the pixels over the detector area was recently reported to affect the localization accuracy [78]. The so-called photoresponse non-uniformity is caused by differences in the conversion of photons to electrons between pixels or even within the same pixel, leading to a non-uniform image even when all pixels are illuminated uniformly. This can lead to localization inaccuracies, on the order of nanometers, especially when the non-uniformities have the same scale as the width of the particle image. This bias can be corrected for by mapping the photoresponse non-uniformity in detail, e.g. by recording the image of an illuminated pinhole that is scanned across the pixels with sub-pixel step size [78].

Another type of detector background is called the pedestal, it is a constant offset value that is added to the pixel intensities of a detector. The pedestal has no effect on accuracy, but can reduce the localization precision for estimators such as the weighted least-squares fitting [22].

4.4.2 Sample

Sample drift

Drift of the sample negatively affects the localization precision in a way that is similar to particle motion during image acquisition (cfr. **Section 4.4.3**). Drift on the nanometer scale is hard to avoid as it can be caused by a variety of sources, such as vibration and mechanical relaxation of the microscope or motion within the sample. One often reported drift correction approach is to relate all position estimates to the position of a fiduciary marker that is embedded in the sample [12,14] or attached to the cover slip [79,80]. To maintain a good precision of the location estimates, this fiduciary marker should be bright enough so that its location can be determined with near perfect

precision. However, if this bright structure is located too close to the particle of interest, it will add to its background, again reducing the localization precision. On the other hand, if the marker is too far off, it might not represent the local drift sufficiently well. Alternative techniques for drift correction are the use of spatial correlation between subsequent super-resolution images [48,81,82] or the use of structures of the sample itself (e.g. intracellular structures that are imaged separately but simultaneously with transmitted light) as fiduciary markers.

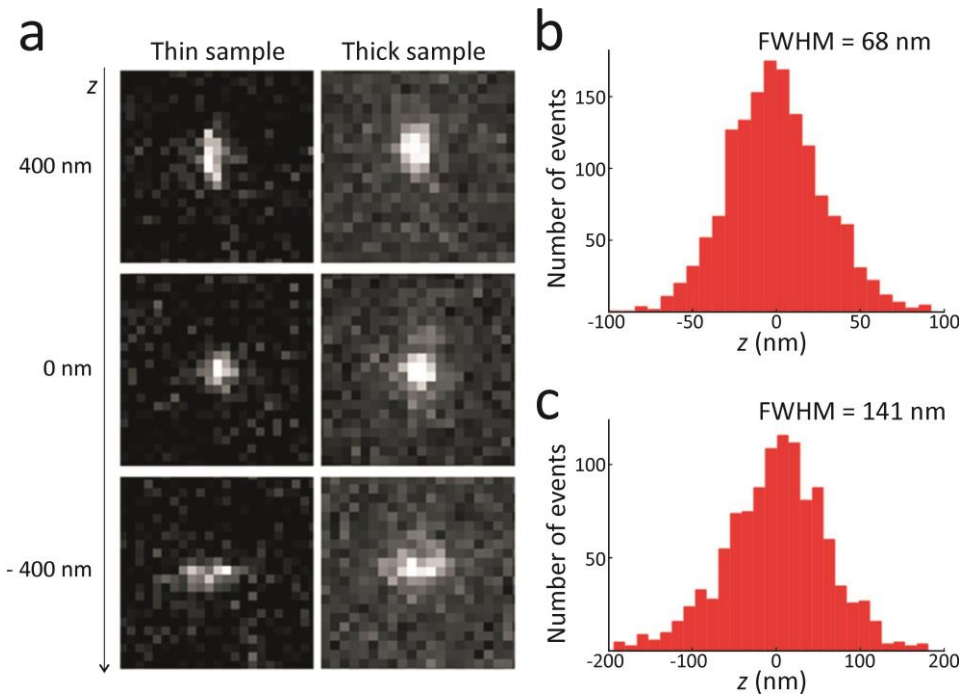


Figure 4.3 | The effect of sample background on the localization precision. (a) Fluorescent sub-resolved objects are localized at different axial depths by means of an astigmatic PSF in a transparent agarose gel (thin sample) and in a 100 μm cellular spheroid (thick sample). Direct estimation of the effective axial localization precision within the cellular spheroid by repeated measurements of sub-resolved point-like objects (cfr. **Section 4.5**) shows a decrease of the localization precision in thicker samples. (b) The experimental localization precision in the agarose gel is 68 nm. (c) The experimental localization deep within the cellular spheroid it is reduced to 141 nm.

Sample background

Sample background fluorescence can significantly reduce the precision, and, for estimators like the centre-of-mass algorithm, also the accuracy [29]. This is especially the case when the particles are located deep inside thick biological samples. For example, the extra background inside cellular spheroids of 100 μm diameter has been shown to lead to a decrease in precision by a factor of two compared to the ideal situation without background [83], as illustrated in **Fig. 4.3**. Homogeneous background fluorescence is often incorporated in the precision and accuracy theories, as indicated in **Table 4.1**. It takes the form of a Poisson distributed background, and is thus equivalent to dark current (cfr. **Section 4.4.1**). In some samples, especially thick ones, the background fluorescence can be heterogeneous, thus also affecting the localization accuracy with a bias of up to tens of nanometers. Although image processing procedures can be used to filter out background heterogeneity to some extent, a complete correction is difficult to achieve.

PSF deformation

The PSF can become deformed because of refractive index variations in the sample, light scattering or absorption by the sample, and refractive index mismatch between sample, embedding medium and cover slip. This results in a deformation of the particle image that becomes more pronounced when focusing deeper into the sample. Position estimators that are based on a particular model of the particle image will no longer perform as intended. In that case, unbiased position estimations can only be achieved by fitting of an experimentally determined particle image model [80,84-86]. These experimental particle reference images are usually obtained from an independently recorded z-stack of a fluorescent non-blinking particle, such as a fluorescent bead. Possible differences in photobleaching [39,42], refractive index mismatch [48,87], or dipole orientation [87] between the actual image and the calibration stack need to be corrected for. Recently, an interesting possibility for at least partially mitigating these complications has been reported which infers an image model is derived from only a couple of experimental images at different z-positions using a phase retrieval algorithm [88].

4.5 MEASURING THE LOCALIZATION PRECISION

Localization theories, as summarized in **Table 4.1**, are often based on simplifying assumptions. Therefore, if at all possible, it is preferable to determine the localization precision experimentally. For stationary molecules (i.e. without translational movement), as it is often the case in LM, this can be done by acquiring a series of images of a sparse set of molecules. By determining the location of the same molecule in subsequent images, the standard deviation on the molecule localization can be determined, which is by definition the localization precision, see Eq. (4.1). As this procedure is sensitive to instrumental drift, it is better to determine the precision from the distance between consecutive particle locations rather than the positions itself [20]. To determine the effective localization precision of particles that are moving during the image acquisition time, as it is typically the case for SPT experiments, a method is introduced in **Chapter 5** that makes use of two simultaneously acquired images, for instance by introducing a 50/50 beam splitter or dichroic mirror in the detection path [71].

4.6 IMPLICATIONS FOR LM AND SPT

4.6.1 Resolution in LM

The major force behind the recent surge in optical super-resolution microscopy techniques is the desire of obtaining increasingly better resolution. In LM, evidently localization and precision are linked to the achievable resolution. However, so far there has been little consensus in the field about how resolution in LM should be measured and reported. A fundamental resolution measure (FREM) [89] has been developed in order to replace the conventional approach of Abbe [1] and Rayleigh [2]. According to the FREM framework, which is based on the localization precision, the resolution of an optical microscope is not limited and can be improved by increasing the number of detected photons. However, the use of localization precision alone as a measure of resolution is risky, since theoretical descriptions can deviate from measured values and because it does not account for position accuracy effects induced by dipole orientation (cfr. **Section 4.3.3**), detector properties (cfr. **Section 4.4.1**), or the labelling method. For example, a combination of primary and secondary antibodies can introduce displacements of 10-20 nm between the fluorophore and the molecule of interest.

Most importantly, however, localization precision alone is not sufficient to describe resolution because it does not account for the effect of label density [90], as illustrated in **Fig. 4.4**.

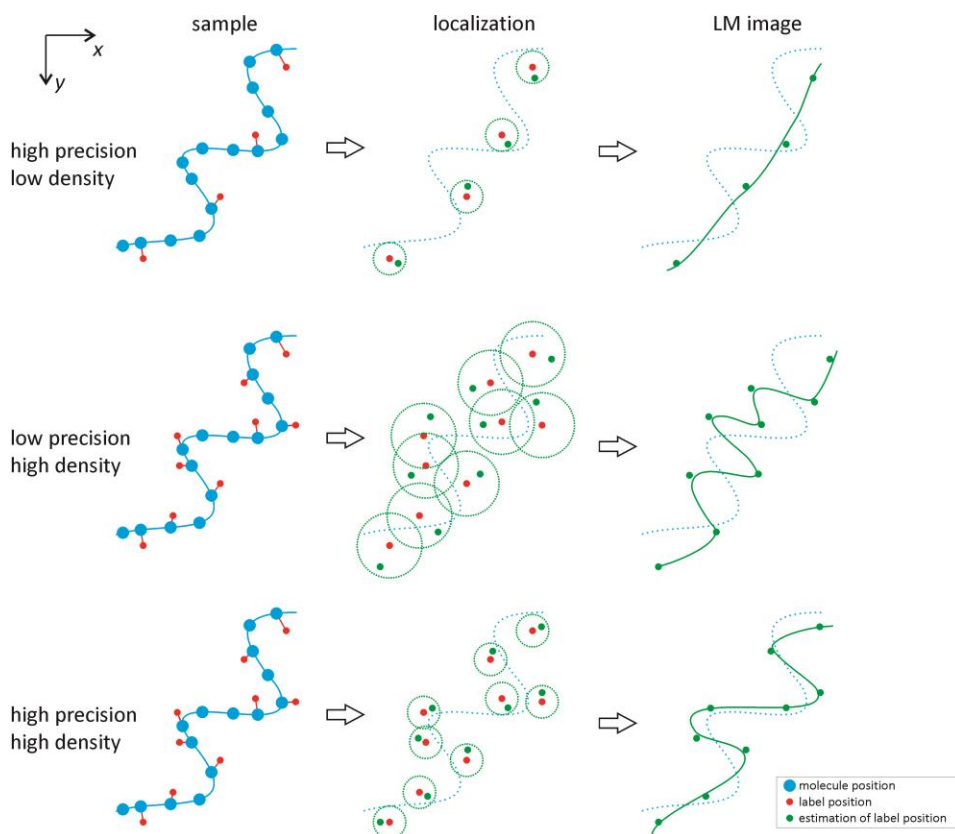


Figure 4.4 | The influence of localization precision and label density on the resolution in LM. Only a sufficiently high localization precision (symbolized by the green dotted circles) and label density result in an image (green line) that faithfully represents the actual structure (blue line). The influence of the displacement between the fluorescent label (red dots) and the actual molecule (blue dots) is also indicated.

An analogy of the Nyquist criterion has been applied for this purpose, stating that the mean distance between two neighbouring emitters must be smaller than half of the smallest sample feature that can be resolved [87,91]. For instance, using this approach, it was calculated that an effective 2-D resolution of 10 nm can only be obtained with a label density of $10^4 \mu\text{m}^{-2}$ or higher [91]. However, it has recently been argued that the

Nyquist criterion does not properly describe the scaling of resolution in LM on label density [92]. Instead, estimation theory was used to develop a measure of spatial resolution in LM that jointly depends on the density of the emitters, the precision of emitter localization, and prior information regarding the spatial frequency content of the labelled object [92,93]. Alternatively, simulation of the particular structure within its context can be useful for determination of the combination of localization precision and density needed to successfully resolve that structure in LM.

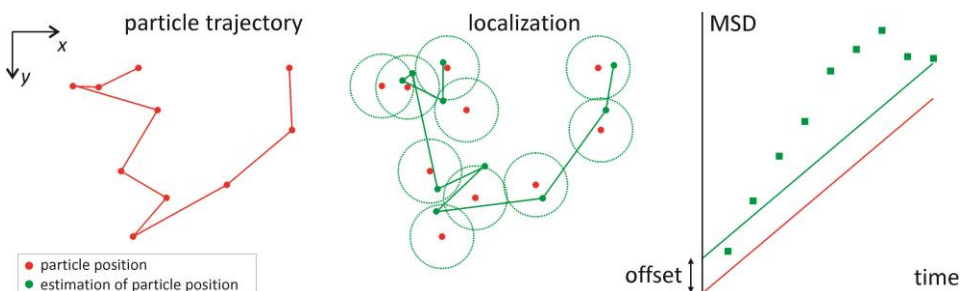


Figure 4.5 | The influence of localization precision on SPT data analysis. The observed trajectory (green line) is different from the actual trajectory (red line) because of the localization precision (symbolized by the green dotted circles). In case of Brownian motion, the observed mean square displacements (MSD) of the observed trajectory (green squares) in function of the time-lags in the trajectory can be modelled by a straight line with an offset value that is related to the localization precision.

4.6.2 SPT analysis

In SPT, the trajectories of individual particles or molecules are determined from their position estimates in a time-series of images. The trajectories are subsequently analysed to obtain information about the particle mobility or its interaction with the surrounding medium. For correct trajectory analysis it is crucial to account for any limited localization precision and accuracy. A popular type of analysis is the fitting of a theoretical model to the mean square displacements (MSD) of the trajectories [10,11,94]. For example, the MSD is linearly proportional to the time-lag between the observed locations in case of free Brownian motion, while typically a power law is considered in case of anomalous diffusion [95]. The effect of limited localization precision has to be included in the model through a constant offset [9,96,97], as illustrated in **Fig. 4.5**. In the context of SPT, where particles or molecules are typically mobile, motion during image acquisition and its effect on localization precision should

be taken into account. Surprisingly it was not until recently that this effect was considered [71,98], see **Chapter 5** for more details. Interestingly, an algorithm was recently reported that determines the optimum number of time-lags that should be included in the trajectory analysis, simultaneously minimizing the effect of the limited trajectory length and the localization precision [99].

4.7 CONCLUSION AND FUTURE OUTLOOK

LM and SPT now provide invaluable insight into biological systems at the nanoscale, but both depend on precise and accurate localization of fluorescent molecules or nanoparticles. Popular position estimators, such as the weighted least-squares fitting of a Gaussian function, only yield optimal precision and accuracy in specific cases, i.e. for stationary and isotropic emitters located in or near the focal plane. This is, however, often a rare situation in SPT or LM experiments, which usually feature emitters that are out of focus, move, or behave like non-rotating dipole emitters. In these cases, complicated image shapes occur, which strongly reduce precision and accuracy, unless specially adapted estimators are used. Sample drift, background fluorescence, detector noise, and other experimental effects reduce the precision and sometimes the accuracy even further. When determining the localization precision and accuracy in LM and SPT, it is crucial to properly account for all these effects. This is not only required for correct optimization of the performance in LM and SPT, but also for correct interpretation of the obtained data. In SPT, it would be of interest to investigate the effect of different types of movement on the localization precision and accuracy, this is the topic of **Chapter 5**. In any case, it needs to be realized that the influence of precision and also accuracy on the analysis of SPT data cannot be neglected. In LM, it is crucial to develop a correct understanding of the role of precision and accuracy on the effective resolution.

REFERENCES

1. E. Abbe, "Beiträge zur Theorie des Mikroskops und der mikroskopischen Wahrnehmung," *Archiv für mikroskopische Anatomie* **9**, 413-418 (1873).
2. L. Rayleigh, "On the theory of optical images, with special reference to the microscope," *Philosophical Magazine* **42**, 167-195 (1896).
3. G. Toraldo di Francia, "Resolving Power and Information," *Journal of the Optical Society of America* **45**, 497-501 (1955).
4. C. W. McCutchen, "Superresolution in Microscopy and Abbe Resolution Limit," *Journal of the Optical Society of America* **57**, 1190-& (1967).
5. L. S. Barak and W. W. Webb, "Diffusion of Low-Density Lipoprotein-Receptor Complex on Human-Fibroblasts," *Journal of Cell Biology* **95**, 846-852 (1982).
6. T. G. Mason and D. A. Weitz, "Optical Measurements of Frequency-Dependent Linear Viscoelastic Moduli of Complex Fluids," *Physical Review Letters* **74**, 1250-1253 (1995).
7. J. Gelles, B. J. Schnapp, and M. P. Sheetz, "Tracking Kinesin-Driven Movements with Nanometre-Scale Precision," *Nature* **331**, 450-453 (1988).
8. W. Schaertl and H. Sillescu, "Dynamics of Colloidal Hard-Spheres in Thin Aqueous Suspension Layers - Particle Tracking by Digital Image-Processing and Brownian Dynamics Computer-Simulations," *Journal of Colloid and Interface Science* **155**, 313-318 (1993).
9. J. C. Crocker and D. G. Grier, "Methods of digital video microscopy for colloidal studies," *Journal of Colloid and Interface Science* **179**, 298-310 (1996).
10. V. Levi and E. Gratton, "Exploring dynamics in living cells by tracking single particles," *Cell Biochemistry and Biophysics* **48**, 1-15 (2007).
11. S. Wieser and G. J. Schutz, "Tracking single molecules in the live cell plasma membrane-Do's and Don't's," *Methods* **46**, 131-140 (2008).
12. E. Betzig, G. H. Patterson, R. Sougrat, O. W. Lindwasser, S. Olenych, J. S. Bonifacino, M. W. Davidson, J. Lippincott-Schwartz, and H. F. Hess, "Imaging intracellular fluorescent proteins at nanometer resolution," *Science* **313**, 1642-1645 (2006).
13. S. T. Hess, T. P. K. Girirajan, and M. D. Mason, "Ultra-high resolution imaging by fluorescence photoactivation localization microscopy," *Biophysical Journal* **91**, 4258-4272 (2006).
14. M. J. Rust, M. Bates, and X. W. Zhuang, "Sub-diffraction-limit imaging by stochastic optical reconstruction microscopy (STORM)," *Nature Methods* **3**, 793-795 (2006).
15. S. W. Hell, "Microscopy and its focal switch," *Nature Methods* **6**, 24-32 (2009).
16. J. Nowakowski and M. Elbaum, "Fundamental Limits in Estimating Light Pattern Position," *Journal of the Optical Society of America* **73**, 1744-1758 (1983).
17. K. A. Winick, "Cramer-Rao Lower Bounds on the Performance of Charge-Coupled-Device Optical Position Estimators," *Journal of the Optical Society of America A-Optics Image Science and Vision* **3**, 1809-1815 (1986).
18. B. Zhang, J. Zerubia, and J. C. Olivo-Marin, "Gaussian approximations of fluorescence microscope point-spread function models," *Applied Optics* **46**, 1819-1829 (2007).
19. R. J. Ober, S. Ram, and E. S. Ward, "Localization accuracy in single-molecule microscopy," *Biophysical Journal* **86**, 1185-1200 (2004).

20. R. E. Thompson, D. R. Larson, and W. W. Webb, "Precise nanometer localization analysis for individual fluorescent probes," *Biophysical Journal* **82**, 2775-2783 (2002).
21. M. K. Cheezum, W. F. Walker, and W. H. Guilford, "Quantitative comparison of algorithms for tracking single fluorescent particles," *Biophysical Journal* **81**, 2378-2388 (2001).
22. K. I. Mortensen, L. S. Churchman, J. A. Spudich, and H. Flyvbjerg, "Optimized localization analysis for single-molecule tracking and super-resolution microscopy," *Nature Methods* **7**, 377-U59 (2010).
23. N. Bobroff, "Position Measurement with A Resolution and Noise-Limited Instrument," *Review of Scientific Instruments* **57**, 1152-1157 (1986).
24. U. Kubitschek, O. Kuckmann, T. Kues, and R. Peters, "Imaging and tracking of single GFP molecules in solution," *Biophysical Journal* **78**, 2170-2179 (2000).
25. H. Li, H. Song, C. Rao, and X. Rao, "Accuracy analysis of centroid calculated by a modified center detection algorithm for Shack-Hartmann wavefront sensor," *Optics Communications* **281**, 750-755 (2008).
26. H. Jia, J. K. Yang, and X. J. Li, "Minimum variance unbiased subpixel centroid estimation of point image limited by photon shot noise," *Journal of the Optical Society of America A-Optics Image Science and Vision* **27**, 2038-2045 (2010).
27. A. V. Abraham, S. Ram, J. Chao, E. S. Ward, and R. J. Ober, "Quantitative study of single molecule location estimation techniques," *Optics Express* **17**, 23352-23373 (2009).
28. R. Parthasarathy, "Rapid, accurate particle tracking by calculation of radial symmetry centers," *Nature Methods* **9**, 724-U291 (2012).
29. A. J. Berglund, M. D. McMahon, J. J. McClelland, and J. A. Liddle, "Fast, bias-free algorithm for tracking single particles with variable size and shape," *Optics Express* **16**, 14064-14075 (2008).
30. C. S. Smith, N. Joseph, B. Rieger, and K. A. Lidke, "Fast, single-molecule localization that achieves theoretically minimum uncertainty," *Nature Methods* **7**, 373-U52 (2010).
31. M. C. DeSantis, S. K. Zareh, X. L. Li, R. E. Blankenship, and Y. M. Wang, "Single-image axial localization precision analysis for individual fluorophores," *Optics Express* **20**, 3057-3065 (2012).
32. A. M. van Oijen, J. Kohler, J. Schmidt, M. Muller, and G. J. Brakenhoff, "3-Dimensional super-resolution by spectrally selective imaging," *Chemical Physics Letters* **292**, 183-187 (1998).
33. S. F. Gibson and F. Lanni, "Diffraction by A Circular Aperture As A Model for 3-Dimensional Optical Microscopy," *Journal of the Optical Society of America A-Optics Image Science and Vision* **6**, 1357-1367 (1989).
34. S. F. Gibson and F. Lanni, "Experimental Test of An Analytical Model of Aberration in An Oil-Immersion Objective Lens Used in 3-Dimensional Light-Microscopy," *Journal of the Optical Society of America A-Optics Image Science and Vision* **8**, 1601-1613 (1991).
35. S. Hell, G. Reiner, C. Cremer, and E. H. K. Stelzer, "Aberrations in Confocal Fluorescence Microscopy Induced by Mismatches in Refractive-Index," *Journal of Microscopy-Oxford* **169**, 391-405 (1993).
36. B. Richards and E. Wolf, "Electromagnetic Diffraction in Optical Systems .2. Structure of the Image Field in An Aplanatic System," *Proceedings of the Royal Society of London Series A-Mathematical and Physical Sciences* **253**, 358-379 (1959).
37. P. Torok, P. Varga, Z. Laczik, and G. R. Booker, "Electromagnetic Diffraction of Light Focused Through A Planar Interface Between Materials of Mismatched Refractive-Indexes - An

- Integral-Representation," *Journal of the Optical Society of America A-Optics Image Science and Vision* **12**, 325-332 (1995).
38. F. Aguet, D. Van De Ville, and M. Unser, "A maximum-likelihood formalism for sub-resolution axial localization of fluorescent nanoparticles," *Optics Express* **13**, 10503-10522 (2005).
 39. M. F. Juetten, T. J. Gould, M. D. Lessard, M. J. Mlodzianoski, B. S. Nagpure, B. T. Bennett, S. T. Hess, and J. Bewersdorf, "Three-dimensional sub-100 nm resolution fluorescence microscopy of thick samples," *Nature Methods* **5**, 527-529 (2008).
 40. P. Prabhat, S. Ram, E. S. Ward, and R. J. Ober, "Simultaneous imaging of different focal planes in fluorescence microscopy for the study of cellular dynamics in three dimensions," *IEEE Transactions on Nanobioscience* **3**, 237-242 (2004).
 41. E. Toprak, H. Balci, B. H. Blehm, and P. R. Selvin, "Three-dimensional particle tracking via bifocal imaging," *Nano Letters* **7**, 2043-2045 (2007).
 42. M. J. Mlodzianoski, M. F. Juetten, G. L. Beane, and J. Bewersdorf, "Experimental characterization of 3D localization techniques for particle-tracking and super-resolution microscopy," *Optics Express* **17**, 8264-8277 (2009).
 43. C. Von Middendorff, A. Egner, C. Geisler, S. Hell, and A. Schonle, "Isotropic 3D Nanoscopy based on single emitter switching," *Optics Express* **16**, 20774-20788 (2008).
 44. S. Ram, P. Prabhat, J. Chao, E. S. Ward, and R. J. Ober, "High Accuracy 3D Quantum Dot Tracking with Multifocal Plane Microscopy for the Study of Fast Intracellular Dynamics in Live Cells," *Biophysical Journal* **95**, 6025-6043 (2008).
 45. M. D. McMahon, A. J. Berglund, P. Carmichael, J. J. McClelland, and J. A. Liddle, "3D Particle Trajectories Observed by Orthogonal Tracking Microscopy," *Acs Nano* **3**, 609-614 (2009).
 46. J. Y. Tang, J. Akerboom, A. Vaziri, L. L. Looger, and C. V. Shank, "Near-isotropic 3D optical nanoscopy with photon-limited chromophores," *Proceedings of the National Academy of Sciences of the United States of America* **107**, 10068-10073 (2010).
 47. L. Holtzer, T. Meckel, and T. Schmidt, "Nanometric three-dimensional tracking of individual quantum dots in cells," *Applied Physics Letters* **90**, (2007).
 48. B. Huang, W. Q. Wang, M. Bates, and X. W. Zhuang, "Three-dimensional super-resolution imaging by stochastic optical reconstruction microscopy," *Science* **319**, 810-813 (2008).
 49. M. Badieirostami, M. D. Lew, M. A. Thompson, and W. E. Moerner, "Three-dimensional localization precision of the double-helix point spread function versus astigmatism and biplane," *Applied Physics Letters* **97**, (2010).
 50. D. Baddeley, M. Cannell, and C. Soeller, "Three-dimensional sub-100 nm super-resolution imaging of biological samples using a phase ramp in the objective pupil," *Nano Research* **4**, 589-598 (2011).
 51. J. Yajima, K. Mizutani, and T. Nishizaka, "A torque component present in mitotic kinesin Eg5 revealed by three-dimensional tracking," *Nature Structural & Molecular Biology* **15**, 1119-1121 (2008).
 52. Y. Sun, J. D. McKenna, J. M. Murray, E. M. Ostap, and Y. E. Goldman, "Parallax: High Accuracy Three-Dimensional Single Molecule Tracking Using Split Images," *Nano Letters* **9**, 2676-2682 (2009).
 53. M. D. Lew, S. F. Lee, M. Badieirostami, and W. E. Moerner, "Corkscrew point spread function for far-field three-dimensional nanoscale localization of pointlike objects," *Optics Letters* **36**, 202-204 (2011).

54. S. R. P. Pavani and R. Piestun, "Three dimensional tracking of fluorescent microparticles using a photon-limited double-helix response system," *Optics Express* **16**, 22048-22057 (2008).
55. M. A. Thompson, M. D. Lew, M. Badieirostami, and W. E. Moerner, "Localizing and Tracking Single Nanoscale Emitters in Three Dimensions with High Spatiotemporal Resolution Using a Double-Helix Point Spread Function," *Nano Letters* **10**, 211-218 (2010).
56. S. R. P. Pavani, A. Greengard, and R. Piestun, "Three-dimensional localization with nanometer accuracy using a detector-limited double-helix point spread function system," *Applied Physics Letters* **95**, (2009).
57. S. R. P. Pavani, M. A. Thompson, J. S. Biteen, S. J. Lord, N. Liu, R. J. Twieg, R. Piestun, and W. E. Moerner, "Three-dimensional, single-molecule fluorescence imaging beyond the diffraction limit by using a double-helix point spread function," *Proceedings of the National Academy of Sciences of the United States of America* **106**, 2995-2999 (2009).
58. G. Grover, R. P. Pavani, and R. Piestun, "Performance limits on three-dimensional particle localization in photon-limited microscopy," *Optics Letters* **35**, 3306-3308 (2010).
59. D. Aquino, A. Schonle, C. Geisler, C. Von Middendorff, C. A. Wurm, Y. Okamura, T. Lang, S. W. Hell, and A. Egner, "Two-color nanoscopy of three-dimensional volumes by 4Pi detection of stochastically switched fluorophores," *Nature Methods* **8**, 353-U108 (2011).
60. G. Shtengel, J. A. Galbraith, C. G. Galbraith, J. Lippincott-Schwartz, J. M. Gillette, S. Manley, R. Sougrat, C. M. Waterman, P. Kanchanawong, M. W. Davidson, R. D. Fetter, and H. F. Hess, "Interferometric fluorescent super-resolution microscopy resolves 3D cellular ultrastructure," *Proceedings of the National Academy of Sciences of the United States of America* **106**, 3125-3130 (2009).
61. A. P. Bartko and R. M. Dickson, "Imaging three-dimensional single molecule orientations," *Journal of Physical Chemistry B* **103**, 11237-11241 (1999).
62. J. Enderlein, E. Toprak, and P. R. Selvin, "Polarization effect on position accuracy of fluorophore localization," *Optics Express* **14**, 8111-8120 (2006).
63. J. Engelhardt, J. Keller, P. Hoyer, M. Reuss, T. Staudt, and S. W. Hell, "Molecular Orientation Affects Localization Accuracy in Superresolution Far-Field Fluorescence Microscopy," *Nano Letters* **11**, 209-213 (2011).
64. S. Stallinga and B. Rieger, "Accuracy of the Gaussian Point Spread Function model in 2D localization microscopy," *Optics Express* **18**, 24461-24476 (2010).
65. F. Aguet, S. Geissbuhler, I. Marki, T. Lasser, and M. Unser, "Super-resolution orientation estimation and localization of fluorescent dipoles using 3-D steerable filters," *Optics Express* **17**, 6829-6848 (2009).
66. S. Stallinga and B. Rieger, "Position and orientation estimation of fixed dipole emitters using an effective Hermite point spread function model," *Optics Express* **20**, 5896-5921 (2012).
67. M. P. Backlund, M. D. Lew, A. S. Backer, S. J. Sahl, G. Grover, A. Agrawal, R. Piestun, and W. E. Moerner, "Simultaneous, accurate measurement of the 3D position and orientation of single molecules," *Proceedings of the National Academy of Sciences of the United States of America* **109**, 19087-19092 (2012).
68. S. Manley, J. M. Gillette, G. H. Patterson, H. Shroff, H. F. Hess, E. Betzig, and J. Lippincott-Schwartz, "High-density mapping of single-molecule trajectories with photoactivated localization microscopy," *Nature Methods* **5**, 155-157 (2008).
69. S. Ram, E. S. Ward, and R. J. Ober, "A stochastic analysis of performance limits for optical microscopes," *Multidimensional Systems and Signal Processing* **17**, 27-57 (2006).

Chapter 4

70. Y. Wong, Z. P. Lin, and R. J. Ober, "Limit of the Accuracy of Parameter Estimation for Moving Single Molecules Imaged by Fluorescence Microscopy," *Ieee Transactions on Signal Processing* **59**, 895-911 (2011).
71. H. Deschout, K. Neyts, and K. Braeckmans, "The influence of movement on the localization precision of sub-resolution particles in fluorescence microscopy," *Journal of Biophotonics* **5**, 97-109 (2012).
72. J. Chao, E. S. Ward, and R. J. Ober, "Fisher information matrix for branching processes with application to electron-multiplying charge-coupled devices," *Multidimensional Systems and Signal Processing* **23**, 349-379 (2012).
73. J. R. Janesick, *Scientific Charge-Coupled Devices*, (SPIE Press, Bellingham, 2001).
74. Z. L. Huang, H. Y. Zhu, F. Long, H. Q. Ma, L. S. Qin, Y. F. Liu, J. P. Ding, Z. H. Zhang, Q. M. Luo, and S. Q. Zeng, "Localization-based super-resolution microscopy with an sCMOS camera," *Optics Express* **19**, 19156-19168 (2011).
75. T. W. Quan, S. Q. Zeng, and Z. L. Huang, "Localization capability and limitation of electron-multiplying charge-coupled, scientific complementary metal-oxide semiconductor, and charge-coupled devices for superresolution imaging," *Journal of Biomedical Optics* **15**, (2010).
76. M. C. DeSantis, S. H. DeCenzo, J. L. Li, and Y. M. Wang, "Precision analysis for standard deviation measurements of immobile single fluorescent molecule images," *Optics Express* **18**, 6563-6576 (2010).
77. J. Hynecek and T. Nishiwaki, "Excess noise and other important characteristics of low light level imaging using charge multiplying CCDs," *Ieee Transactions on Electron Devices* **50**, 239-245 (2003).
78. A. Pertsinidis, Y. X. Zhang, and S. Chu, "Subnanometre single-molecule localization, registration and distance measurements," *Nature* **466**, 647-U11 (2010).
79. S. H. Lee, M. Baday, M. Tjioe, P. D. Simonson, R. B. Zhang, E. Cai, and P. R. Selvin, "Using fixed fiduciary markers for stage drift correction," *Optics Express* **20**, 12177-12183 (2012).
80. A. G. York, A. Ghitani, A. Vaziri, M. W. Davidson, and H. Shroff, "Confined activation and subdiffractional localization enables whole-cell PALM with genetically expressed probes," *Nature Methods* **8**, 327-U73 (2011).
81. C. Geisler, T. Hotz, A. Schonle, S. W. Hell, A. Munk, and A. Egner, "Drift estimation for single marker switching based imaging schemes," *Optics Express* **20**, 7274-7289 (2012).
82. M. J. Mlodzianoski, J. M. Schreiner, S. P. Callahan, K. Smolkova, A. Dlaskova, J. Santorova, P. Jezek, and J. Bewersdorf, "Sample drift correction in 3D fluorescence photoactivation localization microscopy," *Optics Express* **19**, 15009-15019 (2011).
83. F. Cella Zanacchi, Z. Lavagnino, M. P. Donnorso, A. Del Bue, L. Furia, M. Faretta, and A. Diaspro, "Live-cell 3D super-resolution imaging in thick biological samples," *Nature Methods* **8**, 1047-+ (2011).
84. Y. Deng and J. W. Shaevitz, "Effect of aberration on height calibration in three-dimensional localization-based microscopy and particle tracking," *Applied Optics* **48**, 1886-1890 (2009).
85. M. Speidel, A. Jonas, and E. L. Florin, "Three-dimensional tracking of fluorescent nanoparticles with subnanometer precision by use of off-focus imaging," *Optics Letters* **28**, 69-71 (2003).
86. Z. P. Zhang and C. H. Menq, "Best linear unbiased axial localization in three-dimensional fluorescent bead tracking with subnanometer resolution using off-focus images," *Journal of the Optical Society of America A-Optics Image Science and Vision* **26**, 1484-1493 (2009).

87. S. A. Jones, S. H. Shim, J. He, and X. W. Zhuang, "Fast, three-dimensional super-resolution imaging of live cells," *Nature Methods* **8**, 499-U96 (2011).
88. S. Quirin, S. R. P. Pavani, and R. Piestun, "Optimal 3D single-molecule localization for superresolution microscopy with aberrations and engineered point spread functions," *Proceedings of the National Academy of Sciences of the United States of America* **109**, 675-679 (2012).
89. S. Ram, E. S. Ward, and R. J. Ober, "Beyond Rayleigh's criterion: A resolution measure with application to single-molecule microscopy," *Proceedings of the National Academy of Sciences of the United States of America* **103**, 4457-4462 (2006).
90. T. J. Gould, S. T. Hess, and J. Bewersdorf, "Optical Nanoscopy: From Acquisition to Analysis," *Annual Review of Biomedical Engineering*, Vol 14 **14**, 231-254 (2012).
91. H. Shroff, C. G. Galbraith, J. A. Galbraith, and E. Betzig, "Live-cell photoactivated localization microscopy of nanoscale adhesion dynamics," *Nature Methods* **5**, 417-423 (2008).
92. J. E. Fitzgerald, J. Lu, and M. J. Schnitzer, "Estimation Theoretic Measure of Resolution for Stochastic Localization Microscopy," *Physical Review Letters* **109**, (2012).
93. E. A. Mukamel and M. J. Schnitzer, "Unified Resolution Bounds for Conventional and Stochastic Localization Fluorescence Microscopy," *Physical Review Letters* **109**, (2012).
94. M. J. Saxton and K. Jacobson, "Single-particle tracking: Applications to membrane dynamics," *Annual Review of Biophysics and Biomolecular Structure* **26**, 373-399 (1997).
95. M. J. Saxton, "Single-particle tracking: The distribution of diffusion coefficients," *Biophysical Journal* **72**, 1744-1753 (1997).
96. M. Goulian and S. M. Simon, "Tracking single proteins within cells," *Biophysical Journal* **79**, 2188-2198 (2000).
97. T. Savin and P. S. Doyle, "Static and dynamic errors in particle tracking microrheology," *Biophysical Journal* **88**, 623-638 (2005).
98. X. Michalet, "Mean square displacement analysis of single-particle trajectories with localization error: Brownian motion in an isotropic medium," *Physical Review e* **82**, (2010).
99. X. Michalet and A. J. Berglund, "Optimal diffusion coefficient estimation in single-particle tracking," *Physical Review e* **85**, (2012).

Chapter 5

The influence of movement on the localization precision of sub-resolution particles in fluorescence microscopy

This chapter is published as:

Hendrik Deschout^{1,2}, Kristiaan Neyts^{3,2}, and Kevin Braeckmans^{1,2}. *Journal of Biophotonics*, Volume 5, Issue 1, Pages 97-109 (2012).

¹Laboratory for General Biochemistry and Physical Pharmacy, Ghent University, Belgium

²Centre for Nano- and Biophotonics, Ghent University, Belgium

³Liquid Crystals and Photonics Group, Ghent University, Belgium

ABSTRACT

Obtaining sub-resolution particle positions in fluorescence microscopy images is essential for single particle tracking and high-resolution localization microscopy. While the localization precision of stationary single molecules or particles is well understood, the influence of particle motion during image acquisition has been largely neglected, as discussed in **Chapter 4**. Here, we address this issue and provide a theoretical description on how particle motion influences the centroid localization precision, both in case of 2-D and 3-D diffusion. In addition, a novel method is proposed, based on dual-channel imaging, for the experimental determination of the localization precision of moving particles. For typical single particle tracking experiments, we show that the localization precision is approximately two-fold worse than expected from the stationary theory. Strikingly, we find that the most popular localization method, based on the fitting of a Gaussian distribution, breaks down in case of significant lateral diffusion during the image acquisition time. Instead, the centroid localization method is found to perform well under all conditions.

5.1 INTRODUCTION

A fundamental property of imaging a point-like object with any optical set-up is that the observed spot has a certain spatial intensity distribution known as the point spread function (PSF). The radial and axial extent of the PSF determines the imaging resolution, which is around 250 nm and 900 nm, respectively, for a research grade epi-fluorescence microscope [1]. Despite the limited spatial resolution, the position of such a small object can be determined with much better precision by locating the centre point of the PSF, as detailed in **Chapter 4**. This is an important trick that is applied extensively in single particle/molecule tracking (SPT/SMT) microscopy [2-4], in sub-resolution imaging techniques, such as STORM or PALM [5,6], and a combination thereof [7].

It is, therefore, of great interest to have a detailed knowledge of the different parameters that determine the localization precision. Independent of the method that is used for determining the PSF centre position, it was shown that the theoretical lower limit for the localization precision of a stationary particle scales inversely with the square root of the number of detected photons [8,9]. While this result corroborates the common knowledge that as many photons as possible should be collected, there are two other important factors that determine the localization precision. First, due to the fact that images are recorded with a finite pixel size, the sampling of the PSF is not perfect. Secondly, a certain amount of background will usually be present as well. Thompson et al. gave the first approximate theoretical description taking all three factors into account for the case of a stationary particle whose position is determined by the least-squares fitting of a circular 2-D Gaussian function to the PSF in the focal plane [10]. By a more rigorous theoretical derivation, an important correction to this often used equation was recently published by Mortensen et al. [11]. In addition, they provided similar formulas for a fitting algorithm based on maximum likelihood estimation and for more complicated PSF models that describe the dipole emission of single fluorescent molecules. A different way to obtain the particle position, although used less often, is calculating the intensity weighted centre position of the PSF spot, also known as the centroid [12,13].

While a sound theoretical basis now exists for the localization precision of stationary particles, the case of moving particles, which is ubiquitous in SPT/SMT experiments, has been largely neglected. Particle movement during image acquisition alters the shape of the observed intensity distribution compared to the stationary PSF, as illustrated in **Fig. 5.1**, so the localization precision can be expected to be substantially affected. One

recent study gives a theoretical treatment of the influence of the special cases of linear and circular movement during image acquisition on the localization precision [14]. However, on a molecular scale, stochastic motion is much more common and of practical relevance. In this case, the observed intensity distribution does not necessarily have a symmetric shape, rendering the popular Gaussian approximation problematic. It should be noted that the effect of particle diffusion during image acquisition was already studied on the level of motion quantification in SPT experiments. A correction on the classical expression for the mean squared displacement (MSD) was proposed, but the influence on the localization precision was not considered [15-18].

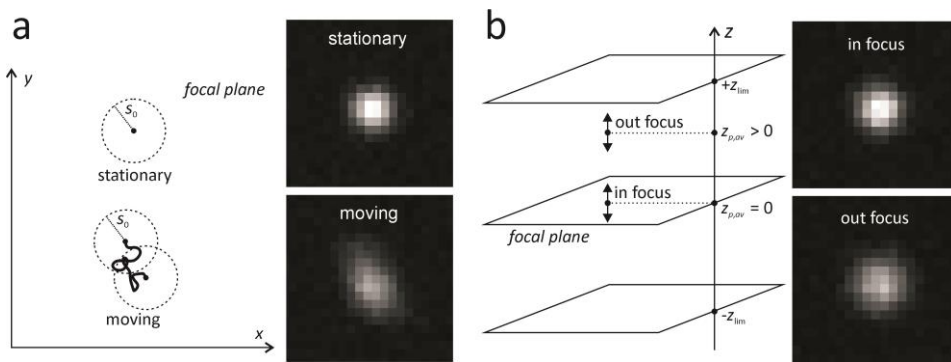


Figure 5.1 | The effect of motion during image acquisition on the observed intensity distribution. (a) Illustration of the influence of lateral movement parallel to the focal plane on the PSF. Two different situations are shown: a stationary particle and a diffusing particle in the focal plane. The trajectories during the image acquisition time are shown together with their PSF. The circular Gaussian approximation of the stationary PSF has a standard deviation s_0 . (b) Illustration of the influence of axial movement perpendicular to the focal plane on the PSF. Two different situations are shown: a particle on average in focus with $z_{p,av} = 0$ and a particle on average out focus with $z_{p,av} > 0$. The PSF of the particle in focus has a smaller standard deviation than the PSF of the particle out focus.

In this study, we address the important but currently unanswered question of how 2-D or 3-D stochastic motion influences the localization precision of sub-resolution particles. It is shown that the centroid localization algorithm is the most robust one in the case that the particles move substantially during image acquisition. Therefore, a formula that describes the centroid localization precision in case of 2-D and 3-D stochastic motion is derived. Our theory is validated both by computer simulations as well as experiments by using a novel procedure based on SPT in two different (spectral) channels. It is shown that particle movement can significantly affect the localization

precision for all image acquisition times. Furthermore, the centroid estimator is compared to the popular method of least-squares fitting of a circular 2-D Gaussian distribution. Notably, we find that the localization precision for the Gaussian least-squares fitting rapidly deteriorates for increasing image acquisition times. Instead, the much simpler and faster centroid algorithm is found to give a superior localization precision if all pixels that belong to the particle intensity distribution are included.

5.2 THEORY

5.2.1 Localization precision of diffusing particles

The position of stationary sub-resolution particles in microscopy images is usually estimated by determining the centre location of the particle PSF. If multiple images of the same particle are recorded, its apparent centre position will be slightly different in each image due to a limited signal-to-noise ratio (SNR). The precision σ with which a particle can be localized, can be defined as the standard deviation on these apparent centre positions. According to the Fisher information theory, this precision is fundamentally limited according to [8]:

$$\sigma \geq \frac{\lambda}{2\pi n\sqrt{N}}, \quad (5.1)$$

with λ the photon wavelength, n the refractive index and N the total number of collected photons. This limit is fundamental, not only because it assumes an ideal noiseless detection process and an infinitely small pixel size, but also because it is independent of the type of PSF centre estimator. In real situations, the precision will be worse compared to the limit provided in Eq. (5.1). The most frequently used method to identify the PSF centre location $\vec{r}_p = (x_p, y_p)$ in the focal plane (xy -plane), is the least-squares fitting of a circular 2-D Gaussian distribution to the observed PSF:

$$I(x, y) = \frac{N}{2\pi s^2} e^{-\frac{(x-x_p)^2 + (y-y_p)^2}{2s^2}} + B, \quad (5.2)$$

with s the standard deviation of the Gaussian distribution and B a constant background. Note that this is only an approximate description, the more exact description of the PSF is an Airy distribution with an infinite standard deviation [19]. Arguably, the popularity of this method is due to the frequently cited work of Cheezum et al., where it was argued that this algorithm performs best in low SNR situations, as is

often the case in SPT or nanoscopy experiments [12]. An approximate model for the localization precision σ_g of this method was put forward by Thompson et al. in 2002, which was refined by a more rigorous mathematical derivation by Mortensen et al. in 2010 [10,11]:

$$\sigma_g^2 = F \left\{ \frac{16(s^2 + a^2/12)}{9N} + \frac{8\pi b^2(s^2 + a^2/12)^2}{a^2 N^2} \right\}, \quad (5.3)$$

with a the pixel size and b the background. We will only consider a Poisson distributed photon background, which means that b can also be interpreted as the background standard deviation. The factor F is equal to 1 in case of a CCD or CMOS detector, while it is equal to 2 for an electron multiplying CCD (EMCCD) camera [11,20,21].

A different type of estimator for the PSF centre is the well-known centroid [12]:

$$x_p = \frac{\sum_{i,j} (I_{i,j} - B) x_{i,j}}{\sum_{i,j} (I_{i,j} - B)} \text{ and } y_p = \frac{\sum_{i,j} (I_{i,j} - B) y_{i,j}}{\sum_{i,j} (I_{i,j} - B)}. \quad (5.4)$$

The sum goes over all the pixels (i,j) that belong to the particle PSF, with $I_{i,j}$ the intensity and $\vec{r}_{i,j} = (x_{i,j}, y_{i,j})$ the pixel coordinate. Similar to Eq. (5.3) for the Gaussian fitting method, it is possible to derive an expression for the centroid localization precision σ_c of a stationary sub-resolution particle (see **Appendix A**):

$$\sigma_c^2 = F \left\{ \frac{s^2 + a^2/12}{N} + \frac{81\pi b^2(s^2 + a^2/12)^2}{4a^2 N^2} \right\}. \quad (5.5)$$

This expression is valid on condition that all relevant pixels belonging to the particle intensity distribution are included in the centroid calculation, see Eq. (5.4), while the background is excluded.

Now, we consider the effect of random motion on the localization precision. If a particle is diffusing during image acquisition, the shape of the observed intensity distribution will be significantly distorted compared to the stationary PSF. In case of movement inside the focal plane, the intensity distribution can even become asymmetrical. Fitting of a circular Gaussian function, therefore, does not seem to be a suitable approach (as will be demonstrated in **Section 5.4**). Instead, if all relevant pixels are taken into account, the centroid algorithm does not make any assumption on the shape of the intensity distribution and is expected to be a better estimator in case of particle motion.

We, therefore, expand the theory of the centroid precision to include particle diffusion during image acquisition. It is important to realize that the centroid is the intensity

weighted centre, which corresponds to the *average* particle position during the time over which the image is acquired. Furthermore, it should be noted that it is impossible to determine the localization precision of an individual diffusing particle, since its trajectory is unknown and unpredictable by definition. Instead, it is rather the effect on a large ensemble of particles that can be described, i.e. the localization precision that is expected *on average* given a certain diffusion rate and image acquisition time. Since we will investigate 3-D diffusion, the PSF should be considered in 3-D. In extension of the circular 2-D Gaussian PSF for a particle in focus (see Eq. (5.2)), the fundamental Gaussian beam solution can be used to describe its intensity distribution in a region near the focal plane [22]:

$$I_{\text{gbs}}(x, y) = \frac{N}{2\pi s^2(z_p)} e^{-\frac{(x-x_p)^2 + (y-y_p)^2}{2s^2(z_p)}}, \quad (5.6)$$

with the Gaussian standard deviation $s(z_p)$ defined by:

$$s^2(z_p) = s_0^2 \left(1 + \frac{z_p^2}{z_0^2} \right), \quad (5.7)$$

where s_0 is the Gaussian standard deviation in the focal plane and $z_0 = (4\pi n/\lambda)s_0^2$. It should be noted that at a certain distance from the focal plane (e.g. in the order of μm), the PSF shape becomes more complicated and the fundamental Gaussian beam solution is not valid anymore. From a rigorous mathematical derivation (see **Appendix A**), it follows that the apparent PSF of particles undergoing lateral diffusion in the focal plane only (i.e. diffusion in the xy -plane, see **Fig. 5.1a**) can on average still be approximated by a circular 2-D Gaussian distribution with variance:

$$s_{xy}^2 = s_0^2 + \frac{1}{3}D\Delta t, \quad (5.8)$$

with D the diffusion coefficient and Δt the image acquisition time. A similar but slightly different correction was already proposed by Michalet et al. [16]. However, they performed their calculations assuming that the initial position of the particle during image acquisition is known. In experimental images, this is not the case and it is rather the average position during image acquisition which can be estimated. It is this consideration that leads to the factor 1/3 in Eq. (5.8), which was omitted in the work by Michalet et al.

For particles diffusing in the axial direction along the optical axis (diffusion along the z -axis, see **Fig. 5.1b**), a detailed calculation shows that the apparent PSF can also be

described on average by a circular 2-D Gaussian distribution with variance (see **Appendix A**):

$$s_z^2 = s_0^2 + \left(\frac{z_{\text{lim}}^2}{3z_0^2} + \frac{D\Delta t}{3z_0^2} \right) s_0^2, \quad (5.9)$$

where the average position during the image acquisition time is restricted between the boundaries $z = -z_{\text{lim}}$ and $z = z_{\text{lim}}$ along the optical axis, an assumption based on the apparent PSF becoming indistinguishable from the background if the particle is located too far from the focal plane. In order to reasonably estimate z_{lim} , it can be assumed that a particle becomes undetectable if its peak intensity drops to e^{-2} times its peak intensity in the focal plane, leading to (see **Appendix A**):

$$z_{\text{lim}} = z_0 \sqrt{e^2 - 1}. \quad (5.10)$$

In reality, z_{lim} will depend not only on the optical properties of the objective lens, but also on the particle SNR and image processing settings for detecting the particles. We recently worked out a theoretical framework that allows to accurately determine z_{lim} from SPT images of 3-D diffusing particles [23]. For clarity, however, in this work we have consistently used Eq. (5.10), since it was sufficiently accurate for this purpose. Equations (5.8) and (5.9) show that both the diffusion in the focal plane and along the optical axis result in an apparent PSF that has on average a circular 2-D Gaussian distribution, with a variance that increases linearly with the image acquisition time and diffusion coefficient:

$$s^2 = s_0^2 + \left(\frac{z_{\text{lim}}^2}{3z_0^2} + \frac{D\Delta t}{3z_0^2} \right) s_0^2 + \frac{1}{3} D\Delta t. \quad (5.11)$$

For a stationary particle ($D = 0$) that is observed in the focal plane ($z_{\text{lim}} = 0$), we find that $s = s_0$, as expected. Substituting Eq. (5.11) in Eq. (5.5), we propose the following description of the average localization precision for centroids, corrected for the influence of 3-D diffusion during image acquisition:

$$\sigma_c^2 = F \frac{s_0^2 + \left(\frac{z_{\text{lim}}^2}{3z_0^2} + \frac{D\Delta t}{3z_0^2} \right) s_0^2 + \frac{1}{3} D\Delta t + \frac{a^2}{12}}{N} + \frac{81\pi b^2 \left(s_0^2 + \left(\frac{z_{\text{lim}}^2}{3z_0^2} + \frac{D\Delta t}{3z_0^2} \right) s_0^2 + \frac{1}{3} D\Delta t + \frac{a^2}{12} \right)^2}{4a^2 N^2}. \quad (5.12)$$

The average localization precision of diffusing particles is thus equal to the localization precision for a PSF blurred by the average diffusion.

5.2.2 Experimental determination of the localization precision of moving particles

Not only a theoretical description of the localization precision, but also a method that allows experimental determination of this value is of interest. It is well-known that the MSD of a the 2-D trajectory of a diffusing particle is given by [15-17,24,25]:

$$\text{MSD} = 4Dt - \frac{4}{3}D\Delta t + 4\sigma^2, \quad (5.13)$$

with t the time interval between the positions in the trajectory (determined by the camera frame rate). When a particle is stationary ($D = 0$), the localization precision σ can be easily determined experimentally by making images of that particle at sequential time points. The MSD of the apparent particle trajectory is then equal to $4\sigma^2$. We will refer to this method as the *single-channel method*, as opposed to the *dual-channel method* for moving particles, which will be explained below.

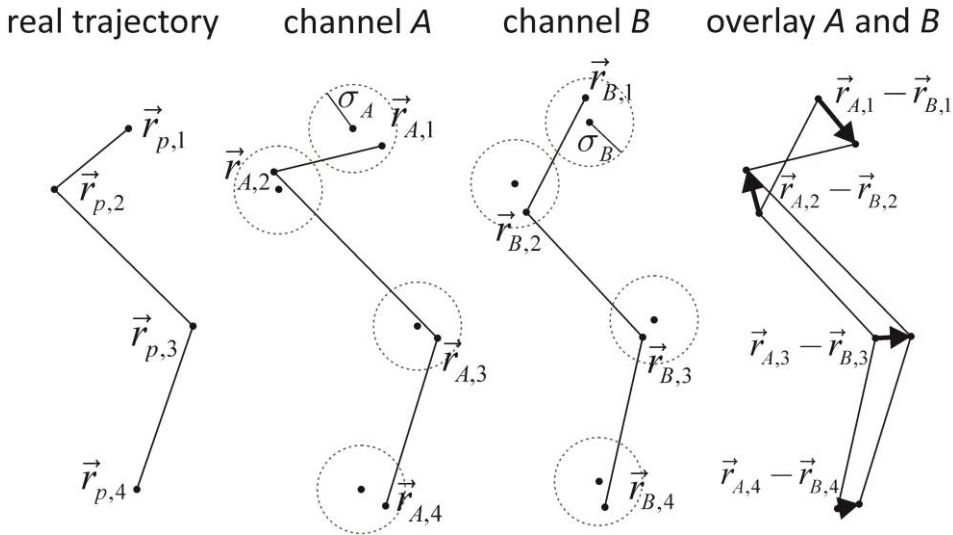


Figure 5.2 | The dual-channel method for determining the localization precision of moving particles. The true particle trajectory consists out of 4 positions $\vec{r}_{p,i}$ ($i = 1, \dots, 4$). The particle positions $\vec{r}_{A,i}$ and $\vec{r}_{B,i}$ that are detected in channel A and B, respectively, are normally distributed around the true position $\vec{r}_{p,i}$ with standard deviations σ_A and σ_B , respectively. Making an overlay of the images in both channels and taking the standard deviation of the difference between the positions $\vec{r}_{A,i} - \vec{r}_{B,i}$ for every i , results in the localization precision σ_A and σ_B .

For a moving particle, Eq. (5.13) suggests that σ could be determined from the intercept of the MSD plot, by fitting of a straight line. However, in reality, one typically has to deal with relatively short trajectories so that, according to our experience, the localization precision cannot be accurately determined this way. Instead, we have developed a novel method, based on SPT in two channels, to determine the localization precision reliably. These can be spectrally different channels (e.g. green and red fluorescence by using a dichroic mirror), but also the same image that is acquired on two detectors (e.g. by using a 50/50 mirror). Consider a particle that is imaged simultaneously in two different channels A and B . The observed trajectories of the particle are described by the positions $\vec{r}_{A,i}$ and $\vec{r}_{B,i}$ (with $i = 1, 2, \dots$) in channel A and B , respectively (see **Fig. 5.2**). These positions can be assumed to be distributed around the true particle positions $\vec{r}_{p,i}$. We will consider only the x -dimension, since the same reasoning applies to the y -dimension. The precisions corresponding to the particle locations $x_{A,i}$ and $x_{B,i}$ are defined as σ_A and σ_B , respectively. If the photons in both channels are detected independently from each other, the standard deviation of the differences $x_{A,i} - x_{B,i}$ between the positions in both channels is given by:

$$\sigma_{A-B} = \sqrt{\sigma_A^2 + \sigma_B^2}. \quad (5.14)$$

In addition, there might be an error on the overlay of the images of both channels, which can be taken into account by introducing an extra overlay contribution σ_o [26]:

$$\sigma_{A-B} = \sqrt{\sigma_A^2 + \sigma_B^2 + \sigma_o^2}. \quad (5.15)$$

If a 50/50 mirror is used, σ_A and σ_B will be equal to each other, immediately resulting in:

$$\sigma_A = \sigma_B = \sqrt{\frac{\sigma_{A-B}^2 - \sigma_o^2}{2}}. \quad (5.16)$$

If rather a dichroic mirror is used for detection in two spectrally different channels, a correction has to be made for the different wavelengths and intensities in both channels. If we assume in a first approximation that both σ_A and σ_B are described by the photon shot noise according to Eq. (5.1), their ratio is given by:

$$\frac{\sigma_A}{\sigma_B} = \frac{\lambda_A}{\lambda_B} \sqrt{\frac{N_B}{N_A}}, \quad (5.17)$$

with λ_A and λ_B the (average) wavelength in channel A and B , respectively, and N_A and N_B the corresponding number of collected photons. Combining Eq. (5.17) with Eq. (5.15) yields:

$$\sigma_A = \sqrt{\frac{\sigma_{A-B}^2 - \sigma_o^2}{1 + \left(\frac{\lambda_B}{\lambda_A}\right)^2 \frac{N_A}{N_B}}} \text{ and } \sigma_B = \sqrt{\frac{\sigma_{A-B}^2 - \sigma_o^2}{1 + \left(\frac{\lambda_A}{\lambda_B}\right)^2 \frac{N_B}{N_A}}}. \quad (5.18)$$

For equal intensities and wavelengths Eq. (5.18) indeed reduces to Eq. (5.16). In conclusion, by tracking a diffusing particle in two channels and calculating the variance on the difference between the two positions, the effective localization precision in both channels can be readily calculated with the dual-channel method according to Eq. (5.16) or (5.18). Note that the dual-channel method does not make any explicit assumption on the type of motion.

5.3 MATERIALS AND METHODS

5.3.1 Computer simulated single particle images

The simulations of images of the apparent PSF of diffusing particles were performed in the Matlab programming environment (The MathWorks, USA). First, the arrival times $t_{A,i}$ and $t_{B,j}$ ($i = 1, \dots, N_A$ and $j = 1, \dots, N_B$) of N_A and N_B detected photons in channel A and B , respectively, were determined. For an observed photon emission rate r_A and r_B in channel A and B , respectively, the expected number of photons during image acquisition time Δt is given by $r_A \Delta t$ and $r_B \Delta t$. These are the averages of the Poisson distributions describing the photon numbers in both channels. Two numbers N_A and N_B were generated from these Poisson distributions using the Matlab function *poissrnd*. The arrival times $t_{A,i}$ and $t_{B,j}$ in channel A and B , respectively, were then determined by generating N_A and N_B random numbers in the interval $[0, \Delta t]$ using the Matlab function *rand*. The image acquisition times Δt were chosen between 1 and 30 ms and photon emission rates r_A and r_B had the same value of $2 \cdot 10^5 \text{ s}^{-1}$, in accordance with our experiments.

As a second step, the particle positions $\vec{r}_{p,k} = (x_p(t_k), y_p(t_k), z_p(t_k))$ were calculated at the times $t_k = \{t_{A,i}, t_{B,j}\}$ ($k = 1, \dots, N_A + N_B$) for channel A and B together, with diffusion coefficient $D = 1 \text{ } \mu\text{m}^2/\text{s}$. For 1-D diffusion, the position $x_p(t_k)$ was determined

by taking the position $x_p(t_{k-1})$ and adding a distance from the Gaussian diffusion propagator with variance $2D(t_k - t_{k-1})$ using the Matlab function *randn*. The starting position $\vec{r}_{p,0} = (x_{p,0}, y_{p,0}, z_{p,0})$ at time $t = 0$ was chosen as $x_{p,0} = y_{p,0} = 0$ and $z_{p,0}$ a random number in the interval $[-z_{\text{lim}}, z_{\text{lim}}]$, with $z_{\text{lim}} = 1.5 \mu\text{m}$. If the average particle position during Δt was located outside these boundaries, the trajectory was discarded from the analysis. Next, in order to apply the single-channel method for determining the localization precision, the average position of all simulated particle trajectories during Δt should be identical. This was achieved by shifting each time the average position of the trajectory to the origin in the centre of the image. Subsequently, the trajectory of the particle in channel *A* or *B* was obtained by extracting the positions $\vec{r}_{p,k}$ corresponding to the photon arrival times $t_k = t_{A,i}$ or $t_k = t_{B,j}$, respectively.

The positions $\vec{r}_{p,k}$ represent the real positions of the particle during Δt . The observed photon positions \vec{r}_k' for every t_k were obtained from the probability distribution described by the 3-D Gaussian PSF according to Eq. (5.6), using the Matlab function *randn*. The standard deviation s_0 of the PSF for a stationary particle in the focal plane was taken equal to $0.15 \mu\text{m}$. If all photon positions were generated, they were assigned to $M \times M$ pixels, with a pixel size of $0.1 \mu\text{m}$. Finally, a normally distributed photon background was added, with a variance equal to $500 \text{ s}^{-1} \Delta t$, in the same order of magnitude as for the experimental situation. The variance was assumed to increase linearly with Δt , corresponding to our experiments. The resulting matrix was saved as a 16-bit image. For each image acquisition time typically 1000 images were simulated. The overlay error σ_o in the overlap between the images of both channels was taken equal to zero. Once all simulated images were obtained, the image processing software that was used in the actual experiments and described in **Section 5.3.4**, was used to identify and localize the particles.

5.3.2 Experimental set-up

The SPT experiments were carried out on a custom-built laser widefield epi-fluorescence microscope set-up that is described elsewhere in more detail [27]. Briefly, two solid state lasers were used for illumination: a 100 mW Calypso 491 nm (Cobolt, Sweden) and a IQ1C 30 mW 636 nm (Power Technology, USA). The microscope was a Nikon TE2000-E with a Nikon Plan Apochromat 100× oil immersion objective lens with a numerical aperture of 1.4 (Nikon, Belgium). The fluorescence light coming from the sample was collected again by the objective lens and sent through the side port of the microscope towards the Cascade II:512 EMCCD camera (Roper Scientific, USA). A pair of achromat lenses was placed in between the camera and microscope side port for an

extra 2× magnification of the image on the CCD chip so that one pixel corresponded to a distance of 89 nm in the sample. A dichroic mirror placed between both achromat lenses reflected the fluorescent light with a wavelength below 560 nm and transmitted the wavelengths above 560 nm. Accompanying mirrors and notch filters (AHF Analysentechnik, Germany) guided the reflected and transmitted part of the fluorescence each to one half of the CCD chip. High-speed movies were recorded using the Nikon Elements R imaging software. The camera does not output photon numbers but pixel values in analogue-to-digital units that are linearly related to the number of photons collected by the pixels. The conversion factor, which is called the gain, was calibrated with the method published by Janesick [28], using the intensity average and variance from both a dark and an even illuminated image, for an electron multiplication factor that was kept constant throughout the experiments.

5.3.3 Sample preparation and experimental protocol

SPT experiments were performed on 200 nm diameter Tetraspeck polystyrene nanospheres (Molecular Probes, Belgium), containing, among other fluorescent labels, a green (505 nm excitation peak, 515 nm emission peak) and a red (660 nm excitation peak, 680 nm emission peak) fluorescent label. The fluorescence emission of the green and red label was detected each on a separate half of the CCD chip to enable simultaneous dual-colour imaging. The beads were diluted in water to a concentration of approximately 10^9 particles per ml. A microscope sample was prepared by applying 5 μ l of the bead suspension between a microscope slide and a cover glass with a double-sided adhesive Secure-Seal Spacer of 120 μ m thickness (Molecular Probes, The Netherlands) in between. To obtain a sample with stationary particles, 5 μ l (with typical concentration of 10^8 particles per ml) was applied on the cover slip and allowed to evaporate, leaving only the nanospheres behind. A microscope sample was prepared by applying 5 μ l of water on top of the beads, and the sample was sealed with a cover glass using the double-sided adhesive Secure-Seal Spacer. To increase the camera frame rate, a subregion of the CCD chip of 256 by 512 pixels was selected. Typical image acquisition times were between 1 and 32 ms per frame, with a corresponding frame rate of about 20 to 40 frames per second. For each sample typically 20 movies of about 10 s were recorded at different locations within the sample, with about 20 to 100 particles detected in each movie. All experiments were performed at 22.5° C.

5.3.4 Single particle tracking data analysis

In case of experimental data, the images from both channels were first aligned, making use of an affine transformation with parameter values derived from an image with stationary multi-colour particles. This procedure resulted in an average overlay precision σ_o of approximately 3 nm over the entire field of view, as obtained from Eq. (5.15) with σ_{A-B} the standard deviation of the differences between the positions of the same particle in both channels and σ_A and σ_B the localization precisions in both channels separately.

Analysis of the experimental and simulated SPT images was performed in Matlab with custom image processing software for identifying and tracking of the individual particles. The procedure that was used to identify the particles in all experimental and simulated images is illustrated in **Fig. 5.3** and is described elsewhere [24]. First, a simple algorithm was applied that automatically determines an intensity threshold value for every separate image in a single particle tracking (SPT) movie. Briefly, in each image, a Gaussian function was fitted to the pixel intensity distribution. The pixel intensities from the background are approximately described by the Gaussian function itself, while the (relatively few) pixel intensities coming from the brighter particle spots are outliers. A threshold T could, therefore, be defined as $T = \mu + K\sigma$, where μ is the mean and σ the standard deviation of the Gaussian function. A good value for K was determined beforehand by visually inspecting a number of representative images and was subsequently used for all movies of a single series of experiments. This procedure resulted for each separate image in a corresponding binary image that was used to calculate the contours that circumscribe every particle intensity distribution. The pixels within each contour thus belong to the observed intensity distribution of a particle. Note that the contours do not have a predefined shape. Also, a second contour was defined at a distance of typically 4 pixels around each original contour. The average pixel value along this contour defines the local background B for each particle.

Once all particle contours had been obtained, the centre position $\vec{r}_p = (x_p, y_p)$ of each particle was calculated based on the pixels within the contours, using the centroid algorithm defined in Eq. (5.4). A suitable intensity threshold has to be chosen in order to include all relevant pixels belonging to the intensity distribution into the sum of Eq. (5.4), while excluding the background pixels. Another, more popular, method that we have also used, is the least-squares fitting of a circular 2-D Gaussian defined in Eq. (5.2) to the PSF images.

Chapter 5

Additionally, least-squares fitting of an elliptical 2-D Gaussian distribution to each PSF image was also performed:

$$I_{\text{ell}}(x, y) = \frac{N}{2\pi s_a s_b} \times e^{-\left\{\left(\frac{\cos^2 \theta}{2s_a^2} + \frac{\sin^2 \theta}{2s_b^2}\right)(x-x_p)^2 + 2\left(-\frac{\sin 2\theta}{4s_a^2} + \frac{\sin 2\theta}{4s_b^2}\right)(x-x_p)(y-y_p) + \left(\frac{\sin^2 \theta}{2s_a^2} + \frac{\cos^2 \theta}{2s_b^2}\right)(y-y_p)^2\right\}} + B, \quad (5.19)$$

with θ the angle describing the orientation of the distribution relative to the x -axis, and s_a and s_b the standard deviation along the major and minor axis, respectively. The full variation of shapes was thus included in the fit to the elliptical 2-D Gaussian distribution. Both Gaussian functions are fitted to the pixels within the second background contour, because in this case it is necessary to include some background pixels in order to determine the baseline B of the Gaussian function accurately.

After all centre positions of all particles in each image were calculated, the trajectories of the particles are determined by a nearest neighbour algorithm that connects the positions of particles that are closest to each other in subsequent images. To ensure that positions that are too far removed from each other are not connected, a maximum distance that a particle can reasonably move from one image to another was defined, based on the probability distribution of diffusional motion.

5.3.5 Calculation of the theoretical localization precision

In order to use Eq. (5.5) for the determination of the localization precision of stationary particles, several parameters had to be determined. Since an EMCCD camera was used, the factor F was taken equal to 2. The number of photons N could be obtained from the particle spot intensities (i.e. the pixel values within the contour) and was found to be on average $1.97 \cdot 10^5 \text{ s}^{-1} \Delta t$ in the green channel and $2.01 \cdot 10^5 \text{ s}^{-1} \Delta t$ in the red channel. The PSF standard deviation s_0 was determined to be $0.143 \text{ }\mu\text{m}$ in the green and $0.157 \text{ }\mu\text{m}$ in the red channel. The photon background variance was estimated from the experimental SPT movies as $54 \text{ s}^{-1} \Delta t$ in the green and $25 \text{ s}^{-1} \Delta t$ in the red channel. Note that this variance is equal to Fb^2 instead of b^2 in Eq. (5.5), considering the electron multiplication process of the EMCCD camera.

In case of diffusing particles, the theoretical localization precision was calculated from Eq. (5.12) (with F equal to 2). The number of photons N was found to be on average

$0.98 \cdot 10^5 \text{ s}^{-1} \Delta t$ in the green channel and $0.72 \cdot 10^5 \text{ s}^{-1} \Delta t$ in the red channel. The photon background variance Fb^2 was estimated from the experimental SPT movies as $184 \text{ s}^{-1} \Delta t$ in the green and $78 \text{ s}^{-1} \Delta t$ in the red channel. The diffusion coefficient was calculated from least-squares fitting Eq. (5.13) to the mean squared displacements of the particle trajectories. Only the displacements corresponding to the first 25% of the time lags were included, with the localization precision as a free parameter, resulting in an average diffusion coefficient D of $1.6 \text{ } \mu\text{m}^2/\text{s}$ [29]. Weights were added to the least-squares fitting according to the theory from Qian et al. [30]. The maximum detection distance from the focal plane z_{lim} , estimated from Eq. (5.10), was found to be around $1.66 \text{ } \mu\text{m}$ and $1.82 \text{ } \mu\text{m}$ in the green and red channel, respectively.

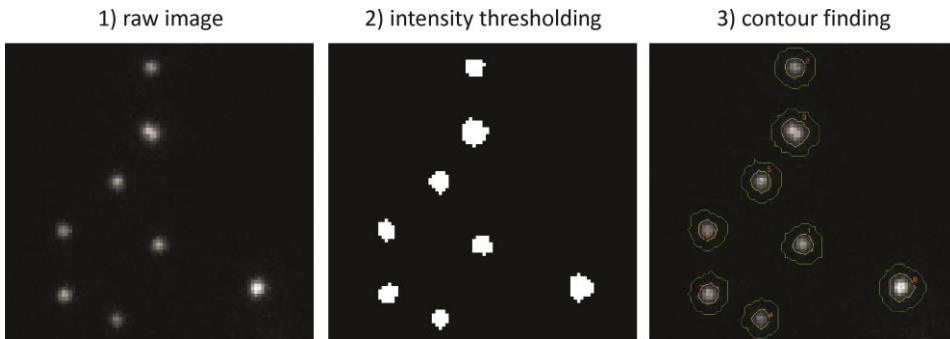


Figure 5.3 | SPT data analysis on a typical experimental image. First, an intensity threshold is applied, resulting in a binary image with a black background and white particles. Next, the binary image is used to calculate the contours that circumscribe the particle PSF (yellow contours), together with a second contour describing the local background (green contours). Subsequently, the pixels within these contours are used to calculate the apparent PSF centre positions.

5.4 RESULTS

5.4.1 Simulations

A first validation of the theory for determining the localization precision of diffusing particles, as well as the experimental dual-channel method, was performed using computer simulated images of diffusing sub-resolution particles. For several acquisition times, images of the PSF of stationary and diffusing particles were simulated. Subsequently, the particle locations in these simulated images were obtained by the

centroid algorithm, and additionally also by least-squares fitting of the circular and elliptical 2-D Gaussian functions. Since the average particle position in the simulated images is located in the origin, the classic single-channel method could also be used to determine the localization precision in case of the diffusing particles, allowing validation of the theory. This would not have been possible for experimental images of a moving particle whose trajectory, and hence time-averaged position, during image acquisition is variable and unknown *a priori*. All images were simulated in two channels with equal wavelength and equal intensity, to validate the dual-channel method by comparison with the single-channel method.

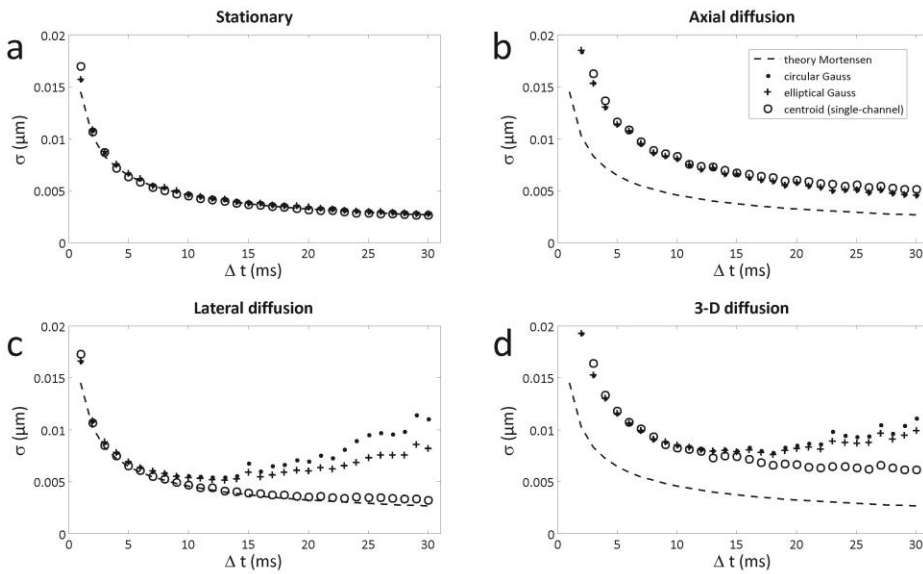


Figure 5.4 | The effect of motion during image acquisition on the localization precision. The localization precision, as determined from simulated images, is shown in function of the image acquisition time. The results for 3 different PSF centre estimators (the centroid (\circ) and the least-squares fitting of a circular (\bullet) and elliptical ($+$) 2-D Gaussian function) are shown in case of: (a) stationary particles, (b) particles diffusing along the axial direction only, (c) particles diffusing in the focal plane only, (d) particles diffusing in 3-D. The dashed line represents the theoretical prediction according to Mortensen et al. for the stationary particles (see Eq. (5.3) with $F = 1$).

As can be seen in **Fig. 5.4a**, for each PSF centre estimator, the localization precision decreases with the image acquisition time, as expected for stationary particles. Both least-squares methods result in approximately the same localization precision, which is

in excellent agreement with the theory of Mortensen et al., see Eq. (5.3) (with $F = 1$). The localization precision of the centroid method performs nearly identical as well. To investigate the effect of diffusion during acquisition, images were simulated for a particle diffusing with a diffusion coefficient of $1 \mu\text{m}^2/\text{s}$ for different image acquisition times. First, the particle was allowed to move along the z -direction only, obtaining the situation of axial diffusion along the optical axis. As can be seen from the results in **Fig. 5.4b**, the three PSF centre estimators produced nearly identical results in this case. For all acquisition times, the localization precision becomes $> 80\%$ worse compared to the stationary theory of Mortensen et al. The effect of lateral diffusion, i.e. movement restricted to the xy -plane, on the localization precision is shown in **Fig. 5.4c**. In this situation, the three estimators behave quite differently from each other. The centroid precision becomes only slightly worse than the stationary case with increasing image acquisition times. Strikingly, however, the precision of both least-squares fits rapidly deteriorates for longer image acquisition times. Fitting of the elliptical 2-D Gaussian function (see **Section 5.3.4**) results in a localization precision that is somewhat better than for the circular symmetric 2-D Gaussian, but is still much worse than the centroid method. When the particle is diffusing in all 3 dimensions, a combination of the behaviour in the axial and lateral diffusion case can be seen for the three estimators in **Fig. 5.4d**. We can conclude that the centroid estimator has the best overall performance in case of particle diffusion, while the Gaussian fitting methods rapidly break down for lateral diffusion in case of longer image acquisition times.

We have used the centroid data of the diffusing particles, obtained with the single-channel method, to validate Eqs. (5.5) and (5.12) (with $F = 1$) which we derived in **Section 5.2.1**. As can be seen from **Fig. 5.5a**, the theory accurately describes the behaviour of the centroid precision in case of stationary particles. In the case of axial diffusion, the correction from Eq. (5.9) nicely accounts for the $> 80\%$ decrease in precision, as can be seen from **Fig. 5.5b**. The small decrease in centroid precision for larger image acquisition times, if the particle is laterally diffusing, is captured well by the correction from Eq. (5.8), as demonstrated in **Fig. 5.5c**. Also in case of 3-D diffusion, we now see a very good correspondence between theory and simulated data (see **Fig. 5.5d**). From the results in **Fig. 5.5**, it can be seen that the centroid precision theory slightly underestimates the simulated values (typically less than 10% , which is less than 2 nm in absolute terms). A hypothesis for this deviation is provided in **Section 5.5**.

We performed similar simulations for two detection channels as well, allowing to validate the new dual-channel method that we put forward for the experimental determination of the localization precision of diffusing particles. As can be seen from **Fig. 5.5**, the precision values of the dual-channel method correspond well to the values from the classic single-channel method, demonstrating the validity of this method.

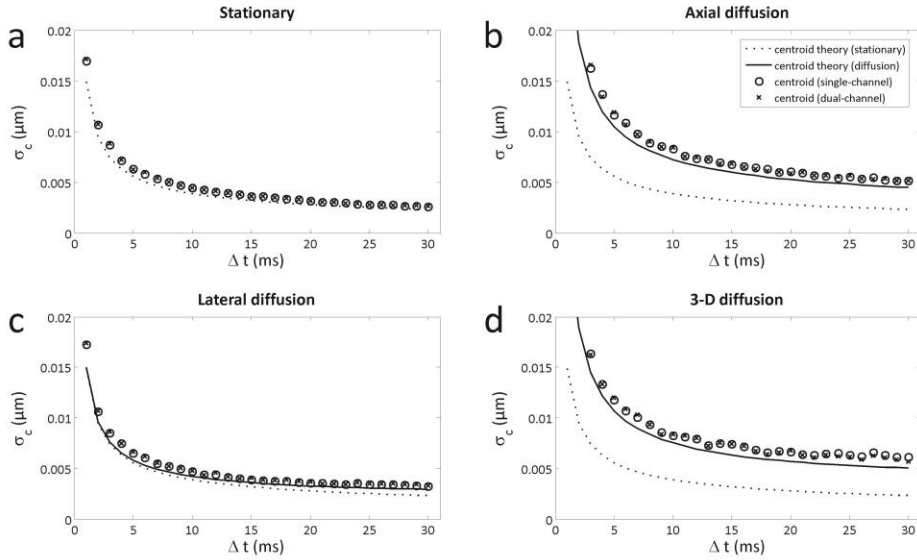


Figure 5.5 | Validation of the localization precision theory and dual-channel method by simulations. The localization precision, as determined from simulated images, is shown in function of the image acquisition time. The results for the centroid are shown in function of case of: (a) stationary particles, (b) particles diffusing along the axial direction only, (c) particles diffusing in the focal plane only, (d) particles diffusing in 3-D. The centroid precision values obtained by both the single-channel (\circ) and dual-channel (\times) method are shown. The dotted line is the same and represents the theory for the stationary particles (see Eq. (5.5) with $F = 1$). The full line shows the theory that takes the diffusion (axial, lateral or both) during image acquisition time into account (see Eq. (5.12) with $F = 1$).

5.4.2 Single particle tracking experiments

Through simulations, we showed that our model accurately describes the localization precision of the centroid algorithm in case of diffusion. In a last step, we wanted to verify this model against experimental data using SPT movies of multi-colour fluorescent 200 nm diameter nanospheres that are diffusing in water. To this end, we have developed the dual-channel method that allows to calculate the localization precision of particles that are moving during image acquisition from experimental SPT images. To apply the dual-channel method, the SPT movies are recorded in two different colours, referred to as the green and red channel.

First, it was checked if the dual-channel method performs correctly on stationary beads in comparison with the classic single-channel method. The dual-channel precision values were obtained for the green and red channel separately using Eq. (5.18). As can

be seen from the results in **Fig. 5.6a**, the single and dual-channel methods are in excellent agreement with each other for the green channel, and both methods are in agreement with the theoretical prediction for stationary particles, see Eq. (5.5) (with $F = 2$). The same result was found for the red channel (data not shown). We then applied the dual-channel method to the diffusing particles, the results correspond well with the theoretical prediction according to Eq. (5.12) (with $F = 2$), as shown in **Fig. 5.6b**. Comparison with the theoretical predication that does not take the diffusion into account (Eq. (5.5) with $F = 2$) shows that the stationary theory underestimates the diffusion localization precision significantly, by roughly a factor of 2, for all image acquisition times, see **Fig. 5.6b**.

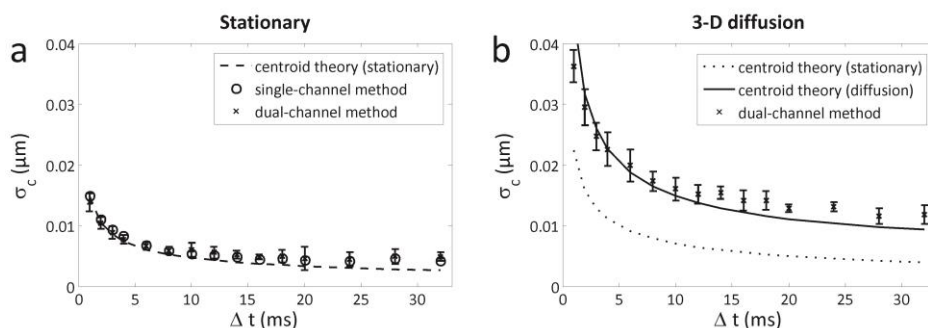


Figure 5.6 | Validation of the localization precision theory by experiments. The experimentally determined centroid precision from dual-colour SPT movies of stationary and diffusing 200 nm diameter nanospheres is shown in function of the image acquisition time. The results from for the green channel are shown for: **(a)** the stationary particles, and **(b)** the diffusing particles. For the stationary particles, both the single-channel (\circ) and dual-channel (\times) precision values are shown, for the diffusing particles only the dual-channel (\times) values. The error bars represent the 95% confidence intervals of the dual-channel values. The dashed line shows the theoretical prediction for the stationary particles (see Eq. (5.5) with $F = 2$). The dotted line shows the theoretical prediction if the diffusion is not taken into account (see Eq. (5.5) with $F = 2$). The full line represents the theoretical prediction that takes the diffusion during image acquisition time into account (see Eq. (5.12) with $F = 2$).

5.5 DISCUSSION

When sub-resolution particles or molecules are localized in microscopy images, typically a theoretical PSF model is fitted to the observed intensity distribution and the

real particle position is estimated by the fitted PSF centre. This results in a localization precision that is significantly better than the width of the intensity distribution, a property that has been conveniently used for decades in SPT and more recently in nanoscopy methods based on fluorophore localization [3,5,6]. Up to now, most efforts in estimating this localization precision explicitly or implicitly assume that the particle is immobile during image acquisition [8,10,11]. This is a reasonable assumption, because strictly speaking the location of a mobile particle during the image acquisition time cannot be defined. Nonetheless, moving particles have an average position during image acquisition, and localization of this average position is possible. Particle movement, however, affects the observed intensity distribution so that the localization precision for moving particles can be expected to be significantly worse compared to the stationary case. In recent work, the effect of *a priori* known linear and circular motion on the localization precision was studied within the framework of the Fisher information theory [14,31]. We, on the other hand, have considered stochastic motion, which is more relevant on the molecular scale. Since, to the best of our knowledge, stochastic motion is not easily implemented in the Fisher information approach, we have expanded the popular existing theories on stationary particle localization to include the effects of 2-D and 3-D diffusion during image acquisition.

It is important to realize that, due to the stochastic motion, it is impossible to predict the localization precision of an individual particle. What is possible, though, is to give a description of the *average* localization precision of a large ensemble of particles. The PSF of a stationary sub-resolution particle is often described as a circular 2-D Gaussian distribution. The theory presented in this work, shows that a Gaussian description is *on average* still valid in case of 2-D and 3-D diffusion, but now with a variable standard deviation that depends on the diffusion coefficient and the image acquisition time. Note that it was recently shown that the apparent PSF of a single rotating dipole emitter can be approximated by a Gaussian function, which suggests that the proposed theory of a variable Gaussian variance can also be applied on moving fluorophores with dipole photon emission [32]. For an individual particle, the observed intensity distribution shape can deviate substantially from a circular Gaussian distribution. This explains why we found that determining the position of diffusing particles by the classic Gaussian fitting method ceased to work correctly for longer image acquisition times. The elliptical 2-D Gaussian function could possibly take the spot deformation somewhat better into account. However, our results showed that the localization precision was only slightly improved, compared to the circular 2-D Gaussian. Most likely, this is due to the fact that, compared to the stationary case, the shape of the apparent PSF becomes distorted and asymmetrical in such a way that it starts to exhibit multiple maxima for longer image acquisition times.

The centroid algorithm, which does not rely on any assumption on the shape of the observed intensity distribution, was found to be a superior particle location estimator in case of movement during image acquisition, compared to the least-squares fitting of the 2-D Gaussian. Through a rigorous mathematical derivation, we succeeded in deriving an expression that predicts the centroid localization precision for particles diffusing in the focal plane or even in 3-D. The theory matched almost perfectly with both simulated and experimental particle localization data. It was found that motion along the optical axis decreases the centroid precision nearly independently of the image acquisition time. The lateral motion in the focal plane only affects the centroid precision for long image acquisition times or large diffusion coefficients. For diffusing particles we conclude that the centroid method globally outperforms the much used least-squares fitting of a circular or elliptical Gaussian function. This would appear to be in disagreement with the conclusion put forward in the article by Cheezum et al., who made a systematic comparison between different localization algorithms [12]. By simulating images of stationary particles, they found that the Gaussian fitting method performed better than the centroid algorithm in low SNR conditions. However, particle motion was not considered, which turns out to be the determining factor for longer image acquisition times.

We would like to note that, although the theory accurately describes the centroid precision, it was derived under the specific assumption that all relevant pixels that contribute to the PSF are included in the centroid calculation, while background pixels should be excluded. Any deviation from this assumption might lead to a decrease in the localization precision compared to what is expected theoretically. We hypothesize that this, at least partially, could explain the small underestimation of the simulated values by the theory that we found. Possibly not all relevant pixels were included by the automated selection procedure, so that somewhat less photons were taken into account, leading to a slightly higher uncertainty on the particle locations as determined from the simulated images. An additional contribution to the experimental localization uncertainty could stem from the fact that a particle is never exactly located at the centre of a pixel. As a consequence, when selecting an iso-intensity contour, some more pixels might be included on one side of the centre compared to the other side. This in turn can lead to an additional contribution to the error in the determination of the particle location. Nevertheless, if these effects are present, they are in any case quite small considering the excellent agreement between theory and experiment.

Apart from applications in high-resolution localization microscopy (e.g. STORM/PALM), the theory of the localization precision that takes movement during image acquisition into account, can also be used to more precisely determine the diffusion coefficient from the MSD plot. The MSD expression in Eq. (5.13) for free diffusion contains two

important corrections. The first correction comes from the fact that the diffusing particle does not have a unique location during the image acquisition. Instead, the particle location is rather the average position of the particle during the image acquisition time [15-17]. The second correction was investigated in this study and takes into account the finite localization precision, which we have shown to depend on the diffusion coefficient, see Eq. (5.12). For accurate diffusion measurements we suggest to use Eq. (5.13) in combination with Eq. (5.12) for fitting to the MSD curves:

$$\text{MSD}_c = 4Dt - \frac{4}{3}D\Delta t + 4F \frac{\left(s_0^2 + \frac{z_{\text{lim}}^2}{3z_0^2}s_0^2 + \frac{a^2}{12}\right) + \left(\frac{1}{3} + \frac{s_0^2}{3z_0^2}\right)D\Delta t}{N} \quad (5.20)$$

$$+ 4F \frac{81\pi b^2 \left(\left(s_0^2 + \frac{z_{\text{lim}}^2}{3z_0^2}s_0^2 + \frac{a^2}{12}\right) + \left(\frac{1}{3} + \frac{s_0^2}{3z_0^2}\right)D\Delta t\right)^2}{4a^2N^2}.$$

By doing so, there is only one free fitting parameter, namely the diffusion coefficient D in all three terms. To check if this leads to a better precision of the fitted D -values, we least-squares fitted both Eqs. (5.13) and (5.20) to the MSD of the trajectories of diffusing particles in our SPT experiments (for an image acquisition time of 10 ms in the green channel). Only the MSD corresponding to the first 25% of the time lags were included [33]. Weights were included in the least-squares fitting according to the theory from Qian et al. [30]. The resulting diffusion coefficient distributions for both cases are shown in **Fig. 5.7**. Equation (5.13) resulted in a mean diffusion coefficient of $1.6 \mu\text{m}^2/\text{s}$ and a standard deviation of $0.7 \mu\text{m}^2/\text{s}$, while Eq. (5.20) resulted in a larger mean diffusion coefficient of $1.8 \mu\text{m}^2/\text{s}$ and a smaller standard deviation $0.6 \mu\text{m}^2/\text{s}$. The standard two-sample t -test rejected the null hypothesis of equal means, with a p -value $< 10^{-7}$. Although the data is not normally distributed, the sample is large enough to allow the use of the t -test according to the central limit theorem. We also investigated the null hypothesis of equal means for the mean and the standard deviation of both distributions with a simple bootstrap test [34]. This approximate test was run with 10^7 bootstrap replications, resulting in a p -value of 0 for the mean and the standard deviation. We can thus safely assume a p -value $< 10^{-7}$, allowing us to conclude that both the mean and standard deviation of both diffusion coefficient distributions are significantly different. This indeed indicates that fitting Eq. (5.20) to the MSD results in a more precise diffusion coefficient than using the classical MSD expression with two free fitting parameters according to Eq. (5.13). Interestingly, an entirely different approach to determine the diffusion coefficient has recently been reported, making use of the broadening of the observed intensity distribution because of the diffusion during image acquisition [35]. This method might be of interest when diffusion is too fast to

observe sufficiently long trajectories, but generally the MSD analysis should be preferred as it likely has a higher precision.

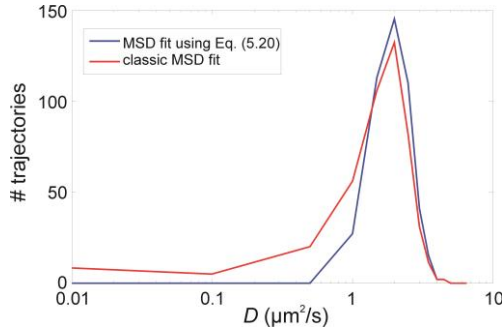


Figure 5.7 | The diffusion coefficient obtained from observed mean square displacements. The distribution of the diffusion coefficients determined by least-squares fitting of the classic Eq. (5.13) (red line) and of Eq. (5.20) (blue line) to the MSD of the particle trajectories from the SPT experiments in the green channel for an image acquisition time of 10 ms.

A practical consequence of our theory is that it allows to estimate an optimal image acquisition time for a given diffusion coefficient. To this end, it is instructive to write the theoretical centroid precision explicitly as a function of the image acquisition time. It is reasonable to assume that $N = r\Delta t$, meaning that the number of photons N increases linearly with the image acquisition time Δt , with r the observed photon emission rate. The localization precision in Eq. (5.12) can thus be rewritten as:

$$\sigma_c^2 = F \frac{\left(s_0^2 + \frac{z_{\text{lim}}^2}{3z_0^2} s_0^2 + \frac{a^2}{12}\right) + \left(\frac{1}{3} + \frac{s_0^2}{3z_0^2}\right) D \Delta t}{r \Delta t} + F \frac{81\pi b^2 \left(\left(s_0^2 + \frac{z_{\text{lim}}^2}{3z_0^2} s_0^2 + \frac{a^2}{12}\right) + \left(\frac{1}{3} + \frac{s_0^2}{3z_0^2}\right) D \Delta t\right)^2}{4a^2 r^2 \Delta t^2}. \quad (5.21)$$

The first term always decreases with larger image acquisition times. In a first approximation, we can assume that the background mainly comes from out-of-focus light, so that it is Poisson distributed with variance $b^2 = \beta \Delta t$.

This causes the second term in Eq. (5.21) to increase with larger image acquisition times (see **Fig. 5.8**), resulting in an optimal localization precision for the following image acquisition time:

$$\Delta t_{\min} = \sqrt{\frac{r \left(s_0^2 + \frac{z_{\lim}^2}{3z_0^2} s_0^2 + \frac{a^2}{12} \right) + \frac{81\pi}{4a^2} \beta \left(s_0^2 + \frac{z_{\lim}^2}{3z_0^2} s_0^2 + \frac{a^2}{12} \right)^2}{\frac{81\pi}{4a^2} \beta D^2 \left(\frac{1}{3} + \frac{s_0^2}{3z_0^2} \right)^2}}. \quad (5.22)$$

Beyond this point, the localization precision will deteriorate. This minimum, however, is quite weak and only occurs for long image acquisition times, for example around 274 ms for typical parameters values used in our experiments (see **Fig. 5.8**). This would result in very slow frame rates and is therefore not an optimal image acquisition time when studying dynamic events. In practice, one will typically have to make a trade-off between the localization precision and a sufficiently high frame rate, using Eq. (5.22).

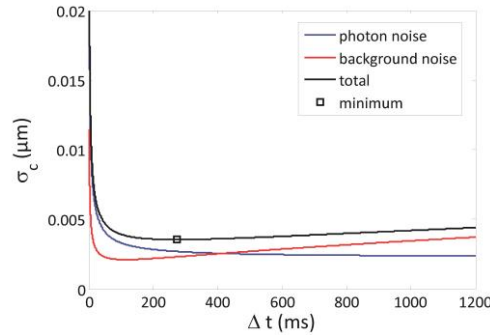


Figure 5.8 | The image acquisition time for optimal localization precision. Illustration of the contribution of the photon shot noise term and the background noise term to the total centroid precision (see Eq. (5.21)) in function of the image acquisition time. Parameter values typical for our experiments (the green channel) were used in Eq. (5.21). The image acquisition time corresponding to the minimum precision (see Eq. (5.22)) is indicated as a square.

Although only the case of free particle diffusion was treated in **Section 5.2**, one could wonder what the effect would be in case of anomalous sub- or super-diffusion. These types of motion can be described by a Gaussian probability distribution that is similar to the one for free diffusion, but with the diffusion coefficient replaced by a time-dependent variable [3]. However, considering the increased complexity, it is likely not worth the effort, since the image acquisition time is short compared to the time scale

over which the MSD curve should be analyzed in order to detect anomalous diffusion. Indeed, for short time lags, the MSD curve is always nearly linear so that it seems sensible to describe the particle movement by free diffusion during the short image acquisition time.

Besides the theoretical model, also a simple empirical method was presented that allows to experimentally determine the localization precision of moving particles. Usually, the localization precision is calculated experimentally by taking the standard deviation of the positions of the same particle determined at several time points. This approach is valid for stationary particles, but of course not for moving particles whose position is unknown and variable over time. The proposed dual-channel method calculates the localization precision using the standard deviation of the differences between the positions of two trajectories of the same particle, determined simultaneously in two different channels. In this study, we have made use of multi-colour beads that are visible in two spectrally different channels. However, it should be noted that this method is not limited thereto, and it is equally possible to make use of e.g. a 50/50 mirror and detect the same image on two detectors (or two halves of a CCD chip as was done here). The only requirement for the dual-channel method to work is that the photons in both channels should be detected independently from each other. Noteworthy, this dual-channel method is not limited to a specific type of motion so that it could be also applied to other types of motion than free diffusion.

5.6 CONCLUSION

We have shown that movement during the image acquisition time degrades the precision with which single particles or molecules can be localized. In agreement with our theory, lateral movement in the focal plane was found only to affect the precision for large image acquisition times, while axial movement perpendicular to the focal plane always degraded the precision. Attention should be paid in case of fitting of a Gaussian function, because the deformation of the point spread function caused by lateral movement results in a rapid deterioration of the localization precision. The centroid algorithm does not suffer from this drawback and is, therefore, a more reliable position estimator for moving particles.

REFERENCES

1. J. E. N. Jonkman and E. H. K. Stelzer, "Resolution and Contrast in Confocal and Two-Photon Microscopy," in *Confocal and Two-Photon Microscopy : Foundation, Applications, and Advances*, A. Alberto, ed., (Wiley-Liss, Inc., New York, 2002), pp. 101-126.
2. V. Levi and E. Gratton, "Exploring dynamics in living cells by tracking single particles," *Cell Biochemistry and Biophysics* 48, 1-15 (2007).
3. M. J. Saxton and K. Jacobson, "Single-particle tracking: Applications to membrane dynamics," *Annual Review of Biophysics and Biomolecular Structure* 26, 373-399 (1997).
4. S. Wieser and G. J. Schutz, "Tracking single molecules in the live cell plasma membrane-Do's and Don't's," *Methods* 46, 131-140 (2008).
5. E. Betzig, G. H. Patterson, R. Sougrat, O. W. Lindwasser, S. Olenych, J. S. Bonifacino, M. W. Davidson, J. Lippincott-Schwartz, and H. F. Hess, "Imaging intracellular fluorescent proteins at nanometer resolution," *Science* 313, 1642-1645 (2006).
6. W. E. Moerner, "New directions in single-molecule imaging and analysis," *Proceedings of the National Academy of Sciences of the United States of America* 104, 12596-12602 (2007).
7. S. Manley, J. M. Gillette, G. H. Patterson, H. Shroff, H. F. Hess, E. Betzig, and J. Lippincott-Schwartz, "High-density mapping of single-molecule trajectories with photoactivated localization microscopy," *Nature Methods* 5, 155-157 (2008).
8. R. J. Ober, S. Ram, and E. S. Ward, "Localization accuracy in single-molecule microscopy," *Biophysical Journal* 86, 1185-1200 (2004).
9. N. Bobroff, "Position Measurement with A Resolution and Noise-Limited Instrument," *Review of Scientific Instruments* 57, 1152-1157 (1986).
10. R. E. Thompson, D. R. Larson, and W. W. Webb, "Precise nanometer localization analysis for individual fluorescent probes," *Biophysical Journal* 82, 2775-2783 (2002).
11. K. I. Mortensen, L. S. Churchman, J. A. Spudich, and H. Flyvbjerg, "Optimized localization analysis for single-molecule tracking and super-resolution microscopy," *Nature Methods* 7, 377-U59 (2010).
12. M. K. Cheezum, W. F. Walker, and W. H. Guilford, "Quantitative comparison of algorithms for tracking single fluorescent particles," *Biophysical Journal* 81, 2378-2388 (2001).
13. R. N. Ghosh and W. W. Webb, "Automated Detection and Tracking of Individual and Clustered Cell-Surface Low-Density-Lipoprotein Receptor Molecules," *Biophysical Journal* 66, 1301-1318 (1994).
14. Y. Wong, Z. P. Lin, and R. J. Ober, "Limit of the Accuracy of Parameter Estimation for Moving Single Molecules Imaged by Fluorescence Microscopy," *Ieee Transactions on Signal Processing* 59, 895-911 (2011).
15. M. Goulian and S. M. Simon, "Tracking single proteins within cells," *Biophysical Journal* 79, 2188-2198 (2000).
16. X. Michalet, "Mean square displacement analysis of single-particle trajectories with localization error: Brownian motion in an isotropic medium," *Physical Review e* 82, (2010).
17. T. Savin and P. S. Doyle, "Static and dynamic errors in particle tracking microrheology," *Biophysical Journal* 88, 623-638 (2005).

18. D. Montiel, H. Cang, and H. Yang, "Quantitative characterization of changes in dynamical behavior for single-particle tracking studies," *Journal of Physical Chemistry B* 110, 19763-19770 (2006).
19. M. Born and E. Wolf, *Principles of optics*, (Cambridge University Press, Cambridge, 1999).
20. T. W. Quan, S. Q. Zeng, and Z. L. Huang, "Localization capability and limitation of electron-multiplying charge-coupled, scientific complementary metal-oxide semiconductor, and charge-coupled devices for superresolution imaging," *Journal of Biomedical Optics* 15, (2010).
21. M. S. Robbins and B. J. Hadwen, "The noise performance of electron multiplying charge-coupled devices," *Ieee Transactions on Electron Devices* 50, 1227-1232 (2003).
22. A. Yariv, *Quantum electronics*, (John Wiley & Sons, Inc., New York, 1989).
23. M. Rödning, H. Deschout, K. Braeckmans, and M. Rudemo, "Measuring absolute number concentrations of nanoparticles using single-particle tracking," *Physical Review e* 84, (2011).
24. K. Braeckmans, D. Vercauteren, J. Demeester, and S. C. De Smedt, "Single Particle Tracking," in *Nanoscopy and Multidimensional Optical Fluorescence Microscopy*, A. Diaspro, ed., (CRC Press / Taylor & Francis Group, Boca Raton, 2010).
25. J. C. Crocker and D. G. Grier, "Methods of digital video microscopy for colloidal studies," *Journal of Colloid and Interface Science* 179, 298-310 (1996).
26. I. Koyama-Honda, K. Ritchie, T. Fujiwara, R. Iino, H. Murakoshi, R. S. Kasai, and A. Kusumi, "Fluorescence imaging for monitoring the colocalization of two single molecules in living cells," *Biophysical Journal* 88, 2126-2136 (2005).
27. K. Braeckmans, K. Buyens, W. Bouquet, C. Vervaeke, P. Joye, F. De Vos, L. Plawinski, L. Doeuvre, E. ngles-Cano, N. N. Sanders, J. Demeester, and S. C. De Smedt, "Sizing Nanomatter in Biological Fluids by Fluorescence Single Particle Tracking," *Nano Letters* 10, 4435-4442 (2010).
28. J. R. Janesick, *Scientific Charge-Coupled Devices*, (SPIE - The International Society for Optical Engineering, Bellingham, Washington, 2001).
29. M. J. Saxton, "Single-particle tracking: The distribution of diffusion coefficients," *Biophysical Journal* 72, 1744-1753 (1997).
30. H. Qian, M. P. Sheetz, and E. L. Elson, "Single-Particle Tracking - Analysis of Diffusion and Flow in 2-Dimensional Systems," *Biophysical Journal* 60, 910-921 (1991).
31. S. Ram, E. S. Ward, and R. J. Ober, "A stochastic analysis of performance limits for optical microscopes," *Multidimensional Systems and Signal Processing* 17, 27-57 (2006).
32. S. Stallinga and B. Rieger, "Accuracy of the Gaussian Point Spread Function model in 2D localization microscopy," *Optics Express* 18, 24461-24476 (2010).
33. M. J. Saxton, "Single-particle tracking: The distribution of diffusion coefficients," *Biophysical Journal* 72, 1744-1753 (1997).
34. B. Efron and R. J. Tibshirani, *An Introduction to the Bootstrap*, (Chapman & Hall/CRC, Boca Raton, 1993).
35. S. K. Zareh, M. C. DeSantis, J. M. Kessler, J. L. Li, and Y. M. Wang, "Single-Image Diffusion Coefficient Measurements of Proteins in Free Solution," *Biophysical Journal* 102, 1685-1691 (2012).

Chapter 6

Correlation of dual colour single particle trajectories for improved detection and analysis of interactions in living cells

This chapter is submitted for publication:

Hendrik Deschout^{1,2}, Thomas Martens^{1,2}, Dries Vercauteren^{1,2}, Katrien Remaut¹, Jo Demeester¹, Stefaan C. De Smedt¹, Kristiaan Neyts^{3,2}, Kevin Braeckmans^{1,2}.

¹Laboratory of General Biochemistry and Physical Pharmacy, Ghent University, Belgium

³Centre for Nano- and Biophotonics, Ghent University, Belgium

³Liquid Crystals and Photonics Group, Ghent University, Belgium

ABSTRACT

Interactions between objects inside living cells are often investigated by looking for colocalization between fluorescence microscopy images that are recorded in separate colours corresponding to the fluorescent label of each object. The fundamental limitation of this approach in case of dynamic objects is that coincidental colocalization cannot be distinguished from true interaction. Instead, correlation between motion trajectories obtained by dual colour single particle tracking provides a much stronger indication of interaction. However, frequently occurring phenomena in living cells, such as immobile phases or transient interactions, can limit the correlation to small parts of the trajectories. The method presented here, developed for the detection of interaction, is based on the correlation inside a window that is scanned along the trajectories, covering different subsets of the positions. This scanning window method was validated by simulations and, as an experimental proof of concept, it was applied to the investigation of the intracellular trafficking of polymeric gene complexes by endosomes in living retinal pigment epithelium cells, which is of interest to ocular gene therapy.

6.1 INTRODUCTION

In the field of gene therapy, a lot of effort goes to the development of nanomedicines, with a size in the order of 100 nm, for the delivery of therapeutic nucleic acids to target cells [1]. The way such nanomedicines are processed inside these cells is one of the main determinants of their effectiveness. In order to optimize the performance of nanomedicines it is, therefore, important to understand how they interact with the intracellular constituents, such as endosomes, that are involved in their transport and final fate. Fluorescence microscopy is the ideal tool to make this type of information available, by simultaneously recording multi-colour live-cell images of fluorescently labelled nanomedicines and intracellular organelles [2-5].

The most common way of investigating interactions in multi-colour images is by comparing pixel values between colours, for which different quantification methods exist [6-11]. However, these pixel based methods are very susceptible to false positives, i.e. all labelled compounds closer together than the microscope resolution (usually 250 nm or more) will contribute to the overall colocalization in the image. Fluorescence resonance energy transfer (FRET) offers an alternative that is not restricted by the resolution, but has a limited working range of 1-10 nm [12]. Another approach is looking for the colocalization of discrete objects, rather than individual pixel values [13-18]. The basic condition here is that the objects of interest can be identified as separate entities in the microscopy images. One possibility to quantify object based colocalization is to compare their intensity weighted centre positions to each other [19]. The objects are classified as colocalized when their intensity weighted centre positions are closer together than a user defined maximum distance. Another possibility to quantify object based colocalization is to calculate the spatial overlap of the objects in both images [16]. Just like FRET, these object based methods are better in excluding false positives than pixel based colocalization, since the object positions can be determined with a precision much better than the microscope's resolution [20,21].

In live-cell imaging, or any other application that involves dynamic events, the objects of interest, such as proteins or organelles, might be mobile. Two objects that are moving past each other by coincidence could, therefore, be identified as being colocalized by either the pixel or object based methods. This can be especially problematic in case of very dense object populations. One potential solution is to perform two-colour image cross-correlation spectroscopy (ICCS) [22,23]. Two interacting objects that move together will give rise to correlated fluorescence intensity

fluctuations between the two simultaneously recorded detection channels. Unfortunately, this method only provides information that is spatially averaged over the part of the image that is included in the analysis. Another solution that retains the spatial information is to look at trajectories of moving objects in dual colour time-lapse movies, as is done in single particle tracking (SPT) [24-26]. When two objects remain together for a significant amount of time (i.e. in multiple consecutive images), this is a strong indication that they are truly interacting. Recently, our group proposed an object based approach for investigating the interaction between moving objects based on the spatial correlation of their trajectories obtained by dual colour SPT [27]. When the correlation between the trajectories exceeds a certain threshold value, the corresponding objects are considered to be interacting. Interestingly, as correlation is translation independent, it does not require a user defined maximum distance and offers the possibility to detect interactions at any distance within the image. This was shown to give more reliable results than in case of classic object based analysis.

However, an objective measure for the correlation threshold has not been determined. Also, as the published correlation method is based on calculating the correlation between complete trajectories, it performs suboptimal in case trajectories are not completely correlated. For instance, intracellular motion can exhibit variable mobility, including immobile phases that inherently do not correlate. Another example is photobleaching of fluorescent labels, which degrades the localization precision in the trajectories, in turn affecting their correlation. There is also the possibility of transient interactions that take place during only a short time span, restricting the correlation to only a part of the trajectories. If the uncorrelated part of the trajectories in these situations is sufficiently large, the correlation determined from all positions in the trajectories will not exceed the correlation threshold, despite (transient) interaction being present. A method that can identify correlation in smaller segments of the trajectories with an objectively determined correlation threshold is, therefore, required. In **Chapter 6**, such a method is presented, based on a scanning window approach in which the correlation is calculated over a limited number of positions within the trajectories. The optimal size of the window and the correlation threshold value are selected according to criteria that account for the localization precision in the trajectories and the mobility of the objects. The scanning window method is verified by simulations and applied to investigate the intracellular trafficking of polymeric gene complexes inside endosomes of living cells.

6.2 THEORY

6.2.1 Identifying interaction by correlated motion

As mentioned in **Section 6.1**, we have recently proposed a new approach to identify interaction [27]. Instead of looking for colocalization in terms of a maximum distance, interaction between two objects is assumed to result in trajectories whose positions are correlated in time. Consider two sequences of images in different colours acquired at time points t_i (with $i = 1, \dots, l$). The observed motion trajectory A of an object in one colour is given by $(x_A(t_i), y_A(t_i))$, and the observed motion trajectory B of an object in the other colour is given by $(x_B(t_i), y_B(t_i))$. The Pearson correlation coefficient ρ between the x -coordinates of both trajectories can be calculated from:

$$\rho = \frac{\sum_{i=1}^l (x_A(t_i) - \langle x_A \rangle)(x_B(t_i) - \langle x_B \rangle)}{\sqrt{\sum_{i=1}^l (x_A(t_i) - \langle x_A \rangle)^2 \sum_{i=1}^l (x_B(t_i) - \langle x_B \rangle)^2}}, \quad (6.1)$$

with $\langle x_A \rangle$ and $\langle x_B \rangle$ the average x -coordinates of the trajectories A and B , respectively. The same definition applies to the y -coordinates. From now on, we will only consider the x -coordinates as the theory equally applies to the other dimensions. Define σ_A and σ_B as the localization precisions with which $x_A(t_i)$ and $x_B(t_i)$, respectively, were determined. Besides various experimental noise sources, the localization precision is essentially determined by the number of detected photons and their spatial distribution in the image [20,21]. Define σ_o as the overlay precision with which both colour images are aligned, which can be calculated as the standard deviation of the differences between identical positions in the images after overlay [26].

The effect of σ_A , σ_B and σ_o on the correlation ρ between the trajectories is illustrated in **Fig. 6.1**, showing that, even if both objects are interacting, perfect correlation will not be obtained. This means that the computed correlation coefficient $\rho < 1$ should have a p -value smaller than 0.05, to make sure that it reflects true correlation rather than being obtained by coincidence under the null hypothesis that there is actually no correlation. However, a condition based on the p -value alone would mean that there is 5% chance of getting false positives in case of non-correlated trajectories. To reduce this probability, a correlation threshold ρ_{\min} , defined as the minimum correlation that is expected in case of correlated trajectories, can be imposed. As will be explained below, the ρ_{\min} threshold value depends on σ_A , σ_B and σ_o , as well as on other trajectory properties.

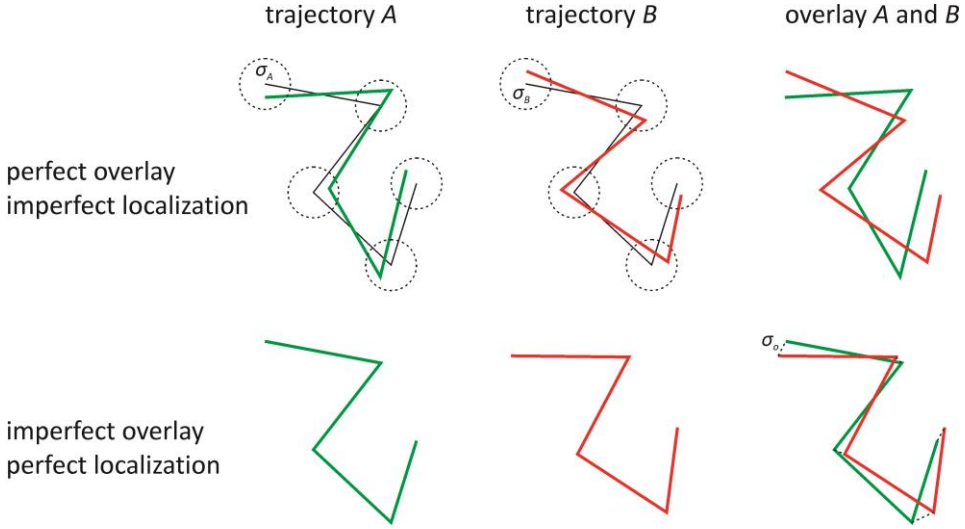


Figure 6.1 | The effect of the localization and overlay precision on the observed trajectories. The localization precision σ_A and σ_B of the positions in the observed trajectories A (green) and B (red), respectively, are defined as the standard deviation (dotted circles) of the observed positions around the true positions (black). The overlay precision σ_o between the images is defined as the standard deviation of the differences (dotted lines) between identical positions in the images after overlay.

6.2.2 Correlation threshold

For a certain localization and overlay precision, the correlation threshold ρ_{\min} can be defined as the minimum correlation with a p -value smaller than 0.05 that a pair of trajectories coming from interacting objects can have. Although the localization precision may vary to some extent along a trajectory, we will assume that it remains constant, as motivated in **Section 6.2.3**.

First, consider the situation of an equal localization precision $\sigma = \sigma_A = \sigma_B$ in both trajectories and a perfect overlay precision $\sigma_o = 0$. For Brownian or linear motion, which is common in live-cell imaging, it can be shown that the expected correlation ρ between trajectories with l positions is completely determined by the relative localization precision r (see **Appendix B**):

$$r = \frac{\sigma}{S}, \quad (6.2)$$

where S is the mean step length in the trajectories, which can be estimated as:

$$S = \frac{1}{2l} \sum_{i=2}^l (|x_A(t_i) - x_A(t_{i-1})| + |x_B(t_i) - x_B(t_{i-1})|). \quad (6.3)$$

The expected value of the observed correlation ρ is thus identical for all trajectory pairs with l positions and relative localization precision r , which means that the same correlation threshold ρ_{\min} can be used for all these trajectories.

It can be shown that the same applies to the general and more realistic case of $\sigma_A \neq \sigma_B$ and $\sigma_o \neq 0$ (see **Appendix B**). In this case, however, the localization precision σ in Eq. (6.2) should be calculated according to:

$$\sigma^2 = -\frac{\text{var}(x_A) + \text{var}(x_B) - \sigma_A^2 - \sigma_B^2 - \sigma_o^2}{2} + \frac{\sqrt{(\text{var}(x_A) + \text{var}(x_B))^2 + (\sigma_A^2 - \sigma_B^2)^2 - 2(\text{var}(x_A) - \text{var}(x_B))(\sigma_A^2 - \sigma_B^2)}}{2} \quad (6.4)$$

where $\text{var}(x_A)$ and $\text{var}(x_B)$ are the variances of the x -coordinates in the trajectories A and B , respectively.

6.2.3 Scanning window concept

In many circumstances, such as live-cell imaging, objects usually exhibit a variable mobility. When a certain part of the trajectories exhibits low mobility, the local mean step length S is smaller than the value over the entire trajectory. From Eq. (6.2), it immediately follows that the local relative localization precision r degrades (i.e. the value r increases), which in turn decreases the correlation in this part of the trajectories. The same effect can be caused by a locally lower localization precision σ_A and σ_B , as can be seen from Eqs. (6.2) and (6.4). Another effect that can cause a change in correlation along the trajectories is the presence of transient interactions, such as binding and unbinding events. These different situations are illustrated in **Fig. 6.2**. Thus, it is clear that assessing interaction by evaluating the correlation over the entire trajectories may not be optimal.

One obvious solution to this problem lies in identifying correlation in smaller parts of the trajectories to which the framework of **Section 6.2.2** can be applied. This idea leads to the scanning window method, as illustrated in **Fig. 6.3**. Basically, the correlation is

calculated in small overlapping subsets of trajectory positions, i.e. in a window that is scanned along the trajectories. If the observed correlation in a window has a p -value smaller than 0.05 and is larger than the threshold ρ_{\min} for that window, the objects are considered to be interacting in that window. This threshold ρ_{\min} depends on the size of the window and the local relative localization precision r (cfr. Eq. (6.2)).

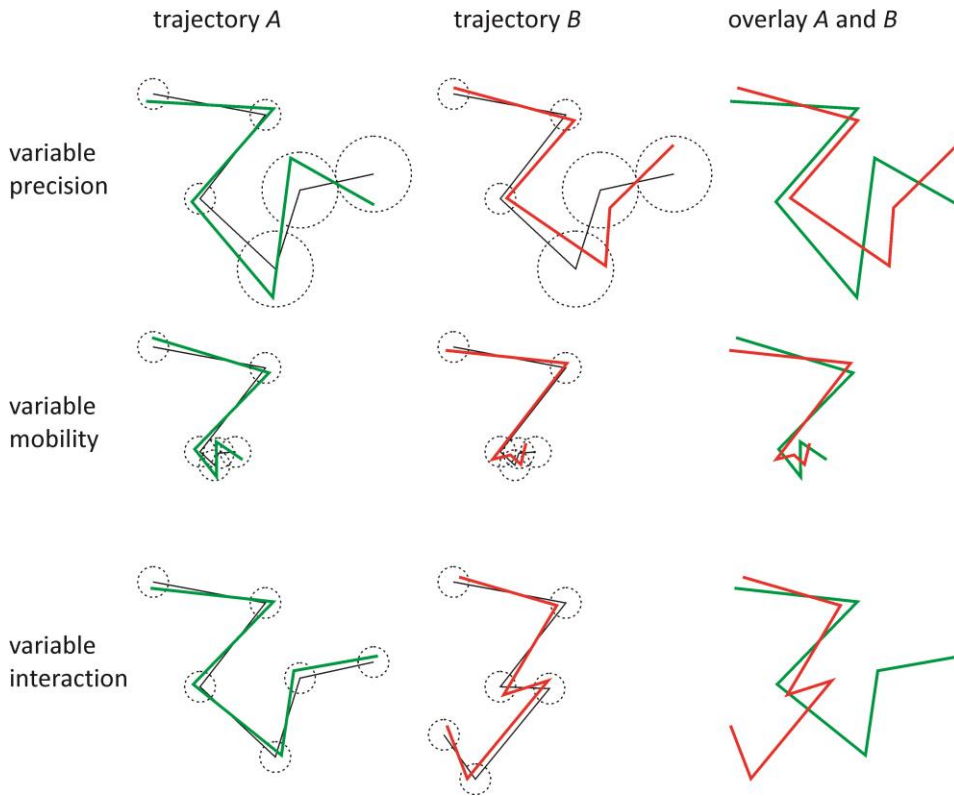


Figure 6.2 | The effect of a time dependent mobility, localization precision or interaction on the observed trajectories. The localization precision of the positions in the observed trajectory A (green) and B (red), respectively, are defined as the standard deviation (dotted circles) of the observed positions around the positions of the true trajectories (black). When one part of the trajectories exhibits low localization precision, the local relative localization precision is high, degrading the correlation in that part. Also, when one part of the trajectories exhibits low mobility, the local relative localization precision is high, which in turn degrades the correlation in that part. When the objects do not interact in one part of the trajectories, there is even no correlation in that part.

This raises the important question of what is the optimal window size. On the one hand, the window should be as small as possible in order to have the best temporal resolution and to ensure that the variation in relative localization precision is minimal. On the other hand, the window should include a sufficient number of positions in order to detect correlation with sufficient statistical significance. Consider correlated trajectories and define P as the probability to observe a correlation with a p -value smaller than 0.05 inside a window with length w . Similar to the correlation threshold ρ_{\min} , this probability P depends on the relative localization precision r . The optimal window length is then defined as the smallest w for which P becomes larger than a user defined value. Since the window size cannot be smaller than 3, each position will be evaluated in at least 3 different windows (except at the trajectory extremities). The probability that the correlation in at least one of those windows has a p -value smaller than 0.05 is given by $1 - (1-P)^3$. A probability of more than 0.99 is achieved by $P = 0.8$, which is the threshold value for P used throughout this study.

6.2.4 Numerical determination of ρ_{\min} and P

The values of the correlation thresholds ρ_{\min} (see **Section 6.2.2**) and the values of the probabilities P to identify the optimal window length (see **Section 6.2.3**) were obtained by simulating correlated trajectory pairs that represent windows of different sizes with different relative localization precisions. The simulations were performed in the Matlab programming environment (The Mathworks, USA). First, one-dimensional trajectories were simulated for each combination of trajectory length w and relative localization precision r from a set of pre-defined values (i.e. $w = 3, 4, \dots, 200$ and $r = 0.01, 0.02, \dots, 1.00$). The number of simulated trajectories N_w depended on the trajectory length w , so that the total amount of positions from all trajectories together was approximately 10^6 in all cases (e.g. for $w = 10$, the number of trajectories was 10^5). The type of motion was chosen to be Brownian motion, since it is common on a microscopic scale, and because unrelated Brownian trajectories on average do not exhibit correlation. The diffusion coefficient was taken to be $D = 1 \mu\text{m}^2/\text{s}$ and the time interval between subsequent positions was $\tau = 0.1 \text{ s}$, resulting in a one-dimensional mean step of $S = \sqrt{2D\tau} = 0.447 \mu\text{m}$. The normally distributed step of the Brownian trajectories was simulated by the Matlab function *randn*. From each simulated trajectory, two correlated trajectories were extracted by separately adding two normally distributed values to each position of the simulated trajectory, again using the Matlab function *randn*. The standard deviation of the normal distribution for the extra value is the localization precision $\sigma = rS$ (cfr. Eq. (6.2)).

Subsequently, the correlation ρ between both trajectories is calculated, using the Matlab function *corrcoef* together with its corresponding p -value. For each value of w and r , let $N_{w,p}$ be the number of trajectory pairs that are correlated with a p -value smaller than 0.05. Then $P = N_{w,p}/N_w$ is the probability of finding a statistically significant correlation ρ in case of interacting objects. The results are partially shown in **Table 6.1**. The minimum value of the statistically significant correlations is selected as the threshold correlation ρ_{\min} for a given w and r , as partially shown in **Table 6.2**. Note that for the smallest trajectory lengths w sometimes a correlation ρ smaller than zero was found (anti-correlation) with a p -value larger than 0.05. These correlations were treated as if they were not statistically significant. Also note that the values of ρ_{\min} do not always increase with the trajectory length w . When the trajectories are too short, only high enough correlations are statistically significant. Only from the point where the trajectories are long enough so that all correlations become significant (i.e. $P = 1$) does ρ_{\min} increase with w . The practical use of **Table 6.1** and **6.2** is explained in **Section 6.2.5**.

Simulated values of the probability P						
	$w = 3$	$w = 4$	$w = 5$	$w = 6$...	$w = 200$
$r = 0.01$	0.97177	0.99992	1	1		1
$r = 0.02$	0.90433	0.99872	1	1		1
$r = 0.03$	0.82096	0.99532	0.99980	1		1
$r = 0.04$	0.73582	0.99020	0.99950	1		1
$r = 0.05$	0.65341	0.98112	0.99815	0.99982		1
\vdots						
$r = 1.00$	0.04623	0.07992	0.12200	0.19284		1

Table 6.1 | Simulated values of the probabilities P . The probability P to observe a statistically significant correlation in a window with length w in a pair of trajectories coming from interacting objects with relative localization precision r . The values were obtained from simulations of completely correlated trajectories for different lengths $w = 3, 4, \dots, 200$ and different relative localization precisions $r = 0.01, 0.02, \dots, 1.00$.

6.2.5 Scanning window method

The main input for the scanning window method consists of the trajectory A given by $(x_A(t_i), y_A(t_i))$ and the trajectory B given by $(x_B(t_i), y_B(t_i))$ at the time points t_i (with $i = 1, 2, \dots, l$). Other required input is the localization precision σ_A and σ_B of trajectory A and B , respectively, calculated within the window as it is scanned along the trajectories, and the overlay precision σ_o between the images (see **Section 6.3.4** for an explanation of how these values can be determined experimentally).

Simulated values of the correlation threshold ρ_{\min}						
	$w = 3$	$w = 4$	$w = 5$	$w = 6$...	$w = 200$
$r = 0.01$	0.99693	0.95043	0.97095	0.99242		0.99998
$r = 0.02$	0.99692	0.95013	0.88554	0.89819		0.9999
$r = 0.03$	0.99692	0.95003	0.88114	0.91113		0.99972
$r = 0.04$	0.99692	0.95004	0.88418	0.87069		0.99965
$r = 0.05$	0.99692	0.95001	0.87854	0.81552		0.99925
\vdots						
$r = 1.00$	0.99693	0.95002	0.87836	0.81141		0.77525

Table 6.2 | Simulated values of the correlation threshold ρ_{\min} . The correlation threshold ρ_{\min} is the minimum statistically significant correlation in a window with length w and local relative localization precision r in a pair of trajectories coming from interacting objects. The values are obtained from simulations of completely correlated trajectories for different lengths $w = 3, 4, \dots, 200$ and different relative localization precisions $r = 0.01, 0.02, \dots, 1.00$.

Consider first the x -coordinates of the trajectories A and B . The scan starts at $x_A(t_1)$ and $x_B(t_1)$, with a window of size $w = 3$, which thus covers the x -coordinates from t_1 to t_3 . The relative localization precision r in that window is calculated, according to Eqs. (6.2) to (6.4). For the relative localization precision r and the window length $w = 3$, the probability P can be derived from **Table 6.1**, after rounding the value of r to the nearest tabulated value. For example, $r = 0.045$ is rounded to 0.05, and the corresponding row in **Table 6.1** shows $P = 0.653$ (for $w = 3$). If the window has a

probability $P \geq 0.8$, it is considered to be the optimal window. If the window has a probability $P < 0.8$, it is extended to a size $w = 4$, covering the x -coordinates from t_1 to t_4 . In the same manner, the probability P is calculated in the new window. This procedure is repeated until the optimal window size is reached for which $P \geq 0.8$. In case the window size would become larger than both trajectories A and B , the calculation is aborted as correlation cannot be determined with sufficient certainty.

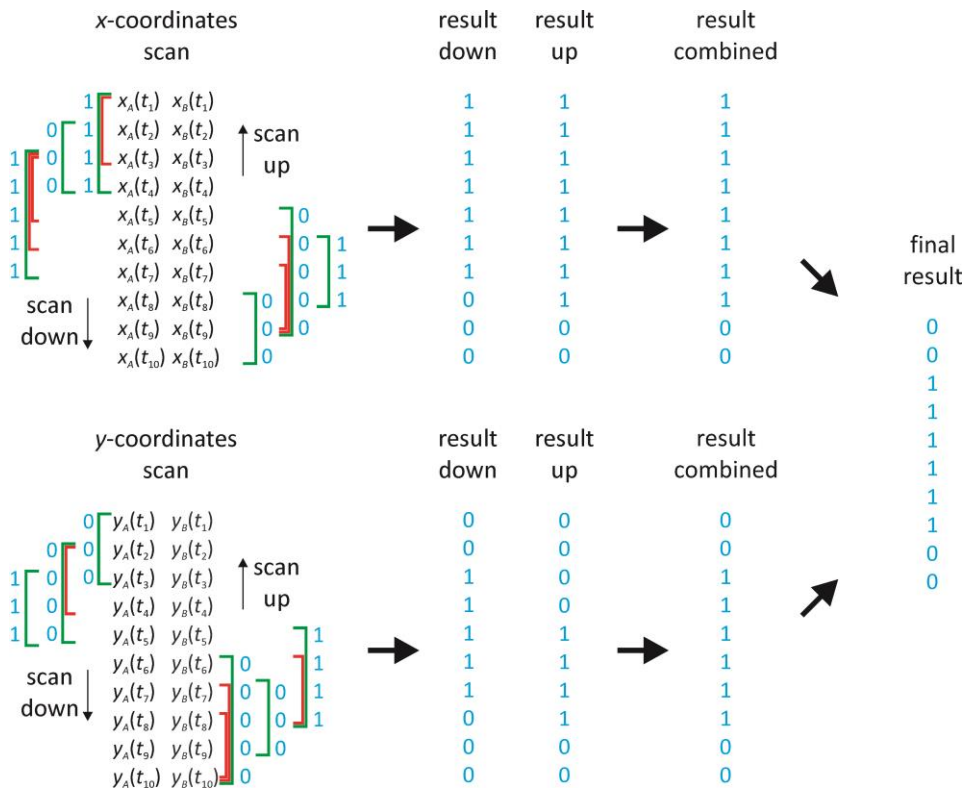


Figure 6.3 | An illustration of the scanning window method. A trajectory A and a trajectory B are analyzed by the scanning window method. The scan happens in two directions (up and down) for both the x - and y -coordinates independently. For each position, the window size starts at $w = 3$, and the probability P is calculated in the window (see **Table 6.1**). If $P < 0.8$ (red window), an extra position is included in the window, until an optimal window size with $P \geq 0.8$ is found (green window) for which the correlation is calculated. If the correlation is larger than the threshold ρ_{\min} of the window (see **Table 6.2**) with a p -value smaller than 0.05, the positions in the window are assumed to interact (symbolized by binary values 1). If this is not the case, the positions are considered not to interact (symbolized by binary values 0). The results of the different windows and of both scans are combined according to the logical OR operation. The results of both coordinates are finally combined according to the logical AND operation.

Having determined the optimal window size w and the local relative localization precision r , the correlation threshold ρ_{\min} can be determined from **Table 6.2**, again after rounding the value of r to the nearest tabulated value. Next, the correlation ρ between x -coordinates from both trajectories within the window is calculated according to Eq. (6.1), together with the corresponding p -value. If the p -value is smaller than 0.05, and the correlation ρ is larger than the correlation threshold ρ_{\min} , all x -coordinates in the window are assigned a binary value 1 (see **Fig. 6.3**). In all other cases, a binary value 0 is assigned to all x -coordinates in that window.

This procedure is repeated, starting at the next positions $x_A(t_2)$ and $x_B(t_2)$. The x -coordinates of the trajectories A and B are further scanned, position by position, until $x_A(t_{l-2})$ and $x_B(t_{l-2})$ have been reached. Except near the start and end of the trajectory, the positions are evaluated at least three times by different windows. Therefore, for each position there are at least three binary values, indicating that correlation was found or not within a particular window. If correlation was found at least one time, the position is flagged as being correlated. This results in a list of binary values that identify the positions where the scan found correlation (see **Fig. 6.3**). The same scanning procedure is repeated in the other direction, starting from $x_A(t_l)$ and $x_B(t_l)$ and moving towards the start of the trajectory. The results from both scanning directions are combined so that a position is correlated if it was flagged in one of both scanning directions (see **Fig. 6.3**).

The identical scanning window procedure as described above is applied to the y -coordinates. Afterwards, interaction is assigned to a position if correlation was found in each dimension (see **Fig. 6.3**). The result is a list of binary values that identify the positions where the objects were found to interact.

6.3 MATERIALS AND METHODS

6.3.1 Validation simulations

The scanning window method was validated by simulations in Matlab. Different sets of 1000 pairs of two-dimensional Brownian motion trajectories with length $l = 20$ and time interval $\tau = 0.1$ s between successive positions were simulated. The Brownian motion step in each dimension was simulated with the Matlab function *randn*, assuming a standard deviation equal to the mean step $S = \sqrt{2D\tau}$. In most sets, the diffusion coefficient was taken $D = 1 \mu\text{m}^2/\text{s}$, resulting in $S = 0.447 \mu\text{m}$. The two

trajectories of each simulated pair start at the same position, and remain identical as long as there is interaction, depending on the set. A normally distributed value was added to each coordinate of each trajectory separately, again using the Matlab function *randn*. The standard deviation of this normal distribution is the localization precision σ , which is equal for both trajectories. The values of the localization precision were either chosen $\sigma = 4.47$ nm or $\sigma = 44.7$ nm, in order to obtain a relative localization precision $r = 0.01$ or $r = 0.10$, respectively, according to Eq. (6.2). The overlay was taken to be perfect, i.e. $\sigma_o = 0$. In one set, the localization precision was different in the first and second half of the trajectories. In another set, the diffusion coefficient was different in the two trajectory halves, both leading to local relative localization precisions in the windows that are variable. The different conditions of each set of simulated trajectories are listed in **Table 6.3**. The scanning window method is applied to each pair of simulated trajectories, as explained in **Section 6.2.5**.

6.3.2 Live-cell sample preparation

The preparation of the sample for the live-cell dual colour SPT experiments is described in detail elsewhere [27]. Briefly, ARPE-19 cells (retinal pigment epithelial cell line; ATCC number CRL-2302) were cultured in DMEM:F12 supplemented with 10% FBS, 2 mM L-glutamine, and 2% P/S. All cells were grown at 37 °C in a humidified atmosphere containing 5% CO₂. The pGL4.13 plasmid was labelled with Cy5 using the Label IT Nucleic Acid Labeling Kit (Mirus Bio Corporation, USA), according to the manufacturer's instructions at a 1:2 (v:w) ratio of Label IT Tracker Reagent and plasmid. Polymeric gene complexes were obtained by adding a poly(N,N'-cystaminebisacrylamide 4-aminobutanol) (p(CBA-ABOL)) solution of 0.6 mg/mL to a plasmid solution of 0.05 mg/mL in a final mass ratio of 48/1 in 25 mM HEPES buffer pH 7.2 and vortexing the mixture for 10 s. ARPE-19 cells were seeded at a concentration of 220.000 cells per well on sterile MatTek coverslips (1.5)-bottom dishes (MatTek Corporation, USA). The next day, cells were transfected with plasmids coding for the EGFP construct EGFPFlot2 using Lipofectamine according to the manufacturer's description. Fresh polymeric gene complexes were diluted 5x in OptiMEM when added to the cells expressing fluorescent protein constructs, corresponding to 4 µg of Cy5-labeled plasmid. Intense contact with the cells was assured through repetitive pipetting at room temperature, allowing electrostatic adhesion of the polyplexes to the plasma membrane. Next, the cells were washed and imaged in fresh OptiMEM to chase the cell-associated fraction of polymeric gene complexes.

Trajectory properties in the validation simulations					
Situation	Positions	Interaction	D	S	σ
interaction, $r = 0.01$	1 - 20	yes	$1 \mu\text{m}^2/\text{s}$	$0.447 \mu\text{m}$	4.47 nm
interaction, $r = 0.10$	1 - 20	yes	$1 \mu\text{m}^2/\text{s}$	$0.447 \mu\text{m}$	44.7 nm
no interaction, $r = 0.01$	1 - 20	no	$1 \mu\text{m}^2/\text{s}$	$0.447 \mu\text{m}$	4.47 nm
no interaction, $r = 0.10$	1 - 20	no	$1 \mu\text{m}^2/\text{s}$	$0.447 \mu\text{m}$	44.7 nm
interaction, variable D	1 - 10	yes	$1 \mu\text{m}^2/\text{s}$	$0.447 \mu\text{m}$	4.47 nm
	11 - 20	yes	$0.01 \mu\text{m}^2/\text{s}$	$0.0447 \mu\text{m}$	4.47 nm
interaction, variable σ	1 - 10	yes	$1 \mu\text{m}^2/\text{s}$	$0.447 \mu\text{m}$	4.47 nm
	11 - 20	yes	$1 \mu\text{m}^2/\text{s}$	$0.447 \mu\text{m}$	44.7 nm
transient interaction	1 - 10	yes	$1 \mu\text{m}^2/\text{s}$	$0.447 \mu\text{m}$	4.47 nm
	11 - 20	no	$1 \mu\text{m}^2/\text{s}$	$0.447 \mu\text{m}$	4.47 nm

Table 6.3 | The conditions for each set of simulated trajectory pairs for the validation of the scanning window method. Each set consists of 1000 pairs of Brownian motion trajectories with trajectory length $l = 20$ and time interval corresponding to successive positions $\tau = 0.1 \text{ s}$. The presence or absence of interaction, the diffusion coefficient D , the mean step S , and the localization precision σ are listed in function of the trajectory positions.

6.3.3 Experimental set-up

The dual colour SPT experiments were carried out on a custom-built laser widefield epi-fluorescence microscope set-up that is described elsewhere in detail [28]. Briefly, the microscope was a Nikon TE2000-E with a Nikon Plan Apochromat NA = 1.4 oil immersion 100 \times objective lens (Nikon, Belgium). EGFP was excited with a 100 mW Calypso 491 nm diode pumped solid state laser (Cobolt, Sweden) and Cy5 was excited with a 30 mW IQ1C 636 nm diode laser (Power Technology, USA). The fluorescence light coming from the sample was collected again by the objective lens and sent

through the side port of the microscope towards a Cascade II:512 electron multiplication charge coupled device (EMCCD) camera (Roper Scientific, USA). A pair of achromat lenses was placed in between the camera and microscope side port for an extra 2× magnification of the image on the CCD chip so that one pixel corresponded to a distance of 89 nm in the sample. A dichroic mirror placed between both achromat lenses reflected the fluorescent light with a wavelength below 630 nm and transmitted the wavelengths above 630 nm. Accompanying mirrors and notch filters (AHF Analysentechnik, Germany) guided the reflected and transmitted part of the fluorescence each to one half of the CCD chip. High-speed movies were recorded using the Nikon NIS Elements (Nikon, Belgium) imaging software. The EMCCD camera was synchronized with an acousto-optical tunable filter to only illuminate the sample during the actual camera exposure time so as to minimize phototoxicity and photobleaching. The living cells were placed on the microscope in a stage top incubation chamber (Tokai Hit, Japan), set at 37 °C, 5% CO₂, and 100% humidity.

6.3.4 SPT experiments and analysis

Movies of 60 seconds were recorded on different time points at a speed of 2 frames per second and with an image acquisition time of 30 ms. For each movie, a different cell was selected for imaging in order to minimize photobleaching and phototoxicity, and to obtain information on a large population of cells. Cells were chosen, based on a relatively low expression level of EGFP-constructs to minimize the possibility of a disturbed cell functioning.

After recording the movies, the images in the two different colours (i.e. with fluorescence light above and below 630 nm) were aligned using an affine transformation. The transformation parameter values were determined from an image of immobilized TetraSpeck microspheres (Molecular Probes, Belgium) that are fluorescent in both colours. Image processing was performed in Matlab on all images for identification of the individual object spots, as explained in detail elsewhere [28]. The object locations were determined using an intensity weighted centroid algorithm, as it was recently shown that it is more robust than the fitting of a Gaussian function in case of moving objects [29]. Using a nearest neighbour algorithm, these positions were used to reconstruct the trajectories. Since the objects are moving, their position during image acquisition is unknown, making it impossible to determine the exact precision with which an individual intensity weighted centre has been determined. However, the average localization precision for an intensity weighted centre was calculated, according to Eq. (5.12) in **Chapter 5**. Besides the localization precision, the overlay

precision was determined as $\sigma_o = 3$ nm for all movies by an experimental procedure as also explained in **Section 5.3.4 of Chapter 5**.

The scanning window method is applied to each such pair of trajectories, as explained in **Section 6.2.5**. To restrict the calculation time, trajectory pairs that cannot realistically correspond to interacting objects are not considered, i.e. at least one pair of positions from both trajectories should be within a distance of 500 nm from each other, in both the x - and y -direction. When the method finds at least one window with correlation, the trajectories are assumed to originate from objects that, at least temporarily, interact with each other. When there are different candidate trajectories in one colour that are correlated with a certain trajectory in the other colour, the pair with the highest number of correlated positions is retained.

6.4 RESULTS

6.4.1 Validation by simulations

The performance of the scanning window method was verified with simulated pairs of two-dimensional Brownian motion trajectories, as explained in **Section 6.3.1**. Brownian motion was chosen, not only because it is common on a microscopic scale, but also because random Brownian motion trajectories are not expected to be correlated. A number of different situations were considered (see **Table 6.3**), for each of which 1000 trajectory pairs with length $l = 20$ and time interval $\tau = 0.1$ s between successive positions were simulated.

The situation of complete interaction was investigated for a diffusion coefficient $D = 1 \mu\text{m}^2/\text{s}$. The results are shown in **Fig. 6.4a**, where for each position along the trajectories the percentage is shown of trajectories where the scanning window method has detected interaction. In case of high localization precision $\sigma = 4.47$ nm, corresponding to a relative localization precision of $r = 0.01$ (cfr. Eq. (6.2) with $S = \sqrt{2D\tau} = 0.447 \mu\text{m}$), the scanning window method correctly finds 100% of the time interaction at almost every position. Only at the trajectory start and end points, the method performs slightly worse, with interaction correctly detected 98% of the time. This can be explained by the smaller number of windows that correspond to the trajectory extremities (see **Fig. 6.3**). For lower localization precision $\sigma = 44.7$ nm, corresponding to a relative localization precision of $r = 0.10$, the scanning window method behaviour is essentially the same.

As shown in **Fig. 6.4a**, these trajectories were also analysed with an earlier reported object based colocalization method that makes use of a maximum distance $d_{\max} = 1.65\sqrt{\sigma_A^2 + \sigma_B^2 + \sigma_o^2}$ to decide whether or not there is interaction at a particular position [26]. Here, $d_{\max} = 1.65\sqrt{2}\sigma$, considering $\sigma_A = \sigma_B = \sigma$ and $\sigma_o = 0$. At almost all positions, the colocalization method finds interaction 81% of the time, for both relative localization precisions $r = 0.01$ and $r = 0.10$.

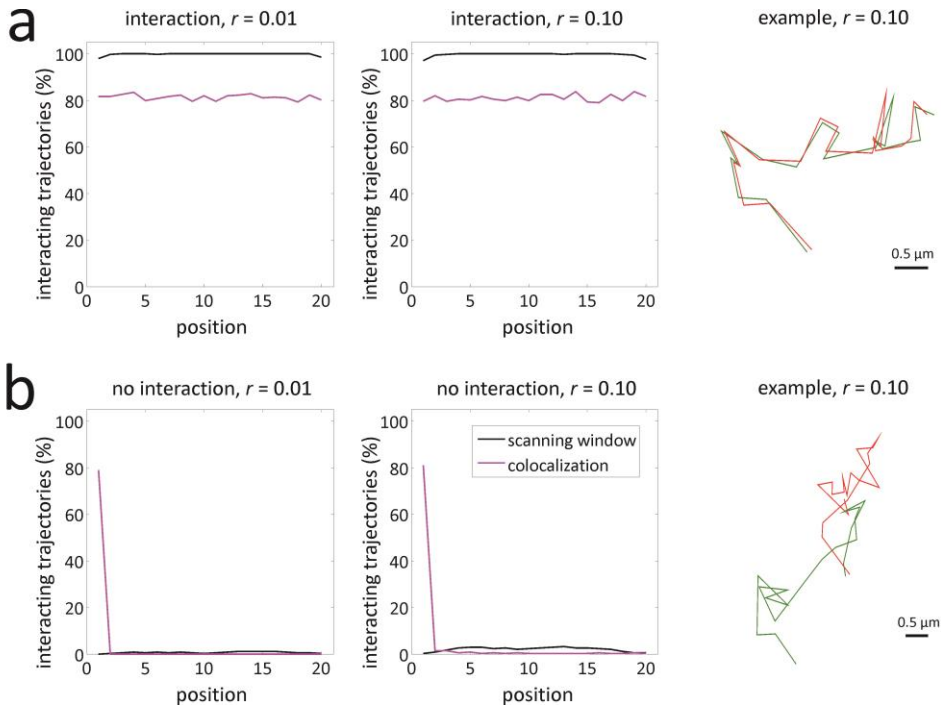


Figure 6.4 | Validation simulations for interaction and no interaction. The percentage of 1000 pairs of simulated Brownian motion trajectories where the scanning window method has found interaction (black line) is shown for each position along the trajectories, in case of **(a)** interaction, and **(b)** no interaction. All simulated trajectories have a length $l = 20$, a diffusion coefficient $D = 1 \mu\text{m}^2/\text{s}$, and a time interval $\tau = 0.1 \text{ s}$ between successive positions. The localization precision was chosen $\sigma = 4.47 \text{ nm}$ or $\sigma = 44.7 \text{ nm}$, corresponding to a relative localization precision of $r = 0.01$ or $r = 0.10$, respectively. The same trajectories were also analysed with an object based colocalization method with $d_{\max} = 1.65\sqrt{2}\sigma$ as maximum distance (purple line). On the right, example pairs of trajectories are shown for the case of $r = 0.10$.

Similarly, it was tested if the scanning window method can correctly detect the absence of interaction. This was investigated for a diffusion coefficient $D = 1 \mu\text{m}^2/\text{s}$, the results

of which are shown in **Fig. 6.4b**. In case of high localization precision $\sigma = 4.47$ nm, corresponding to a relative localization precision $r = 0.01$, the scanning window method finds that less than 1% of the trajectories are interacting at most positions (i.e. false positives). For lower localization precision $\sigma = 44.7$ nm, corresponding to a relative localization precision $r = 0.10$, the method finds less than 3% false positives. The object based method with maximum distance $d_{\max} = 1.65\sqrt{2}\sigma$ finds that 81% of the trajectories are interacting at the first position, both in the case of $r = 0.01$ and $r = 0.10$, since the trajectories were simulated to start in the same position (see **Section 6.3.1**). From position 2, this percentage drops and remains below the percentage found with the scanning window method.

Simulations were also carried out to evaluate the performance of the scanning window method in more complicated situations (representing the ones shown in **Fig. 6.2**). The case of complete interaction with a variable diffusion coefficient was investigated for $D = 1 \mu\text{m}^2/\text{s}$ from position 1 to 10 and $D = 0.01 \mu\text{m}^2/\text{s}$ from position 11 to 20. This results in a corresponding local relative localization precision $r = 0.01$ and $r = 0.10$, respectively, since the localization precision $\sigma = 4.47$ nm was constant at all positions. Thanks to the variable window size, the scanning window method finds interaction 100% of the time at most positions, as shown in **Fig. 6.5a**. Only at the trajectory extremities, the method performs slightly worse, with interaction correctly detected 98% of the time. Although the colocalization method with maximum distance $d_{\max} = 1.65\sqrt{2}\sigma$ is not affected by differences in diffusion coefficient, only 81% of the trajectories is found to interact.

Complete interaction was also investigated with a variable localization precision $\sigma = 4.47$ nm from position 1 to 10 and $\sigma = 44.7$ nm from position 11 to 20. This results in a corresponding local relative localization precision $r = 0.01$ and $r = 0.10$, respectively, since the diffusion coefficient $D = 1 \mu\text{m}^2/\text{s}$ was constant at all positions. The scanning window method finds 100% of the time interaction at most positions, as shown in **Fig. 6.5b**. The colocalization method with maximum distance $d_{\max} = 1.65\sqrt{2}\sigma$ is not affected by differences in localization precision, so that 81% of the trajectories is found to interact at all positions.

Variable interaction was the last situation that was investigated, with the objects only interacting from position 1 to 10 and not interacting from position 11 to 20. The results are shown in **Fig. 6.5c**, for a relative localization precision of $r = 0.01$ (since $D = 1 \mu\text{m}^2/\text{s}$ and $\sigma = 4.47$ nm). Comparison to **Fig. 6.4** shows that the scanning window method performs as expected from the case of full interaction and no interaction. The transition of interaction to no interaction is almost perfectly detected going from position 9 to 11 with a resolution smaller than the expected window length $w = 3$ (see **Table 6.1**).

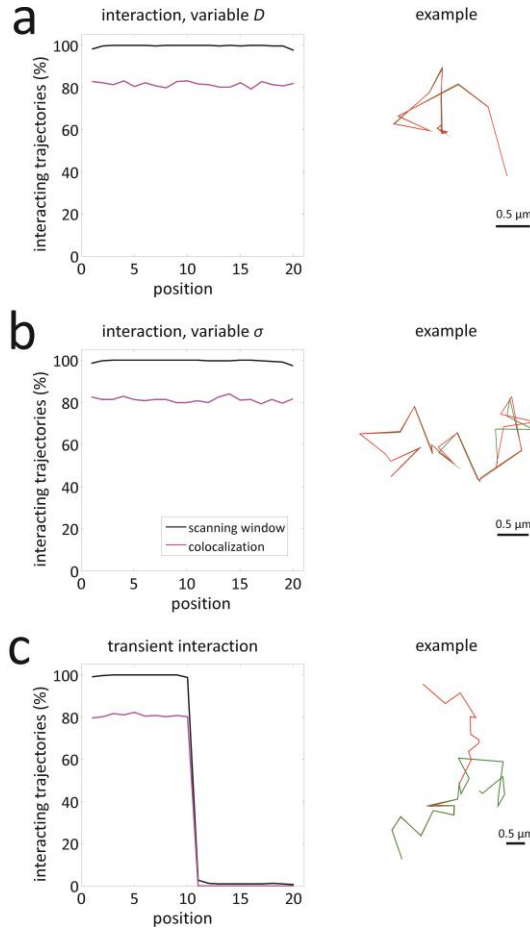


Figure 6.5 | Validation simulations for variable diffusion coefficient, localization precision and interaction. The percentage of 1000 pairs of simulated Brownian motion trajectories where the scanning window method has found interaction (black line) is shown for each position along the trajectories, in case of **(a)** full interaction with localization precision $\sigma = 4.47$ nm, and a diffusion coefficient $D = 1 \mu\text{m}^2/\text{s}$ from position 1 to 10 and $D = 0.01 \mu\text{m}^2/\text{s}$ from position 11 to 20, **(b)** full interaction with a diffusion coefficient $D = 1 \mu\text{m}^2/\text{s}$, and a localization precision $\sigma = 4.47$ nm from position 1 to 10 and $\sigma = 44.7$ nm from position 11 to 20, **(c)** a diffusion coefficient $D = 1 \mu\text{m}^2/\text{s}$, a localization precision $\sigma = 4.47$ nm, and interaction from position 1 to 10 and no interaction from position 11 to 20. All simulated trajectories had a length $l = 20$ and a time interval $\tau = 0.1$ s between successive positions. The same trajectories were also analysed with an object based colocalization method with $d_{\text{max}} = 1.65\sqrt{2}\sigma$ as maximum distance (purple line). On the right, example pairs of trajectories are shown.

Also the colocalization method with maximum distance $d_{\max} = 1.65\sqrt{2}\sigma$ performs as expected, with interaction being found 81% of the time in the first half and virtually no interaction in the second half.

The simulations show that the scanning window method is capable of reliably identifying interaction, independent of the relative localization precision. Even when parts of the trajectories are not correlated because of transient interactions, or exhibit low correlation because of a high local relative localization precision, the scanning window method is still able to detect interaction when it takes place. An important benefit to the object based colocalization method is that the scanning window method is significantly less sensitive for false negatives that cannot be avoided by object based colocalization. Furthermore, it is much less sensitive to false positives in case of coincidental colocalization.

6.4.2 Intracellular trafficking of nanomedicines

In pharmaceutical research, nanomedicines such as polymeric gene complexes (polyplexes) are being developed for the delivery of therapeutic nucleic acids to target cells, such as retinal pigment epithelium (RPE) cells in the context of ocular gene therapy [30]. To improve therapeutic efficacy, it is of interest to have a detailed understanding of the postendocytic trafficking profile of polyplexes inside such cells [1]. In previous work, we have investigated the presence of nanomedicines in different types of endosomes as a function of time in RPE cells. This was done, using dual colour SPT on living RPE cells with one colour corresponding to the fluorescently labelled endosomes and the other to the fluorescently labelled polyplexes [27]. Trajectories of both polyplexes and endosomes were determined from the SPT images. Colocalization of polyplexes in endosomes was measured by determining the correlation, as defined in Eq. (6.1), between the positions of the full trajectories in both colours. From here on, we will refer to this approach as the full trajectory method. This method was found to perform better than classic object based colocalization because it was less prone to find false positives and insensitive to false positives due to coincidental colocalization. However, interactions might be overlooked when they only result in correlation over a limited part of the trajectories (see **Section 6.2.3**). This is especially relevant in the context of intracellular traffic, since such trajectories often exhibit immobile phases that do not correlate. Moreover, transient interactions such as the escape of a polyplex from an endosome or the transferral of the polyplex to another type of (unlabelled) endosome also give rise to trajectory pairs that are not completely correlated.

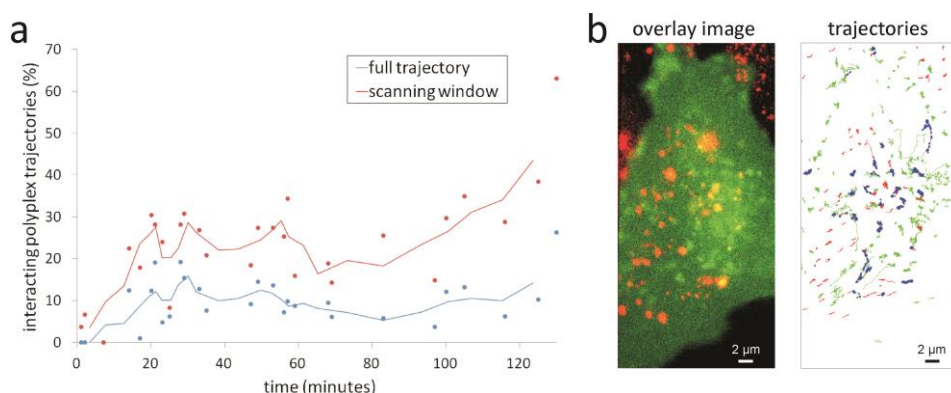


Figure 6.6 | Interactions between endosomes and polyplexes measured by the scanning window method. (a) The percentage of polyplex trajectories that are interacting with a flotillin-2 type endosome trajectory inside living RPE cells at different time points after uptake of the polyplexes is shown. The lines show the trend based on the average of three subsequent measurements, while the dots represent individual values corresponding to a single dual colour SPT measurement. The blue data corresponds to the full trajectory method and the red data corresponds to the scanning window method. A pair of trajectories was considered to interact when the scanning window method found interaction in at least one window. (b) An overlay image and the corresponding trajectories of the dual colour SPT measurement at 53 minutes are shown. The endosomes have a green fluorescent label and the polyplexes have a red fluorescent label. The trajectories are coloured accordingly and the positions where the scanning window method found correlation are indicated in blue.

The scanning window method is, therefore, expected to perform better in the investigation of intracellular trafficking of nanomedicines than the full trajectory method, since it inherently is capable of detecting interaction in small segments of trajectories. As a proof of concept, we here apply the scanning window method to the dual colour SPT data for the flotillin-2 type of endosomes (more details on the experiments can be found in **Sections 6.3.2 to 6.3.4**). The measured percentage of polyplex trajectories that are interacting in at least one window with a flotillin-2 endosome trajectory are shown in **Fig. 6.6**, together with the results obtained with the full trajectory method [27]. Each data point shows the percentage for a different dual colour SPT movie. The wide variability in values is caused by the variability between different living cells, since each experiment was performed on a different cell. Comparison between the values from both methods shows that the scanning window method finds on at least two times more interaction than the full trajectory method. The same qualitative trend is found as for the scanning window method, indicating that the underestimation of the full trajectory method is systematic, and should thus always be accounted for. Visual inspection of the trajectory pairs where the scanning window

method only finds correlation in a couple of positions, suggests that this is mostly caused by either a low mobility or low localization precision in a large part of the trajectories (cfr. **Fig. 6.2**). A clear example of transient interaction was also found, as shown in **Fig. 6.7**. Although this event could be interpreted as endosomal escape, it seems more likely that this is actually an endosomal fusion event where the polyplex is transferred to a different (unlabelled) type of endosome.

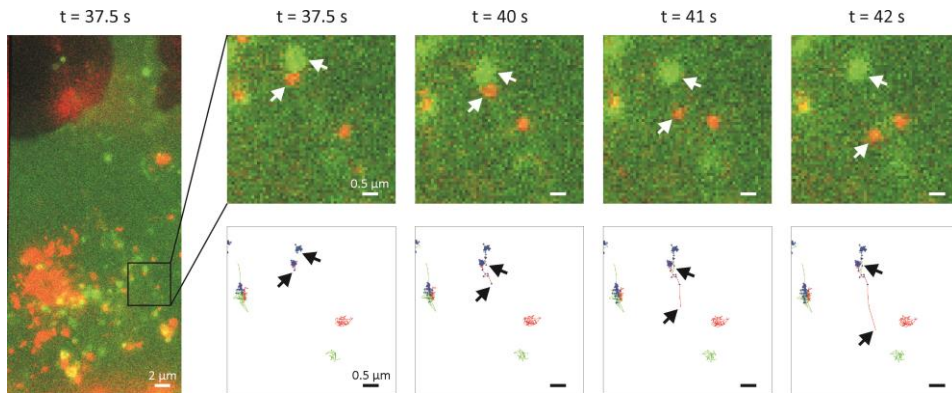


Figure 6.7 | An example of transient interaction detected by the scanning window method. On the left, an overlay image from a dual colour SPT experiment recorded 100 minutes after uptake of the polyplexes. The flotillin-2 type endosomes have a green fluorescent label and the polyplexes a red fluorescent label. On the right, a subregion is shown with the corresponding trajectories at different time points, showing a transient event where the polyplex and endosome are at first exhibiting correlated motion, after which the polyplex moves away from the endosome. The trajectories are coloured according to the fluorescent labels, and the interacting positions found by the scanning window method are indicated in blue. The scanning window method finds interaction until 40 s, afterwards it becomes apparent that both objects are not interacting anymore.

6.5 DISCUSSION

We have recently reported correlation between entire trajectories as a measure for the interaction between two dynamic species that is less prone to false positives and false negatives than object based colocalization [27]. However, this full trajectory method might not detect correlation in situations that are often present in live-cell imaging, such as changing mobility or transient interactions (see **Section 6.2.3**). Moreover, an objective measure for a threshold value of the correlation between trajectories of

interacting objects was not determined. We, therefore, have developed a scanning window method, which allows spatial and temporal characterization of interaction by investigating the correlation in a window with a variable size that is scanned along the trajectories. The optimal window size depends on the local relative localization precision r (cfr. Eq. (6.2)) and is determined as the window size for which the probability $P \geq 0.8$. The correlation threshold ρ_{\min} for the optimal window depends in turn on both the window size and the local relative localization precision r . The values of P and ρ_{\min} can be determined from **Table 6.1 and 6.2**, respectively.

The scanning window method was validated with simulated trajectory pairs (see **Section 6.4.1**). It was shown that the method is able to accurately identify interaction, independent of the relative localization precision r (see **Fig. 6.4a**). This should come as no surprise, since **Table 6.1 and 6.2** were determined from similar simulated trajectories of interacting objects (see **Section 6.2.4**). The scanning window method, however, was demonstrated to perform well in the case of no interaction as well (see **Fig. 6.4b**). Only for a low relative localization precision r , the percentage of false positives was found to increase slightly.

The performance of the scanning window method was also tested with simulated trajectory pairs that represent more complicated behaviour. In case of interaction along the entire trajectory, but with a changing diffusion coefficient, the scanning window method is still able to detect the interaction (see **Fig. 6.5a**), because of the variable window size that accounts for the changing relative localization precision. For the same reason, the method also performs well when the localization precision changes along the trajectory (see **Fig. 6.5b**). Interestingly, the scanning window method is very well capable of detecting transient interactions along trajectories. The point at which the transition from binding to unbinding or vice versa occurs, can be determined with excellent resolution.

As a comparison, the same simulated data was also analysed with an earlier reported object based colocalization method that makes use of a maximum distance to decide whether or not there is interaction at a particular position [26]. As shown in **Fig. 6.4a**, this method was found to be sensitive for false negatives, i.e. interaction is significantly underestimated. It is also more sensitive to false positives in case of coincidental colocalization, which can happen when two independent objects pass by close to each other (see the first position in **Fig. 6.4b**). Thus it is clear that the scanning window method is a more reliable and robust method to detect interaction.

As a proof of concept, the scanning window method was applied to the trajectories of polyplexes and endosomes inside living cells, obtained by dual colour SPT experiments

(see **Section 6.4.2**). When interaction is found in at least one window, the polyplex is considered to be residing in, or at least interacting with, the endosome. Compared to the previously published full trajectory method, the scanning window approach was better capable of detecting this interaction. This is because it is for instance not uncommon for endosomes to exhibit mobility that changes over time [31,32]. In addition, a variable localization precision can occur, e.g. when the fluorescent labels photobleach. Both issues cause a variable local localization precision r and thus a variable correlation along the trajectories. Correlation might also be degraded due to imperfect trajectory determination, for instance because of the difficulty to unambiguously track the objects in crowded environments that are often present in living cells. In some cases, mistakes are unavoidable, leading to trajectories that contain incorrect positions. When there is interaction, the parts of the trajectories that correspond to the interacting objects still correlate, and hence are found to interact by the scanning window method. A decrease in the overall correlation might also be caused by transient interactions, such as the escape of the polyplexes from endosomes, a process that is vital for the functioning of the polymeric gene complexes [1].

Comparison of the scanning window method with the full trajectory method [26], shows that the latter method misses at least half of the interactions (see **Fig. 6.6**). Since it only searches for correlation on the full trajectory scale, the conventional correlation method does not notice many of the trajectory pairs that only partly correlate, due to the reasons discussed above. Interestingly, the scanning window method was capable of detecting transient interactions like the one shown in **Fig. 6.7**, which can be interpreted as the transferral of a polyplex to an unlabelled type of endosome or possibly endosomal escape of the polyplex.

The scanning window method could be tested on other types of motion besides diffusion, and **Tables 6.1 and 6.2** for the determination of P and ρ_{\min} could be adjusted if required. In the specific case that the objects are undergoing different types of motion, trajectory analysis could first be applied to determine the trajectory segments that correspond to these types of motion [33], which could then be analysed separately.

6.6 CONCLUSION

We have developed the scanning window method for measuring the interaction between moving objects in dual colour microscope time-lapse images. Employing a

scanning window along two trajectories in which the correlation between the positions is calculated, not only spatial but also temporal information about the interaction becomes available. The scanning window method was validated with simulations and applied to the trajectories of endosomes and polymeric gene nanoparticles in live-cells. Interaction was more reliably found with the scanning window method than by simple correlation analysis over the entire trajectory at once, which in turn was already proven to perform more reliably than the classic object based approach. The additional temporal information thus allows a more sensitive estimation of the interactions between objects, and moreover provides a means to detect transient interaction events.

REFERENCES

1. K. Remaut, N. N. Sanders, B. G. De Geest, K. Braeckmans, J. Demeester, and S. C. De Smedt, "Nucleic acid delivery: Where material sciences and bio-sciences meet," *Materials Science & Engineering R-Reports* **58**, 117-161 (2007).
2. S. Bolte and F. P. Cordelieres, "A guided tour into subcellular colocalization analysis in light microscopy," *Journal of Microscopy-Oxford* **224**, 213-232 (2006).
3. J. W. D. Comeau, S. Costantino, and P. W. Wiseman, "A guide to accurate fluorescence microscopy colocalization measurements," *Biophysical Journal* **91**, 4611-4622 (2006).
4. V. Zinchuk, O. Zinchuk, and T. Okada, "Quantitative colocalization analysis of multicolor confocal immunofluorescence microscopy images: Pushing pixels to explore biological phenomena," *Acta Histochemica et Cytochemica* **40**, 101-111 (2007).
5. K. W. Dunn, M. M. Kamocka, and J. H. McDonald, "A practical guide to evaluating colocalization in biological microscopy," *American Journal of Physiology-Cell Physiology* **300**, C723-C742 (2011).
6. J. Adler, S. N. Pagakis, and I. Parmryd, "Replicate-based noise corrected correlation for accurate measurements of colocalization," *Journal of Microscopy-Oxford* **230**, 121-133 (2008).
7. S. V. Costes, D. Daelemans, E. H. Cho, Z. Dobbin, G. Pavlakis, and S. Lockett, "Automatic and quantitative measurement of protein-protein colocalization in live cells," *Biophysical Journal* **86**, 3993-4003 (2004).
8. D. Demandolx and J. Davoust, "Multicolour analysis and local image correlation in confocal microscopy," *Journal of Microscopy-Oxford* **185**, 21-36 (1997).
9. P. A. Fletcher, D. R. L. Scriven, M. N. Schulson, and E. D. W. Moore, "Multi-Image Colocalization and Its Statistical Significance," *Biophysical Journal* **99**, 1996-2005 (2010).
10. Q. Li, A. Lau, T. J. Morris, L. Guo, C. B. Fordyce, and E. F. Stanley, "A syntaxin 1, G alpha(o), and N-type calcium channel complex at a presynaptic nerve terminal: Analysis by quantitative immunocolocalization," *Journal of Neuroscience* **24**, 4070-4081 (2004).
11. E. M. M. Manders, F. J. Verbeek, and J. A. Aten, "Measurement of Colocalization of Objects in Dual-Color Confocal Images," *Journal of Microscopy-Oxford* **169**, 375-382 (1993).
12. E. A. Jares-Erijman and T. M. Jovin, "FRET imaging," *Nature Biotechnology* **21**, 1387-1395 (2003).
13. A. Agrawal, R. Deo, G. D. Wang, M. D. Wang, and S. M. Nie, "Nanometer-scale mapping and single-molecule detection with color-coded nanoparticle probes," *Proceedings of the National Academy of Sciences of the United States of America* **105**, 3298-3303 (2008).
14. T. D. Lacoste, X. Michalet, F. Pinaud, D. S. Chemla, A. P. Alivisatos, and S. Weiss, "Ultra-high-resolution multicolor colocalization of single fluorescent probes," *Proceedings of the National Academy of Sciences of the United States of America* **97**, 9461-9466 (2000).
15. S. Malkusch, U. Endesfelder, J. Mondry, M. Gelleri, P. J. Verveer, and M. Heilemann, "Coordinate-based colocalization analysis of single-molecule localization microscopy data," *Histochemistry and Cell Biology* **137**, 1-10 (2012).
16. I. E. G. Morrison, I. Karakikes, R. E. Barber, N. Fernandez, and R. J. Cherry, "Detecting and quantifying colocalization of cell surface molecules by single particle fluorescence imaging," *Biophysical Journal* **85**, 4110-4121 (2003).

17. A. Pertsinidis, Y. X. Zhang, and S. Chu, "Subnanometre single-molecule localization, registration and distance measurements," *Nature* **466**, 647-U11 (2010).
18. W. Trabesinger, B. Hecht, U. P. Wild, G. J. Schutz, H. Schindler, and T. Schmidt, "Statistical analysis of single-molecule colocalization assays," *Analytical Chemistry* **73**, 1100-1105 (2001).
19. E. Lachmanovich, D. E. Shvartsman, Y. Malka, C. Botvin, Y. I. Henis, and A. M. Weiss, "Co-localization analysis of complex formation among membrane proteins by computerized fluorescence microscopy: application to immunofluorescence co-patching studies," *Journal of Microscopy-Oxford* **212**, 122-131 (2003).
20. R. J. Ober, S. Ram, and E. S. Ward, "Localization accuracy in single-molecule microscopy," *Biophysical Journal* **86**, 1185-1200 (2004).
21. R. E. Thompson, D. R. Larson, and W. W. Webb, "Precise nanometer localization analysis for individual fluorescent probes," *Biophysical Journal* **82**, 2775-2783 (2002).
22. C. M. Brown and N. O. Petersen, "An image correlation analysis of the distribution of clathrin associated adaptor protein (AP-2) at the plasma membrane," *Journal of Cell Science* **111**, 271-281 (1998).
23. P. W. Wiseman, J. A. Squier, M. H. Ellisman, and K. R. Wilson, "Two-photon image correlation spectroscopy and image cross-correlation spectroscopy," *Journal of Microscopy-Oxford* **200**, 14-25 (2000).
24. L. S. Churchman, Z. Okten, R. S. Rock, J. F. Dawson, and J. A. Spudich, "Single molecule high-resolution colocalization of Cy3 and Cy5 attached to macromolecules measures intramolecular distances through time," *Proceedings of the National Academy of Sciences of the United States of America* **102**, 1419-1423 (2005).
25. P. D. Dunne, R. A. Fernandes, J. McColl, J. W. Yoon, J. R. James, S. J. Davis, and D. Klenerman, "DySCo: Quantitating Associations of Membrane Proteins Using Two-Color Single-Molecule Tracking," *Biophysical Journal* **97**, L5-L7 (2009).
26. I. Koyama-Honda, K. Ritchie, T. Fujiwara, R. Iino, H. Murakoshi, R. S. Kasai, and A. Kusumi, "Fluorescence imaging for monitoring the colocalization of two single molecules in living cells," *Biophysical Journal* **88**, 2126-2136 (2005).
27. D. Vercauteren, H. Deschout, K. Remaut, J. F. J. Engbersen, A. T. Jones, J. Demeester, S. C. De Smedt, and K. Braeckmans, "Dynamic Colocalization Microscopy To Characterize Intracellular Trafficking of Nanomedicines," *Acs Nano* **5**, 7874-7884 (2011).
28. K. Braeckmans, D. Vercauteren, J. Demeester, and S. C. De Smedt, "Single Particle Tracking," in *Nanoscopy and Multidimensional Optical Fluorescence Microscopy*, A. Diaspro, ed., (CRC Press / Taylor & Francis Group, Boca Raton, 2010).
29. H. Deschout, K. Neyts, and K. Braeckmans, "The influence of movement on the localization precision of sub-resolution particles in fluorescence microscopy," *Journal of Biophotonics* **5**, 97-109 (2012).
30. L. Peeters, N. N. Sanders, A. Jones, J. Demeester, and S. C. De Smedt, "Post-pegylated lipoplexes are promising vehicles for gene delivery in RPE cells," *Journal of Controlled Release* **121**, 208-217 (2007).
31. R. Bausinger, K. von Gersdorff, K. Braeckmans, M. Ogris, E. Wagner, C. Brauchle, and A. Zumbusch, "The transport of nanosized gene carriers unraveled by live-cell imaging," *Angewandte Chemie-International Edition* **45**, 1568-1572 (2006).
32. K. de Bruin, N. Ruthardt, K. von Gersdorff, R. Bausinger, E. Wagner, M. Ogris, and C. Brauchle, "Cellular dynamics of EGF receptor-targeted synthetic viruses," *Molecular Therapy* **15**, 1297-1305 (2007).

Chapter 6

33. J. A. Helmuth, C. J. Burckhardt, P. Koumoutsakos, U. F. Greber, and I. F. Sbalzarini, "A novel supervised trajectory segmentation algorithm identifies distinct types of human adenovirus motion in host cells," *Journal of Structural Biology* **159**, 347-358 (2007).

Chapter 7

On-chip light sheet illumination enables diagnostic size and concentration measurements of submicron membrane vesicles in biofluids

This chapter is submitted for publication:

Hendrik Deschout^{1,2}, Koen Raemdonck¹, Stephan Stremersch¹, Pietro Maoddi³, Guillaume Mernier³, Philippe Renaud³, Sébastien Jiguet⁴, An Hendrix⁵, Marc Bracke⁵, Rudy Van den Broecke⁶, Magnus Röding⁷, Mats Rudemo⁷, Jo Demeester¹, Stefaan C. De Smedt¹, Filip Strubbe^{8,2}, Kristiaan Neyts^{8,2}, Kevin Braeckmans^{1,2}.

¹Laboratory of General Biochemistry and Physical Pharmacy, Ghent University, Belgium

²Centre for Nano- and Biophotonics, Ghent University, Belgium

³Laboratory of Microsystems, Ecole Polytechnique Fédérale de Lausanne, Switzerland

⁴Gersteltec Sàrl, Switzerland

⁵Laboratory of Experimental Cancer Research, Ghent University Hospital, Belgium

⁶Department of Gynaecology, Ghent University Hospital, Belgium

⁷Department of Mathematical Statistics, Chalmers University of Technology and Gothenburg University, Sweden

⁸Liquid Crystals and Photonics Group, Ghent University, Belgium

ABSTRACT

Cell-derived membrane vesicles (MVs) that are released in biofluids like blood, urine, or saliva, are currently emerging as potential non-invasive biomarkers for diseases, such as cancer. Techniques capable of measuring the size and concentration of specific types of MVs directly in biofluids, without the need for pre-processing steps, are urgently needed. As discussed in **Chapter 3**, single particle tracking (SPT) microscopy has the potential of doing exactly that, by labelling the MVs of interest with a specific fluorescent label (e.g. a labelled antibody) and analysing their Brownian motion in the biofluid. However, unbound dye in the biofluid can cause high background intensity that biases the SPT size and concentration measurements, since smaller and dimmer MVs are more easily missed. While such background can be avoided with light sheet illumination, current set-ups require specialty sample holders that are not compatible with high-throughput diagnostics. Here we report on a mass-manufacturable microfluidic chip with integrated light sheet illumination, and demonstrate accurate SPT size and concentration measurements of MVs in cell culture medium and in interstitial fluid collected from primary human breast tumours.

7.1 INTRODUCTION

The relation between specific types of MVs in body fluids and disease progression, e.g. tumour growth and metastasis, is a topic that receives a lot of attention nowadays [1-6]. The size, origin and concentration of cell-derived MVs could entail clinically relevant signatures with diagnostic and prognostic value [2,5,7]. Thus, substantial efforts have gone into evaluating and developing techniques suitable for submicron MV characterization in terms of specificity, size and concentration [8]. Specifically, due to a lack of standardized isolation and purification protocols and in order to avoid manipulation artefacts, techniques capable of performing MV characterization directly in body fluids are urgently needed [2,9,10].

Single Particle Tracking (SPT) was recently shown to be the first technique capable of accurately measuring the size distribution and number concentration of fluorescently labelled nanoparticles in undiluted biofluids, such as whole blood [11,12] (cfr. **Section 7.2.8**). However, being based on epi-fluorescence microscopy, a limitation of the technique is limited contrast due to fluorescence coming from out-of-focus particles or unbound fluorescent dye, as illustrated in **Fig. 7.1a**. Especially the latter aspect can be problematic for SPT characterization of MVs that require staining with fluorescent labels targeted against specific membrane markers to detect MV subpopulations. As the concentration of MVs in e.g. a patient sample is unknown *a priori*, a surplus of labelled antibodies has to be added in order to be certain that all vesicles will be stained. This will typically result in a substantial fraction of unbound fluorescent labels in the sample medium and a concomitant decrease in contrast. Thus, smaller (dimmer) particles are more difficult to detect, resulting in an underestimation of the number concentration and a biased size distribution. This is especially of importance for a correct characterization of the smaller types of MVs, such as exosomes, with a size below 100 nm [10,13].

To enable high-throughput diagnostics of MVs in biofluids, we created a mass producible microfluidic chip with integrated light sheet illumination for SPT size and concentration measurements of submicron MVs that are fluorescently labelled directly in the biofluid without the need for isolation or purification steps. Light sheet illumination presents an attractive alternative to conventional epi-illumination as it combines superior contrast with real-time imaging, as is required to capture the MV's fast Brownian motion [14-16].

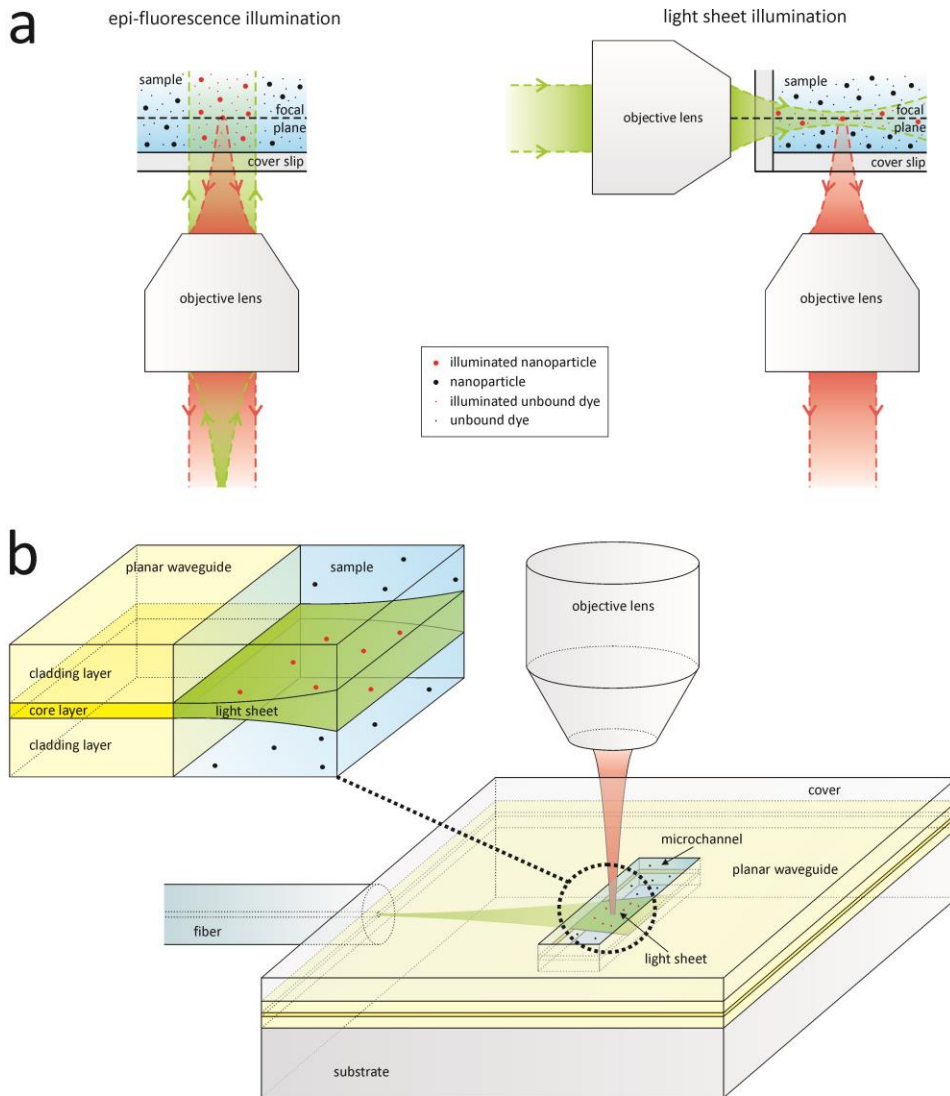


Figure 7.1 | Microfluidic chip with integrated waveguide for light sheet illumination. (a) Illustration of the (green) excitation and (red) fluorescence light path in epi-fluorescence and light sheet illumination. The contrast for the nanoparticles in focus is better with light sheet illumination because the nanoparticles and unbound dye out of focus are not illuminated. (b) Design of microfluidic chip with integrated waveguide for on-chip light sheet illumination. Laser light enters the planar waveguide by means of a butt-coupled optical fiber. While the laser light is confined in the vertical direction, it can spread horizontally in the waveguide so that a sheet of light emerges in the microchannel. The fluorescence light is collected by an objective lens whose focal plane coincides with the light sheet. The drawing is not to scale.

Although light sheet illumination has mainly been applied to mesoscopic imaging set-ups for developmental biology [17-20], some reports demonstrate its usefulness for high-resolution imaging applications as well [14-16,21,22]. As illustrated in **Fig. 7.1a**, this requires two objective lenses positioned perpendicular to one another in very close proximity, one for creating the light sheet, the other one for imaging. This has been shown to be possible for SPT experiments in combination with custom made sample holders having two high-quality optical windows for illumination and imaging [14-16]. However, as they are difficult and expensive to manufacture [23], they are not suitable for high-throughput diagnostic assays for which inexpensive disposable sample holders are preferred to avoid extensive cleaning procedures and sample contamination. One solution has recently been reported in which the light sheet is incident from the top and reflected over 90° by a mirror that is positioned in the sample [24]. However, this still requires placing an extra objective lens for producing the light sheet in the position of the condenser of an inverted microscope.

Here, we realize for the first time light sheet illumination in a mass-manufacturable microfluidic chip by coupling laser light into a planar waveguide structure in which a microchannel, containing the sample, is provided. The light sheet is characterized by acquiring a z-stack through the microchannel containing a dispersion of fluorescent nanospheres, indicating a Full Width at Half Maximum (FWHM) of ~9 µm. The contrast with which the nanospheres are visible is shown to improve substantially compared to classic epi-illumination, close to what has been achieved on dedicated light sheet microscopes. To demonstrate the potential of the microfluidic chip as a diagnostic tool, SPT measurements were performed of MVs in cell culture medium and in interstitial fluid collected from primary human breast tumours. Because of the high background intensity, the on-chip light sheet illumination is found to be essential for correct MV characterization.

7.2 MATERIALS AND METHODS

7.2.1 Chip fabrication process

Multiple microfluidics chips with an integrated planar waveguide are simultaneously fabricated in one process on 10 cm diameter wafers. Two different types of wafers are used, standard silicon wafers and 145 µm thick borosilicate glass wafers. The wafers are first cleaned with an O₂ plasma in a TepPla 300 plasma system. The clean room process exists out of 4 basic steps, as illustrated in **Fig. 7.2**.

Chip fabrication process		
Process step		Details
1. bottom cladding layer	1.1 spin coating	10 s acceleration at 100 rpm/s 40 s at 1000 rpm 1 s acceleration at 400 rpm/s 1 s deceleration at 400 rpm/s 5 s at 1000 rpm 10 s deceleration at 100 rpm/s
	1.2 soft bake	25 min increase at 4°C/min starting from 20°C 25 min decrease at 4°C/min starting from 120°C
2. core layer	2.1 spin coating	5 s acceleration at 100 rpm/s 5 s at 500 rpm 30 s acceleration at 100 rpm/s 40 s at 3500 rpm 1 s acceleration at 400 rpm/s 1 s deceleration at 400 rpm/s 5 s at 3500 rpm 35s deceleration at 100 rpm/s
	2.2 soft bake	idem to step 1.2
3. top cladding layer	3.1 spin coating	idem to step 1.1
	3.2 soft bake	idem to step 1.2
4. photolithography	4.1 UV exposure	13.5 s at 10 mW/cm ² 10 s pause 13.5 s at 10 mW/cm ²
	4.2 post exposure bake	40 min increase at 2°C/min 40 min bake at 95°C uncontrolled cooling down for 90 min
	4.3 developing	3 min in PGMEA bath 2 min in other PGMEA bath N ₂ drying

Table 7.1 | The chip fabrication process. The process for fabrication of the microfluidics chip with integrated planar waveguide consists of 4 basic steps. Details on spin coating and subsequent post baking for each SU-8 layer are given in step 1-3. Details on the UV exposure and subsequent post bake and development for the 3-layer structure are given in step 4.

First, SU-8 type GM 1060 (Gersteltec Sàrl, Switzerland) mixed with 6% of the epoxy resin D.E.R.TM 353 (The Dow Chemical Company, Belgium) is spin coated on the wafer using a Sawatec LSM 200 coater, to obtain a ~25 µm thick bottom cladding layer, followed by soft baking on a Sawatec HP 401 Z hotplate (see **Table 7.1**). Next, pure SU-8 type GM 1060 is spin coated on the bottom cladding layer to obtain a ~5 µm thick core layer, again followed by a soft bake step. Finally, SU-8 type GM 1060 mixed with 6% of

Chapter 7

the epoxy resin D.E.R.TM 353 is spin coated on the core layer to obtain a $\sim 25\ \mu\text{m}$ thick top cladding layer, followed by a final soft bake step.

To create the microfluidic structures, the whole 3-layer structure is exposed to $270\ \text{mJ}/\text{cm}^2$ of the i-line (365 nm) of a Karl Suss MA 6 mask aligner using a Cr mask. Next, the structure is post exposure baked on a programmable hotplate, and developed in a wet bench using propylene glycol methyl ether acetate (PGMEA). Since SU-8 is a negative photoresist, the part that is not exposed to UV does not polymerize during post exposure bake, and is removed by developing with PGMEA. The wafer is finally diced with a Disco DAD 321 Automatic Dicing Saw, to obtain separate microfluidics chips that each contain a planar waveguide and microchannel with in- and outlet reservoir.

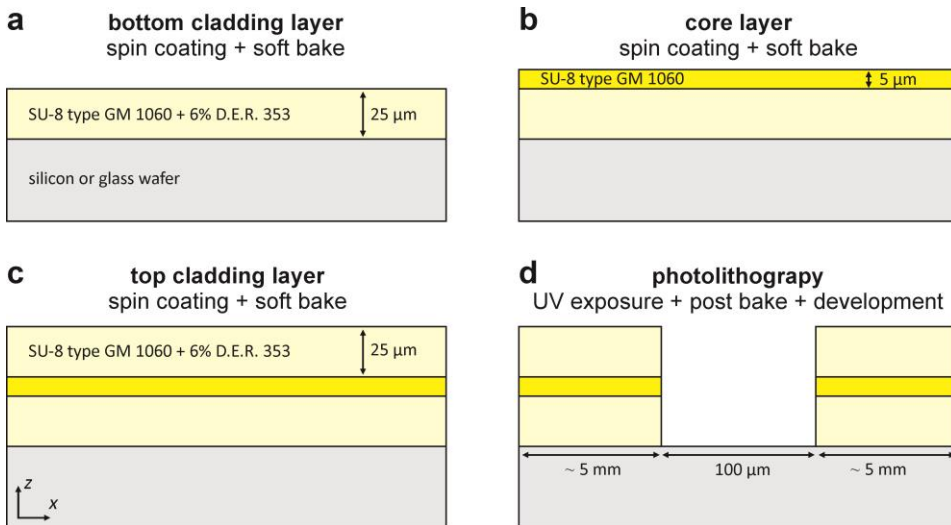


Figure 7.2 | Illustration of the chip fabrication process. (a) In the first step, the bottom cladding layer that consists of SU-8 type GM 1060 mixed with 6% of D.E.R.TM 353 is spin coated on a glass or silicon wafer and soft baked. (b) In the second step, the core layer that consists of pure SU-8 type GM 1060 is spin coated on the bottom core layer and soft baked. (c) In the third step, the top cladding layer that consists of SU-8 type GM 1060 mixed with 6% of D.E.R.TM 353 is spin coated on the core layer and soft baked. (d) In the fourth step, the 3-layer structure is exposed to UV light using a mask, post baked, and developed, in order to create a microchannel of $100\ \mu\text{m}$ width.

7.2.2 Microscope set-up

Excitation light is coupled into the planar waveguide of the chip by illuminating the waveguide core layer with the output of an optical fiber. The cleaved side of a single mode patch cord fiber (Newport, The Netherlands) with an operating wavelength of 633 nm is used for this purpose. The other side of the patch cord contains an FC/PC connector which is used for coupling laser light into the fiber. Excitation light with a wavelength of 640 nm is provided by a 100 mW diode-pumped Excelsior solid state laser (Spectra Physics, The Netherlands). The fiber core is carefully aligned with the planar waveguide core layer using an ULTRAlign precision linear stage (Newport, The Netherlands). This is possible by using a standard CCD camera to monitor the waveguide exit at the other side of the chip, see **Fig. 7.3a**. Optimal alignment between fiber and waveguide results in a light sheet in the microchannel, and part of this light enters the second half of the planar waveguide. This situation is thus obtained when a maximum amount of light emerges from the core layer at the waveguide exit, as depicted in **Fig. 7.3b**.

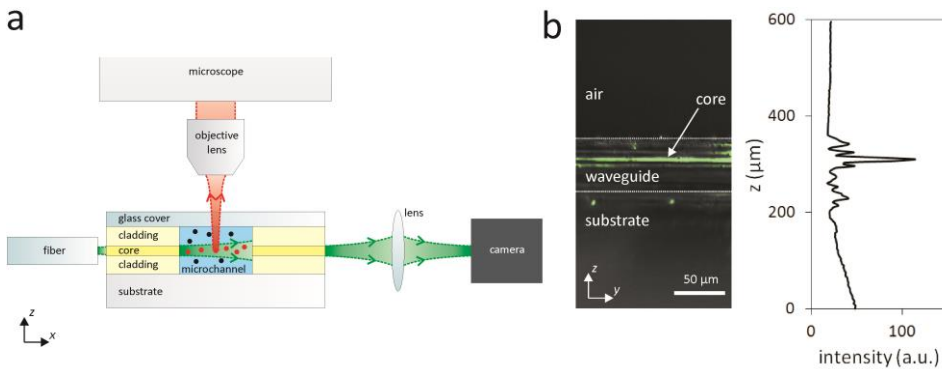


Figure 7.3 | Coupling the excitation light into the planar waveguide. (a) A cross section of the set-up showing the fiber that is used to couple the excitation light into the planar waveguide. The fluorescence light from the sample in the microchannel is detected by the objective lens of the microscope. Successful incoupling of the excitation light into the planar waveguide can be monitored by imaging the other side of the chip. (b) In case of successful alignment between fiber and planar waveguide, the waveguide output as seen by the camera exhibits a clear line profile at the centre of the waveguide.

The chip with fiber is placed under a Nikon Plan Fluorite 40× objective lens with a numerical aperture (NA) of 0.75, using an objective lens inverter (LSM Tech, USA)

connected to a Nikon TE 2000-E microscope (Nikon, Belgium), see **Fig. 7.4**. The fluorescence light coming from the sample is collected by the objective lens, as shown in **Fig. 7.3a**, and imaged on an electron multiplication charge coupled device (EMCCD) Cascade II:512 camera (Roper Scientific, USA). A pair of achromat lenses is placed in between the camera and microscope side port for an extra 2× magnification of the image on the EMCCD chip so that one pixel corresponds to a distance of 196 nm in the sample. High-speed movies and image stacks are recorded using the Nikon Elements AR imaging software.

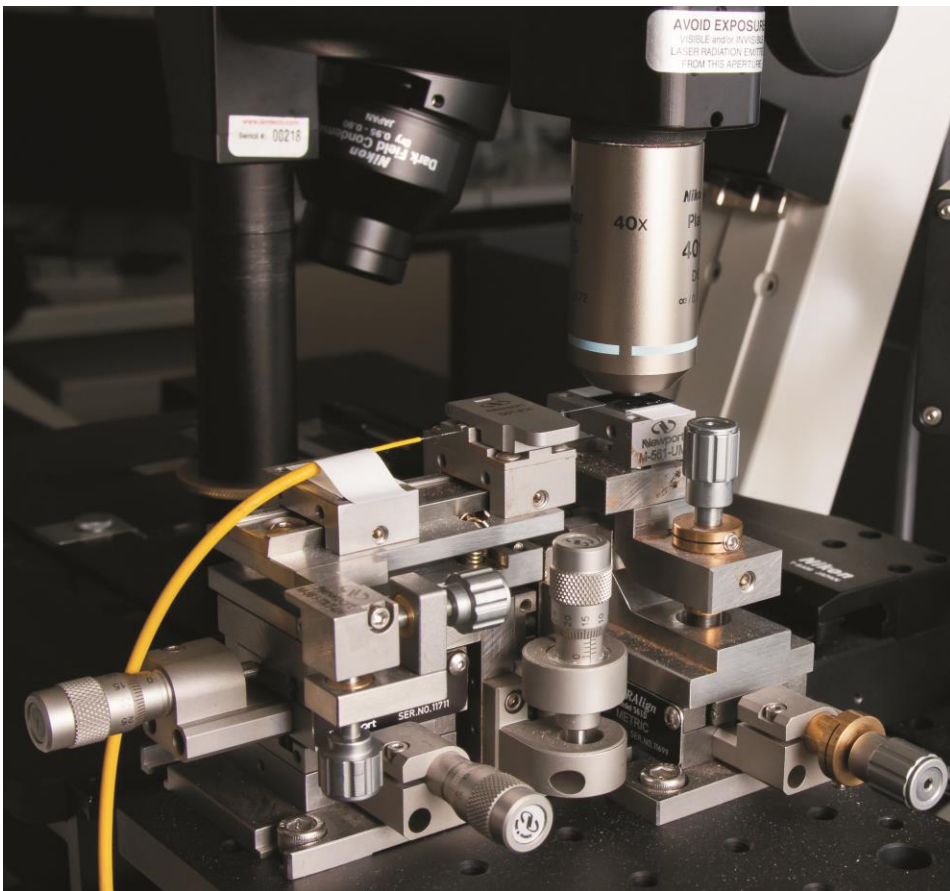


Figure 7.4 | Photograph of the microscope set-up. A chip with silicon substrate is placed under an objective lens that is attached to an objective lens inverter that sends the fluorescence light to the microscope. The cleaved side of a fiber core is carefully aligned with the core layer of the planar waveguide using precision linear stages.

7.2.3 Simulation of the light sheet

Assume a planar waveguide with a core layer of 5 μm thickness surrounded by two cladding layers of 25 μm thick. The core layer has a refractive index $n_{co} = 1.595$ of SU-8, and both core layers have a refractive index $n_{cl} = 1.594$ of SU-8 mixed with epoxy resin [25]. Consider further a sample with the same refractive index as water $n_{sa} = 1.333$ and light with a wavelength of $\lambda = 640$ nm. We have simulated the behaviour of the fundamental waveguide mode exiting the planar waveguide into the sample, using the Python eigenmode modelling framework CAMFR (<http://camfr.sourceforge.net/>).

7.2.4 Experimental characterization of the light sheet

Since out-of-focus light is not rejected in the detection path of the microscope, it is not possible to indirectly characterize the light sheet by simply measuring the intensity of a fluorescent sample in function of the z -position. However, if the sample is a dispersion of fluorescent particles, the background corrected intensity $I_p - I_b$ of the particles in focus does not contain out-of-focus contributions, with I_p the intensity of the particle and I_b the local background intensity. Using image processing, the light sheet can thus be characterized by the background corrected intensities of the particles in focus in each image of z -stack. The range where the light sheet is located, manifests itself as an intensity peak, and the FWHM of that peak is a measure of the light sheet thickness.

Care should be taken when measuring differences between z -positions in microscopy, because it is necessary to account for the possible mismatch between the refractive index of the objective lens immersion medium n_{im} and the refractive index of the sample n_{sa} . In case of a mismatch, the real z -position difference d_{re} will not be equal to the observed difference d_{ob} . We have measured the microchannel height to be 56.6 μm with a Dektak 150 profilometer (Veeco, Germany), which is in good agreement with the 55 μm as expected from the fabrication process. On the other hand, the z -stacks of images recorded in the microchannel suggest a height of 41.1 μm . This leads to the following correction for the refractive index mismatch:

$$d_{re} = 1.38d_{ob}. \quad (7.1)$$

This is close to the ratio of the refractive index $n_{sa} = 1.333$ of the water, which is the sample medium, and the refractive index of air $n_{im} = 1$, which is the objective lens immersion medium, as suggested for low NA [26]. The reported values in the manuscript are corrected for this effect.

The light sheet is characterized for both the glass and silicon chip. The microchannel is filled with a water dispersion of dark red fluorescent (660 nm excitation peak, 680 nm emission peak) polystyrene 0.2 μm diameter FluoSpheres (Molecular Probes, Belgium). A z-stack of images with a step of 0.1 μm is recorded throughout the microchannel, with both sheet illumination and epi-fluorescence illumination. In each frame of the stack, the intensity and local background of each particle was determined off line [27]. The FWHM of the light sheet peak is obtained by fitting a two-dimensional Gaussian function to the average background corrected intensity $I_p - I_b$ in function of the z-position.

7.2.5 Contrast measurements

The contrast is measured by recording images of a dispersion of fluorescent particles inside the light sheet. Using image processing, the intensity I_p and local background I_b of each particle is determined, and $(I_p - I_b)/(I_p + I_b)$ is used to quantify its contrast [14].

The contrast is measured in both the glass and silicon chip. The microchannel is filled with a water dispersion of dark red fluorescent (660 nm excitation peak, 680 nm emission peak) polystyrene 0.2 μm diameter FluoSpheres (Molecular Probes, Belgium). To mimic different fluorescent backgrounds, different concentrations of the red dye Cy5 are added to the water. The microscope was focused at the centre position of the light sheet and several images were recorded with epi-illumination and light sheet illumination. In each image, the average contrast of the nanospheres was calculated off line [27].

7.2.6 Isolation, sizing, and labelling of breast cancer cell-line derived membrane MVs

The MCF-7 breast cancer cell line [28] stably transfected with GFP-Rab27B was maintained at 37°C and 5% CO_2 in Dulbecco's Modified Eagle Medium (DMEM, Invitrogen, Belgium) supplemented with 10% fetal bovine serum (FBS) and penicillin/streptomycin. For MV production, cells were cultured in DMEM supplemented with 10% exosome-depleted FBS (Exo-FBSTM, System Biosciences, Belgium) for 48 hours. MVs were isolated from the conditioned medium by differential centrifugation. Briefly, conditioned cell culture medium was successively centrifuged at 300 g for 10 minutes, 3000 g for 10 minutes and 15000 g for 30 minutes and the

supernatant was collected after each step. Next, the supernatant was concentrated using a Vivaspin 20 with molecular weight cut-off 50 kDa (Sartorius, Belgium) to a volume of about 5 ml. The MVs were then pelleted by ultracentrifugation (UC) for 70 minutes at 120 000 g, washed with phosphate buffered saline (PBS) and again pelleted by UC at 120 000 g for 70 minutes. Finally the MV pellet was resuspended in 200 μ l PBS. After diluting 5 \times in PBS, the MV size distribution was measured by dynamic light scattering measurements at 25°C on a Nano-ZS (Malvern, UK). The MVs were fluorescently labelled by mixing 3 μ l of the isolated MVs with 6 μ l HEPES buffer, 1 μ l 10 \times Annexin V binding buffer (100 mM HEPES, 1.4 M NaCl, and 25 mM CaCl₂, pH 7.4) and 0.1 μ l Annexin V alexa fluor 647 (Molecular Probes, Belgium). The sample was gently mixed and incubated in the dark for 15 minutes at room temperature prior to measurement.

7.2.7 Fluorescent labelling of MVs in tumour interstitial fluid

Primary breast cancer resection specimens were collected at Ghent University Hospital. Written informed consent was obtained from each patient according to the recommendations of the local ethics committee. About 0.25 g of clean fresh tissue was cut into small pieces (1-2 mm³), washed carefully with PBS, and incubated in 1 ml PBS for 1 hour at 37°C in a humidified CO₂ incubator. The samples were centrifuged [29] at 500 g for 10 minutes and 1500 g for 20 minutes. Without any further purification, 4 μ l of the final supernatant (i.e. tumour interstitial fluid) was mixed with 8 μ l of Annexin V binding buffer (10 mM HEPES, 140 mM NaCl, and 2.5 mM CaCl₂, pH 7.4) and 4 μ l of Annexin V alexa fluor 647 (Invitrogen, Belgium). The sample was gently mixed and incubated in the dark for 15 minutes at room temperature prior to measurement.

Note that size measurements by DLS are not an option in this case due to the high protein content and the presence of other light scattering compounds in biofluids like interstitial fluid. Neither does DLS allow to perform concentration measurements, nor can it detect a specific subtype of MVs as can be easily achieved with SPT by using specific labelled antibodies.

7.2.8 SPT size distribution and number concentration measurements

SPT measurements can be used to determine the number concentration and size distribution of particles undergoing Brownian motion in a dispersion [11,12], as explained in **Chapter 3**. Briefly, first a movie is recorded of the diffusing particles and

their motion trajectories are determined, using image processing. From the mean square displacement, a diffusion coefficient can be estimated for each individual trajectory. This leads to a distribution of diffusion coefficients when many particles are analysed. A maximum entropy deconvolution step can subsequently be applied to this distribution to reduce sampling noise and improve its precision [11]. The distribution of diffusion coefficients can be converted to a size distribution via the Stokes-Einstein relation:

$$D = \frac{kT}{3\pi\eta d}, \quad (7.2)$$

where k is the Boltzmann constant, T is the temperature, η is the viscosity of the sample liquid, and d is the particle diameter. The number concentration can be derived from the trajectories as well, since the observation volume can be inherently calibrated from the time that particles appear in focus [12]. By knowing the detection volume and the number of particles in each image, the number concentration immediately follows.

The SPT experiments for determination of the size and concentration are performed in a silicon chip. The microchannel is filled with the dispersion of fluorescently labelled cell-derived MVs, and the objective lens is positioned so that the focal plane coincides with the intensity peak of the light sheet. Subsequently, between 10 and 20 movies with a duration time of 10 seconds are recorded with a frame rate between 22.6 and 27.6 frames per second, an image acquisition time between 20 and 30 ms, and an image size between 436 and 450 pixels in the x -direction, and between 124 and 192 pixels in the y -direction, with a pixel size of 196 nm. Particle trajectories are calculated off line [27]. Only trajectories of minimally 5 positions are included in the size and concentration analysis to remove false positives (noisy features in the image that are sometimes seen as particles by the image processing software). All SPT experiments were performed at 22.5° C.

7.3 RESULTS AND DISCUSSION

To obtain on-chip light sheet illumination, a mass-manufacturable microfluidic chip was designed that consists of substrate with a planar waveguide on top in which a microchannel is provided, as illustrated in **Fig. 7.1b**. The fabrication process of the chip is explained in detail in **Section 7.2.1**. Briefly, the chip is constructed on a glass or silicon substrate on top of which a planar waveguide structure is created consisting of 3 layers

of SU-8 that are sequentially deposited by spin coating followed by a soft bake step. The refractive index of the bottom and top layer ($\sim 25\ \mu\text{m}$ thickness each) is lowered by mixing the SU-8 with the epoxy resin D.E.R.TM 353, making these layers suitable as waveguide cladding while the middle layer ($\sim 5\ \mu\text{m}$ thickness) acts as waveguide core [25]. Finally, a microchannel of $100\ \mu\text{m}$ width containing in- and outlet reservoirs is created in the SU-8 waveguide using standard photolithography (see **Fig. 7.5a-b**).

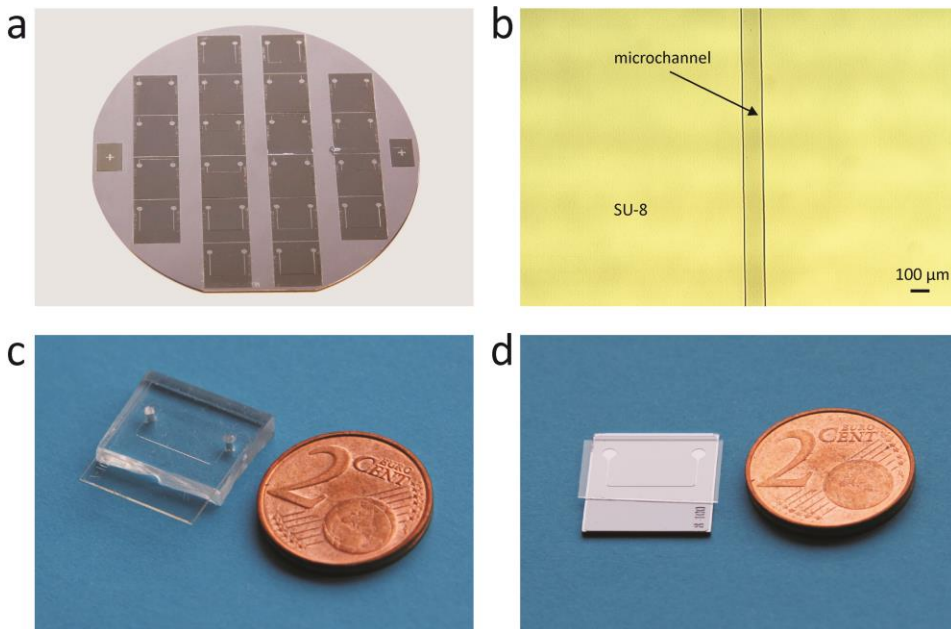


Figure 7.5 | Photographs of the microfluidic chips with planar waveguide for light sheet illumination in a microchannel. (a) Image of a silicon wafer with 20 planar waveguides and microchannels made from SU-8 after photolithography. (b) Light microscopy image of a microfluidic chip showing the $100\ \mu\text{m}$ wide microchannel. (c) Image of microfluidic chip with glass substrate on top of a PDMS block. (d) Image of microfluidic chip with silicon substrate covered with a microscope cover slip.

The entire process is carried out on a 10 cm diameter wafer, thus obtaining 20 chips in parallel after dicing. Chips based on the glass substrate are covered with a polydimethylsiloxane (PDMS) block to seal the microchannel and to provide in and outlets for the sample (see **Fig. 7.5c**). Imaging of the sample is then performed through the $145\ \mu\text{m}$ thick glass substrate. Chips based on the silicon substrate are sealed with a microscopy cover slip containing a thin layer of PDMS through which the sample in the

microchannel can be imaged (see **Fig. 7.5d**). The chips are mounted on a fluorescence microscope for image acquisition of the diffusing nanoparticles. Laser light of 640 nm is coupled into the waveguide using an optical fiber attached to a high precision alignment stage (cfr. **Section 7.2.2**).

Simulations of the fundamental propagating light mode (see **Section 7.2.3**) show that such a planar waveguide is capable of producing a light sheet with a fairly uniform thickness over a large field of view. As shown in **Fig. 7.6**, the FWHM of the spatial intensity distribution coming from the fundamental TE mode is around 4.6 μm right outside the waveguide. At a distance of 50 μm outside the waveguide, the FWHM is around 5.4 μm , and at distance of 100 μm it has increased to 7.5 μm . This indicates that the light sheet generated by the planar waveguide based on SU-8 does not strongly diverge over distances that are typical for the field of view in SPT experiments.

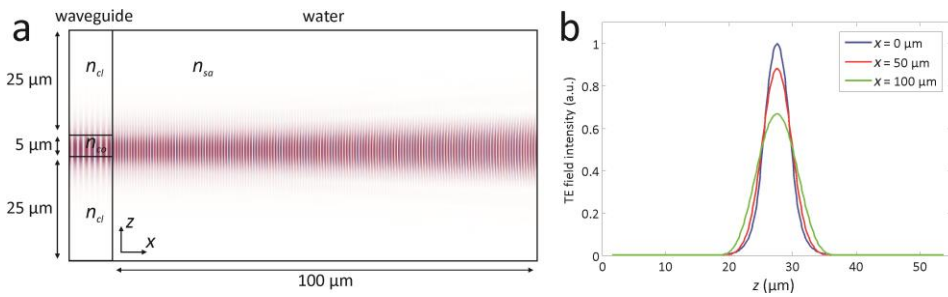


Figure 7.6 | Simulation of the light sheet generated by a planar waveguide in a water sample. (a) Visualization of the real part of the TE field of the fundamental mode exiting the waveguide. The core layer has a thickness of 5 μm and a refractive index $n_{co} = 1.595$, the two surrounding cladding layers have a thickness of 25 μm and a refractive index $n_{cl} = 1.594$, and the sample (water) has a refractive index $n_{sa} = 1.333$. (b) The spatial intensity distribution of the light sheet along the z -axis directly outside the waveguide at $x = 0 \mu\text{m}$ has a FWHM = 4.6 μm . At a distance $x = 50 \mu\text{m}$ from the waveguide this becomes FWHM = 5.4 μm , and after $x = 100 \mu\text{m}$ it becomes FWHM = 7.5 μm . The behaviour of the fundamental TM mode is similar.

The actual light sheet of both types of chips was characterized by acquiring a z -stack through the microchannel containing a dispersion of 0.2 μm fluorescent polystyrene nanospheres (for details, see **Section 7.2.4**). The light sheet intensity profile along the optical axis (i.e. perpendicular to the sheet of light) was calculated from the average intensity of the nanospheres visible in each frame of the z -stack. The average intensity profile across the entire channel width is shown in **Fig. 7.7a**, resulting in an average thickness of $\sim 9 \mu\text{m}$ FWHM. The smaller intensity peaks visible in the intensity profiles

indicate that the waveguide is likely multimodal which could explain the slight difference with the theoretical calculations.

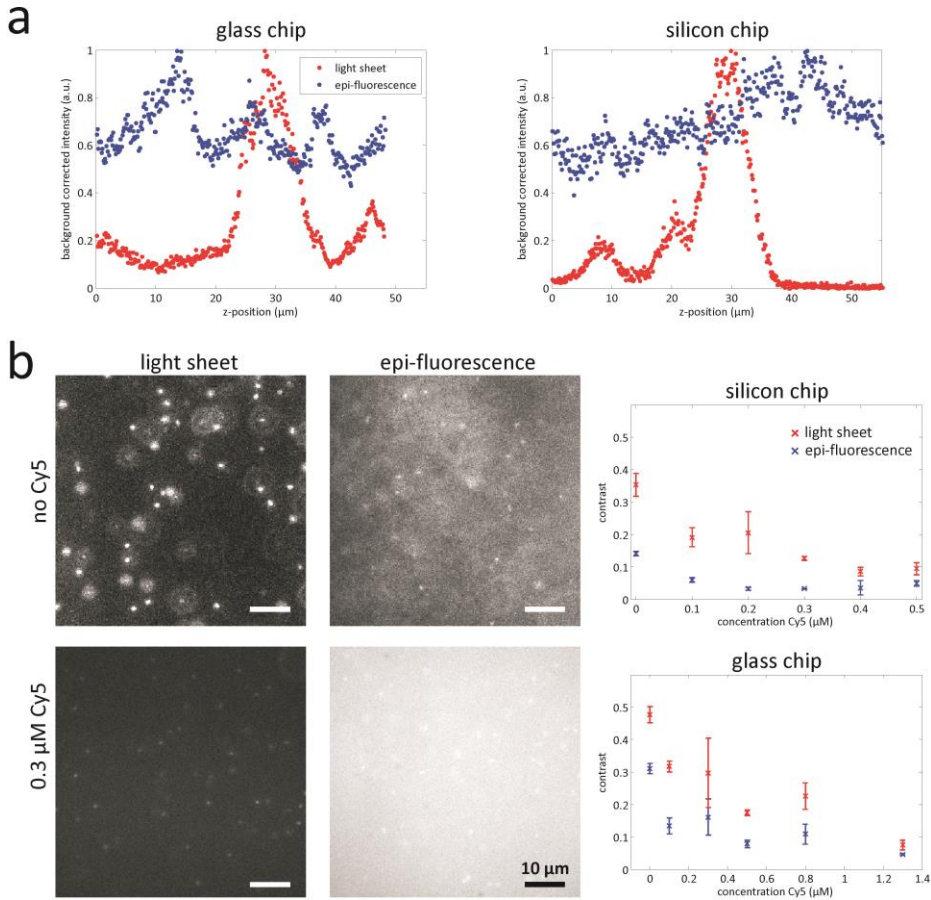


Figure 7.7 | Experimental characterization of the light sheet and contrast. (a) Average light sheet intensity profile along the optical axis of the microscope imaging lens. Contrary to epi-illumination (blue data points), illumination through the planar waveguide results in excitation light that is restricted to a thin region at the centre of the channel with a FWHM of $\sim 9 \mu\text{m}$ (red data points). (b) In order to determine the gain in contrast using light sheet illumination versus epi-illumination, the microchannel is filled with a dispersion of $0.2 \mu\text{m}$ fluorescent polystyrene nanospheres. To mimic different values of background intensity, different concentrations of the red fluorescent dye Cy5 are added. Images are recorded using both illumination modes with the microscope focused at the centre of the light sheet. Example images obtained with a silicon chip are shown to the left. Contrast values for a range of Cy5 concentrations using the silicon and glass chip are shown to the right. The error bars represent the standard deviation.

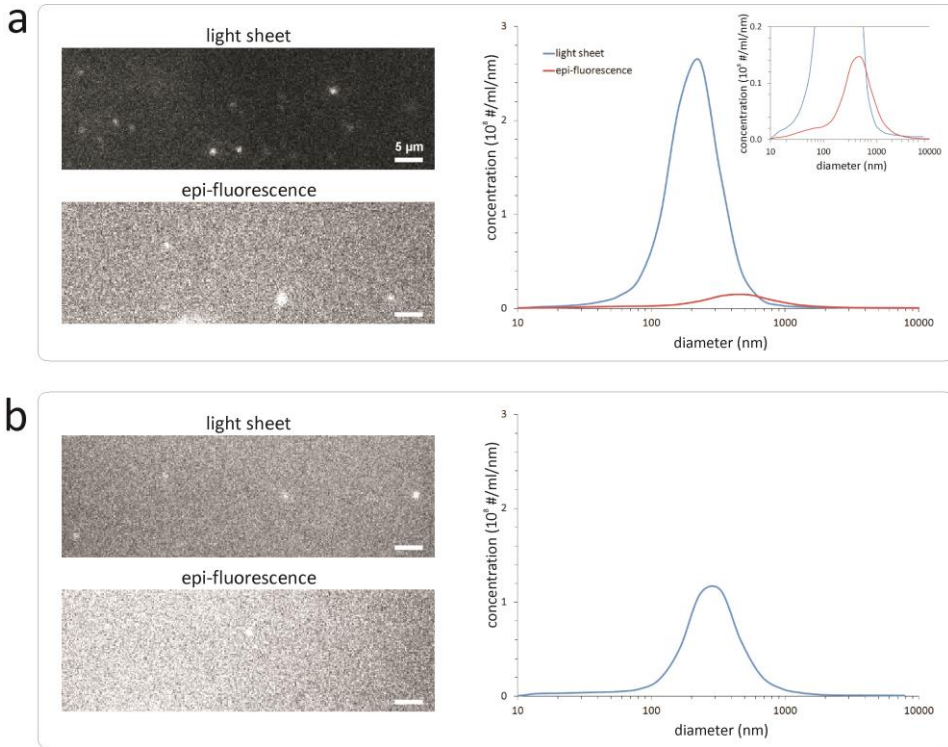


Figure 7.8 | On-chip SPT concentration and size measurements of cell-derived membrane vesicles. (a) SPT size distribution and number concentration measurements are performed on cell-derived MVs in cell culture medium. The MVs are clearly visible when using light sheet illumination, while only a few particles are visible in conventional epi-illumination mode due to the much higher background fluorescence. This results in a 4× underestimation of the number concentration and a bias towards larger (and brighter) MVs for epi- vs. sheet-illumination. (b) Similar SPT experiments are performed on MVs in patient derived interstitial fluid. The MVs are visible when using light sheet illumination, while almost no particles are visible in epi-illumination mode. A meaningful concentration and size distribution could only be obtained when using sheet illumination.

The aim of light sheet illumination is to improve the contrast, which was quantified for both chips according to $(I_p - I_b)/(I_p + I_b)$, with I_p the intensity of the nanoparticle and I_b the average local background intensity [14]. The microchannel was filled with a dispersion of $0.2 \mu\text{m}$ fluorescent polystyrene nanospheres containing various amounts of Cy5 dye to simulate different background intensities coming from free dye. As shown in **Fig. 7.7b**, compared to classic epi-illumination, a contrast improvement of 1.5 - 2.4× was obtained in the glass chip, and 1.9 - 6.4× in the silicon chip, depending on the background intensity (cfr. **Section 7.2.5**). This improvement approaches the

performance of light sheet illumination as created with a high quality objective lens (see **Fig. 7.1a**) [14]. The better relative increase in contrast with the silicon chip is due to the light intensity almost going to zero at the edges of the light sheet, which is not the case for the glass chip (cfr. **Fig. 7.7a**). However, in absolute terms the glass chip produced the best contrast as the silicon chip suffers from a higher background intensity due to the reflectivity of the silicon substrate (i.e. a doubling of the background intensity).

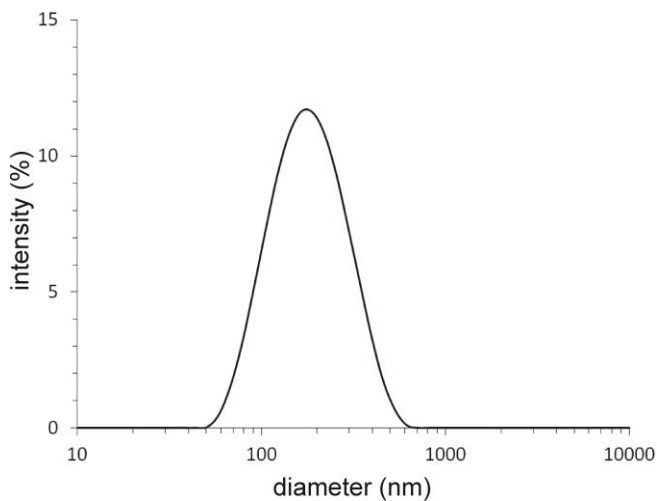


Figure 7.9 | Cell-derived membrane vesicle size distribution obtained by dynamic light scattering. Size distribution measurements are performed by dynamic light scattering on cell-derived MVs in cell culture medium. The MVs have a diameter between 50 nm and 700 nm with a peak around 170 nm.

In a next step, on-chip SPT size and concentration measurements were performed of cell-derived MVs isolated from the conditioned cell culture medium of breast cancer cells [30] (cfr. **Section 7.2.6**). An excess of fluorescently labelled Annexin V was used to label the cell-derived MVs which are known to expose phosphatidylserine (PS) on their surface [13], followed by on-chip SPT analysis without additional purification. As shown in **Fig. 7.8a**, using sheet illumination, the majority of the MVs were situated in the 50 - 700 nm size range (in agreement with dynamic light scattering, see **Fig. 7.9**), and the overall number concentration was $8.4 \cdot 10^8$ #/ml. Using conventional epi-fluorescence, a 4× lower concentration of only $1.9 \cdot 10^8$ #/ml was found with a size distribution that is clearly shifted towards larger values.

To demonstrate the potential of the microfluidic chip with integrated planar waveguide as a diagnostic tool, SPT measurements were performed on cell-derived MVs secreted in the interstitial fluid harvested from fresh human breast cancer specimens [29] (see **Section 7.2.7**). To ensure optimal fluorescent labelling of PS-exposing MVs present in the interstitial fluid, again an excess of dye-conjugated Annexin V was added. Subsequent on-chip SPT analysis was performed without any additional purification steps to remove unbound label. A broad distribution of cell-derived MV sizes was found in the interstitial fluid, as shown in **Fig. 7.8b**. The majority of the MVs are situated in the 90 - 900 nm size range, with a total number concentration of $4.1 \cdot 10^8$ #/ml. Using conventional epi-fluorescence the background fluorescence was so high that only very few MVs were visible and no meaningful size distribution or concentration could be determined. This once more clearly demonstrates that improving contrast by light sheet illumination is essential for correct MV characterization, especially when there is a high background intensity due to out of focus particles and unbound fluorescent dye.

7.4 CONCLUSION AND FUTURE OUTLOOK

Here, we have produced a mass-manufacturable microfluidic chip with integrated light sheet illumination, and successfully demonstrated that it allows accurate SPT size and concentration measurements of MVs in cell culture medium and in interstitial fluid collected from primary human breast tumours.

Nonetheless, further optimization of the chip's performance should be possible. Based on the simulated light sheet created by the fundamental propagating light mode, it seems that at least 30% reduction of the light sheet thickness should be possible by reducing the core thickness and fine-tuning of the refractive indices of core and cladding layers so as to obtain a monomodal waveguide. This requires optimization of the fabrication process, including the amount of D.E.R.TM 353 in the cladding layers, spin coating speeds, and baking times. In case of the silicon chip, contrast could be further improved by applying a non-reflective coating (e.g. black SU-8 formulations) on the silicon wafer before spin coating of the waveguide structure. Furthermore, automation of the coupling of light from the fiber into the waveguide is expected to make the chip more suitable for high-throughput measurements.

Interestingly, one other type of microfluidic chip was recently reported for MV characterization in biological fluids based on labelling with magnetic nanoparticles and miniaturized nuclear magnetic resonance detection [7]. Although it was shown to be

capable of discriminating different types of MVs with high sensitivity, it does not feature independent size and concentration measurements. In contrast, the microfluidic chip presented here is much simpler in design, can be mass-fabricated at a low cost, and allows at the same time MV identification, as well as size and concentration measurements. Thus, it opens the possibility to be used as a diagnostic tool that combine low cost, ease of use, and sensitivity [31,32].

REFERENCES

1. K. Al-Nedawi, B. Meehan, and J. Rak, "Microvesicles Messengers and mediators of tumor progression," *Cell Cycle* **8**, 2014-2018 (2009).
2. C. D'Souza-Schorey and J. W. Clancy, "Tumor-derived microvesicles: shedding light on novel microenvironment modulators and prospective cancer biomarkers," *Genes & Development* **26**, 1287-1299 (2012).
3. F. Fleissner, Y. Goerzig, A. Haverich, and T. Thum, "Microvesicles as Novel Biomarkers and Therapeutic Targets in Transplantation Medicine," *American Journal of Transplantation* **12**, 289-297 (2012).
4. T. H. Lee, E. D'Asti, N. Magnus, K. Al-Nedawi, B. Meehan, and J. Rak, "Microvesicles as mediators of intercellular communication in cancer-the emerging science of cellular 'debris'," *Seminars in Immunopathology* **33**, 455-467 (2011).
5. V. Muralidharan-Chari, J. W. Clancy, A. Sedgwick, and C. Souza-Schorey, "Microvesicles: mediators of extracellular communication during cancer progression," *Journal of Cell Science* **123**, 1603-1611 (2010).
6. J. Skog, T. Wurdinger, S. van Rijn, D. H. Meijer, L. Gainche, M. Sena-Esteves, W. T. Curry, B. S. Carter, A. M. Krichevsky, and X. O. Breakefield, "Glioblastoma microvesicles transport RNA and proteins that promote tumour growth and provide diagnostic biomarkers," *Nature Cell Biology* **10**, 1470-U209 (2008).
7. H. L. Shao, J. Chung, L. Balaj, A. Charest, D. D. Bigner, B. S. Carter, F. H. Hochberg, X. O. Breakefield, R. Weissleder, and H. Lee, "Protein typing of circulating microvesicles allows real-time monitoring of glioblastoma therapy," *Nature Medicine* **18**, 1835-+ (2012).
8. E. van der Pol, A. G. Hoekstra, A. Sturk, T. G. van Leeuwen, and R. Nieuwland, "Optical and non-optical methods for detection and characterization of microparticles and exosomes," *Journal of Thrombosis and Haemostasis* **8**, 2596-2607 (2010).
9. B. Gyorgy, T. G. Szabo, L. Turiak, M. Wright, P. Herczeg, Z. Ledeczki, A. Kittel, A. Polgar, K. Toth, B. Derfalvi, G. Zelenak, I. Borocz, B. Carr, G. Nagy, K. Vekey, S. Gay, A. Falus, and E. I. Buzas, "Improved Flow Cytometric Assessment Reveals Distinct Microvesicle (Cell-Derived Microparticle) Signatures in Joint Diseases," *Plos One* **7**, (2012).
10. E. van der Pol, A. N. Boing, P. Harrison, A. Sturk, and R. Nieuwland, "Classification, Functions, and Clinical Relevance of Extracellular Vesicles," *Pharmacological Reviews* **64**, 676-705 (2012).
11. K. Braeckmans, K. Buyens, W. Bouquet, C. Vervaet, P. Joye, F. De Vos, L. Plawinski, L. Doeuvre, E. ngles-Cano, N. N. Sanders, J. Demeester, and S. C. De Smedt, "Sizing Nanomatter in Biological Fluids by Fluorescence Single Particle Tracking," *Nano Letters* **10**, 4435-4442 (2010).
12. M. Röding, H. Deschout, K. Braeckmans, and M. Rudemo, "Measuring absolute number concentrations of nanoparticles using single-particle tracking," *Physical Review e* **84**, (2011).
13. C. Thery, M. Ostrowski, and E. Segura, "Membrane vesicles as conveyors of immune responses," *Nature Reviews Immunology* **9**, 581-593 (2009).
14. J. G. Ritter, R. Veith, J. P. Siebrasse, and U. Kubitscheck, "High-contrast single-particle tracking by selective focal plane illumination microscopy," *Optics Express* **16**, 7142-7160 (2008).

15. J. G. Ritter, R. Veith, A. Veenendaal, J. P. Siebrasse, and U. Kubitscheck, "Light Sheet Microscopy for Single Molecule Tracking in Living Tissue," *Plos One* **5**, (2010).
16. J. H. Spille, T. Kaminski, H. P. Konigshoven, and U. Kubitscheck, "Dynamic three-dimensional tracking of single fluorescent nanoparticles deep inside living tissue," *Optics Express* **20**, 19697-19707 (2012).
17. J. Huiskens, J. Swoger, F. Del Bene, J. Wittbrodt, and E. H. K. Stelzer, "Optical sectioning deep inside live embryos by selective plane illumination microscopy," *Science* **305**, 1007-1009 (2004).
18. P. J. Keller, A. D. Schmidt, J. Wittbrodt, and E. H. K. Stelzer, "Reconstruction of Zebrafish Early Embryonic Development by Scanned Light Sheet Microscopy," *Science* **322**, 1065-1069 (2008).
19. P. J. Keller, A. D. Schmidt, A. Santella, K. Khairy, Z. R. Bao, J. Wittbrodt, and E. H. K. Stelzer, "Fast, high-contrast imaging of animal development with scanned light sheet-based structured-illumination microscopy," *Nature Methods* **7**, 637-U55 (2010).
20. J. Huiskens and D. Y. R. Stainier, "Selective plane illumination microscopy techniques in developmental biology," *Development* **136**, 1963-1975 (2009).
21. F. Cella Zanacchi, Z. Lavagnino, M. P. Donnorso, A. Del Bue, L. Furia, M. Faretta, and A. Diaspro, "Live-cell 3D super-resolution imaging in thick biological samples," *Nature Methods* **8**, 1047-+ (2011).
22. T. A. Planchon, L. Gao, D. E. Milkie, M. W. Davidson, J. A. Galbraith, C. G. Galbraith, and E. Betzig, "Rapid three-dimensional isotropic imaging of living cells using Bessel beam plane illumination," *Nature Methods* **8**, 417-U68 (2011).
23. F. Cutrale and E. Gratton, "Inclined selective plane illumination microscopy adaptor for conventional microscopes," *Microscopy Research and Technique* **75**, 1461-1466 (2012).
24. J. C. M. Gebhardt, D. M. Suter, R. Roy, Z. W. Zhao, A. R. Chapman, S. Basu, T. Maniatis, and X. S. Xie, "Single-molecule imaging of transcription factor binding to DNA in live mammalian cells," *Nature Methods* **10**, 421-426 (2013).
25. J. M. Ruano-Lopez, M. Aguirregabiria, M. Tijero, M. T. Arroyo, J. Elizalde, J. Berganzo, I. Aranburu, F. J. Blanco, and K. Mayora, "A new SU-8 process to integrate buried waveguides and sealed microchannels for a Lab-on-a-Chip," *Sensors and Actuators B-Chemical* **114**, 542-551 (2006).
26. S. Hell, G. Reiner, C. Cremer, and E. H. K. Stelzer, "Aberrations in Confocal Fluorescence Microscopy Induced by Mismatches in Refractive-Index," *Journal of Microscopy-Oxford* **169**, 391-405 (1993).
27. K. Braeckmans, D. Vercauteren, J. Demeester, and S. C. De Smedt, "Single Particle Tracking," in *Nanoscopy and Multidimensional Optical Fluorescence Microscopy*, A. Diaspro, ed., (CRC Press / Taylor & Francis Group, Boca Raton, 2010).
28. A. Hendrix, W. Westbroek, M. Bracke, and O. De Wever, "An Ex(o)citing Machinery for Invasive Tumor Growth," *Cancer Research* **70**, 9533-9537 (2010).
29. A. De Boeck, P. Pauwels, K. Hensen, J. Rummens, W. Westbroek, A. Hendrix, D. Maynard, H. Denys, K. Lambein, G. Braems, C. Gespach, M. Bracke, and O. De Wever, "Bone marrow-derived mesenchymal stem cells promote colorectal cancer progression through paracrine neuregulin 1/HER3 signalling," *Gut* (2012).
30. A. Hendrix, D. Maynard, P. Pauwels, G. Braems, H. Denys, R. Van den Broecke, J. Lambert, S. Van Belle, V. Cocquyt, C. Gespach, M. Bracke, M. C. Seabra, W. A. Gahl, O. De Wever, and W. Westbroek, "Effect of the Secretory Small GTPase Rab27B on Breast Cancer Growth, Invasion, and Metastasis," *Journal of the National Cancer Institute* **102**, 866-880 (2010).

Chapter 7

31. K. K. Ghosh, L. D. Burns, E. D. Cocker, A. Nimmerjahn, Y. Ziv, A. El Gamal, and M. J. Schnitzer, "Miniaturized integration of a fluorescence microscope," *Nature Methods* **8**, 871-U147 (2011).
32. H. Y. Zhu, S. O. Isikman, O. Mudanyali, A. Greenbaum, and A. Ozcan, "Optical imaging techniques for point-of-care diagnostics," *Lab on A Chip* **13**, 51-67 (2012).

Summary

A variety of nanoparticles, like nanomedicines or biological vesicles, play an important role in many emerging pharmaceutical technologies. The efficient and rational development of these technologies can, therefore, strongly benefit from a detailed knowledge of the characteristics of these nanoparticles within the relevant biological materials. A suitable technique for this purpose is fluorescence microscopy, as it allows to non-invasively visualize fluorescently labelled nanoparticles with excellent specificity in biomaterials. However, the limited spatial resolution in optical microscopy restricts these observations to the micrometer scale. Advanced methods based on fluorescence microscopy are, therefore, developed to determine nanoparticle properties in an indirect way, based on their motion inside the biomaterials.

The topic of **PART I** was FRAP, an advanced fluorescence microscopy based method that is capable of measuring the diffusion and interaction of fluorescently labelled molecules or nanoparticles inside biomaterials. FRAP has already found a variety of applications in pharmaceutical research, as reviewed in **Chapter 1**. This showed that the method has proven to be particularly useful in the field of drug delivery, where it was used extensively to measure the diffusion of tracer molecules inside drug delivery systems, such as hydrogels, yielding important clues for their optimization. FRAP has also been applied numerously to investigate the mobility of drug molecules and nanoparticles inside extracellular matrices, as well as inside living cells. Such information is essential in the development or optimization of nanomedicine formulations that guide drug molecules inside these biomaterials to reach their site of action. Besides drug delivery, FRAP has also been helpful to improve several medical therapies, for instance by observing the effect of candidate anti-cancer drugs on the mobility of tumour related proteins, or by measuring the diffusion of peptide and protein aggregates related to neuro-degenerative diseases inside the brain. Yet another application of FRAP is situated in the field of diagnostics, where it was found that some medical conditions can be detected in an early stage by a change in mobility of tracer molecules inside the affected tissue.

Although FRAP has proven to be useful in pharmaceutical, biomedical and biological research for several decades, most theoretical FRAP models for fitting to the observed fluorescence recovery still rely on approximations that in many circumstances affect their accuracy. In particular, these models usually either neglect or incorrectly account for the imaging and photobleaching point spread functions (PSFs), in particular when a standard confocal laser scanning microscope is used. Generally, this degrades the accuracy of the FRAP analysis, unless an area is photobleached that is sufficiently large compared to both PSFs. However, often one is interested in measuring the diffusion in a very small area close to the microscope resolution, necessitating a more refined type of analysis. This usually requires prior knowledge or calibration of the size and shape of

Summary

both PSFs. However, this is problematic for the (effective) photobleaching PSF, since its properties strongly depend on the photobleaching light power and the photochemistry of the fluorophore inside the sample. A new FRAP model that addresses these issues was, therefore, developed in **Chapter 2**. This model describes the spatial profile of the fluorescence recovery after photobleaching of a rectangular area, assuming a linear photobleaching process and approximating the photobleaching and imaging PSFs by Gaussian functions with each a different standard deviation. Since not only temporal but also spatial information is used in the fit, more degrees of freedom are allowed than with conventional models that only describe the average fluorescence over the photobleached area. This, in turn, allows the standard deviations of the two Gaussian shaped PSFs to be treated as free fitting parameters, which removes the necessity of prior knowledge or calibration. The rectangle FRAP model was extensively validated on solutions of dextrans with different viscosities. It was shown that the rectangle can be arbitrarily small and have any aspect ratio. Interestingly, diffusion during photobleaching did not impact the value of the measured diffusion coefficient. Empirically, it was found that, despite the linear approximation of the photobleaching process, up to 50% of bleaching was allowed. In collaboration with Dr. Niklas Lorén from the Swedish Institute for Food and Technology, the model was used to study the diffusion of dextrans in a mixture of gelatin and maltodextrin that exhibits separate phases with a characteristic length scale down to a few micron. Due to the ability of the rectangle FRAP model to perform diffusion measurements in micron sized regions, the diffusion coefficient in the separate phases could be accurately determined. The diffusion in the phase separated system was found to differ slightly from the corresponding pure phases, indicating that there is some mixing of both components. Since additional free parameters can be included in the fit, more complex types of analysis should be possible in the future, such as measurements of anomalous or anisotropic diffusion, distribution of diffusion coefficients, or diffusion and binding.

Besides FRAP, other advanced methods based on fluorescence microscopy for investigating the motion of fluorescently labelled molecules or nanoparticles inside biomaterials have been developed as well. The topic of **PART II** was single particle tracking (SPT), a particularly interesting method since it allows to determine a variety of nanoparticle properties like size, diffusion rate, concentration, or interaction inside biomaterials. As the method is based on measurements of individual nanoparticles, it is inherently more precise in comparison to an ensemble average method like FRAP. In recent years, SPT has started to attract attention in pharmaceutical research, as discussed in **Chapter 3**. Just like FRAP, SPT is particularly useful in the field of drug delivery, as it can provide valuable information for a systematic optimization of drug delivery systems. For instance, in the context of gene therapy, complexes of

therapeutic nucleic acids and liposomes or polymers are being developed for delivery of the nucleic acids to target cells. SPT has been applied to study their aggregation in the blood circulation and their intracellular trafficking. The method also has much potential in the field of diagnostics, where it is believed that the concentration and size of cell-derived membrane vesicles are predictive of several diseases. SPT can be used to measure these nanoparticle properties directly in body fluids like blood or urine.

In order to realize the full potential of SPT, there are several important technical issues that need to be settled. An essential step in every SPT experiment is determining the location of the individual nanoparticles in the recorded fluorescence microscope images. This is often done by fitting a two-dimensional Gaussian function to the observed nanoparticle intensity distribution. However, this only yields precise and accurate estimations of the nanoparticle position in the specific case that it is located near the focal plane and emits photons in an isotropic fashion. Else, the Gaussian function is no longer guaranteed to be a good approximation of the nanoparticle image, resulting in a potentially significant increase in localization uncertainty. Several other aspects of the SPT experiment, such as detector noise and out of focus fluorescence from the sample, can also degrade the localization precision and accuracy. In order to correctly analyse SPT data and optimize SPT experiments, theoretical descriptions of the localization uncertainty that account for these different cases have been developed, as reviewed in **Chapter 4**. Moreover, since the localization of single molecules is the essence of some recently developed super resolution microscopy techniques, the relevance of localization uncertainty has also been treated in this context.

Despite being inherent to SPT, motion during image acquisition is generally ignored in theoretical descriptions of localization precision and accuracy. In **Chapter 5**, it is shown that this effect strongly increases the localization uncertainty in case of Gaussian fitting. Instead, the simple centre-of-mass algorithm that does not make assumptions about the shape of the nanoparticle image is found to perform much more reliably. A theory is developed for the average precision of the centre-of-mass, taking diffusion during image acquisition into account. Besides this theoretical model, also a method for the experimental determination of the average localization precision of moving nanoparticles is proposed, based on SPT performed simultaneously in two different imaging channels. Both the theory and the experimental method are validated by simulations and applied to determine the localization precision of diffusing nanospheres. Both predictions agree with each other and show that diffusion during imaging results in a localization precision that is significantly worse than for stationary nanoparticles. Furthermore, in the context of determining the diffusion coefficient from the trajectory mean square displacements, it was shown that incorporating the

Summary

localization precision theory into the model of these displacements increases the accuracy of the fitted diffusion coefficient. Interestingly, the theory can also be used to define an optimal image acquisition time that maximizes the localization precision.

Taking the effect of motion during image acquisition on the localization precision into account is thus essential for correct analysis of SPT measurements. In **Chapter 6**, this knowledge is applied to a new method for the investigation of the interaction between dynamic objects that each have a different fluorescent label by comparing their trajectories. The basic idea is that, if two objects are interacting, they will move together. In other words, the positions in both trajectories exhibit a certain amount of correlation during the interaction time frame. The new method scans the positions in both trajectories with a window in which the correlation is calculated. If this correlation is statistically significant and larger than a certain threshold, the nanoparticles are considered to interact in that window. Both the window size and the correlation threshold depend on the local localization precision and travelled distance. This scanning window method thus allows to build a picture of both the spatial and temporal behaviour of the interaction. The method is validated with simulated trajectories, showing that interaction and absence of interaction are correctly distinguished from each other. Moreover, simulated trajectories that feature more complex situations such as transient interaction or variable localization precision also do not pose a problem to the scanning window method. As a proof of concept, the method is applied in the context of gene therapy to investigate the endosomal trafficking of gene complexes inside living cells. More than twice the amount of correlated trajectory pairs is found compared to a more simple method that does not scan the trajectories. This is likely caused by several experimental complications such as a changing mobility or a changing localization precision in the trajectories. Moreover, it is found that the scanning window method is able to detect transient events, such as trajectories that stop interacting at some point. Such a method will possibly allow to detect the escape of nanomedicine particles from endosomes into the cytosol of cells, a required step for nucleic acids to perform their intended therapeutic action. Endosomal escape is considered to be one of the major bottlenecks in intracellular macromolecular drug delivery and methods capable of studying this barrier are urgently sought for.

Besides precise and accurate localization of nanoparticles in the images, an even more fundamental requirement for SPT is that the nanoparticles are visible with sufficient contrast. When widefield illumination is used, the contrast is limited because the nanoparticles and unbound dye located out of focus are also illuminated and, therefore, contribute to the image background. A solution to this problem is light sheet illumination, in which only a thin layer surrounding the focal plane is illuminated. The out of focus nanoparticles and unbound dye thus remain dark and the contrast

improves significantly. However, such a light sheet is usually produced by an extra objective lens, making the microscope set-up complicated and requiring a special sample holder with a transparent side window in addition to the imaging window. As explained in **Chapter 7**, we have developed a simple microfluidics chip with an integrated planar waveguide that generates a light sheet inside a microchannel containing the sample. This allows for SPT measurement in biofluids with light sheet illumination, without the need for an extra objective lens. Moreover, the mass producible chip can be made disposable, which, in turn, removes the necessity of cleaning procedures between samples and avoids sample contamination. The chip was used to perform SPT on cell-derived membrane vesicles in cell culture medium and in interstitial fluid from a human breast tumour. An accurate and precise size distribution and concentration could be derived from the SPT measurements using the light sheet illumination, while this was not possible with widefield illumination because of limited contrast. This shows the potential of the chip as a diagnostic tool, since the size and concentration of such membrane vesicles are believed to be linked to different stadia of cancer. Further optimization of the fabrication process of the chip should lead to a thinner light sheet, which enhances the contrast in SPT experiments even more. The chip could also be equipped with for instance more advanced microfluidics, leading to a diagnostic tool that can be used outside a laboratory setting.

The results of this PhD thesis are expected to contribute to the on-going effort of making accurate SPT and FRAP measurements of molecules and nanoparticle properties in biomaterials more accessible to the pharmaceutical research community. This access is crucial for further developments in the field of drug delivery and diagnostics, where nanoparticles, such as nanomedicines and biological vesicles, are finding more and more applications.

Summary

Samenvatting

Een verscheidenheid aan nanopartikels, zoals nanomedicijnen of biologische vesikels, spelen een belangrijke rol in heel wat nieuwe farmaceutische technologieën. De efficiënte en rationele ontwikkeling van deze technologieën kan daarom sterk profiteren van een gedetailleerde kennis van de karakteristieken van deze nanopartikels in de relevante biologische materialen. Een geschikte techniek voor dit doeleinde is fluorescentiemicroscopie, aangezien fluorescent gelabelde nanopartikels hiermee op een niet-invasieve manier kunnen gevisualiseerd worden met uitstekende specificiteit in biomaterialen. De beperkte spatiale resolutie van optische microscopie limiteert deze observaties echter tot op de micrometerschaal. Geavanceerde methodes gebaseerd op fluorescentiemicroscopie worden daarom ontwikkeld om de eigenschappen van nanopartikels op een indirecte wijze te bepalen, gebaseerd op hun beweging in de biomaterialen.

Het onderwerp van **DEEL I** was *fluorescence recovery after photobleaching* (FRAP), een geavanceerde techniek gebaseerd op fluorescentiemicroscopie die in staat is om de diffusie en interactie van fluorescent gelabelde moleculen of nanopartikels in biomaterialen te meten. FRAP heeft reeds een verscheidenheid aan toepassingen gevonden in farmaceutisch onderzoek, zoals besproken in **Hoofdstuk 1**. Dit overzicht toonde aan dat de methode vooral nuttig is gebleken in het veld van *drug delivery*, waarbij metingen van de diffusie van fluorescent gelabelde moleculen in systemen voor geneesmiddelaafgifte, zoals hydrogels, belangrijke aanwijzingen opleveren voor hun verdere optimalisatie. FRAP is ook veelvuldig gebruikt geweest om de mobiliteit van geneesmiddelmoleculen en nanopartikels in extracellulaire matrices en zelfs in levende cellen te onderzoeken. Dergelijke informatie is essentieel voor de ontwikkeling of optimalisatie van de formulering van nanomedicijnen die geneesmiddelmoleculen begeleiden in deze biomaterialen opdat ze hun werkingsgebied zouden bereiken. Naast geneesmiddelaafgifte is FRAP ook nuttig geweest bij de verbetering van verschillende medische therapieën, bijvoorbeeld door het observeren van het effect van potentiële anti-kankergeneesmiddelen op de mobiliteit van tumor-gerelateerde eiwitten, of door het meten van de diffusie van peptide- of eiwitaggregaten die gerelateerd zijn aan neurodegeneratieve ziektes in de hersenen. Nog een andere toepassing van FRAP is gesitueerd in the veld van de diagnostiek, waar sommige medische aandoeningen in een vroeg stadium kunnen worden gedetecteerd via een verandering in de mobiliteit van fluorescent gelabelde moleculen in het aangetaste weefsel.

Alhoewel FRAP al enkele decennia nuttig is gebleken in farmaceutisch, biomedisch en biologisch onderzoek, zijn de meeste theoretische FRAP modellen voor het fitten van het geobserveerde herstel van de fluorescentie na fotobleiking nog steeds gebaseerd op benaderingen die in heel wat omstandigheden hun nauwkeurigheid aantasten. De *point spread function* (PSF) tijdens het fotobleiken en tijdens het observeren van het herstel

Samenvatting

van de fluorescentie wordt door de meeste modellen ofwel genegeerd ofwel op de verkeerde manier in rekening gebracht, vooral wanneer een standaard confocale laserfluorescentiemicroscopie wordt gebruikt. In het algemeen zal dit de FRAP analyse minder nauwkeurig maken, tenzij een gebied wordt gefotobleekt dat voldoende groot is vergeleken met beide PSF-en. Men is echter meestal geïnteresseerd in diffusiemetingen in een zeer kleine gebieden die de resolutie van de microscopie benaderen, zodat een meer verfijnd type van analyse nodig is. Dit vergt meestal voorafgaande kennis of kalibratie van de grootte en vorm van beide PSF-en. Dit is problematisch voor de (effectieve) PSF tijdens het fotobleken, aangezien de eigenschappen van deze PSF sterk afhangen van het vermogen van het licht dat gebruikt werd om te fotobleken en van de fotochemie van het fluorofor in het staal. Een nieuw FRAP model dat een oplossing aanbiedt voor deze problemen, werd daarom ontwikkeld in **Hoofdstuk 2**. Dit model beschrijft het ruimtelijk profiel van het herstel van de fluorescentie na fotobleking van een rechthoekig gebied, waarbij wordt verondersteld dat het fotoblekingsproces lineair is en waarbij de PSF-en tijdens het fotobleken en tijdens het observeren van het herstel van de fluorescentie worden benaderd door Gaussiaanse functies met elk een verschillende standaardafwijking. Aangezien zo niet enkel temporele, maar ook spatiale informatie wordt gebruikt in de fit, zijn meer vrijheidsgraden toegelaten dan met conventionele modellen die enkele de gemiddelde fluorescentie over het gefotobleekte gebied beschrijven. Dit laat op zijn beurt toe om de standaardafwijkingen van de twee Gaussiaanse PSF-en te behandelen als vrijheidsgraden, wat de noodzaak van voorafgaande kennis of kalibratie wegneemt. Het *rectangle* FRAP model werd uitgebreid gevalideerd aan de hand van oplossingen van dextranen met verschillende viscositeit. Hiermee werd aangetoond dat de rechthoek arbitrair klein kan zijn en elke *aspect ratio* kan hebben. Interessant was ook de vondst dat diffusie tijdens het fotobleken geen invloed had op de waarde van de gemeten diffusiecoëfficiënt. Empirisch werd aangetoond dat, ondanks de lineaire benadering van het fotoblekingsproces, tot en met 50% fotobleking was toegelaten. In samenwerking met Dr. Niklas Lorén van het Zweedse Instituut voor Voedsel en Technologie, werd het model gebruikt om de diffusie van dextranen te bestuderen in een mengsel van gelatine en maltodextrine. Dit mengsel organiseert zich als gescheiden fases die een karakteristieke lengte van een paar micrometer hebben. Dankzij het vermogen van het *rectangle* FRAP model om diffusiemetingen uit te voeren in gebieden met microscopische afmetingen, kon de diffusiecoëfficiënt in deze afzonderlijke fases worden bepaald met grote nauwkeurigheid. De diffusie in het mengsel met gescheiden fases bleek licht te verschillen van de overeenkomstige waarde in pure fases, wat erop wijst dat beide componenten enigszins met elkaar mengen. Aangezien de fit nog extra vrijheidsgraden toelaat, zijn meer complexe types van FRAP analyse mogelijk in de

toekomst, zoals metingen van anomale of anisotrope diffusie, distributies van diffusiecoëfficiënten, of diffusie en binding.

Naast FRAP zijn er ook andere geavanceerde methodes gebaseerd op fluorescentiemicroscopie ontwikkeld voor het bestuderen van de beweging van fluorescent gelabelde moleculen of nanopartikels in biomaterialen. Het onderwerp van **DEEL II** was *single particle tracking* (SPT), een erg interessante methode die toelaat om een verscheidenheid aan nanopartikeleigenschappen zoals grootte, diffusiesnelheid, concentratie of interactie te bestuderen in biomaterialen. Aangezien SPT gebaseerd is op metingen van individuele nanopartikels, is de techniek inherent meer precies dan een ensemble gemiddelde methode zoals FRAP. Sinds enkele jaren begint SPT aandacht te krijgen in farmaceutisch onderzoek, zoals werd besproken in **Hoofdstuk 3**. Net zoals FRAP, is ook SPT bijzonder nuttig voor het veld van *drug delivery*, aangezien met deze methode informatie kan worden bekomen die erg belangrijk is voor een systematische optimalisatie van systemen voor geneesmiddelafgifte. Bijvoorbeeld, in de context van gentherapie worden complexen van therapeutische nucleïnezuuren en liposomen of polymeren ontwikkeld voor de afgifte van de nucleïnezuuren aan bepaalde cellen. SPT werd gebruikt om de aggregatie van deze complexen in de bloedsomloop te bestuderen en om na te gaan hoe ze intracellulair worden verwerkt. De methode heeft ook veel potentieel in het veld van de diagnostiek, waar er wordt vanuit gegaan dat de concentratie en de grootte van membraanvesikels die worden afgescheiden door cellen kan gerelateerd worden aan verschillende ziektes. SPT kan worden gebruikt om de eigenschappen van deze nanopartikels rechtstreeks te meten in lichaamsvloeistoffen zoals bloed of urine.

Om het potentieel van SPT ten volle te kunnen realiseren, zijn er echter nog heel wat technische moeilijkheden die moeten worden aangepakt. Een essentiële stap in elk SPT experiment is het bepalen van de lokatie van de individuele nanopartikels in de opgenomen fluorescentiemicroscopie-beelden. Dit wordt vaak gedaan door een tweedimensionale Gaussiaanse functie aan de geobserveerde intensiteitsdistributie van elk nanopartikel te fitten. Dit levert echter enkel een precieze en accurate schatting van de positie van het nanopartikel op in het specifieke geval dat het zich dicht bij het focusvlak bevindt en fotonen uitzendt op een isotrope manier. In elk ander geval is de Gaussiaanse functie niet noodzakelijk een goede benadering van het beeld van het nanopartikel, wat resulteert in een mogelijk significante toename in de onzekerheid waarmee de locatie wordt bepaald. Verschillende andere aspecten van het SPT experiment, zoals ruis in de detector of fluorescentie van het staal buiten het focusvlak, kunnen de precisie en accuraatheid van de lokalisatie ook verminderen. Om de data van SPT experimenten correct te kunnen analyseren en om SPT experimenten te kunnen optimaliseren, werden theoretische beschrijvingen van deze lokalisatie-

Samenvatting

onzekerheid ontwikkeld die deze verschillende gevallen in rekening brengen, zoals werd besproken in **Hoofdstuk 4**. Aangezien het lokaliseren van afzonderlijke moleculen de essentie is van sommige onlangs ontwikkelde superresolutiemicroscopie-technieken, werd de relevantie van lokalisatie-onzekerheid ook in deze context behandeld.

Ondanks het feit dat beweging tijdens de beeldopname inherent aanwezig is in SPT experimenten, wordt dit over het algemeen genegeerd in de theoretische beschrijvingen van de precisie en accuraatheid van de lokalisatie. In **Hoofdstuk 5** werd aangetoond dat dit effect de onzekerheid van de lokalisatie sterk doet toenemen wanneer een Gaussiaanse functie wordt gefit. Het eenvoudige massacentrum-algoritme, dat geen veronderstellingen maakt over de vorm van het beeld van het nanopartikel, is daarentegen veel meer betrouwbaar. Een theorie werd ontwikkeld voor de beschrijving van de gemiddelde lokalisatieprecisie van het massacentrum, waarbij rekening wordt gehouden met diffusie tijdens de beeldopname. Naast dit theoretische model werd ook een methode voor de experimentele bepaling van de gemiddelde lokalisatieprecisie van bewegende nanopartikels voorgesteld, gebaseerd op SPT die simultaan wordt uitgevoerd in twee verschillende beeldkanalen. Zowel de theorie als de experimentele methode werden gevalideerd aan de hand van simulaties en toegepast om de lokalisatieprecisie van diffunderende nanosferen te bepalen. Beide resultaten bevestigen elkaar en tonen aan dat diffusie tijdens de beeldopname resulteert in een lokalisatieprecisie die aanzienlijk slechter is dan in het geval van stationaire nanopartikels. In de context van het bepalen van de diffusiecoëfficiënt uit de gemiddelde kwadratische verplaatsingen in trajecten, werd er bovendien aangetoond dat het in rekening brengen van de theorie voor de lokalisatieprecisie in het model van deze verplaatsingen de nauwkeurigheid van de gefitte diffusiecoëfficiënt verhoogt. Noemenswaardig is ook dat de theorie kan worden gebruikt om een optimale beeldopnametijd te definiëren die de lokalisatieprecisie maximaliseert.

Het in rekening brengen van het effect van beweging tijdens de beeldopname op de lokalisatieprecisie is dus essentieel voor een correcte analyse van SPT-metingen. In **Hoofdstuk 6** wordt deze kennis toegepast op een nieuwe methode voor het bestuderen van de interacties tussen dynamische objecten die elk een verschillend fluorescent label hebben, via het vergelijken van hun trajecten. Het achterliggende idee is dat wanneer twee objecten met elkaar interageren, ze samen zullen bewegen. Met andere woorden, in geval van interactie zullen de posities van beide trajecten een zekere correlatie vertonen gedurende de periode dat ze interageren. De nieuwe methode scant de posities in beide trajecten met een venster waarin de correlatie wordt berekend. Als deze correlatie statistisch significant en groter dan een bepaalde drempelwaarde is, worden de nanopartikels verondersteld te interageren in dat

venster. Zowel de grootte van het venster als de drempelwaarde voor de correlatie hangen af van de lokale lokalisatieprecisie en afgelegde afstand. Deze *scanning window* methode laat dus toe om een beeld te krijgen van het spatiaal en temporeel gedrag van de interactie. De methode werd gevalideerd aan de hand van gesimuleerde trajecten, waaruit blijkt dat interactie en afwezigheid van interactie op een correcte manier van elkaar wordt onderscheiden. Bovendien heeft de methode ook geen probleem met gesimuleerde trajecten die worden gekenmerkt door meer complexe situaties, zoals tijdelijke interactie of variabele lokalisatieprecisie. Om het concept te bewijzen, wordt de methode toegepast in de context van gentherapie om het transport van gencomplexen door endosomen in levende cellen te bestuderen. In vergelijking met een meer eenvoudige methode die de trajecten niet scant met een venster, worden meer dan twee keer zoveel gecorreleerde trajecten gevonden. Dit verschil wordt naar alle waarschijnlijkheid veroorzaakt door experimentele complicaties zoals een veranderende mobiliteit of een veranderende lokalisatieprecisie in de trajecten. De *scanning window* methode is bovendien in staat om tijdelijke gebeurtenissen te detecteren, wat bijvoorbeeld het geval is als trajecten op een zeker punt stoppen met interageren. Een dergelijke methode zal mogelijk toelaten om nanomedicijnen die ontsnappen vanuit endosomen naar het cytosol van cellen te detecteren, een noodzakelijke stap voor nucleïnezuuren om hun therapeutische actie te verwezenlijken. Endosomale ontsnapping wordt gezien als een van de belangrijkste knelpunten in intracellulaire afgifte van macromoleculaire geneesmiddelen, er wordt daarom intensief gezocht naar methodes die in staat zijn om deze barrière te bestuderen.

Naast het precies en nauwkeurig lokaliseren van nanopartikels in de opgenomen beelden, is een nog fundamentele voorwaarde voor SPT het zichtbaar zijn van de nanopartikels met voldoende contrast. Wanneer *widefield* belichting wordt gebruikt, zal het contrast beperkt zijn, aangezien de nanopartikels en ongebonden fluorescente labels die zich buiten het focusvlak bevinden ook worden belicht en daarom bijdragen tot de achtergrond in de beelden. Een oplossing voor dit probleem is *light sheet* belichting, waarbij enkel een dunne laag rond het focusvlak wordt belicht. De nanopartikels en ongebonden fluorescente labels die zich buiten het focusvlak bevinden, blijven daardoor donker, zodat het contrast aanzienlijk verbetert. Een dergelijke belichting wordt meestal geproduceerd met behulp van een extra objectieflens, wat niet alleen de microscoopopstelling complex maakt, maar ook een speciale staalhouder vereist met, naast het venster voor de beeldvorming, ook een transparant venster aan de zijkant. Zoals uitgelegd in **Hoofdstuk 7**, hebben we een eenvoudige microfluidica chip ontwikkeld met een geïntegreerde vlakke golfgeleider die een *light sheet* genereert in een microkanaal dat het staal bevat. Dit laat toe om SPT metingen in biologische vloeistoffen uit te voeren met *light sheet* belichting, zonder de

Samenvatting

noodzaak van een extra objectieflens. Daarbovenop kan de massaproduceerbare chip wegwerpbaar worden gemaakt, wat op zijn beurt reiniging tussen het meten van verschillende stalen onnodig maakt en de contaminatie tussen verschillende stalen verhindert. De chip werd gebruikt om SPT metingen uit te voeren in celcultuurmedium en interstitieel vocht van een menselijke borsttumor waarin zich membraanvesikels bevinden die door cellen zijn afgescheiden. Een nauwkeurige grootte- en concentratiedistributie en concentratie kon worden bepaald aan de hand van de SPT metingen met behulp van de *light sheet* belichting, terwijl dit niet mogelijk was voor de *widefield* belichting, gezien het beperkte contrast. Dit illustreert het potentieel van de chip als een diagnostisch instrument, aangezien de grootte en concentratie van dergelijke membraanvesikels mogelijk kan worden gelinkt aan verschillende stadia van kanker. Verdere optimalisatie van het fabricatieproces van de chip zou moeten leiden tot een dunnere *light sheet*, wat het contrast in SPT experimenten nog meer kan verbeteren. Daarnaast zou de chip ook kunnen uitgerust worden met bijvoorbeeld meer geavanceerde microfluidica, wat moet resulteren in een diagnostisch instrument dat ook buiten een laboratorium kan worden gebruikt.

We verwachten dat de resultaten van deze doctoraats thesis zullen bijdragen tot de huidige inspanningen om nauwkeurige SPT en FRAP metingen van de eigenschappen van moleculen en nanopartikels in biomaterialen meer toegankelijk te maken voor de farmaceutische onderzoeksgemeenschap. Deze toegang is cruciaal voor verdere ontwikkelingen in het veld van *drug delivery* en diagnostiek, waar nanopartikels, zoals nanomedicijnen en biologische vesikels, steeds meer toepassingen vinden.

Acknowledgements

First and foremost I would like to thank prof. Kevin Braeckmans for encouraging me in my pursuit of a PhD in pharmaceutical sciences. As a physicist and engineer, this was not a straightforward choice, but it has turned out to be a wonderful experience. I would like to thank Kevin for his guidance, inspiration, enthusiasm, and support in achieving my goal.

Of course I also would like to thank prof. Kristiaan Neyts of the Liquid Crystals and Photonics Group and prof. Jo Demeester for being co-promoters of this work. Although prof. Stefaan De Smedt was not officially a co-promoter, he is acknowledged just as much. My thanks also go to prof. Marcel Ameloot of Hasselt University, dr. Davide Mazza of the San Raffaele Research Center, prof. Johan Hofkens of the University of Leuven, prof. André Skirtach of the Department of Molecular Biotechnology, and dr. Ilse Christiaens of the Department of Material Science and Engineering for their willingness to be part of the reading or examination committee of this thesis.

I definitely want to thank my colleagues at the Laboratory of General Biochemistry and Physical Pharmacy for their support. In particular, I acknowledge Thomas Martens, Dries Vercauteren, and Katrien Remaut for helping me to develop the scanning window method and for joining me in my (unfortunately fruitless) efforts to detect endosomal escape. I acknowledge the assistance of Koen Raemdonck and Stephan Stremersch in performing the on-chip SPT measurements of the cell-derived membrane vesicles. Others that were not involved in my research helped me in more indirect ways. I thank Katrien Forier for keeping the microscopy room tidy and organized. Thomas Martens and Broes Naeye are acknowledged for helping me out with life's little computer problems. Also thanks to Bart Lucas, Katharine Wullaert, Bruno Vandenbussche, and Ilse Dupon, who I could annoy with administrative burdens any time of day. And last, but certainly not least, I would like to thank to everyone in the lab (no, I'm not going to list them) for the pleasant and friendly atmosphere. The road is more important than the destination.

Besides my colleagues in the lab, many other people in Ghent have helped me over the years. I would like to express my gratitude to Toon Brans, Filip Strubbe, Hamidreza Azarinia, prof. Kristiaan Neyts, prof. Jeroen Beeckman, and others of the Liquid Crystals and Photonics Group for assisting me in the initial fabrication process of the chip and in the design the experimental set-up. On this matter, I also thank prof. Roel Baets, prof. Dries Van Thourhout, and others of the Photonics Research Group for their helpful advice. I would like to thank Steven Verstuyft for helping me out in the cleanroom in Zwijnaarde. I also acknowledge An Hendrix, prof. Marc Bracke, and prof. Rudy Van den broecke of Ghent University Hospital for providing me with relevant patient samples for the on-chip SPT measurements.

Acknowledgements

I also would like to thank many people from outside Ghent University for several rewarding collaborations. The expertise of Pietro Maoddi, Guillaume Mernier, Sébastien Jiguet, and prof. Phillipe Renaud of the Swiss Federal Institute of Technology in Lausanne was crucial for the current fabrication process of the chip. The contributions of prof. Niklas Lorén, Sophia Fransson, and Joel Hagman of the Swedish Institute of Food and Biotechnology to the development of the rectangle FRAP model are strongly appreciated. I thank Magnus Röding, Jenny Jonasson, and prof. Mats Rudemo of Chalmers University of Technology for solving almost 100% of my statistics problems. I acknowledge Francesca Cella Znacchi and prof. Alberto Diaspro of the Italian Institute of Technology, prof. Sam Hess of the University of Maine, and prof. Joerg Bewersdorf of Yale University School of Medicine for their helpful and interesting ideas on localization microscopy. I would like to thank Ben De Clercq, Kristof Notelaers, Nick Smisdom, and prof. Marcel Ameloot of Hasselt University for the interesting discussions on SPT and FRAP. I also acknowledge Roberta Censi and Ellen Verheyen of Utrecht University for providing me with challenging hydrogel samples to test the rectangle FRAP model.

I want to conclude with thanking my friends and family. Their support and encouragement have made all the difference. This also applies to one special person. Clara, *matondi mingi*.

Ghent, May 2013

Hendrik Deschout

Appendix A

Supplementary information of Chapter 5

Localization precision of the centroid algorithm

The point spread function (PSF) of a stationary particle in position $\vec{r}_p = (x_p, y_p)$ in the focal plane can be described by the circular 2-D Gaussian distribution [3]:

$$I(x, y) = \frac{N}{2\pi s^2} e^{-\frac{(x-x_p)^2 + (y-y_p)^2}{2s^2}}, \quad (\text{A.1})$$

with s the standard deviation of the Gaussian distribution and N the total number of photons. Consider an image of the PSF that consists of pixels with size a . The intensity of pixel (i, j) with centre position $\vec{r}_{i,j} = (x_{i,j}, y_{i,j})$ can approximately be described by [7]:

$$I_{i,j} = a^2 \frac{N}{2\pi(s^2 + a^2/12)} e^{-\frac{(x_{i,j}-x_p)^2 + (y_{i,j}-y_p)^2}{2(s^2 + a^2/12)}}. \quad (\text{A.2})$$

The intensity weighted centre or centroid of the PSF in the image is defined as:

$$x_p = \frac{\sum_{i,j} (I_{i,j} + R_{i,j}) x_{i,j}}{\sum_{i,j} (I_{i,j} + R_{i,j})} \text{ and } y_p = \frac{\sum_{i,j} (I_{i,j} + R_{i,j}) y_{i,j}}{\sum_{i,j} (I_{i,j} + R_{i,j})}. \quad (\text{A.3})$$

A noise contribution for every pixel (i, j) is explicitly introduced as $R_{i,j}$. Note that a possible constant background is assumed to be subtracted from the image. According to Cao et al., the localization precision σ_c of the centroid coordinate x_p (defined as the standard deviation on the centroids) resulting from noise $R_{i,j}$ with standard deviation $r_{i,j}$ in every pixel (i, j) can be described by [2,5]:

$$\begin{aligned} \sigma_c^2 = & \frac{\sum_{i,j} x_{i,j}^2 r_{i,j}^2}{\{\sum_{i,j} (I_{i,j} + R_{i,j})\}^2} \\ & + \frac{\{\sum_{i,j} (I_{i,j} + R_{i,j}) x_{i,j}\}^2 \sum_{i,j} r_{i,j}^2}{\{\sum_{i,j} (I_{i,j} + R_{i,j})\}^4} - \frac{2\{\sum_{i,j} (I_{i,j} + R_{i,j}) x_{i,j}\} \sum_{i,j} x_{i,j} r_{i,j}^2}{\{\sum_{i,j} (I_{i,j} + R_{i,j})\}^3}. \end{aligned} \quad (\text{A.4})$$

A similar definition is valid for the centroid coordinate y_p . We assume that the noise consists of Poisson distributed photon noise and background noise with a constant standard deviation b [10]:

$$r_{i,j}^2 = I_{i,j} + b^2. \quad (\text{A.5})$$

Appendix A

If $\sum_{i,j}(I_{i,j} + R_{i,j})$ is approximated by $\sum_{i,j} I_{i,j}$, the substitution of Eq. (A.5) in Eq. (A.4) can be shown to result in [5]:

$$\sigma_c^2 = \frac{\sum_{i,j}(x_{i,j} - x_p)^2 I_{i,j}}{\{\sum_{i,j} I_{i,j}\}^2} + \frac{b^2 \sum_{i,j}(x_{i,j} - x_p)^2}{\{\sum_{i,j} I_{i,j}\}^2}. \quad (\text{A.6})$$

If all pixels are included that belong to the particle PSF, then:

$$\sum_{i,j} I_{i,j} = N. \quad (\text{A.7})$$

The sum in the numerator of the first term of Eq. (A.6) can be approximated by an integration over the entire plane:

$$\sum_{i,j} (x_{i,j} - x_p)^2 I_{i,j} \approx \frac{1}{a^2} \int_{-\infty}^{+\infty} \int_{-\infty}^{+\infty} (x - x_p)^2 \frac{a^2 N}{2\pi(s^2 + a^2/12)} e^{-\frac{(x-x_p)^2 + (y-y_p)^2}{2(s^2 + a^2/12)}} dx dy, \quad (\text{A.8})$$

resulting in:

$$\sum_{i,j} (x_{i,j} - x_p)^2 I_{i,j} \approx N(s^2 + a^2/12). \quad (\text{A.9})$$

The sum in the numerator in the second term of Eq. (A.6) can also be approximated by integration over the entire image plane. However, this leads to infinity. We, therefore, limit the integration to a circular area around the PSF centre location $\vec{r}_p = (x_p, y_p)$ with radius equal to three times the PSF standard deviation, meaning that 99.7% of the N photons are included. This leads to:

$$\sum_{i,j} (x_{i,j} - x_p)^2 \approx \frac{1}{a^2} \int_0^{2\pi \cdot 3\sqrt{s^2 + a^2/12}} \int_0^{2\pi \cdot 3\sqrt{s^2 + a^2/12}} r^3 \cos^2 \theta dr d\theta, \quad (\text{A.10})$$

resulting in:

$$\sum_{i,j} (x_{i,j} - x_p)^2 = \frac{81\pi(s^2 + a^2/12)^2}{4a^2}. \quad (\text{A.11})$$

Substituting Eqs. (A.7), (A.9), and (A.11) in Eq. (A.6) readily leads to the following expression for the localization precision of the centroid:

$$\sigma_c^2 = \frac{s^2 + a^2/12}{N} + \frac{81\pi b^2(s^2 + a^2/12)^2}{4a^2N^2}. \quad (\text{A.12})$$

Note the similarity with the much used expression published by Mortensen et al. [7]. The first term shows the effect of the Poisson distributed photon noise and the second term takes the background noise into account. Equation (A.12) is valid for a CCD or CMOS camera, in case of an electron multiplying (EMCCD) CCD detector, the electron multiplication process adds a factor of two to the photon noise, leading to [8,9]:

$$\sigma_c^2 = 2 \left\{ \frac{s^2 + a^2/12}{N} + \frac{81\pi b^2(s^2 + a^2/12)^2}{4a^2N^2} \right\}, \quad (\text{A.13})$$

where it is assumed that b mainly consists of photon background noise.

Gaussian point spread function

Consider an image of a light emitting point-object with position $\vec{r}_p = (x_p, y_p, z_p)$ projected in the image space (xyz -space). The focal plane of the objective lens is projected at $z = 0$. The positions $\vec{r} = (x, y)$ of the photons in the image plane (xy -plane) are described by a probability distribution according to the PSF. For a particle in the focal plane with isotropic photon emission, the PSF is given by the Airy distribution with an infinite standard deviation [1]. To facilitate calculations, the PSF of a particle in the focal plane is often approximated by a circular 2-D Gaussian distribution, which is a reasonable approximation for all applications where the higher order diffraction features can be neglected [3]. The same reasoning can be extended to the third dimension. In that case, the PSF can be approximated by the fundamental Gaussian beam solution [11]:

$$I_{\text{gbs}}(\vec{r}; \vec{r}_p) = \frac{N}{2\pi s^2(z_p)} e^{-\frac{(x-x_p)^2 + (y-y_p)^2}{2s^2(z_p)}}, \quad (\text{A.14})$$

where the Gaussian variance $s^2(z_p)$ is defined by:

$$s^2(z_p) = s_0^2 \left(1 + \frac{z_p^2}{z_0^2} \right), \quad (\text{A.15})$$

Appendix A

with s_0^2 the Gaussian variance in case the particle is located in the focal plane ($z_p = 0$). The parameter z_0 is defined by:

$$z_0 = \frac{4\pi n}{\lambda} s_0^2, \quad (\text{A.16})$$

with n the refractive index of the medium and λ the wavelength of the emitted photons. The further from the focal plane the particle is located, the more the value of $s^2(z_p)$ increases, leading to a broader PSF with a smaller amplitude. However, if the point-object is not stationary but moving during the image acquisition, its movement will affect the shape of the observed intensity distribution. Let $\vec{r}_p(t)$ be the particle trajectory during the image acquisition time Δt , then the resulting apparent PSF will be:

$$I_{\text{app}}(\vec{r}) = \frac{1}{\Delta t} \int_0^{\Delta t} I_{\text{gbs}}(\vec{r}; \vec{r}_p(t)) dt. \quad (\text{A.17})$$

The exact trajectory $\vec{r}_p(t)$ of an individual particle during Δt is usually unknown. However, if the average position $\vec{r}_{p,av}$ during the image acquisition time can be estimated and if information about the type of motion is available, it is possible to compose the probability distribution $P(\vec{r}_p)$ of all particle positions \vec{r}_p during Δt . The convolution of this probability distribution with the PSF then immediately yields an *average* apparent PSF. In the following, free diffusion will be considered as the particle motion type.

Lateral diffusion

Diffusion in the xy -plane parallel to the focal plane ($z = 0$) will cause the apparent PSF to deviate from the stationary situation in Eq. (A.1). We consider particle movement in the x -direction only, since the obtained results equally apply to the y -dimension. Assume a diffusing particle during image acquisition time Δt with starting point $x_{p,0}$. The probability distribution of the particle position x_p at time t is given by [4]:

$$P(x_p, t) = \frac{1}{\sqrt{4\pi Dt}} e^{-\frac{(x_p - x_{p,0})^2}{4Dt}}, \quad (\text{A.18})$$

with D the diffusion coefficient. Now consider a particle trajectory that consists of $M + 1$ positions $x_{p,i}$ at different times $t_i = i\Delta t / M$ ($i = 0, 1, \dots, M$).

The average position $x_{p,av}$ of the particle during Δt is estimated by:

$$x_{p,av} = \frac{1}{M+1} \sum_{i=0}^M x_{p,i}. \quad (\text{A.19})$$

Assume $x_{p,0} = 0$, the other particle positions $x_{p,i}$ with $i > 0$ can then be rewritten as:

$$x_{p,i} = (x_{p,i} - x_{p,i-1}) + (x_{p,i-1} - x_{p,i-2}) + \dots + (x_{p,1} - x_{p,0}). \quad (\text{A.20})$$

Every $x_{p,k} - x_{p,k-1}$, with $1 \leq k \leq i$, can be seen as the position after diffusion over a time $t_k - t_{k-1} = \Delta t/M$ with start position in $x_{p,k-1}$. This means, using Eq. (A.18), that the probability distribution of $x_{p,k} - x_{p,k-1}$ is given by:

$$P(x_{p,k} - x_{p,k-1}) = \frac{1}{\sqrt{4\pi D \frac{\Delta t}{M}}} e^{-\frac{(x_{p,k} - x_{p,k-1})^2}{4D \frac{\Delta t}{M}}}. \quad (\text{A.21})$$

The $x_{p,k} - x_{p,k-1}$ values are normally distributed with variance $2D\Delta t/M$. Position $x_{p,i}$, being the sum of i normally distributed variables with variance $2D\Delta t/M$, is also normally distributed with variance:

$$V_{0,i} = i2D \frac{\Delta t}{M}. \quad (\text{A.22})$$

Since position $x_{p,0}$ is set equal to zero, the corresponding variance $V_{0,0}$ is also equal to zero. The average particle position defined in Eq. (A.19) is the sum of $M+1$ normally distributed variables, therefore it is also normally distributed with variance:

$$V_0 = \frac{1}{M+1} \sum_{i=0}^M V_{0,i} = D\Delta t. \quad (\text{A.23})$$

This result, already derived by Michalet et al. [6], has to be interpreted with care. Equation (A.23) expresses that the positions of a diffusing particle, always starting from the same initial position, are normally distributed with variance $D\Delta t$, see **Fig. A.1**. This, however, has limited practical use because in reality, when taking an image from a diffusing particle with illumination time Δt , the initial position is usually unknown. Therefore, of more relevance is the variance V_{av} of the positions with respect to the average position of the trajectory.

Consider a particle trajectory during Δt that consists of $M+1$ positions $x_{p,i}$ at different times $t_i = i\Delta t/M$ ($i = 0, 1, \dots, M$). Contrary to the previous derivation of V_0 , no

Appendix A

assumption is made here on the value of $x_{p,0}$. Take a random position $x_{p,j}$ of the trajectory, with $0 \leq j \leq M$, the difference $x_{p,i} - x_{p,j}$ for every i can be written as:

$$\begin{aligned} & x_{p,i} - x_{p,j} \\ &= \begin{cases} (x_{p,i} - x_{p,i-1}) + (x_{p,i-1} - x_{p,i-2}) + \dots + (x_{p,j+1} - x_{p,j}) & \text{if } i \geq j \\ (x_{p,i} - x_{p,i+1}) + (x_{p,i+1} - x_{p,i+2}) + \dots + (x_{p,j-1} - x_{p,j}) & \text{if } i \leq j \end{cases} \end{aligned} \quad (\text{A.24})$$

As shown in Eq. (A.21), every $x_{p,k} - x_{p,k\pm 1}$ is normally distributed with variance $2D\Delta t/M$, meaning that $x_{p,i} - x_{p,j}$ is also normally distributed. If the variances of $x_{p,i}$ and $x_{p,j}$ are defined as $V_{av,i}$ and $V_{av,j}$, respectively, the variance of $x_{p,i} - x_{p,j}$ is equal to $V_{av,i} + V_{av,j}$, resulting in:

$$V_{av,i} + V_{av,j} = \begin{cases} (i-j)2D\frac{\Delta t}{M} & \text{if } i \geq j \\ (j-i)2D\frac{\Delta t}{M} & \text{if } i \leq j \end{cases}. \quad (\text{A.25})$$

The average particle position, defined in Eq. (A.19), is the sum of normally distributed variables, therefore it is also normally distributed with variance:

$$V_{av} = \frac{1}{M+1} \sum_{i=0}^M V_{av,i}. \quad (\text{A.26})$$

Equation (A.25) can thus be written as:

$$\begin{aligned} V_{av} + V_{av,j} &= \frac{1}{M+1} \sum_{i=0}^M (V_{av,i} + V_{av,j}) \\ &= \frac{1}{M+1} \sum_{i=0}^{j-1} \left((j-i)2D\frac{\Delta t}{M} \right) + \frac{1}{M+1} \sum_{i=j}^M \left((i-j)2D\frac{\Delta t}{M} \right), \end{aligned} \quad (\text{A.27})$$

which leads to:

$$V_{av} + V_{av,j} = \frac{1}{M+1} \left\{ \frac{j(j-1)}{2} 2D\frac{\Delta t}{M} + \frac{(M-j+1)(M-j)}{2} 2D\frac{\Delta t}{M} \right\}. \quad (\text{A.28})$$

The same reasoning can be applied for the values $x_{p,j}$, resulting in:

$$2V_{av} = \frac{1}{M+1} \sum_{j=0}^M (V_{av} + V_{av,j}) = \frac{2}{3} D\Delta t. \quad (\text{A.29})$$

This immediately yields:

$$V_{av} = \frac{1}{3} D \Delta t. \quad (\text{A.30})$$

The trajectory positions caused by diffusion during Δt are thus normally distributed with a variance $D\Delta t/3$ with respect to the average trajectory position, as illustrated in **Fig. A.1**.

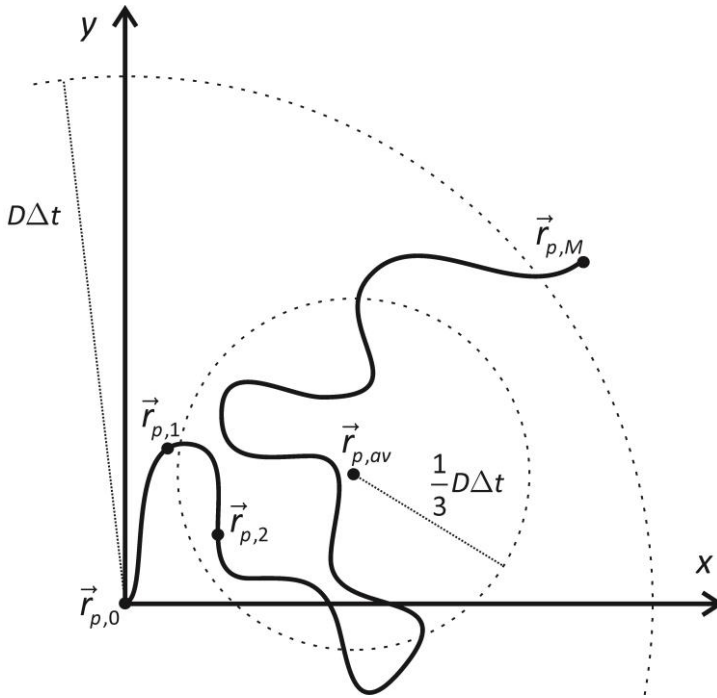


Figure A.1 | The standard deviation of the trajectory positions of a diffusion particle. An illustration of a trajectory of a particle with diffusion coefficient D during image acquisition time Δt starting in the origin $\vec{r}_{p,0}$. The positions $\vec{r}_{p,i}$ with $i = 0, 1, \dots, M$ of all possible trajectories are normally distributed around $\vec{r}_{p,0}$ with variance $D\Delta t$, while the positions $\vec{r}_{p,i}$ of an individual trajectory are normally distributed around the average trajectory position $\vec{r}_{p,av}$ with variance $D\Delta t/3$.

Appendix A

This result can be extended to the two dimensions in the focal plane, leading to the following probability distribution:

$$P(\vec{r}_p) = \frac{1}{\sqrt{\frac{2}{3}\pi D\Delta t}} e^{-\frac{(x_p - x_{p,av})^2 + (y_p - y_{p,av})^2}{\frac{2}{3}D\Delta t}}, \quad (\text{A.31})$$

with $\vec{r}_{p,av} = (x_{p,av}, y_{p,av})$ the average position during Δt . Convolution with Eq. (A.14) in the focal plane ($z_p = 0$) leads to the average apparent PSF for the lateral movement:

$$I_{\text{app}}(x, y) \propto e^{-\frac{(x - x_{p,av})^2 + (y - y_{p,av})^2}{2s_0^2 + \frac{2}{3}D\Delta t}}. \quad (\text{A.32})$$

The average apparent PSF in the case of lateral diffusion still has a Gaussian shape with a variance given by:

$$s_{xy}^2 = s_0^2 + \frac{1}{3}D\Delta t. \quad (\text{A.33})$$

This variance is larger than in the stationary case, and it becomes larger with increasing image acquisition time Δt or diffusion coefficient D .

Axial diffusion

Now consider a particle that is diffusing along the optical axis (z -direction). From Eq. (A.14), it follows that further away from the focal plane the PSF becomes wider, while the amplitude drops. The apparent PSF due to diffusion perpendicular to the focal plane will, therefore, deviate from the stationary PSF. Assume, however, that the apparent PSF can still be approximated by the Gaussian distribution in Eq. (A.14), where the variance $s^2(z_p)$ has to be replaced by an average value. In analogy with Eq. (A.31), the probability distribution of the particle positions z_p in the axial direction is given by:

$$P(z_p) = \frac{1}{\sqrt{\frac{2}{3}\pi D\Delta t}} e^{-\frac{(z_p - z_{p,av})^2}{\frac{2}{3}D\Delta t}}, \quad (\text{A.34})$$

with $z_{p,av}$ the average position during the image acquisition time.

This probability distribution can be applied to calculate the average variance using Eq. (A.15):

$$s^2(z_{p,av}) = \int_{-\infty}^{+\infty} s^2(z_p)P(z_p)dz_p = s_0^2 \left(1 + \frac{z_{p,av}^2}{z_0^2} + \frac{D\Delta t}{3z_0^2} \right). \quad (\text{A.35})$$

Except for the ideal situation where the image background is zero, the apparent PSF will become indistinguishable (as a separate object) from the background for sufficiently large $z_{p,av}$ -values. It is, therefore, assumed that the particle is only visible for $z_{p,av}$ -values between certain boundaries in the axial direction, defined as $-z_{lim}$ and z_{lim} . For free diffusion, every position along the axial direction can be occupied with the same probability by a particle. This means that the possible $z_{p,av}$ are uniformly distributed over the interval $[-z_{lim}, z_{lim}]$, resulting in an average value of:

$$\langle s^2(z_{p,av}) \rangle = \frac{1}{2z_{lim}} \int_{-z_{lim}}^{z_{lim}} s^2(z_{p,av})dz_{p,av} = s_0^2 \left(1 + \frac{z_{lim}^2}{3z_0^2} + \frac{D\Delta t}{3z_0^2} \right). \quad (\text{A.36})$$

The average apparent PSF thus has a Gaussian shape with a variance given by:

$$s_z^2 = s_0^2 + s_0^2 \left(\frac{z_{lim}^2}{3z_0^2} + \frac{D\Delta t}{3z_0^2} \right). \quad (\text{A.37})$$

As in the case of the lateral movement, axial movement also results in a variance that is larger than in the stationary case and increases with the image acquisition time and the diffusion coefficient, but to a lesser extent as can be seen by comparing with Eq. (A.33). The value of z_{lim} can be roughly estimated from the peak value of the PSF in Eq. (A.14):

$$I_{gbs}(\vec{r}_p; \vec{r}_p) \propto \frac{1}{s^2(z_p)}. \quad (\text{A.38})$$

Assume that a particle at \vec{r}_p can no longer be distinguished from the background at a certain $z_p = z_{lim}$, where the peak value drops to e^{-2} times the value $1/s^2(0)$ it has if the particle is in the focal plane ($z_p = 0$). With Eq. (A.15), this leads to:

$$z_{lim} = z_0 \sqrt{e^{-2} - 1}. \quad (\text{A.39})$$

REFERENCES

1. M. Born and E. Wolf, *Principles of optics*, (Cambridge University Press, Cambridge, 1999).
2. G. R. Cao and X. Yu, "Accuracy Analysis of A Hartmann-Shack Wave-Front Sensor Operated with A Faint Object," *Optical Engineering* **33**, 2331-2335 (1994).
3. M. K. Cheezum, W. F. Walker, and W. H. Guilford, "Quantitative comparison of algorithms for tracking single fluorescent particles," *Biophysical Journal* **81**, 2378-2388 (2001).
4. J. Crank, *The Mathematics of Diffusion*, (Clarendon Press, Oxford, 1975).
5. H. Li, H. Song, C. Rao, and X. Rao, "Accuracy analysis of centroid calculated by a modified center detection algorithm for Shack-Hartmann wavefront sensor," *Optics Communications* **281**, 750-755 (2008).
6. X. Michalet, "Mean square displacement analysis of single-particle trajectories with localization error: Brownian motion in an isotropic medium," *Physical Review e* **82**, (2010).
7. K. I. Mortensen, L. S. Churchman, J. A. Spudich, and H. Flyvbjerg, "Optimized localization analysis for single-molecule tracking and super-resolution microscopy," *Nature Methods* **7**, 377-U59 (2010).
8. T. W. Quan, S. Q. Zeng, and Z. L. Huang, "Localization capability and limitation of electron-multiplying charge-coupled, scientific complementary metal-oxide semiconductor, and charge-coupled devices for superresolution imaging," *Journal of Biomedical Optics* **15**, (2010).
9. M. S. Robbins and B. J. Hadwen, "The noise performance of electron multiplying charge-coupled devices," *Ieee Transactions on Electron Devices* **50**, 1227-1232 (2003).
10. R. E. Thompson, D. R. Larson, and W. W. Webb, "Precise nanometer localization analysis for individual fluorescent probes," *Biophysical Journal* **82**, 2775-2783 (2002).
11. A. Yariv, *Quantum electronics*, (John Wiley & Sons, Inc., New York, 1989).

Appendix B

Supplementary information of Chapter 7

The effect of the localization and overlay precision on the correlation

Consider a one-dimensional trajectory X_A and a one-dimensional trajectory X_B . The Pearson correlation R between both trajectories is given by:

$$R = \frac{\text{cov}(X_A, X_B)}{\sqrt{\text{var}(X_A)\text{var}(X_B)}} \quad (\text{B.1})$$

The numerator is called the covariance and is defined as:

$$\text{cov}(X_A, X_B) = E[(X_A - E[X_A])(X_B - E[X_B])], \quad (\text{B.2})$$

where $E[X]$ is the expected value of X . The denominator in Eq. (B.1) is the square root of the product of two variances, defined by:

$$\begin{aligned} \text{var}(X_A) &= E[(X_A - E[X_A])^2] \\ \text{var}(X_B) &= E[(X_B - E[X_B])^2]. \end{aligned} \quad (\text{B.3})$$

Assume now that the observed trajectories x_A and x_B deviate from the real trajectories X_A and X_B , respectively, because of experimental uncertainty:

$$\begin{aligned} x_A &= X_A + \delta_A \\ x_B &= X_B + \delta_B, \end{aligned} \quad (\text{B.4})$$

with δ_A and δ_B deviations caused by the finite localization and overlay precision. The part coming from the localization precision follows a distribution around zero with standard deviation σ_A and σ_B , respectively. The deviations caused by the overlay process are not strictly defined, besides that their difference is following a distribution around zero with standard deviation σ_o , which is called the overlay precision. For mathematical convenience, it is therefore assumed that δ_A and δ_B are distributed around zero with a standard deviation $\sigma'_A = \sqrt{\sigma_A^2 + \sigma_o^2/2}$ and $\sigma'_B = \sqrt{\sigma_B^2 + \sigma_o^2/2}$, respectively. Combining Eqs. (B.2) and (B.4), the covariance between x_A and x_B is given by:

$$\text{cov}(x_A, x_B) = \text{cov}(X_A, X_B). \quad (\text{B.5})$$

Appendix B

The variance of x_A and x_B follow from Eqs. (B.3) and (B.4):

$$\begin{aligned}\text{var}(x_A) &= \text{var}(X_A) + \sigma_A'^2 \\ \text{var}(x_B) &= \text{var}(X_B) + \sigma_B'^2.\end{aligned}\tag{B.6}$$

The Pearson correlation ρ between the observed trajectories x_A and x_B is thus given by:

$$\rho = \frac{\text{cov}(X_A, X_B)}{\sqrt{\text{var}(X_A)\text{var}(X_B) + \sigma_B'^2\text{var}(X_A) + \sigma_A'^2\text{var}(X_B) + \sigma_B'^2\sigma_A'^2}}.\tag{B.7}$$

Consider now the special situation $\sigma_A' = \sigma_B' = \sigma$, in this case the correlation becomes:

$$\rho = \frac{\text{cov}(X_A, X_B)}{\sqrt{\text{var}(X_A)\text{var}(X_B) + \sigma^2\text{var}(X_A) + \sigma^2\text{var}(X_B) + \sigma^4}}.\tag{B.8}$$

Both correlations will be equal if the following condition for σ is fulfilled:

$$\sigma_B'^2\text{var}(X_A) + \sigma_A'^2\text{var}(X_B) + \sigma_B'^2\sigma_A'^2 = \sigma^2\text{var}(X_A) + \sigma^2\text{var}(X_B) + \sigma^4.\tag{B.9}$$

This is a quadratic equation in σ^2 , with solution:

$$\begin{aligned}\sigma^2 &= -\frac{\text{var}(X_A) + \text{var}(X_B)}{2} \\ &+ \frac{\sqrt{(\text{var}(X_A) + \text{var}(X_B))^2 + 4\{\sigma_B'^2\text{var}(X_A) + \sigma_A'^2\text{var}(X_B) + \sigma_A'^2\sigma_B'^2\}}}{2}.\end{aligned}\tag{B.10}$$

Using Eq. (B.6) and considering the definitions of σ_A' and σ_B' , this can be rewritten as:

$$\begin{aligned}\sigma^2 &= -\frac{\text{var}(x_A) + \text{var}(x_B) - \sigma_A'^2 - \sigma_B'^2 - \sigma_o'^2}{2} + \\ &\frac{\sqrt{(\text{var}(x_A) + \text{var}(x_B))^2 + (\sigma_A'^2 - \sigma_B'^2)^2 - 2(\text{var}(x_A) - \text{var}(x_B))(\sigma_A'^2 - \sigma_B'^2)}}{2}.\end{aligned}\tag{B.11}$$

This expression is more useful than Eq. (B.10), since the variances $\text{var}(X_A)$ and $\text{var}(X_B)$ cannot be determined experimentally.

In reality, the complete trajectories x_A and x_B are not known, only discrete positions $x_A(t_i)$ and $x_B(t_i)$ at different time points t_i ($i = 1, 2, \dots, l$) are measured, from which the sample variances can be determined:

$$\begin{aligned} \text{var}(x_A) &= \frac{1}{l-1} \sum_{i=1}^l (x_A(t_i) - \langle x_A \rangle)^2 \\ \text{var}(x_B) &= \frac{1}{l-1} \sum_{i=1}^l (x_B(t_i) - \langle x_B \rangle)^2, \end{aligned} \quad (\text{B.12})$$

with $\langle x_A \rangle$ and $\langle x_B \rangle$ the average positions of the observed trajectories x_A and x_B , respectively:

$$\begin{aligned} \langle x_A \rangle &= \frac{\sum_{i=1}^l x_A(t_i)}{l} \\ \langle x_B \rangle &= \frac{\sum_{i=1}^l x_B(t_i)}{l}. \end{aligned} \quad (\text{B.13})$$

Correlation between trajectories of interacting objects

Consider a one-dimensional trajectory X_A of one object and a one-dimensional trajectory X_B of another object. Assume that both objects are interacting, resulting in identical trajectories, aside from a constant displacement d :

$$\begin{aligned} X_A &= x \\ X_B &= x + d. \end{aligned} \quad (\text{B.14})$$

The observed trajectories x_A and x_B deviate from the real trajectories, because of experimental uncertainty:

$$\begin{aligned} x_A &= x + \delta_A \\ x_B &= x + d + \delta_B, \end{aligned} \quad (\text{B.15})$$

with δ_A and δ_B deviations caused by the finite localization and overlay precision. As explained above, both can be assumed to be distributed around zero with equal standard deviation σ defined in Eq. (B.10).

Appendix B

According to Eq. (B.8), the Pearson correlation between the observed trajectories x_A and x_B is thus given by:

$$\rho = \frac{\text{cov}(x, x + d)}{\sqrt{\text{var}(x)\text{var}(x + d) + \sigma^2\text{var}(x) + \sigma^2\text{var}(x + d) + \sigma^4}}. \quad (\text{B.16})$$

According to Eqs. (B.2) and (B.3), the covariance $\text{cov}(x, x + d)$ and the variance $\text{var}(x + d)$ are equal to:

$$\begin{aligned} \text{cov}(x, x + d) &= \text{var}(x) \\ \text{var}(x + d) &= \text{var}(x). \end{aligned} \quad (\text{B.17})$$

This allows to rewrite Eq. (B.16) as:

$$\rho = \frac{1}{\sqrt{1 + 2\frac{\sigma^2}{\text{var}(x)} + \left(\frac{\sigma^2}{\text{var}(x)}\right)^2}}. \quad (\text{B.18})$$

The correlation between observed trajectories of interacting objects is thus completely determined by the ratio of $\sigma^2/\text{var}(x)$. Assume for instance that the interacting objects are undergoing Brownian motion with diffusion coefficient D . If the trajectories are observed during a time t , the variance is given by [1]:

$$\text{var}(x) = \frac{1}{3}Dt. \quad (\text{B.19})$$

The mean step in the trajectory over a time interval $\tau < t$ is known to be [2]:

$$S = \sqrt{2D\tau}. \quad (\text{B.20})$$

Combining Eqs. (B.19) and (B.20) immediately results in:

$$\text{var}(x) = \frac{t}{6\tau}S^2. \quad (\text{B.21})$$

Another example is linear motion with velocity v . If the trajectories are observed during a time t , the variance is given by:

$$\text{var}(x) = \frac{1}{12}v^2t^2. \quad (\text{B.22})$$

The (mean) step in the trajectory over a time interval $\tau < t$ is:

$$S = v\tau. \quad (\text{B.23})$$

Combining Eqs. (B.22) and (B.23) immediately results in:

$$\text{var}(x) = \frac{t^2}{12\tau^2} S^2. \quad (\text{B.24})$$

Linear and Brownian motion thus give rise to the following relationship between trajectory variance and mean step:

$$\text{var}(x) = fS^2, \quad (\text{B.25})$$

where f is a factor that depends on the ratio t/τ between the observation time and time interval for the step. Inserting this expression in Eq. (B.18) gives:

$$\rho = \frac{1}{\sqrt{1 + f\left(\frac{\sigma}{S}\right)^2 + \left(\frac{\sigma}{S}\right)^4}}. \quad (\text{B.26})$$

In other words, for a certain ratio t/τ , the observed correlation between two interacting objects undergoing Brownian or linear motion is completely determined by the following ratio, termed the relative localization precision:

$$r = \frac{\sigma}{S}. \quad (\text{B.27})$$

However, the mean step S cannot be determined experimentally. In reality, the actual trajectory x is not known, only discrete positions $x_A(t_i)$ and $x_B(t_i)$ at different time points t_i ($i = 1, 2, \dots, l$) are measured. In this case the time interval is given by $\tau = t_i - t_{i-1}$ ($i = 2, \dots, l$) and the total observation time by $t = l\tau$, from which immediately follows that the ratio $t/\tau = l$. From the trajectories the sample mean steps can be determined as:

$$S_{AB} = \frac{1}{2l} \sum_{i=2}^l \{|x_A(t_i) - x_A(t_{i-1})| + |x_B(t_i) - x_B(t_{i-1})|\}. \quad (\text{B.28})$$

These are estimations of the mean steps defined in Eqs. (B.20) and (B.23). All observed trajectories with length l of interacting objects that are undergoing Brownian or linear motion will thus have the same expectation value for the correlation if they have the same relative localization precision r . This result is valid for all types of motion that

Appendix B

fulfil the condition in Eq. (B.25), i.e. the variance of the trajectories of the interacting objects should be linearly related to the square of the mean step.

REFERENCES

1. H. Deschout, K. Neyts, and K. Braeckmans, "The influence of movement on the localization precision of sub-resolution particles in fluorescence microscopy," *Journal of Biophotonics* **5**, 97-109 (2012).
2. M. J. Saxton and K. Jacobson, "Single-particle tracking: Applications to membrane dynamics," *Annual Review of Biophysics and Biomolecular Structure* **26**, 373-399 (1997).

Appendix C

Scientific curriculum vitae

PERSONALIA

Surname	Deschout
First names	Hendrik Georges
Date of birth	September 16, 1984
Place of birth	Oostende, Belgium
Laboratory	Biophotonic Imaging Group Laboratory of General Biochemistry and Physical Pharmacy Ghent University
Address	Harelbekestraat 72 B-9000 Gent Belgium
Phone	+3292648074
E-mail	hendrik.deschout@ugent.be
URL	www.biofys.ugent.be

DEGREES

2006-2008	Master of Engineering Physics Ghent University <i>with great distinction</i>
2002-2006	Master of Physics Ghent University <i>with distinction</i>

PUBLICATIONS

Hendrik Deschout, Kristiaan Neyts, Kevin Braeckmans. The influence of movement on the localization precision of sub-resolution particles in fluorescence microscopy. *Journal of Biophotonics*, Volume 5, Issue 1, Pages 97-109, 2012.

Hendrik Deschout, Joel Hagman, Sophia Fransson, Jenny Jonasson, Mats Rudemo, Niklas Lorén, Kevin Braeckmans. Straightforward FRAP for quantitative diffusion measurements with a laser scanning microscope. *Optics Express*, Volume 18, Issue 22, Pages 22886-22905, 2010.

Selected by the editors for extra publication in the *Virtual Journal for Biomedical Optics*, Volume 6, Issue 1, Pages 22886-22905.

Dries Vercauteren, Hendrik Deschout, Katrien Remaut, Johan Engbersen, Arwyn Jones, Jo Demeester, Stefaan De Smedt, Kevin Braeckmans. Dynamic colocalization microscopy to characterize intracellular trafficking of nanomedicines. *ACS Nano*, Volume 5, Issue 10, Pages 7874-7884, 2011.

Magnus Röding, Hendrik Deschout, Kevin Braeckmans, Mats Rudemo. Measuring absolute number concentrations of nanoparticles using single-particle tracking. *Physical Review E*, Volume 84, Issue 3, 031920, 2011.

Magnus Röding, Hendrik Deschout, Kevin Braeckmans, Mats Rudemo. Measuring absolute nanoparticle number concentrations from particle count time series. *Journal of Microscopy*, E-published ahead of print, 2013.

Broes Naeye, Hendrik Deschout, Magnus Röding, Mats Rudemo, Joris Delanghe, Katrien Devreese, Jo Demeester, Kevin Braeckmans, Stefaan De Smedt, Koen Raemdonck. Hemocompatibility of siRNA loaded dextran nanogels. *Biomaterials*, Volume 32, Issue 34, Pages 9120-9127, 2011.

Broes Naeye, Hendrik Deschout, Vicky Caveliers, Benedicte Descamps, Kevin Braeckmans, Christian Vanhove, Jo Demeester, Tony Lahoutte, Stefaan De Smedt, Koen Raemdonck. In vivo disassembly of IV administered siRNA matrix nanoparticles at the renal filtration barrier. *Biomaterials*, Volume 34, Issue 9, Pages 2350-2358, 2013.

Ellen Verheyen, Steffen van der Wal, Hendrik Deschout, Kevin Braeckmans, Stefaan De Smedt, Arjan Barendregt, Wim Hennink, Cornelus van Nostrum. Protein macromonomers containing reduction-sensitive linkers for covalent immobilization and

glutathione triggered release from dextran hydrogels. *Journal of Controlled Release*, Volume 156, Issue 3, Pages 329-336, 2011.

Nick Smisdom, Kevin Braeckmans, Hendrik Deschout, Martin vandeVen, Jean-Michel Rigo, Stefaan De Smedt, Marcel Ameloot. Fluorescence recovery after photobleaching on the confocal laser-scanning microscope: generalized model without restriction on the size of the photobleached disk. *Journal of Biomedical Optics*, Volume 16, Issue 4, 046021, 2011.

Kevin Braeckmans, Kevin Buyens, Broes Naeye, Dries Vercauteren, Hendrik Deschout, Koen Raemdonck, Katrien Remaut, Niek Sanders, Jo Demeester, Stefaan De Smedt. Advanced fluorescence microscopy methods illuminate the transfection pathway of nucleic acid nanoparticles. *Journal of Controlled Release*, Volume 148, Issue 1, Pages 69-74, 2010.

Roberta Censi, Tina Vermonden, Hendrik Deschout, Kevin Braeckmans, Piera di Martino, Stefaan De Smedt, Cornelus van Nostrum, Wim Hennink. Photopolymerized thermosensitive poly(HPMA lactate)-PEG-based hydrogels: effect of network design on mechanical properties, degradation, and release behavior. *Biomacromolecules*, Volume 11, Issue 8, Pages 2143-2151, 2010.

Roberta Censi, Tina Vermonden, Mies van Steenberghe, Hendrik Deschout, Kevin Braeckmans, Stefaan De Smedt, Cornelus van Nostrum, Piera di Martino, Wim Hennink. Photopolymerized thermosensitive hydrogels for tailorable diffusion-controlled protein delivery. *Journal of Controlled Release*, Volume 140, Issue 3, Pages 230-236, 2009.

Katrien Forier, Anne-Sophie Messiaen, Koen Raemdonck, Hendrik Deschout, Joanna Rejman, Frans De Baets, Hans Nelis, Stefaan De Smedt, Jo Demeester, Tom Coenye, Kevin Braeckmans. Transport of nanoparticles in cystic fibrosis sputum and bacterial biofilms by single-particle tracking microscopy. *Nanomedicine*, E-published ahead of print, 2012.

Thomas Martens, Dries Vercauteren, Katrien Forier, Hendrik Deschout, Katrien Remaut, Rik Paesen, Marcel Ameloot, Johan Engbersen, Jo Demeester, Stefaan De Smedt, Kevin Braeckmans. Measuring the intravitreal mobility of nanomedicines with single-particle tracking microscopy. *Nanomedicine*, E-published ahead of print, 2013.

PATENT APPLICATIONS

Kevin Braeckmans, Hendrik Deschout, Kristiaan Neyts, Jo Demeester, Stefaan De Smedt. Methods and systems for optical characterisation, WO2011073410. Filed December 17, 2010.

Magnus Röding, Mats Rudemo, Kevin Braeckmans, Stefaan De Smedt, Jo Demeester, Hendrik Deschout. Method and system for dispersion measurements, WO2012004320. Filed July 6, 2011.

BOOK CHAPTERS

Kevin Braeckmans, Hendrik Deschout, Jo Demeester, Stefaan De Smedt. Measuring molecular dynamics by FRAP, FCS, and SPT. *Optical fluorescence microscopy: from the spectral to the nano dimension* (edited by Alberto Diaspro), Pages 153-164. Springer, Heidelberg, 2011.

ORAL PRESENTATIONS

Hendrik Deschout, Jo Demeester, Kevin Braeckmans. Rectangle FRAP method for diffusion measurements without prior knowledge of bleaching resolution. *Workshop on Transport through Heterogeneous Materials*, Gullmarsstrand, Sweden, 2009.

Hendrik Deschout, Katrien Forier, Dries Vercauteren, Kristiaan Neyts, Kevin Braeckmans. The effect of movement on the localization precision of single molecules and particles. *Focus on Microscopy*, Konstanz, Germany, 2011.

Hendrik Deschout, Pietro Maoddi, Guillaume Mernier, Sébastien Jiguët, Philippe Renaud, Kristiaan Neyts, Kevin Braeckmans. On-chip sheet illumination for single-particle tracking measurements in bio-fluids. *Optics Within Life Sciences*, Genoa, Italy, 2012.

Hendrik Deschout. Fluorescence microscopy methods for studying the interaction of nanoscopic particles with bio-materials. *NB-Photonics Annual Meeting*, Gent, Belgium, 2012.

Invited presentation

SELECTION OF POSTER PRESENTATIONS

Hendrik Deschout, Jo Demeester, Kevin Braeckmans. Colocalisation of dynamic objects in digital fluorescence microscopy movies based on correlated movement. *Belgian Biophysical Society Meeting*, Hasselt, Belgium, 2009.

Hendrik Deschout, Jo Demeester, Kevin Braeckmans. Colocalisation of dynamic objects in digital fluorescence microscopy movies based on correlated movement. *Focus on Microscopy*, Krakow, Poland, 2009.

Hendrik Deschout, Dries Vercauteren, Jo Demeester, Stefaan De Smedt, Kevin Braeckmans. Quantitative colocalisation of dynamic objects in fluorescence microscopy movies. *Focus on Microscopy*, Shanghai, China, 2010.

Hendrik Deschout, Joel Hagman, Sophia Fransson, Jenny Jonasson, Mats Rudemo, Niklas Lorén, Kevin Braeckmans. A versatile rectangle FRAP method for diffusion measurements with a laser scanning microscope. *Advanced Light Microscopy Symposium*, Gent, Belgium, 2010.

Hendrik Deschout, Filip Strubbe, Hamidreza Azarinia, Kristiaan Neyts, Kevin Braeckmans. Optofluidics device with sheet illumination for single particle tracking microscopy. *The 6th International Conference on Microtechnologies in Medicine and Biology*, Luzern, Switzerland, 2011.

Hendrik Deschout, Filip Strubbe, Hamidreza Azarinia, Kristiaan Neyts, Kevin Braeckmans. Optofluidics device with sheet illumination for single particle tracking microscopy. *NanoBioTech*, Montreux, Switzerland, 2011.

Hendrik Deschout, Filip Strubbe, Hamidreza Azarinia, Kristiaan Neyts, Kevin Braeckmans. Optofluidics device with sheet illumination for single particle tracking microscopy. *NB-Photonics Annual Meeting*, Gent, Belgium, 2011.

Appendix C

Hendrik Deschout, Kristiaan Neyts, Kevin Braeckmans. Lab-on-a-chip with sheet illumination for nanoparticle tracking in biological fluids. *Knowledge for growth*, Gent, Belgium, 2012.

Hendrik Deschout, Pietro Maoddi, Guillaume Mernier, Sébastien Jiguet, Philippe Renaud, Filip Strubbe, Kristiaan Neyts, Kevin Braeckmans. On-chip sheet illumination for single-particle tracking measurements in bio-fluids. *NB-Photonics Annual Meeting*, Gent, Belgium, 2012.

